Understanding Heart Failure in Patients with Dilated Cardiomyopathy
A Direct Tissue Analysis from Explanted Human Hearts

by

Hao Zhang

A thesis submitted in partial fulfillment of the requirements for the degree of

Doctor of Philosophy

Department of Medicine
University of Alberta

Abstract

Background

Chronic heart failure (HF) remains a rising global epidemic that affects both adults and children population. The causes of HF are heterogeneous, and syndromes are often complicated by concomitant disorders such as iron deficiency (ID) and diabetes. Comorbidities not only complicate the presentation and treatment of HF, but also play an instrumental role in its development. Thus, in recent years, elucidating and treating comorbidities have gained increasing importance in the management of HF.

As the most prevalent malnutritional disease globally, iron deficiency often co-exists with HF regardless of abnormal blood cell parameters. Prior studies have confirmed its unfavorable impact on patients' physical capacity and clinical outcomes, and iron supplementations exhibited remarkable benefits representing a promising therapeutic target. However, emerging evidence highlighted the presence of myocardial iron deficiency (MID) in several small HF cohorts, and consistently revealed a weak association with systemic iron status indicating distinct cardiac iron regulations. Furthermore, the diagnosis and pathophysiological implications of MID in HF patients remain largely unexplored.

Dilated cardiomyopathy (DCM) represents the most common cause of terminal HF, and consequently, the most common indication for heart transplantation in adult and pediatric patients with HF. Despite similar phenotypes characterized as systolic dysfunction and eccentric ventricular dilation, the causes of DCM are also heterogeneous, which can be genetic, acquired (non-genetic) or a mixed form of both. The causative mutations account for up to one-third of idiopathic DCM cases and affect genes encoding structural components of desmosome, sarcomere, and nuclear envelop proteins, whereas the non-genetic forms of DCM can be a result of a variety

of conditions such as viral infections, systemic autoimmune, endocrine, and neuromuscular diseases, and exposure to toxins, alcohol, or certain drugs. As such, the clinical course of this disease is remarkably variable. Most patients become symptomatic across a wide range of ages (20-60 years old), while infants and children can also be affected by DCM which accounts for up to 60% of all childhood cardiomyopathies. Pediatric DCM (P-DC) are pathologically distinct entities from their adult counterparts, with causes largely idiopathic and with age- and development-specific features in the immature failed hearts. However, current guideline-recommended medications for children and adolescents with HF are primarily extrapolated from adults and have been proven ineffective, which clearly indicates the disparate pathophysiology underlying the children's failing hearts. Moreover, P-DC always occurs in the absence of common comorbidities seen in adult counterparts (A-DC), thereby offering an invaluable opportunity to examine the pathogenesis of primary DCM.

Methods and Results

We investigated end-stage dilated cardiomyopathic disease directly from explanted human heart specimens. In Chapter 3, the high prevalence of comorbid MID in adult HF patients and its poor correlation with hematopoietic indices were determined in the largest cohort of its kind to date. We assessed the pathophysiological role of MID in the remodeling progression to advanced HF. The feasibility of using cardiac magnetic resonance (CMR) imaging to non-invasively monitor this hidden disease in the human explants was further evaluated. Mechanistically, iron uptake pathways were found impeded in iron deficient failing hearts, coupled with pathologically elevated levels of ferroprotein in the sarcolemma. In Chapter 4, the explanted failing hearts from adults and children with DCM, and age-matched non-cardiomyopathic (NC) controls were examined. Unlike

A-DC, P-DC demonstrated minimal myocardial remodeling characteristics with maintained contractile properties. Divergent transcriptomic and (phospho-)proteomic tissue phenotypes of P-DC were characterized by a systems biology approach, further complemented with an array of *in vitro* biomolecular validations on canonical pathways and functional assessments. Notably, P-DC exhibited remarkably dysfunctional mitochondrial electron carriers, namely, complex I, likely imputable to oxidative stress-induced cardiolipin peroxidation and remodeling.

Conclusions

Our studies demonstrated MID is an integral pathophysiology of HF, which exacerbates the pathological remodeling in adults driven primarily by dysfunctional mitochondria and inflamed oxidative stress within LV. CMR exhibits clinical potential as a non-invasive surrogate of myocardial iron status. Moreover, P-DC represents a clinically distinct entity warrants focused investigation. Defective electron transporting activities, specifically at complex I, in the absence of major adult-dominant cardiac remodeling, remain a potential target for treating pediatric HF patients. Our implementation of state-of-the-art multi-omics on explanted human hearts offers a unique opportunity to profile robust biosignatures to differentiate P-DC from adult counterparts and explore children-appropriate pharmaceutical targets.

Preface

This thesis is an original work by Hao Zhang, which is completed during the years of a world-wide pandemic. The work presented in this dissertation was mainly carried out in Dr. Oudit's laboratory in the University of Alberta, Edmonton, Alberta, Canada.

Human heart specimens were collected as part of the Human Organ Procurement and Exchange program (HOPE) and Human Explanted Heart Program (HELP). Informed and signed consents were obtained from all research subjects or their power of attorney. The collection of explanted human cardiac tissues and research ethics were approved by the Mazankowski Alberta Heart Institute and the Institutional Ethics Committee of the University of Alberta.

The format of this thesis is paper-based, and it includes writing and data from published and unpublished manuscripts. Specific details of the manuscripts, including my contributions to the listed projects, are outlined as below.

Part of Chapter 1 is adopted from: Zhang H, Zhabyeyev P, Wang S, and Oudit GY. Role of iron metabolism in heart failure: From iron deficiency to iron overload. *Biochimica et Biophysica Acta (BBA)-Molecular Basis of Disease.* 2019;1865:1925-1937. **Role of H.Z.:** Participated in the study design, drafted the manuscript, prepared the figures and illustrations, and integrated contributions and edits from coauthors.

Part of Chapter 2 is adopted from: Zhang H, Viveiros A, Nikhanj A, Nguyen Q, Wang K, Wang W, Freed DH, Mullen JC, MacArthur R, Kim DH, Tymchak W, Sergi CM, Kassiri Z, Wang S, and Oudit GY. The Human Explanted Heart Program: A translational bridge for cardiovascular medicine. Biochimica et Biophysica Acta (BBA)-Molecular Basis of Disease. 2021;1867:165995. **Role of H.Z.:** Participated in the study design, drafted the manuscript, prepared the figures and illustrations, and integrated contributions and edits from coauthors.

A version of Chapter 3 is adopted from: **Zhang H**, Jamieson KL, Grenier J, Nikhanj A, Tang Z, Wang F, Wang S, Seidman JG, Seidman CE, Thompson RB, Seubert JM, and Oudit GY. Myocardial iron deficiency and mitochondrial dysfunction in advanced heart failure in humans. Journal of the American Heart Association. 2022;e022853. **Role of H.Z.**: Participated in the study design, performed the experiments (including explanted human heart collections), interpreted all acquired data with statistical analyses, constructed the clinical database, prepared the figures and illustrations, drafted the manuscript and integrated contributions and edits from coauthors.

A version of Chapter 4 is adopted from: **Zhang H**, Kuzmanov U, Joseph KB, Viveiros A, Kim Y, Morton S, Urschel S, Seubert JM, Wang S, Seidman JG, Seidman CE, Gramolini A, and Oudit GY. Multi-omics profiling of pediatric dilated cardiomyopathy: A focus on metabolism phenotypic switching. (**Unpublished data and text**; **Role of H.Z.**: Participated in the study design, performed the experiments (including explanted human heart collections), interpreted all acquired data with statistical analyses, constructed the clinical database, prepared the figures and illustrations, drafted the manuscript and integrated contributions and edits from coauthors. Dr. Gramolini's laboratory assisted with proteomic and phosphoproteomic data acquisition and analyses)

THIS THESIS IS DEDICATED

To my grandparents Jia-Cai He and Ya-Qing Fang, who brought me up.

and

To my mother Xiu-Ling He, for her love and sacrifice.

Acknowledgements

First and foremost, I would like to thank Drs. Gavin Y. Oudit and Shaohua Wang for their supervision and invaluable support over the course of my graduate studies. I also would like to thank Dr. John M. Seubert for serving on my supervisory committee, who provided patient advice and professional guidance throughout the Ph.D. program. Furthermore, I would like to extend my sincere gratitude to the rest of my thesis committee: Drs. Gary Lopaschuk and Filio Billia, for their precious time, insightful comments, and constructive suggestions during the preparation of the thesis.

In addition, I am grateful for the state-of-the-art collaborations with many extraordinary research teams from the University of Alberta, University of Toronto, and Harvard Medical School, and for their wonderful contributions to my research projects. Indeed, the members of Dr. Oudit's research group have been more than a source of research partnership; the days we worked or spent together as close colleagues and intimate friends were unforgettable.

Last but not least, I would like to acknowledge the professional and multidisciplinary collaborations between all the Human Explanted Heart Program (HELP) team members, and the strong support we have received from all altruistic heart organ donors and their families. And I would like to express special thanks to our graduate program coordinator, Dr. Nadia.Jahroudi, and graduate program advisors Mr. Julian Schulz and Mrs. Barb Thomson for their exceptional administrative assistance throughout my Ph.D. studies. This research would not have been possible without the financial assistances from China Scholarship Council (CSC), Motyl Graduate Studentship in Cardiac Sciences from Faculty of Medicine & Dentistry, and Canadian Institutes of Health Research (CIHR) operating grant(s) under Dr. Oudit.

Table of Contents

List of Tables

List of Figures

List of Abbreviations

(Acronym or abbreviation is defined at first use in parentheses for each Chapter)

4-HNE	4-hydroxynoneal
ABACUS	Alberta Cardiovascular and Stroke Research Center
AC	Arrhythmogenic cardiomyopathy
ACC	Acetyl-CoA carboxylase
ACE2	Angiotensin converting enzyme 2
ACEi	Angiotensin converting enzyme inhibitor
A-DC	Adult dilated cardiomyopathy
AF	Atrial fibrillation
AHA	American Heart Association
AKT	Protein kinase B
AMPK	5'-AMP activated protein kinase
A-NC	Adult non-dilated cardiomyopathy
Ang II	Angiotensin II
ATP	Adenosine triphosphate
AT_1R	Ang II type 1 receptor
ARB	Angiotensin receptor blockers
BiV-ICD	Bi-ventricular implantable cardioverter-defibrillator
BMI	Body mass index
BMP(R)	Bone morphogenic protein (receptor)
BNP	Brain natriuretic peptide
BP	Biological processes
BSA	Body surface area
CAD	Coronary artery disease
CAD-NI	Non-infarcted from coronary artery disease
CAD-PI	Peri-infarcted from coronary artery disease
CAMKII	Ca^{2+} calmodulin-dependent kinase II
CASP3	Caspase 3

CAT	Catalase
CC	Cellular components
CHD	Congenital heart defects
CICR	Ca^{2+} induced Ca^{2+} release
CL	Cardiolipin
CM	Cardiomyopathy
CMR	Cardiac magnetic resonance
COPD	Chronic obstructive pulmonary diseases
COX I/II/III/IV	Complexes I/II/III/IV
CPT-1/2	Carnitine palmitoyltransferase-1/2
CRISPR-Cas9	Clustered regularly interspaced short palindromic repeats and CRISPR-associated protein 9
CS	Citrate synthase
CVD	Cardiovascular diseases
Cyto	Cytosol
DAPI	4’,6-diamidino-2-phenylindole
DBP	Diastolic blood pressure
DCM	Dilated cardiomyopathy
DEG	Differentially expressed gene
DHE	Dihydroethidium
DM2	Type 2 diabetes mellitus
DMEM	Dulbecco’s modified Eagle’s medium
DMT-1	Divalent metal transporter-1
DO	Disease Ontology
DORV	Double outlet right ventricle
Drp-1	dynamin-related protein-1
DTYCB	Duodenal cytochrome B
EAT	Epicardial adipose tissue
EC	Excitation-contraction

ECM	Extracellular matrix
eGFR	Estimated glomerular filtration rate
ERK	Extracellular signal regulated kinase
ESC	European Society of Cardiology
ETC	Electron transport chain
FA	Fatty acid
FD	Fabry disease
FDR	False discovery rate
Fe-S	Iron-sulfur
FLVCR	Feline leukemia virus type C receptor
FPN	Ferroportin
FTN	Ferritin
GLUT	Glucose transporter
GO	Gene Ontology
GPX	Glutathione peroxidase
GR	Glutathione reductase
GSEA	Gene set enrichment analysis
GSH	Reduced glutathione
GSK-3β	Glycogen synthase kinase-3β
GSSG	Oxidized glutathione
HAMP	Hepcidin antimicrobial peptide
HBSS	Hank’s balanced salt solution
HCM	Hypertrophic cardiomyopathy
HCP1	Heme/folate transporter 1
HELP	Human Explanted Heart Program
HF	Heart failure
HFE	Hemochromatosis protein
HF-MID	Heart failure with myocardial iron deficiency
HF-NID	Heart failure without myocardial iron deficiency

HF-pEF	Heart failure with preserved ejection fraction
HF-rEF	Heart failure with reduced ejection fraction
HIF2α	Hypoxia inducible factor 2α
HJV	Hemojuvelin
HLA	Human leukocyte antigen
HLHS	Hypoplastic left heart syndrome
HOPE	Human Organ Procurement and Exchange Program
HP	Human Phenotype Ontology
HR	Heart rate
ICD	Implantable cardioverter defibrillator
ID	Iron deficiency
IF	Immunofluorescence
IHD	Ischemic heart disease
IMM	Inner mitochondrial membrane
iPSC	Induced pluripotent stem cells
IREs	Iron response elements
IRP-1/2	Iron response proteins-1/2
IV	Intravenous (injection)
IVCD	Intraventricular conduction delay
JNK	c-Jun N-terminal kinase
KDH	Alpha-ketoglutarate dehydrogenase
KEGG	Kyoto Encyclopedia of Genes and Genomes
LA/RA	Left/right atria
LAD	Left anterior descending artery
LBBB/RBBB	Left/right bundle branch block
LCC/RCC/NCC	Left/right/non-coronary cusp
LC-MS/MS	Liquid chromatography with tandem mass spectrometry
LCX	Left circumflex artery

LDH	Lactate dehydrogenase
LTCC	L-type Ca^{2+} channels
LV/RV	Left/right ventricle
LVAD	Left ventricular assist device
LVEF	LV ejection fraction
LVIDd/LVIDs	LV internal dimensions at end-diastole/end-systole
LVPWT	LV posterior wall thickness
MAHI	Mazankowski Alberta Heart Institute
MAPK	Mitogen-activated protein kinase
MCD	Malonyl-CoA decarboxylase
MCHC	Mean corpuscular hemoglobin concentration
MCV	Mean corpuscular volume
MD	Muscular dystrophy
MDA	Malondialdehyde
Mem	Membrane
MF	Molecular functions
Mfn-1/2	Mitofusin-1/2
MI	Myocardial infarction
MID	Myocardial iron deficiency
MMP	Matrix metalloproteinase
mMPT	Ca^{2+}-triggered membrane permeability transition pore
MnSOD	Manganese superoxide dismutase
MRA	Mineralocorticoid receptor antagonists
MT	Mason's trichrome staining
mtDNA	Mitochondrial DNA
NADPH	Reduced nicotinamide adenine dinucleotide phosphate
NCX1	Sodium calcium exchanger 1
NFC	Non-failing control hearts
NGS	Next generation RNA sequencing

NTBI	Non-transferrin bound iron
NT-proBNP	N-terminal pro b-type natriuretic peptide
NYHA	New York Heart Association Classification
OCT	Optimal cutting temperature compound
OMM	Outer mitochondrial membrane
Opa-1	Optic atrophy-1
OXPHOS	Oxidative phosphorylation
PAH	Pulmonary artery hypertension
PAT	Pericardial adipose tissue
PCA	Principal component analysis
PCR	Polymerase chain reaction
P-DC	Pediatric dilated cardiomyopathy
PDH	Pyruvate dehydrogenase
PDK	Pyruvate dehydrogenase kinase
PDP	Pyruvate dehydrogenase phosphatase
PGC-1α	PPAR and its coactivator-1α
PI3K	Phosphoinositide 3 kinases
PINK-1	Mitochondrial PTEN-induced kinase-1
PKA	Protein kinase A
PLN	Phospholamban
P-NC	Pediatric non-dilated cardiomyopathy
PPAR	Peroxisome proliferator activated receptor
PPI	Proton pump inhibitor
PSR	Picrosirius red staining
PVD	Peripheral vascular diseases
PVs	Pathogenic variants
QC	Quality control
QTI	QT interval
RCA	Right coronary artery

RCM	Restrictive cardiomyopathy
ROS	Reactive oxygen species
RPKM	Reads per kilobase of exon model per million mapped reads
RT	Room temperature
RT-PCR	Reverse transcription polymerase chain reaction
RVd Basal	Basal right ventricular diameter
RVSP	Right ventricular systolic pressure
RYR	Ryanodine receptor
SBP	Systolic blood pressure
sc/snRNA-Seq	Single-cell/-nucleus RNA sequencing
SDS-PAGE	Sodium dodecyl sulfate polyacrylamide gel electrophoresis
SERCA2a	Sarco/endoplasmic reticulum Ca^{2+}-ATPase 2a
SID	Systemic iron deficiency
smFISH	Single-molecule fluorescence in situ hybridization
SNVs	Single nucleotide variants
SCD	Sudden cardiac death
SOD	Superoxide dismutase
SR	Sarcoplasmic reticulum
sTF	Saturation of transferrin
T_1	Longitudinal relaxation time
T_2	Transverse relaxation time
TAPSE	Tricuspid annular plane systolic excursion
TCA	Tricarboxylic acid cycle
TEM	Transmission electron microscopy
TF	Transferrin
TFM	Tissue freezing medium

TFR-1/2	Transferrin receptor-1/2
TIBC	Total iron binding capacity
TIMP	Tissue inhibitor of metalloproteinase
TGA	Transposition of great artery
TLR4	Toll-like receptor 4
ToF	Tetralogy of Fallot
TSAT	Transferrin saturation
UA	Uranyl acetate
UMAP	Uniform manifold approximation and projection
UTR	Untranslated regions
VDAC	Voltage dependent anion channel
VHD	Valvular heart disease
VSQR	Variant score quality recalibration
VT	Ventricular tachycardia
WES	Whole exome sequencing
WGA	Wheat germ agglutinin
WGS	Whole genome sequencing

Chapter 1

Introduction

1.1. Iron Deficiency in Heart Failure

1.1.1. Importance of Treating Comorbidities in Heart Failure

Chronic heart failure (HF) is a global epidemic that affects both adults and children population. Statistically, it has affected over 37.7 million individuals worldwide[1], including approximately 14M Europeans, 6.2M Americans, and 1.3-6.7% Asian and 1.5-2% Canadian population[2, 3]. Furthermore, this illness is estimated to continue growing rapidly over the next decades which will impose tremendous medical and societal burdens. Specifically, it is projected to double in North America (amounting to ~$70B in the US and ~$8B in Canada) within the next two decades[2, 4].

HF is known as a highly complex and multifactorial disorder, and it represents the final phase of cardiac structural or functional impairment secondary to varying etiologies[5], which is often complicated by extrinsic factors such as comorbidities and environment leading to poor quality of life and high mortality rate. Typically, it is characterized by activation of a cascade of signaling pathways associated with pathological tissue remodeling, altered electrophysiology, defective intermediary metabolism, imbalanced extracellular matrix (ECM) and cellular adhesion[6-8], leading to overall poor cardiac performance, decreased vascular compliance, and deadly arrhythmias. Of note, most comorbid conditions play a key role in the disease pathogenesis or progression as a risk or perpetuating factor, and the number of HF patients carrying multiple comorbidities has increased significantly during the last decade[9]. Thus, management of comorbidities is gaining equal importance to treating the primary cause of HF itself[10-12], and elucidating the pathogenesis of comorbidities in HF patients represents an imperative task for minimizing the morbidity and mortality in this vulnerable population.

1.1.2. Role of Iron Metabolism Disorders in Heart Failure

In the aging society, HF is a problem of epidemic proportions, which projected to rise in the next decades imposing tremendous societal and economic costs[13]. Major physiological functions of iron include oxygen transport as a component of hemoglobin in blood (and myoglobin in striated muscle), energy production through oxidative phosphorylation as an integral component of iron-sulphur cluster-containing enzymes such as cytochromes, NADPH, and succinate dehydrogenases,

and as a component of peroxide- and nitric oxide-generating enzymes. Both iron deficiency (ID) and iron overload (primary hemochromatosis and secondary iron-overload) have high prevalence.

In the developed world, the prevalence of ID in population varies from 10 to 16% depending on the sex, age, and race with pregnant women having the highest risk[14]. Prevalence of iron-deficient anemia varies from 2.6 to 5%[14]. Socio-economic status considerably influences prevalence of iron deficiency; for example, although iron deficiency prevalence in Northern and Western Europe was 4-18%, the prevalence was considerably higher in Eastern Europe (9-50%)[15]. Alleles causing primary hemochromatosis have considerably high frequency (about 10% in western Europeans) with approximately 1% population being affected[16-18]. Secondary iron overload associated with treatment of hemolytic anemias mainly thalassemias and sickle cell disease[19]. Thalassemias is caused by reduced synthesis of globin chains, and worldwide about 5% population carry globin variants with considerably higher allele frequency in Mediterranean, Middle East, North India, and South-West Asia with some population reaching 100% for α-thalassemia variants[20-22]. Prevalence of sickle cell disease is high in sub-Saharan Africa, India, Middle East, and Mediterranean with about 300,000 babies born worldwide with sickle cell disease[23, 24]. Both iron deficiency and iron-overload can lead to cardiomyopathy and ultimately HF[25, 26]. Iron deficiency emerges as a major comorbidity in a large fraction of HF patients[27, 28]. However, the mechanism linking HF and iron deficiency remains poorly understood. Therefore, in this review, we highlight the key role of iron metabolism in cardiac function and illustrate the central importance of maintaining normal myocardial iron levels.

1.1.3. Systemic Iron Metabolism and Regulation

Distribution of Iron Through the Body. Normally, male adults have 35 to 45 mg of iron per kilogram of body weight[16, 29], while premenopausal women have somewhat lower amount due to recurrent menstruation. Out of total amount of iron in the body (about 3500 mg) erythrocytes (1800 mg) and liver (1000 mg) contain the highest amount of iron (**Figure 4.1A**). Normally, in the absence of blood loss, only small amounts of iron (1-2 mg/day) are lost due to desquamation of epithelial cells, and these losses are replenished by the uptake of dietary iron. The iron present in the body is constantly recycled with the erythrocytes and macrophages being the major part of the recycling process. As erythrocytes age, they undergo phagocytosis by macrophages, and the iron

contained in the hemoglobin of these erythrocytes is released back to the plasma to be reuptaken by bone marrow for the synthesis of new erythrocytes. Other organs uptake iron from plasma to synthesize iron-containing molecules (*e.g.*, myoglobin) and extrude excesses of iron back to the plasma. Plasma contains only small amounts of iron (3 mg) bound to transferrin with liver acting as a main storage site of the excess of iron containing about 1000 mg (**Figure 4.1A**). These depots ensure seamless iron recycling and erythropoiesis because under normal circumstances, less than 10% of daily iron needs are supplied from diet. Lack of specialized extrusion pathway for iron makes regulation of the iron uptake to be especially important to ensure optimal iron metabolism.

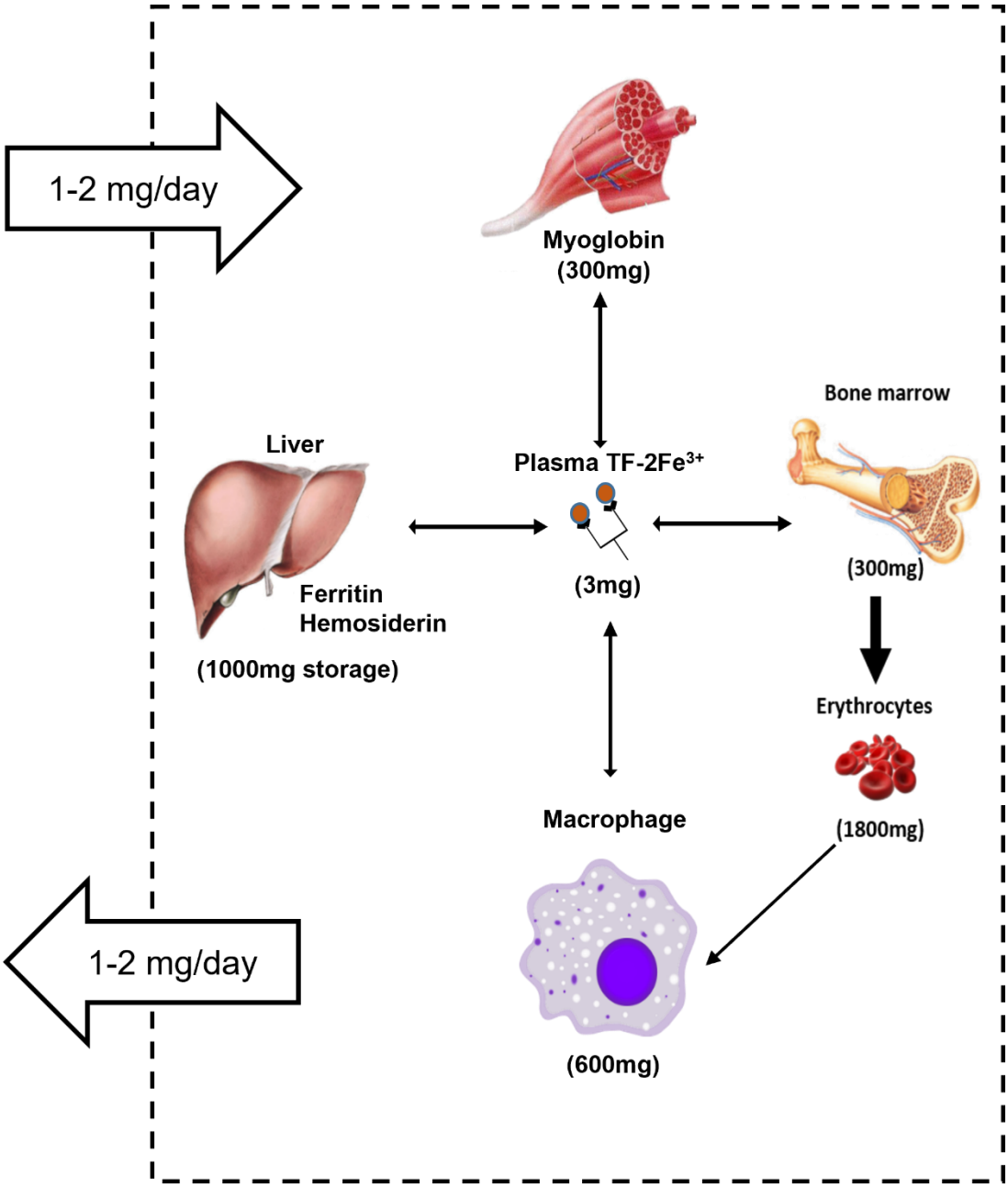

Figure 1.1. Systemic Iron Distribution. The absorption and losses of iron are normally balanced with an average amount being 1-2 mg daily. Iron is distributed through the body by the plasma, which contains only small amount of iron (3 mg) in the form holotransferrin (TF-2Fe^{3+}). Majority of iron is contained in the erythrocytes (1800 mg) as a part of hemoglobin, hemopoietic cells in the bone marrow (300 mg), and macrophages (600 mg), which are recycling iron from aging erythrocytes. Liver acts as a major storage site for iron and contains about 1000 mg. Skeletal muscles contain about 300 mg of iron in the form of myoglobin.

Iron Absorption and Regulation. Iron is available to biological system in two distinct forms: organic form (heme iron) and inorganic form (ionic iron). Though the amount extracted from diet is tiny (1-2mg/day), dietary ferric iron (Fe^{3+}) is the major source of total iron intake[16]. Epithelial cells of small intestine that are responsible for dietary iron uptake are capable to absorb both inorganic and heme forms of iron *via* two distinct mechanism (**Figure 4.2A**). Inorganic form of iron is absorbed at the apical membrane of duodenal epithelial cells after duodenal cytochrome b (DTYCB) reduces Fe^{3+} to ferrous form (Fe^{2+}), which is transported by divalent transporter 1 (DMT1) across the plasma membrane. After Fe^{2+} enters cytoplasmic pool, it can leave the epithelial cell at the basolateral membrane *via* iron transporter (ferroportin, FPN)[29]. Once Fe^{2+} leaves the cell via ferroportin (FPN), it is oxidized by hephaestin to Fe^{3+}, which is bound by transferrin (TF), and distributed through the body as transferrin-iron complex (holo-transferrin or Holo-TF; **Figure 4.2A**). The organic form of iron (heme) is absorbed *via* heme/folate transporter 1 (HCP1) at the apical membrane[30-32]. Once absorbed, heme can leave the cell *via* heme transporter (feline leukemia virus type C receptor, FLVCR) in the basal membrane or be oxidized by heme oxygenase releasing Fe^{2+} to cytoplasm[32, 33] (**Figure 4.2A**). Only inorganic iron uptake is regulated by hepatic hormone hepcidin-25, which binds to ferroportin inhibiting iron transfer across basolateral membrane and promoting ferroportin degradation due to internalization[34]. Hepcidin is produced in the liver in response to increase in saturation of transferrin (higher concentration of holo-transferrin, Holo-TF; **Figure 4.2B**). When the iron content of the plasma is low, apo-transferrin (transferrin without iron) is unable to disassociate human hemochromatosis protein (HFE) from transferrin receptor 1 (TFR1). Without HFE protein iron-sensing complex cannot be formed, so no hepcidin is produced (**Figure 4.2B**). In the absence of hepcidin, enterocytes are absorbing dietary iron. As iron absorbed, it binds to transferrin turning transferrin in to holo-transferrin, which can bind to TFR1 and displace HFE protein. Once HFE protein is released, it will promote a formation of iron-sensing complex consisting of transferrin receptor type 2 (TFR2), HFE protein, hemojuvelin (HJV), bone morphogenic protein (BMP), and bone morphogenic protein receptor (BMPR). Formation of iron-sensing complex activates SMAD signaling pathway triggering expression of hepcidin gene (*Hamp*), which leads to production of hepcidin to reduce iron uptake *via* enterocytes (**Figure 4.2B**)[35-38]. Disruptions in this intricate machinery lead to dysregulation of iron uptake resulting in iron overload or iron deficiency.

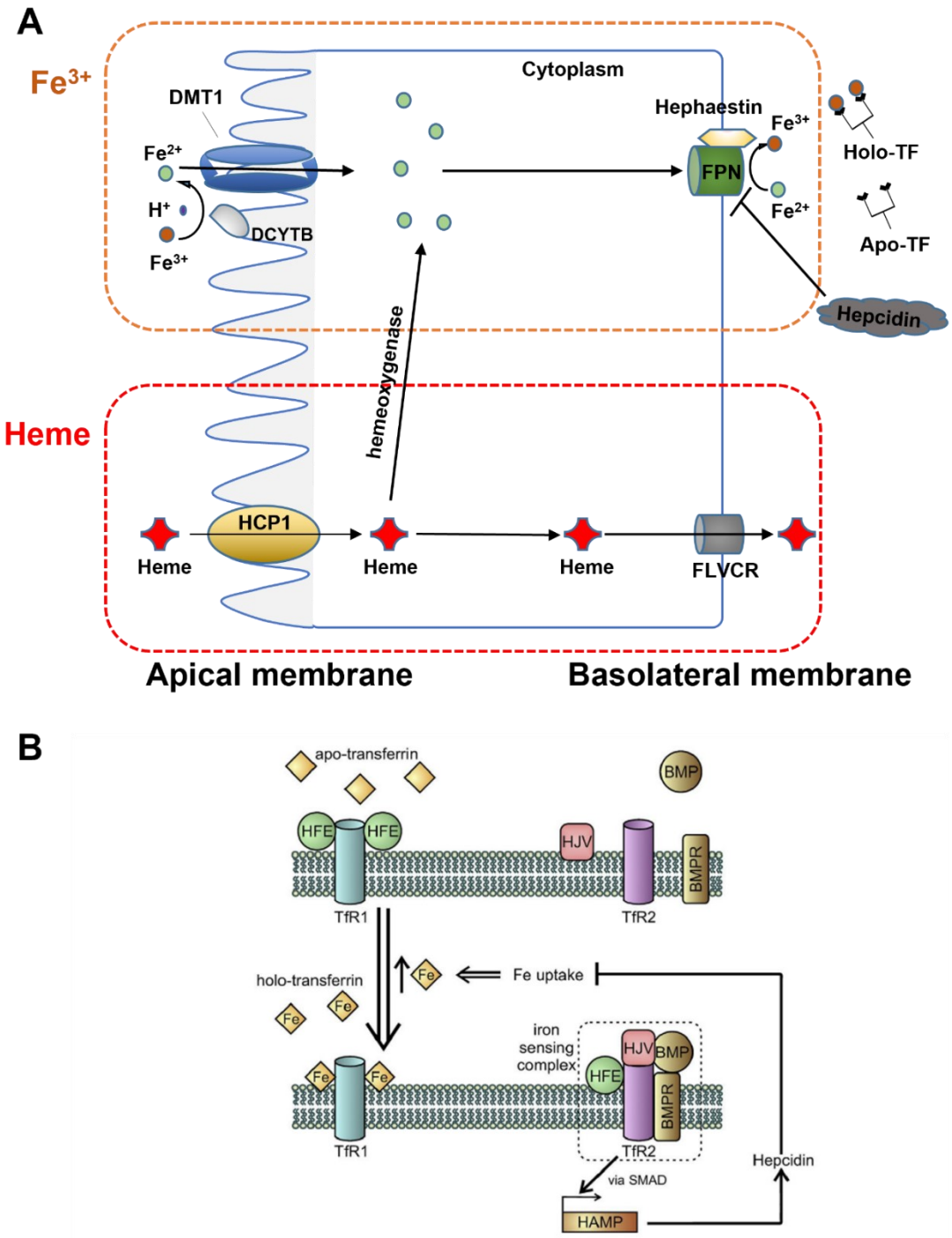

Figure 1.2. Iron absorption and systemic regulation of iron absorption. A. Iron absorption in the enterocyte. Iron is uptaken via enterocyte in inorganic (Fe^{3+}) and organic (heme) form. Absorption of inorganic form of iron. At apical membrane, Ferric iron (Fe^{3+}) is reduced by duodenal cytochrome b (DCYTB) to ferrous form (Fe^{2+}), which is transported by divalent metal transporter 1 (DMT1) in to the cytoplasm. At basolateral membrane, Fe^{2+} is exported by ferroportin (FPN) and then immediately oxidized by closely linked enzyme hephaestin to Fe^{3+}, which is bound by apotransferrin (Apo-TF) to form

holotransferrin (Holo-TF). Absorption of organic form of iron. Organic form of iron (heme) is absorbed by heme/folate transporter (HCP1). Once in the cytoplasm, heme can be oxidized by hemeoxygenase releasing Fe^{2+}, or be transported out in to the plasma by heme transporter (FLVCR) in the basolateral membrane. B. Sensing of systemic iron levels and systemic regulation of iron absorption. Systemic iron is assessed by hepatocytes via sensing transferrin saturation levels. If circulation iron is low, plasma contains mainly apo-transferrin (no iron), which cannot displace human hemochromatosis protein (HFE) from its complex with transferrin receptor 1 (TFR1), so in the absence of HFE iron sensing complex cannot be formed and hepcidin production cannot be initiated. If circulating iron is high, plasma contains holo-transferrin (iron containing form), which binds to TFR1 displacing HFE. Released HFE forms iron sensing complex with transferrin receptor 2 (TFR2), hemojuvelin (HJV), bone morphogenetic protein (BMP), and bone morphogenetic protein receptor (BMPR). Iron-sensing complex activates expression of hepcidin gene (Hamp) via SMAD pathway leading to hepcidin production and release. Circulating hepcidin suppresses iron uptake inhibiting ferroportin in the enterocytes (see panel A).

1.1.4. Cellular Iron Metabolism and Regulation

Intracellular iron content is maintained as a balance of absorption, loss, storage, and mobilization of iron. Absorption of iron happens *via* several distinct mechanisms such as transferrin-mediated endocytosis, divalent metal transporter 1 (DMT1), voltage-gated Ca^{2+} channels (mainly L-type Ca^{2+} channels, LTCC), and heme/folate transporter (HCP1) (**Figure 4.3A**). Transferrin-mediated endocytosis and DMT1 are ubiquitous mechanisms of iron absorption[39-41], whereas entry of Fe^{2+} *via* voltage-gated Ca^{2+} channels is limited to excitable cells like myocytes and neurons mainly under iron overload conditions[17]. CD163 is mainly expressed in monocytes/macrophages, microglia, and some neurons[42, 43] making it important for iron recycling[44-46] and neuronal damage due to hemorrhage and iron overload[42, 43]. Transferrin-mediated endocytosis occurs when holo-transferrin binds to transferrin receptor 1 (TFR1). This binding triggers formation of clathrin-coated endosome containing TFR1-holo-transferrin complexes, H^+ pumps, metalloreductases STEAP3, and DMT1s. H^+ pumps decrease endosomal pH to 5.5 facilitating dissociation of Fe^{3+} from transferrin and conversion of Fe^{3+} to Fe^{2+} by metalloreductase STEAP3. Fe^{2+} leaves endosome for cytoplasm via DMT1. Following this, endosome re-integrates with plasma membrane completing transferrin cycle (**Figure 4.3A**)[39-41]. Inside the cells, Fe^{2+} is used for synthesis of metalloproteins in the cytosol and uptaken to mitochondria *via* mitoferrin for

utilization mainly in iron-sulfur clusters of oxidative-phosphorylation proteins, heme synthesis, and DNA repair enzymes[47, 48] (**Figure 4.3A**). Excess of iron is stored intracellularly by complexing iron with ferritin with the help of poly-(rC)-binding proteins acting as chaperons (PCBP)[49] or removed from the cell *via* iron transporter (ferroportin, FPN; **Figure 4.3A**)[29].

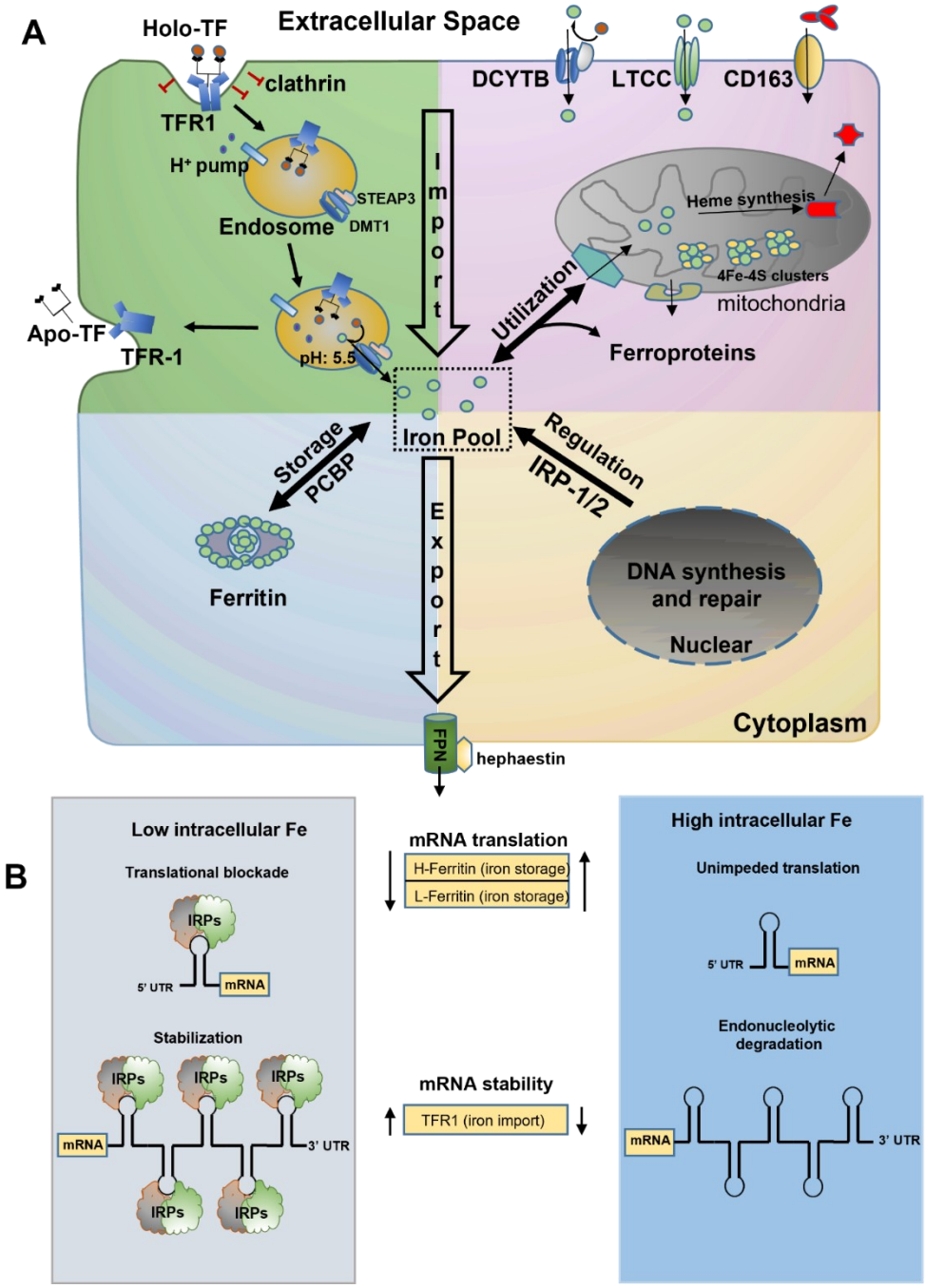

Figure 1.3. Cellular iron metabolism and its post-translational regulation. A. Cellular iron metabolism. Iron is absorbed via clathrin-mediated endocytosis of holo-transferrin (holo-TF) bound to transferrin

receptor 1 (TFR1). After formation of endosome, H^+ pump lowers pH to facilitate reduction of Fe^{3+} to Fe^{2+}, which can leave the endosome for cytoplasm via divalent metal transporter 1 (DMT1). Once in the cytoplasm Fe^{2+} is utilized for ferroprotein synthesis, uptaken to mitochondria to form iron-sulfur clusters (4Fe-4S) of oxidative-phosphorylation proteins, stored in iron-ferritin complexes with poly-(rC)-binding proteins (PCBP) acting as chaperons, or exported out of the cell via ferroportin. B. IRP/IRE post-translational regulation of cellular iron metabolism. Iron response elements are "hairpin" structure on the untranslated regions (UTR) of mRNA that can bind iron response proteins (IRPs). In the low intracellular iron state, IRP binding to IRE promotes translational blockade of storage proteins (e.g., ferritin) and stabilization of mRNA of iron import proteins (e.g., TFR1) mobilizing iron from storage and facilitating import of iron, respectively. The opposite process happens in the high intracellular iron state. IRPs are bound to iron-sulfur clusters (4Fe-4S) preventing them from binding to IREs. In the absence of IRP binding to IRE, translation of storage proteins (e.g., ferritin) is disinhibited, whereas mRNA of import proteins (e.g., TFR1) is no longer stabilized and undergoes endonucleolytic degradation resulting in facilitation of storage and inhibition of iron import, respectively.

Post-translational Regulation of Cellular Iron Metabolism. Post-translational regulation of the expression of the proteins involved in the iron metabolism is achieved via iron response elements (IREs) and iron regulatory proteins (IRPs). IREs are highly conserved hairpin structures of mRNAs found in 5' and 3' untranslated regions[50-52] (**Figure 4.3B**). H- and L-ferritin mRNA contains single IRE in the 5' untranslated region[50, 51], whereas TFR1 mRNA has five IREs in the 3' untranslated region[51, 52]. IREs act as binding sites for IRPs that either prevent translation (IRP binding to IRE in 5' untranslated region) or stabilize mRNA preventing endonucleolytic degradation (IRP binding to IRE in 3' untranslated region) (**Figure 4.3B**)[53, 54]. Capability of IRPs to bind to IRE depends upon presence of iron (Fe^{2+}) in the cell. In the low intracellular Fe^{2+} environment IRPs do not have iron-sulfur clusters (4Fe-4S) bound to them, so IRPs bind to IRE leading to suppression of translation of mRNAs of ferritins (storage proteins) and stabilization of mRNA of TFR1 (iron-uptake protein). The resultant action is decrease in storage proteins facilitating release of iron from storage and increase in cellular iron uptake (**Figure 4.3B**). As concentration of Fe^{2+} rises in the cell, more iron is incorporated into the iron-sulfur clusters (4Fe-4S), which bind to IRPs preventing IRP-IRE interaction[55-57]. In the absence of IRP's inhibitory action on storage proteins and stabilizing action of iron-uptake proteins, translation of storage proteins (ferritins) increases, and translation of iron-uptake proteins decreases (TFR1) resulting in

more available iron storage and less iron uptake (**Figure 4.3B**). A number of other proteins were identified that are subject of IRP/IRE regulation, *e.g.*, DMT1, ferroportin, 5-aminolevulinic acid synthase 2 (ALAS2; heme biosynthesis), hypoxia inducible factor 2 alpha (HIF2α), and some others (for review see[54]).

1.1.5. Systemic Iron Deficiency: Definition, Impacts and Relation with Anemia

Iron metabolism is a balancing act, and biological systems have evolved exquisite regulatory mechanisms to maintain iron homeostasis at both systemic and local levels. While both types of iron disorders are linked to HF[25, 26], systemic iron deficiency (SID) is the most prevalent malnutrition worldwide, and it frequently coexists with HF independent of the presence of anemia.

Systemic iron depletion frequently results from inadequate dietary intake or chronic blood loss. However, iron deficiency, which is the focus of this review, is inability to utilize the circulating iron or failure to meet excessive iron demands. The accepted criterion of systemic iron deficiency is serum ferritin < 100 μg/L, and functional iron deficiency defined as serum ferritin 100-300 μg/L with transferrin saturation (*TSAT*) < 20%[58, 59]. Use of ferritin by itself as diagnostic criterion of iron deficiency is unreliable because inflammation and oxidative stress may increase ferritin levels independent of iron status[58, 59]. Similarly, use of transferrin saturation by itself to define iron deficiency lacks sensitivity, because catabolism and malnutrition may lower serum transferrin levels artificially inflating transferrin saturation despite actual low iron levels[58, 59]. Another approach in defining iron deficiency is to use combination of low serum hepcidin (< 14.5 ng/mL, the 5th percentile in healthy peers) as a reflection of depletion of iron stores and high serum soluble transferrin receptor (> 1.59 mg/L, 95th percentile in healthy peers) as a reflection of unmet cellular requirements[59]. Interestingly, systemic and myocardial iron markers are poorly correlated indicating different regulatory mechanisms[60]. The relationship between systemic iron deficiency and myocardial iron deficiency remains unclear. However, clinically, iron deficiency is present in up to 66% of HF patients and leads to reduced exercise tolerance, progessive HF, and increased mortality[25, 61-63].

Anemia that is intuitively seems to be related to iron deficiency is diagnosed primarily based on hemoglobin concentration (< 130 g/L in men and < 120 g/L in non-pregnant women) in

clinical practices[64]. Anemic conditions lead to changes in corpuscular cell volume and hemoglobin content. By volume of red blood cells, anemia could be microcytic (< 82-98 fL), normocutic (82-98 fL), and macrocytic (> 82-98 fL). By hemoglobin content per erythrocyte, hypochromic (< 27-31 pg), normochromic (27-31 pg), and hyperchromic (> 27-31 pg)[65]. However, counter-intuitevely, iron deficiency and anemia coexist infrequently (only in 17% of patients)[27]. Interestingly, anemia itself did not affect mitochondrial functions; nor the correction of anemia (*e.g.*, using erythropoietin-stimulating agents) was associated with significant improvement of HF symptoms, though the risk of thromboembolic events was increased[60, 66-69].

1.1.6. Myocardial Iron Deficiency: Definition, Pathophysiology and Relation with SID

Iron is an essential micronutrient in the heart that plays a key role in oxygen transport, erythropoiesis, cellular energetics, and oxidative stress homeostasis. Given the high-energy demand of the heart, ID is believed to have a particularly negative impact on mitochondrial and heart function and exacerbates the progression to end-stage HF.

A plethora of prior studies including FAIR-HF[70] and CONFIRM-HF[71] have reported the unfavorable effects of ID on HF patients' physical performance and clinical prognosis, which could be evidently improved by various iron supplementations indicating a promising pharmaceutical target. In fact, current clinical practice guidelines such as 2016 European Society of Cardiology's (ESC)[11] and 2017 American Heart Association's (AHA)[10] for the diagnosis and management of HF endorse a class II recommendations for screening and correction of ID in all patients. However, the previous studies have predominantly focused on SID, with only few investigating the occurrence and pathophysiology of myocardial iron deficiency (MID), in the HF cohort. Given that the dominant mechanisms of intracellular iron regulation happen at the tissue level, myocardial iron homeostasis could be uncoupled from the systemic iron status. Indeed, emerging evidence has revealed the presence of MID irrespective of the systemic iron or hematopoietic status from several small HF cohorts[28, 59], yet the exact relationship and interplay between systemic and cardiac iron regulations as well as the primary determinant causing MID in HF patients remain unclear which clearly warrants tailored investigations.

1.1.7. Role of IRP1 and IRP2 in the Development of Iron-Deficient HF

Iron deficiency defined as depleted iron stores and unmet cellular iron demand was present in 37% of patients with chronic HF and up to 66% of patients with acute HF[25, 61-63]. HF is associated with low IRP activity and reduced tissue iron that is potentially detrimental since iron is critical element for energy production[57]. Cardiac-specific deletion of both IRP1 and IRP2 in mice led to non-anemic and normal mice at baseline conditions; however, cardiac function in these mice was vulnerable to dobutamine challenge due to failure to increase mitochondrial respiration in response to higher workload. These mice also developed more severe LV dysfunction in response to myocardial infarction. Iron supplementation was able to restore both mitochondrial and contractile function in these mice (**Figure 4.4A**)[57]. In another mouse model of anemia, cardiac-specific knockout of *Tfr1* had more severe phenotype: mice were dying in the second week due to cardiomegalia, poor cardiac function, failure of mitochondrial respiration, and ineffective mitophagy. Similarly to IRP1/2 knockout model, *Tfr1* knockouts were rescued by aggressive iron supplementation (**Figure 4.4A**)[72]. Currently, several ongoing clinical trials explore iron supplementation to restore intracellular cardiac iron levels (**Figure 4.4B**) as an option for treatment of HF in the patients with iron deficiency[73-76]. For instance, the double-blinded IV injections of either ferric carboxymaltose or saline to 459 HF patients with iron deficiency for 6 month showed notable improvement in the experimental arm on primary endpoints (patient global assessment and NYHA class) and secondary endpoints (6-minute walking distance and quality-of-life assessments), but not on hard endpoints (rate of re-hospitalization and mortality), with no statistical difference between anemic and non-anemic patients[70]. Iron dextran, iron sucrose, and iron gluconate are other popular IV iron supplements, with similar compound structure: iron (core) and carbohydrate (coat). Though the data on their efficacy and safety profiles are currently incomplete, anaphylaxis, which is triggered by the carbohydrate coat, remains as the major concern[77-79]. More comparative clinical data on the long-term safety of IV iron therapy are needed. Another possible mechanism for development of iron deficiency associated with HF in humans proposes that excessive levels of catecholamines and aldosterone down-regulate expression of *Tfr1* and *Tfr2* resulting in reduced iron uptake by cardiomyocytes[80]. In this regard, use of β-blockers and mineralocorticoid receptor antagonists (MRA) not only a good conventional HF treatment[11, 81], but may also benefit cardiac iron metabolism by improving iron uptake *via* TFR1 (**Figure 4.4B**) due to normalization of *Tfr1* and *Tfr2* expression[47]. Future approaches to treatment of iron deficiency

in HF may consider upregulation of alternative import routs for iron entry (e.g., DMT1 agonists) or inhibition of iron export via ferroportin (FPN) by blockers or suppression of ferroportin expression (**Figure 4.4B**)[47].

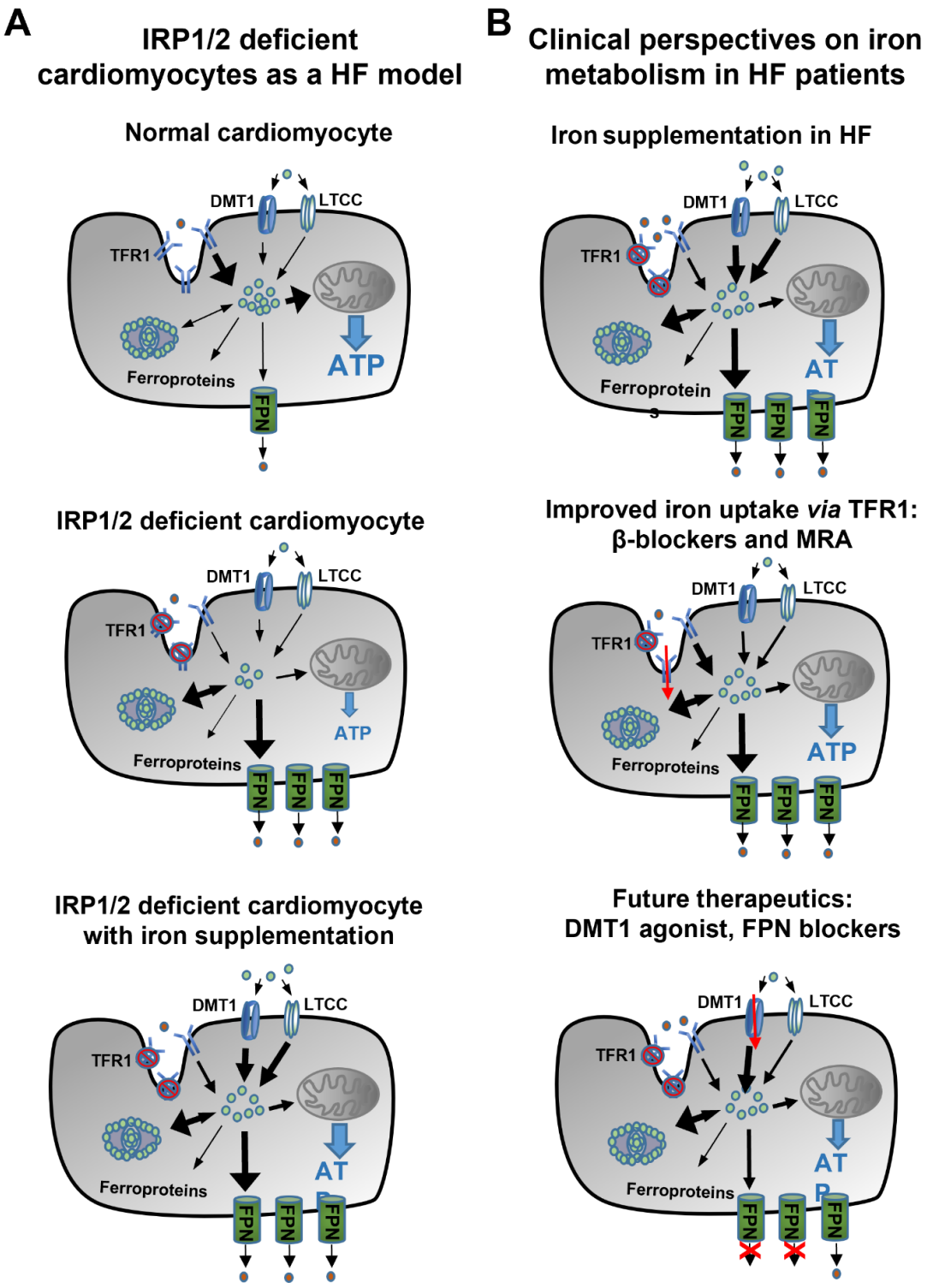

Figure 1.4. Iron deficiency in animal model and patients. A. IRP1/2 deficient cardiomyocytes as a HF model. Cardiomyocyte-specific deletion of IRP1 an IRP2 leads to reduction in iron uptake due to TFR1 deficiency and increase of iron efflux via overexpressed ferroportin (FPN) resulting in low intracellular

iron, which compromises energy (ATP) production. The model can be rescued by iron supplementation, which raises intracellular iron and normalizes ATP production. B. Clinical perspective on iron metabolism in HF patients. Direct iron supplementation has been proposed to normalize intracellular iron concentration and ATP production. Improved iron uptake via TFR1 due to β-blockade and mineralocorticoid receptor antagonist (MRA). Future therapeutics to consider are DMT1 agonist and ferroportin (FPN) blockers to facilitated iron uptake and block iron efflux, respectively.

1.1.8. Role of Hepcidin in the Development of Iron-Deficient HF

The heart has the second highest expression levels of hepcidin[82]. Systemic hepcidin produced by the liver is known to inhibit iron transfer by ferroportin and to promote internalization of ferroportin[34]. Recent work by Robbins group proposed a similar role for cardiac hepcidin in regulation of iron efflux from cardiomyocytes[83]. Cardiomyocyte-specific ablation of hepcidin in mice led to a large reduction in whole-heart levels of hepcidin and lack of hepcidin immunofluorescent staining in the cardiomyocytes. Mice lacking hepcidin production in the heart exhibited shortened lifespan (~30% survival to the 1-year age), systolic dysfunction (ejection fraction about 45%), and cardiac hypertrophy. Strangely, cardiac tissue iron levels were not changed, but direct measurement of $^{55}Fe^{2+}$-efflux confirmed an increased iron loss. Cardiac-specific hepcidin knockouts also had reduced complex I and complex IV levels suggesting mitochondria-dependent metabolic dysfunction. Similarly to IRP1/2 knockout model, supplementation of iron to cardiac-specific hepcidin knockouts rescued mitochondrial function[83]. However, lack of change in iron levels in the cardiac tissue still leave a possibility that function of cardiac hepcidin is not limited to control of iron levels. Hepcidin has been shown to have anti-apoptotic, anti-hypertrophic and anti-fibrotic effects in HF models[84-86].

1.1.9. Translational Insights in Management of Iron-Deficient HF Patients

Currently, the therapeutic emphasis is gradually shifting from alleviating HF symptoms to managing the co-morbidities exacerbating HF, including iron deficiency, as reflected in the newest ESC Guidelines for multidisciplinary management of HF[11]. In HF patients, iron deficiency is highly prevalent and is an independent predictor of clinical outcomes and exercise intolerance,

even in the absence of anemia, necessitating the use of oral or parenteral iron supplementation[25, 61-63].

Oral iron supplements, such as ferrous fumarate, ferrous gluconate, and ferrous sulphate, are easily administrable and cheap option, but may lead to drug intolerance (mainly gastrointestinal discomfort), impaired diversity of microbiota, and counteractive action of hepcidin may prevent effective absorption of additional iron[87-90]. Moreover, efficacy of dietary iron absorption can be impeded by many other factors, such as food (*e.g.*, polyphenols and phytates in tea and coffee)[91], medications (*e.g.*, Ca^{2+} supplements and proton pump inhibitors)[92, 93], and co-morbidities like intestinal edema and inflammation[94, 95]. However, oral iron supplementation failed to improve clinical outcomes for HF patients in a randomized clinical trial[63] suggesting that iron deficiency in HF is more complex problem than a mere lack of dietary iron, which can be prevented by iron supplements (*e.g.*, use of "sprinkles" and iron-fish ingots in South West Asia)[96, 97].

Parenteral iron supplementation is achieved by intramuscular or intravenous injections. Intramuscular injections, although easier to perform, are painful and is associated with siderosis (iron deposition in tissues) and a higher risk of intramuscular neoplasm[98, 99]. Intravenous injections rapidly correct iron levels bypassing gastrointestinal absorption and all problems associated with this route of administration. Each administration can be accurately tailored to the current body weight and hemoglobin levels using Ganzoni's equation (dose = body weight (kg) * [15 – actual hemoglobin (g/dL)] * 2.4 + 500 mg)[100]. Clinically, intravenous supplementation of HF patients with ferric carboxymaltose improved heart functions and other HF symptoms in patients with iron deficiency[70, 80]. This approach is associated with less gastrointestinal distress and drug intolerance than oral regimens and is more suitable for those with functional iron deficiency[70, 80]. The elucidation of signaling pathways of iron regulation in HF continues to be a priority for developing heart-oriented delivery of iron to optimize myocardial iron contents, which remains a bottleneck in practical application. Besides that, more research is required to improve monitoring of cardiac iron status in HF.

1.2. Dilated Cardiomyopathy

1.2.1. DCM in Adults: Causes, Epidemiology and Pathophysiology

Cardiomyopathies (CMs) represent diseases of the heart muscle marked by aberrant chamber size, wall thickness, and/or consecutive contractile abnormalities including either systolic or diastolic dysfunctions in the absence of other identifiable pathologies such as hypertension, valvular and congenital heart diseases[101-103]. As a miscellaneous group of myocardial diseases associated with electromechanical impairment[104], cardiomyopathies can be further categorized as either primary or secondary depending on the underlying causes. Primary CMs refer to illnesses that affect only or predominantly the myocardium with identified genetic, non-genetic (acquired), or mixed conditions, whereas secondary CMs represent myocardial injuries resulting from systemic or extracardiac disorders[101, 102].

Dilated cardiomyopathy (DCM) is the most common cardiomyopathy worldwide, and is characterized by the presence of left ventricular (LV) dilation and contractile dysfunction without abnormal loading conditions or severe coronary artery diseases (CAD)[104]. It is an insult predominantly impacting the left ventricle (LV), characterized by a spectrum of pathological remodeling alterations involving ventricular architecture, electrophysiology, and cellular metabolism. DCM has a wide range of causes, including myocarditis, metabolic or endocrine malfunction, and exposure to alcohol, toxins or certain drugs[105]. In addition, genetic mutations account for up to 35% of all idiopathic cases in a familial pattern involving genes that encode cytoskeletal, sarcomere, and nuclear envelope proteins[104, 105]. Patients with DCM typically demonstrate systolic heart failure symptoms, but diastolic dysfunction could also be presented as the disease progresses. Based on the respective underlying cause(s), arrhythmias, thromboembolic events, and circulatory collapse can be the presenting symptoms of patients with DCM. Although guideline-recommended medications, namely, angiotensin converting enzyme inhibitors (ACEi) and β-blockers, demonstrated substantial benefits in terms of survival rate and hospitalization readmission, the prognosis of patients with DCM is primarily determined by the balance between disease progression and adverse remodeling within the myocardium. The poorest prognosis is often seen in individuals with lowest LV ejection fraction (LVEF) or significant diastolic dysfunction, eventually leading to terminal HF requiring the implantation of mechanical unloading devices or heart transplantation[104, 105]. Given the heterogeneous nature and phenotypical

complexities of DCM, it is imperative to develop a comprehensive genetic and diagnostic work-up to confirm the exact cause of disease and to exclude other coexisting conditions with possible phenotype overlap[105].

1.2.2. DCM in Children: Epidemiology, Clinical Course and Translational Insights

Cardiomyopathies can occur in children regardless of age, gender, and ethnicity, with an annual incidence of 1.1-1.5 per 100,000 individuals[106, 107]. Although the morbidity rate is much lower than congenital heart diseases (1.8 per 100 live births)[108-111], CMs have remained the most common indication (>43%) of heart transplantation among children and adolescents (>1 year old)[112, 113]. Among them, DCM is the leading cause of advanced HF with reduced LVEF[114]. Despite the typical DCM phenotypes, pediatric DCM (P-DC) represent pathologically distinct entities from their adult counterparts, with causes that are largely idiopathic, and with age- and development-specific features in the failing heart[115-119]. Moreover, P-DC always occur in the absence of comorbidities that were commonly seen in adults, for example, hypertension, diabetes, and atherosclerosis; therefore, they offer a unique opportunity to study the pathogeneses underlying the course of primary DCM.

While numerous studies have investigated into adult patients with DCM (A-DC) leading to targetable anti-remodeling therapies, few of them were successfully translated from P-DCM. Statistically, there were two longitudinal studies have evidently reported that the all-cause mortality rate in adults with systolic dysfunction were remarkably decreased with the advancement of HF therapies over the past decade[120], whereas no definitive improvements of clinical prognoses were observed in the pediatric cohorts with primary DCM[114]. Given the paucity of large randomized controlled trials dedicated to the pediatric cohort with HF, current pharmaceutical recommendations for them are primarily extrapolated from adult clinical trials[121, 122] which could be problematic. For example, recent randomized clinical trials in either pediatric HF cohort using the β-blocker Carvedilol, or in infants with single ventricle using Enalapril (ACEi), both failed to show definite improvements or benefits as observed in adult HF patients[123, 124]. Despite the mixed etiologies of enrolled subjects, these striking findings clearly indicated the disparate pathophysiology and remodeling patterns underlying children's failing hearts, which warrant focused examination rather than simple extrapolation from the adults. It is especially true given

the inferior prognoses of transplant-free or survival rate in children at 5 years[125]. Indeed, a variety of age-specific features such as adrenergic adaptability and fibrotic patterns have been reported between adult and pediatric dilated failing hearts by a growing body of literature, which helped to partially explain their differed responsiveness to therapy[126-128]. Our recent work on the ECM components of pediatric dilated failing hearts also identified intrinsic differences between these two pathological entities at the level of non-myocyte remodeling[129]. Nevertheless, the full picture of disease mechanisms driving P-DC remain largely uncharted, due to extremely limited availability of ideal control hearts from human species, the paucity of reliable preclinical models that can adequately approximate the unique microenvironment within children's failing heart, and the practical limitations of conventional techniques.

1.2.3. Genetic Background and Pathological Variants Underlying DCM

DCM has a heterogenous underlying causes[130], among which genetic mutations account for about 35% of all familial cases which involve genes encoding cytoskeletal, sarcomere, and nuclear envelope proteins[104, 105, 130, 131]. Most demonstrate autosomal dominant trait, whereas X-linked, autosomal recessive or mitochondrial inherent pattern remains rare[105, 132]. Specific causative mutations include cardiac actin (*ACTC1*)[133], beta-myosin heavy chain (*MYH7*) and troponin T (*TNNT2*)[134], titin (*TTN*)[135] and lamin A/C (*LMNA*)[131, 136-139]. Aberrant *TTN* remains the most common DCM-causing mutations affecting up to 25% of DCM patients preferentially in middle-aged population[105, 135, 140]. This gene locates on chromosome 2 (2q31.2) and encodes the largest protein in humans – titin - with a size of 4 megadalton that forms a polypeptide chain with dimension of 1μm (length) and 3-4 nm (diameter)[105, 141]. Titin plays an important role in a plethora of intracellular signaling cascades including sarcomere assembly, contractile activity, and cellular division during mitosis. *TTN* truncation represent the common form of the mutations, and its deleterious effects on the disease progression can be aggravated by environmental risk factors such as alcohol abuse, chemotherapeutic agents (e.g., anthracyclines), viral infections and antidepressants[141]. The genetic susceptibility of *TTN-mutated* carriers is of particular importance because *TTN-truncating* pathologic variants (PVs) could affect up to 1% of general population in the absence of DCM[105].

Specifically, lamins A/C are structural components of intermediate filament proteins that support the nuclear envelope surrounding the nucleus, and *LMNA-related* DCM are often familial and with high penetrance within young family members[142, 143]. Atrioventricular conduction blocks and major arrythmias (i.e., VT) are frequently seen in *LMNA-mutated* carriers, and sudden cardiac death (SCD) can occur preceding any systolic manifestations[142, 143]; therefore, its identification provides the only genetic evidence to modify clinical managements in DCM, which include using implantable cardioverter defibrillator (ICD) as the primary prevention without regards to LVEF[131, 139, 144]. Recently, RNA-binding motif protein 20 (*RBM20*)[145, 146], a splicing factor primarily targeting *TTN* and *CAMK2D* (calcium/calmodulin-dependent kinase II delta), has been reported to induce a clinically aggressive form of DCM with malignant VT due to defective intracellular Ca^{2+} cycling[147]. In addition, DCM can be part of a genetic syndrome that affects other organs or initially presents as systemic disorders, such as muscular dystrophies by mutated dystrophin (*DMD*)[148, 149], delta-sarcoglycan (*SGCD*)[150], and myofibrillar myopathies (desminopathy) by aberrant desmin (*DES*)[151]. Novel PVs previously associated with other cardiomyopathies have also been identified in triggering DCM in recent years, namely, *FLNC* (filamin C)[152], *TPM1* (alpha-tropomyosin)[153], and *LAMP2* (lysosome-associated membrane 2 protein)[154] and *TAFAZZIN* (tafazzin)[155].

1.2.4. Distinct Maturation-Related Intermediary Metabolism in Pediatric and Adults Failing Hearts

Substantial maturational changes occur in cardiac metabolism during embryonic cardiogenesis, fetal proliferation and differentiation, and postnatal development. The difference in intermediary energy metabolism can be dramatic between developmental phases, which is largely dependent on circulating substrates and hormones, cellular regulators (e.g., enzymes, transcription factors), and cardiovascular (patho-)physiology[156]. As an electromechanical "engine", human heart constantly contracts to supply the whole body with oxygenated blood in an autonomic manner, thereby placing high-energy demands on the "powerhouse" – mitochondria – within the cardiomyocytes. Apart from energy provision in the form of adenosine triphosphate (ATP), mitochondrial major functions also include biosynthesis utilizing metabolic intermediates, balancing of oxidative stress, buffering of intracellular calcium (Ca^{2+}) ions, and regulation of mitophagy and apoptosis events via fusion-fission mechanisms[157].

The dominant nuclear transcriptional pathways regulating cardiac metabolism include: 1) hypoxia-inducible factor 1α (HIF-1α) pathway; 2) peroxisome proliferator activated receptor γ (PPARγ) and its coactivator-1α (PGC-1α) pathway; and 3) PGC-1α/PPARβ/δ pathway[156]. Briefly, HIF-1α regulates the protein-coding genes involved in glucose metabolism which favor the shift towards or maintenance of anerobic glycolysis in oxygen-deficiency environment (i.e., the fetal or immediate newborn heart). It functions by binding to the hypoxia response elements of targeted genes that express lactate dehydrogenase (LDH)-A, pyruvate dehydrogenase kinase (PDK)-1, glucose transporter (GLUT)-1 and so on. The axis of PGC-1α/PPARγ, on the contrary, mainly controls the expression of genes that promote fatty acid metabolism as a ubiquitous regulator. It binds to the PPAR response elements within the promotor regions of individual gene, namely fatty acyl-CoA synthase, carnitine palmitoyltransferase (CPT)-1, and acyl-CoA dehydrogenases, which is involved throughout the activation, uptake, and beta-oxidation of fatty acids. While relatively similar regulatory effects on fatty acid metabolism have been observed from the PGC-1α/PPARβ/δ pathway[158], it also regulates certain genes implicated in glucose metabolism such as GLUT-4 and phosphofructokinase, and with a heart-specific overexpression of PPARβ/δ, myocardial glycose oxidation was remarkedly increased[156, 159].

During cardiac development, the aforementioned regulatory pathways will evolve concomitantly and interact in a reciprocal manner. In healthy mature hearts, over 90% of total cardiac energy demands are sustained by the oxidative phosphorylation, of which fatty acid oxidation (≈40-60%) represents the primary energy source followed by carbohydrate (≈20-30%) and ketone bodies (≈10-20%)[160]. Normally, healthy heart is an omnivore organ that is metabolically flexible and can readily consume any type of energy substrates supplied from coronary circulations. However, the metabolic profile during heart development is evolving and can be rather distinct. To illustrate, the fetal heart is highly dependent of anerobic glycolysis and lactate oxidation due to the low-oxygen environment it resides, and at this stage, the fatty acid beta-oxidation contributes a minimal portion of total myocardial ATP production[161]. This glycolytic phenotype is formed under normal prenatal physiology partially attributable to circulating substrates supplied to the fetal hearts, which contain very low level of fatty acids but ample amount of glucose that is comparable to newborn and adult. The activated HIF-1α axis either stimulates or maintains glycolysis and lactate oxidation fueling the cellular proliferation and growth during this period[156, 162]. Days after birth, the neonatal heart undergoes significant

metabolic phenotype switch from carbohydrates glycolysis to lipid-dominant oxidation, which is in line with myocardial developmental physiology characterized as hypertrophy and binucleation during the neonatal phase[163]. It is widely accepted that the rapid maturation of fatty acid oxidation is a direct result of drastic decrease of cardiac malonyl-CoA level in the myocardium, which is a potent inhibitor of the fatty acyl-CoA transporter (CPT-1) located at OMM. The inhibition of malony-CoA is attributable to elevated activity of malonyl-CoA decarboxylase (MCD, which degrades malonyl-CoA), and concomitant decreased activity of acetyl-CoA carboxylase (ACC, which synthesize malonyl-CoA) due to the phosphorylation of 5'-AMP activated protein kinase (AMPK)[163]. Seminal work by Lapaschuk et al has previously characterized the age-dependent expressional profiles of those regulators in ventricular biopsies from newborn humans (with varying degree of hypertrophy), and the authors evidently demonstrated a positive association between expression of MCD and children's age, whereas a negative correlation between the expression of ACC and AMPK was also noted[163]. Interestingly, fatty acids do not become the primary contributor of energy despite its rapidly increased level immediately after birth[156, 164]. This phenomenon is likely caused by the inhibitions of the pathways that regulate the uptake of fatty acids by the mitochondria[156, 165, 166]. Briefly, the level of myocardial malonyl-CoA elevates during peri-neonatal period but then immediately decreases a few days later. This shift is simultaneously accompanied by reduced activity of ACC that are subject to the phosphorylation (inhibition) by AMPK, and increased expression of MCD potentially due to activated PPAR pathways[156]. These age-dependent alterations have been previously described by a few elegant studies supported by data from human heart explants[163, 167-170]. And fatty acid oxidation remains to be the predominant energy source in healthy individuals till adulthood.

1.2.5. Role of Calcium Cycling in Metabolic Process in Pediatric and Adult Failing Hearts

Ca^{2+} plays an integral role in orchestrating cardiac muscle contraction and relaxation via the excitation-contraction (EC) coupling mechanism[171]. Physiologically, it is triggered by an incoming action potential that depolarizes the membrane of cardiomyocyte and stimulates the opening of voltage-dependent L-type Ca^{2+} channels (LTCC, $Ca_V1.2$). This small influx of cationic current (I_{Ca}) further triggers a relatively larger amount of intracellular Ca^{2+} release from the nearby sarcoplasmic reticulum (SR) reservoir through ryanodine receptor (RyR2) channels. This

mechanism is well known as Ca^{2+} induced Ca^{2+} release (CICR), thereby promoting a summed and global rise of the intracellular Ca^{2+} transient to initiate cardiac contraction and sustain ATP consumption by the myosin ATPase. While RyR2 and LTCC being inactivated by the intracellular Ca^{2+} sparks, SERCA2a rapidly reuptakes the excessive intracellular Ca^{2+} back to the SR following each prior contraction, and with concomitant removal of cytosolic Ca^{2+} to extracellular space by the Na^{+}/Ca^{2+} exchanger (NCX1) on plasma membrane. The function of SERCA2a is closely regulated by the reversible dephosphorylation (inhibition) and phosphorylation (lack of inhibition) of phospholamban, which is under control of a plethora of phosphatases and stress-induced protein kinases such as cAMP-dependent protein kinase A (PKA), and Ca^{2+} calmodulin-dependent kinase II (CAMKII)[171]. Dysregulated calcium signaling has been observed to underlie the adverse remodeling of failing hearts including depressed contractility due to defective cross bridge cycling, and fatal arrhythmias[171-173]. Indeed, studies examining the Ca^{2+} cycling profile directly from human explanted hearts have unraveled distinct molecular characteristics between pediatrics HF and their aged counterparts. The differences could include age-related differential β-adrenergic adaptation and downstream signaling pathways, to name a few.

Apart from EC coupling, Ca^{2+} cycling is instrumental in regulating cardiac metabolism by the mitochondria. Specifically, it is the Ca^{2+} concentration within mitochondrial matrix ($[Ca^{2+}]m$) that modulates the key enzymes involved in the tricarboxylic acid cycle (TCA), ETC, and ATP synthase[174]. Firstly, it must enter the intermembrane space through the Ca^{2+}-permeable channel (commonly known as voltage dependent anion channel, VDAC) on outer mitochondrial membrane (OMM). Then the Ca^{2+} influx needs to pass another highly selective and low-conductance mitochondrial calcium uniporter (MCU) channels on the inner mitochondrial membrane (IMM) to enter matrix. Conversely, the Ca^{2+} in matrix can be extruded back to the intermembrane space primarily via the mitochondrial Na^{+}/Ca^{2+} exchanger (NCX) in cardiomyocytes, while the H^{+}/Ca^{2+} exchanger may play a similar role in those non-excitable cells[174]. The negative $\Delta\Psi m$, generated by pumping of protons across IMM along with transporting of electrons at complex I, III and IV, also drives Ca^{2+} entry into the mitochondrial matrix[174]. The dynamic balance between the bi-directional passage maintains the Ca^{2+} homeostasis and $[Ca^{2+}]m$ for better adaptation to varying cardiac workload. Another important determinant of steady-state $[Ca^{2+}]m$ is the matrix Ca^{2+} buffering capacity in relation to the cytosolic Ca^{2+} concentrations ($[Ca^{2+}]c$) and varying metabolic demands[174].

$[Ca^{2+}]$m is a major player regulating energy production in the format of ATP within hearts, with strong evidence from previous studies demonstrating its close interplay with the staged cellular respiration including TCA cycle and ETC inside the mitochondria. Briefly, adult human heart mainly relies on oxidative phosphorylation to yield ATP from the source of fatty acids, while children undergo phenotypic switch between different developmental stages. As an omnivore organ, the heart metabolizes virtually all types of energy substrates supplied to it via the coronary circulations, and acetyl-CoA is eventually generated from all energy sources in an anaplerotic manner and entering the TCA cycle as the only starting intermediate. Subsequently, three NADH and one FADH are produced for every acetyl-CoA, and these high-energy reduced dinucleotides will provide the energy required for proton pumping and electron transferring along the respiratory chain. Ca^{2+}-dependent regulation of key enzymes and proteins associated with TCA cycle and ETC have been identified, including PDH, alpha-ketoglutarate dehydrogenase (KDH) of the TCA cycle and ubiquinone and complexes I, III, & IV from the transport chain[175]. However, emerging evidence has revealed that the lipid beta-oxidation is less sensitive to $[Ca^{2+}]$m than glycolysis, TCA cycling and oxidative phosphorylation[176]. In addition, Ca^{2+} has been a crucial regulator for ATP synthase (complex V)[177]. While substantial work has been focusing on the (patho-)physiological association between Ca^{2+} cycling and cardiac metabolism in adult hearts, their modulations within the human pediatric hearts under normal and failing conditions have not been fully understood which warrants further investigation including our current study.

1.3. Hypotheses and Objectives

As elucidated in the literature review above, managing comorbid MID in patients with chronic HF is gaining increasing importance as reflected in the clinical guidelines, yet little is known about its underlying pathogeneses as well as pathological implications on heart functions. In addition, P-DC represents a clinically distinct entity from their adult counterparts (A-DC), who currently does not respond well to the adult-based HF medications. Despite similar clinical phenotypes, disparate remodeling characteristics between the young and aged failing hearts were reported by several pioneering studies; however, the mechanistic explanations behind this are largely lacking due to the extreme rarity of clinical specimens from children and the complexities of disease course affected by developmental traits in kids. Ethically acquired human heart biospecimens play an

invaluable role in advancing our fundamental knowledge into the specific pathogeneses and pathophysiological implications in the adult and pediatric cohort, respectively. Our Human Explanted Heart Program (HELP) program serves as a discovery platform in search of therapeutic targets and robust biosignatures for an etiological spectrum of heart diseases, including the iron-deficient failing hearts secondary to non-ischemic DCM or CAD (with LAD blockade) in adults, and idiopathic DCM in children. Accordingly, our studies presented in this thesis set out to address the following hypotheses and objectives based on the aforementioned knowledge gaps and research importance.

Firstly, I hypothesize that MID remains as a hidden yet highly prevalent comorbidity in adult HF patients secondary to non-ischemic DCM or CAD (with LAD blockade). I also anticipate that MID would primarily affect the systemic ventricle, and that MID would exacerbate cardiac performance and pathological myocardial remodeling in the failing human hearts. I speculate that myocardial iron depletion would severely affect mitochondrial functions characterized as metabolic dysfunctions and inflamed oxidative stress. Lastly, I hypothesize that MID could be detected *in vitro* by cardiac magnetic resonance imaging (CMR). Specifically, the following objectives have been set to test the hypothesis:

Objective 1: To investigate the occurrence and prevalence of MID in both ventricles, and to determine the association between MID and systemic hematopoietic profiles (i.e., systemic iron status) in adult HF patients with an etiology of non-ischemic DCM or CAD.

Objective 2: To evaluate the impact of MID on patient's physical capacities, cardiac performances, adverse tissue remodeling, and mitochondrial functions within both ischemic and non-ischemic dilated failing hearts, respectively.

Objective 3: To characterize the mechanistic pathogeneses of iron trafficking system at both myocardial and subcellular levels in ischemic and non-ischemic dilated failing hearts, which could possibly underlie MID in relation to HF.

Objective 4: To assess the applicability of CMR imaging (mapping sequences: T_1, T_2, T_2*) to non-invasively reflect myocardial iron status and detect MID in adult ischemic and non-ischemic dilated failing hearts.

Next, I hypothesize that P-DC would demonstrate disparate adverse tissue remodeling compared to A-DC, which is characterized as minimal cardiomyocyte hypertrophy, myocardial fibrosis, and cytoskeletal alteration. In addition, I hypothesize that P-DC would demonstrate maintained contractile properties at the tissue level, which happens to be the primary target of adult-based HF therapies. I also anticipate that P-DC would exhibit worsened mitochondrial profile shown as severely impaired electron transporting activities, reduced respiration rate, defective intermediary metabolism, and elevated oxidative stress. The maladaptation of intermediary metabolism to the formula of principal nutrients (as energy source) that will be changing along the development could possibly explain the early manifestation of HF in children primarily driven by mitochondrial failure. Moreover, I expect to recapitulate the fundamental differences between P-DC and A-DC by implementing the unbiased integrative omics on the explanted human dilated failing hearts, including non-cardiomyopathic controls (NC). Specific objectives are as follows:

Objective 5: To examine the myocardial adverse remodeling characteristics in P-DC hearts and compare it to A-DC, following normalization to their respective age-matched non-cardiomyopathic controls to minimize development-related interferences.

Objective 6: To determine the mitochondrial functional capacity and health in P-DC hearts and contrast them with alterations seen in A-DC, following normalization to their respective age-matched non-cardiomyopathic controls. Specifically, electron transferring activities, overall respiration rate, and oxidative stress status (including ROS production and antioxidant capacities) and ultrastructural integrities.

Objective 7: To screen age-specific disease biomarkers in P-DC hearts, in a non-biased approach combining the whole transcriptome sequencing and global- and phospho-proteomics. Uniquely and/or differentially expressed gene, coupled with functional pathway enrichment analyses, would provide a comprehensive coverage of molecular functions implicated in the three analyzed comparisons (A-DC vs. A-NC; P-DC vs. P-NC; A-DC vs. P-DC). Further, to highlight those uniquely expressed and/or significantly altered gene markers in different cell types and states using single-cell and single-nucleus RNA sequencing (sc/snRNA-Seq) techniques.

Objective 8: To retrospectively validate the key probed biomarkers in P-DC or A-DC hearts using conventional molecular techniques. For instance, to apply immunoblotting, histology, and

immunofluorescence and functional assessments to the key biomarkers of the signaling pathways that are involved in cardiac contraction, metabolic regulation, immune response, and cell death.

Chapter 2

Materials and Methods

2.1. Materials

2.1.1. Study Design

The Mazankowski Alberta Heart Institute (MAHI) administers the largest research-integrated Human Explanted Heart Program (HELP) nationwide, which encompasses a sizable collection of diseased explanted human heart tissues associated with comprehensive biomedical database[178]. In parallel, we have compiled an inventory of non-failing (NFC) or non-cardiomyopathic (NC) hearts that serve as the "control" group for adults or pediatrics, respectively, via the Human Organ Procurement and Exchange (HOPE) program in our translational study. Informed consents were obtained from all patients or power of attorney. Both programs conformed to the ethical principles of the Declaration of Helsinki, and were approved by the institutional review committee and Health Research Ethics Board at the University of Alberta, Edmonton, Canada. Clinical data was obtained by chart review. Refer to **Chapter 3** for a comprehensive overview of the research programs and protocols within which all my thesis work has been conducted.

2.1.2. Explanted Human Hearts: Tissue Procurement and Preparation

Heart tissue procurement strictly followed our well-established protocols[179-183]. Refer to **Chapter 3** for an extensive description of the sample procurement and preparation of both failing (adult and pediatric) and non-failing control hearts throughout the heart collection process in **Section 3.4**.

Briefly, our diseased cohort consisted of patients with end-stage HF secondary to a confirmed etiology such as DCM and/or CAD who underwent heart transplantation. The control hearts were obtained from brain dead donors with no past history of major comorbidities or cardiovascular diseases, and their antemortem echocardiography demonstrated normal ejection fraction of the left and right ventricles as well as normal LV dimensions[179-183]. For my studies, transmural ventricular myocardial samples were obtained by avoiding the epicardial fat and scar tissues. To minimize anatomy-specific interferences, specimens were consistently captured from the mid-anterior ventricular walls from both LV (approximately two-thirds below the aortic valves) and right ventricle (RV, approximately two-thirds below the tricuspid valves) from the NFC and DCM failing hearts, as applicable. The full-thickness specimens were snap-frozen and/or OCT-mounted frozen in liquid nitrogen, and then stored in the -80°C freezers for subsequent molecular

and histochemical analyses[182]. Meanwhile, the remaining transmural pieces were fixed in 10% formalin (containing approximate 4% formaldehyde) or 2% glutaraldehyde for long-term storage.

2.2. Methods

According to different research focuses and study aims, a variety of methods were performed as applicable in **Section 4.4 and 5.4** in the data chapter, respectively. Detailed and expanded methodologies were also included as follows:

2.2.1. Patient Genotyping

Genomic DNA was isolated from the frozen LV specimens using Genomic DNA Extraction Kit (Qiagen) followed by whole genome sequencing (WGS) on Illumina NovaSeq instruments. All sequencing reads were aligned to GRCh37 (hg 19) using BWA-MEM[184]. Single nucleotide variants (SNVs) and small indels were identified using the HaplotypeCaller from Genome Analysis Tool Kit (GATK; version 3.8)[185]. dbNSFP[186], gnomAD (version 2.1)[187], and SnpEff (version 4.3t , bundled with GRCh37.75) were applied for annotating variant call format files. High quality variants passed GATK, Variant Score Quality Recalibration (VSQR, truth sensitivity threshold 99.5 for SNVs, 99.0 for indels), a minimum depth (Dp) of 10, and genotype quality (Gq) ≥ 20, and quality ≥ 30 were filtered for rare (defined as minor allele frequency <1.00e-04 in gnonAD version 2.1) pathogenic variants.

2.2.2. Tissue Iron Level Measurement

Chamber- and etiology-specific myocardial tissue iron levels were directly measured by inductively-coupled plasma resonance mass spectrometry as previously described at the Department of Pathology and Laboratory Medicine, London Health Sciences Center and St. Joseph's Health Care, London, Western Ontario.[17, 26, 188] Measurement of myocardial iron content was carried out from both ventricles in non-ischemic DCM and NFC hearts, while the levels from peri- and non-infarction regions in LV were anatomized in relation to LAD blockade. Tissue

samples were analyzed in triplicate and the average values were reported in this study.

2.2.3. Spectrophotometric Assays for ETC Enzymes

Ground tissues from the left ventricle (LV) were homogenized in ice-cold homogenization buffer (20mM Tris, 40mM KCl, 2mM EGTA, pH=7.4, with 50mM sucrose added day of homogenization). Samples were centrifuged at 600g for 10 minutes at 4°C to remove cellular debris. Supernatant was collected and used to assess the electron transport chain (ETC) enzyme activity of NADH:ubiquinone oxidoreductase (COX I), succinate dehydrogenase (SDH, COX II), decylubiquinol cytochrome c oxidoreductase (COX III), NADH cytochrome c oxidoreductase (COX I + III), succinate cytochrome c reductase (COX II + III), cytochrome c oxidase (COX IV) and citrate synthase (CS).[382] Enzyme activity ($nmol \cdot min^{-1} \cdot mg^{-1}$) was normalized to volume and protein concentration, following protein determination with Bradford assay. Specifically, it is calculated based on the following equation: enzyme activity = (△Absorbance/min x 1000)/[(extinction coefficient x volume of sample loaded in ml) x (protein concentration of sample in mg/ml)]. Furthermore, the reaction specificity was assured by subtracting the inhibitor-resistant activity from the total enzymatic activity, which were conducted in parallel. The inhibitor for COX I (1mM rotenone), COX II (1M malonate), COX III (1mg/ml antimycin A), COX I + III (1mM rotenone), COX II + III (1M malonate), and COX IV (10mM KCN) were added to each corresponding reaction mixture prepared separately.[382] Measurements were performed in triplicate.

2.2.4. Spectrophotometric Assays for Antioxidant Enzymes

As described previously, flash-frozen LV tissues were homogenized by using TissueLyser II (r=25rpm, 3min; Qiagen) and total protein were extracted in ice-cold CelLytic™ M (C2978, Sigma, MO, USA) supplemented with protease (Complete Protease Inhibitor) and phosphatase inhibitor (PhosSTOP EasyPack) (Roche, Mannheim, Germany) cocktails.[26, 383] The homogenate was centrifuged at 14,800rpm (21,100g) for 12mins (4°C), and the enzymatic activities were examined in the aliquoted supernatants after quantitation of protein concentration using Bradford assay. All measurements were repeated in duplicate, and the average value was used.

CAT Enzyme Assay. Catalase (CAT) activity was measured according to the method described previously with minor modification.[384, 385] Briefly, 20-40µl tissue homogenate (100-

300μg protein) was added to 600μl assay buffer, which contained 50mM KH_2PO4 and 50mM Na_2HPO4 (pH 7.0), and baseline absorbance was recorded at 240nm for 3 minutes at room temperature (RT) using a quartz cuvette. Reactions were started upon addition of 300μl H_2O_2 (30mM) and the changes to absorbance was followed for 5 minutes. Specific activity (units/mg) was defined as the rate of H_2O_2 consumption per minute per milligram of protein sample.

SOD Enzyme Assay. Superoxide dismutase (SOD) activity was assayed based on the competition for O_2^- between (ferri-)cytochrome c and SOD following its spontaneous dismutation.[384, 386] One unit of activity was defined as the amount of SOD required to inhibit the initial reduction rate of ferri-cytochrome c by 50%. A reaction cocktail containing 50mM KH_2PO4/0.1mM EDTA (pH 7.8), 50μM xanthine (X0626, Sigma, MO, USA) and 10μM cytochrome c (C2867, Sigma, MO, USA) was prepared at RT. Xanthine oxidase (6nM, X4376, Sigma, MO, USA) was added to the mixture to obtain a stable baseline reading (0.015-0.025 Abs/min) at 418 nm for 3 minutes. Reactions were started by the addition of whole cell lysate (3-15μg protein) to a quartz cuvette and absorbance was continuously monitored for 5 minutes to calculate the total SOD activities (SOD1-3). Mitochondrial SOD (SOD2, Mn/Fe-SOD) activity was determined by adding 100mM KCN to a matched reaction mixture prepared from the same sample. The overall Cu/Zn-SOD activities from cytosol (SOD1) and extracellular matrix (SOD3) are completely inhibited by the KCN (100mM) added.[34] The purity of cytochrome c (potential SOD contamination) was checked by adding 1mM KCN to reaction mixtures prior to the addition of any SOD-containing samples; no significant increase in cytochrome c reduction rate were noted after addition of KCN.

GPX Enzyme Assay. Glutathione peroxidase (GPX) activity was measured based on the oxidation of reduced glutathione (GSH) by GPX coupled to the disappearance of NADPH catalyzed by glutathione reductase (GR).[384, 387] The rate of NADPH oxidation was monitored spectrophotometrically at 340nm. Briefly, two assays (A & B) were prepared each containing 0.1M K_2HPO4/1mM EDTA (pH 7.0), 10mM L-glutathione reduced (G4251, Sigma, MO, USA), 2.4unit/ml glutathione reductase (G3664, Sigma, MO, USA). Both assays were firstly pre-incubated at 37°C for 10 minutes in the presence (assay A) and absence (assay B) of the whole cell lysate (50-150μg protein). The H_2O_2-independent NADPH oxidation in both assay reactions were monitored for 3 minutes immediately after the addition of 1.5mM NADPH (10107824001, Sigma, MO, USA). Next, pre-warmed 1mM sodium azide (catalase inhibitor; S2002, Sigma, MO,

USA) and 1.5 mM H_2O_2 were added simultaneously to both assays and the reduced NADPH optical density was read every 30 seconds for 5 minutes. The non-enzymatic and H_2O_2-independent NADPH depletion were subtracted from the total GPX activity, by comparing the absorbance changes after addition of H_2O_2 in two assays. Activities were normalized to the added lysate volume and protein concentration.

2.2.5. Measurement of Myocardial Lipid Peroxidation

Malondialdehyde (MDA), as an established indicator of lipid peroxidation, was measured colorimetrically using a commercial kit (Abcam, ab233471) according to the manufacturer's instructions. In detail, flash-frozen myocardium samples (~150 mg) from LV were chopped into smaller pieces and then fully homogenized using Dounce homogenizer in low pH lysis buffer (500µl/each, 20mM NaH_2PO_4 & 0.5% TritonX-100, pH 3.0-3.2) with the addition of protease (Complete Protease Inhibitor) and phosphatase (PhosSTOP EasyPack) (Roche, Mannheim, Germany) inhibitor cocktails. Following a 10-min incubation on ice, the tissue lysates were centrifuged at top speed for 6 min (13,000 rpm, 4℃) and the clear supernatants were collected or stored at -80℃ for further studies. Protein concentrations were quantitated using the Bio-Rad BCA assay as aforementioned, and all the prepared reagents and materials were gently agitated after equilibrated to RT. Next, 50 µl of each sample lysate and serially diluted MDA standards (0, 6.25, 12.5, 25, 50, 100, 200, and 400 µM) were pipetted into a 96-well clear bottom microplate, immediately followed by adding 10 µl of MDA Color Reagent solution to each well and incubating at RT for 15 min in the dark. Finally, 40 µl of Reaction Solution was added to each mixture with another 45-min incubation at RT. The absorbance increases were monitored by a microplate reader (SpectraMax iD5, Molecular Devices, San Jose, CA) with path-check correction at 695 nm. The absorbance readings of blank controls (with dilution buffer or lysis buffer only) were used as the negative controls, and were subtracted from the detected values from both the standards and experimental samples. The total concentration of free MDA (µM/mg) was determined by reference to the MDA standard curve correcting for the sample lysate dilution as well as total amount of protein loaded.[26, 388] The assay conditions (e.g., low pH) served to minimize potential interferences from other lipid peroxidation natural by-products, such as 4-hydroxyalkenals (4-HNE), and our

protocol specifically probed the free MDA level within the myocardium. Each sample was assayed in duplicate, with the average value accepted.

2.2.6. Tissue Glutathione Level (GSH/GSSG) Measurement

Reduced (GSH), oxidized (GSSG) myocardial glutathione and their redox ratio (GSH:GSSG) were quantitated by enzymatic recycling method as described previously.[188, 383, 389] Each sample was analyzed in triplicate, and the average value was used.

2.2.7. Subcellular Fractionation and Western Blot

Subcellular fractionations were performed as previously described with modifications.[392] Tissues from LV were lysed and homogenized (20 rpm/minute, 2 minutes, 4°C) in 500 µl radioimmunoprecipitation assay (RIPA, 50 mM Tris-HCl, 150mM NaCl and 1mM EDTA, pH=7.4) buffer with the addition of 1X protease inhibitor cocktail (Roche), followed by centrifugation (2900 g, 20 minutes, 4°C) to precipitate the crude nuclear from the cytosolic and membrane proteins (first supernatant). The pellet was gently washed and homogenized again using the above methods, followed by a second homogenization (25 rpm/minute, 3 minutes, 4°C) in 200 µl commercial RIPA buffer (ThermoFisher, 25mM Tris-HCl, 150mM NaCl, 1% NP-40, 1% sodium deoxycholate and 0.1% SDS) supplemented with 1X protease inhibitor cocktail (Roche), producing pure nuclear fraction. The first supernatant was further ultra-centrifuged (29000 g, 45 minutes, 4°C) to pellet the membrane and simultaneously harvest cytosolic components from the second supernatant. The purity of each fraction was further validated by using anti-rabbit TLR-4 (Santa Cruz, sc-10741; membrane marker), anti-rabbit Caspase-3 (Cell Signaling, 9662S; cytosolic marker) and anti-rabbit Histone H3 (Cell Signaling, 4499s; nuclear marker).[331]

For mitochondrial fractionation, frozen LV tissues were ground and homogenized in fractionation buffer containing 250mM sucrose, 10mM Tris-HCL, 1mM EDTA, 1mM sodium orthovanadate, 1mM sodium fluoride, 10µg/L aproptinin, 2µg/L leupeptin, and 100µg/L pepstatin.[189] Homogenate was first centrifuged for 10 minutes at 700g (4°C) to remove the debris. The supernatant was decanted and centrifuged for 20 minutes at 10,000g (4°C) to obtain the "crude" mitochondrial fractions as pellet. Subsequently, the mitochondrial pellet was resuspended

in fractionation buffer and protein concentrations was calorimetrically determined using the Bio-Rad BCA protein assay kit (with bovine serum albumin as standards).

Western blotting was performed on flash snap-frozen human myocardium tissues.[331, 392] In total, 500 μg protein was extracted; and aliquots of protein (45 - 60 μg) were separated on 6% - 20% gradient sodium dodecyl sulfate polyacrylamide gel electrophoresis (SDS-PAGE) and transferred onto 0.2μm PVDF membranes. They were subject to immunoblotting with the following primary antibodies: anti-rabbit TFR-1 (Cell Signaling, 13208s); anti-rabbit FPN (Novus, NBP1-21502); anti-rabbit FTN (Abcam, ab75973); anti-mouse DMT-1 (Abcam, ab55735) in Chapter 4, and anti-mouse NCX1 (Invitrogen, MA3-926); anti-rabbit SERCA2 (Cell Signaling, 9580s); anti-rabbit phosphor-(Ser16)/anti-mouse total PLN (Badrilla, phosphor A010-12, total A010-14); anti-rabbit phosphor-(Thr172)/anti-rabbit total AMPKα (Cell Signaling, phosphor 2531s, total 2532s); anti-rabbit phosphor-(Ser473)/anti-rabbit total AKT (Cell Signaling, phosphor 9271, total 9272); anti-rabbit phosphor-(Thr308)/anti-rabbit total AKT (Cell Signaling, phosphor 9275, total 9272); anti-rabbit phosphor-(Ser9)/anti-rabbit total GSK3β (Cell Signaling, phosphor 9336s, total 9315); anti-rabbit phosphor-(Thr180/Tyr182)/anti-rabbit total p38 MAPK (Cell Signaling, phosphor 9215s, total 9212s); anti-rabbit phosphor-(Thr202/Tyr204)/anti-rabbit total p44/42 MAPK (Erk1/2) (Cell Signaling, phosphor9101Ss, total 9102s); anti-rabbit phosphor-(Thr183/Tyr185)/anti-rabbit total SAPK/JNK (Cell Signaling, phosphor 4668, total 9252) in Chapter 5, and subsequently incubated with HRP-conjugated secondary antibodies at 1/5000 dilution (Cell Signaling) against the host species of individual primary antibody for 2 hrs at 37℃. All blots were visualized by ImageQuant LAS 4000 (28955810, GE Health Care, Biosciences, Uppsala, Sweden) with band intensity quantitation, and total protein amount were determined by MemCodeTM reversible stain (24585, Thermo ScientificTM) as a loading control for all proteins. The level of phosphorylation was calculated by normalizing signaling intensity of the phosphorylated protein by the band intensity of total protein of interest. To avoid exhausting valuable samples, some blots were reprobed with a second targeted protein after incubation in Restore™ Western Blot Stripping Buffer (ThermoFisher 21059) for 15-30 minutes (RT), followed by vigorous washing using combination of 1X TBST (3rpm, 5min x3) and 1X TBS (3rpm, 5min x3), and complete blocking by 5% non-fat milk for 1 hour (3rpm, RT). ImageJ software (NIH, USA) was used for band intensity quantitation.

2.2.8. Histological Analysis

The excised transmural biopsies were immediately fixed in 10% buffered formalin (containing 4% formaldehyde) followed by embedding in paraffin. Thin sections (5μm) of the tissue were stained with picro-sirius red (PSR) and Masson's trichrome stain for morphometric analysis. The tissue sections were first deparaffinized in xylene and alcohol grades, then rehydrated in water and subjected to respective staining protocols as described previously.[26, 188] The fibrotic pattern was assessed by visualization under a bright field microscope (DM 4000 B, Leica), together with fibrillar content quantification under Olympus IX81 fluorescence microscope. Image analysis was performed on MetaMorph software (Basic version 7.7.0.0, Molecular Devices, Inc). From each heart, n=2 sections were stained with n=20-25 random images analyzed from each section in a blinded manner.

2.2.9. Dihydroethidium Staining and Densitometry

Dihydroethidium (DHE), a cell-permeable oxidative fluorescent probe, was applied to directly reflect the total superoxide levels from the LV specimens as previously demonstrated.[26, 312, 388, 390, 391] Briefly, the 5-10 μm OCT-embedded cryosections were washed using Hank's Balanced Salt Solution (HBSS, #14025092, Gibco^{TM}) with calcium chloride and magnesium chloride at RT for 5 min. A sufficient amount of (100-200 μl) TrueBlack Lipofuscin Quencher (1:20 in 70% ethanol, #23007, Biotium) was quickly applied to both experimental and control sections at RT for 5-10 min, followed by washing with HBSS (5 min/each) for another 3 times. Then, the experiment sections were incubated with DHE (1:100 in HBSS, D1168, Invitrogen) at RT for 20 min in the dark, while the negative control sections were incubated with 1X HBSS simultaneously. The sections were finally mounted using prolong gold DAPI antifade (#P36931, Invitrogen). In situ generation of superoxide was then detected qualitatively using an Olympus IX81 fluorescence microscope with multi channels (i.e., TxRed:DHE and DAPI:nuclei) selected, and the overall oxidative stress was represented as the red fluorescence intensity of the product upon oxidation – (oxy)ethidium – within the nuclei, which was readily quantifiable by MetaMorph software (Basic version, 7.7.0.0, Molecular Devices, *Inc*.). Specifically, the RGB pictures were converted into 8-bit gray scale (intensity profile: 0 to 255), and regions (n=5-10) congruent to the cell nuclei boundaries from both experimental and negative control sections were randomly drawn to

calculate the average pixel intensities as the background noise. Given that all the image acquisition settings (i.e., exposure time, brightness/contrast, etc.) remained unvaried between groups, the actual oxidized DHE fluorescence was obtained by subtracting the background signal from the average pixel intensity of the nuclei using Fiji ImageJ (National Institute of Health, Bethesda, MD, USA) software.[190] n=20 images/sample were blindly taken as the technical replicate with n=20-25 nuclei analyzed from each tissue section.

2.2.10. Immunofluorescence (IF) and Fluorescence Microscopy

Cardiomyocyte morphology was evaluated fluorescently by applying wheat germ agglutinin (WGA) staining on the optimal cutting temperature (OCT) compound-mount (TFM, General Data Company) tissue blocks, which was snap frozen in liquid nitrogen as previously published.[26, 129, 191] Similarly, the 5-10 μm cryo-sectioned slices were fixed with 4% paraformaldehyde for 20 mins and then rehydrated in 1X PBS for 30 mins at RT. Sections were permeabilized using 100% precool methanol (-20℃) for 10mins, followed by blocking with 4% BSA for 1 hr at RT. After thorough washings, the sections were incubated with WGA (1:200, W11261, Invitrogen) for 30 mins at RT and then applied with 20μl/section DAPI gold anti-fade mountant (#P36931, Invitrogen). The plasma membrane was fluorescently visualized under Olympus IX81 fluorescence microscope and analyzed using MetaMorph software (Basic version 7.7.0.0, Molecular Devices, Inc). From each heart, n=2 sections (including one technical control) were examined, with n=20-25 random images captured from each section in a blinded manner. Within each image, n=25 cardiomyocytes were unbiasedly sampled from whole regions (four corners & center) into our analyses.

2.2.11. Autofluorescence Quench and Confocal Microscopy

Non-specific autofluorescences (mainly lipofuscin) from the human OCT-embedded blocks were significantly eliminated by applying TrueBlack® Lipofuscin Quencher (#23007, Biotium) to the cryosections for 5 mins at RT, followed by standardized tissue fixation, deparaffinization, antigen retrieval and permeabilization as described above. The sections were gently washed with 1XPBS for 3 times, blocked with 5% serum for 1 hr at RT, and incubated with primary antibody as per manufacturer instructions, namely anti-rabbit TFR-1 (Cell Signaling, 13208s), anti-rabbit FPN

(Novus, NBP1-21502), and anti-mouse DMT-1 (Abcam, ab55735) overnight in a humidified hood at 4℃. Next the sections were incubated with Alexa Fluor 594-conjugated secondary antibodies (Invitrogen, USA) against the host species of individual primary antibody for 2 hrs at 37℃. Lastly the sections were stained with Alexa Fluor 488-conjugated WGA (W11261, Invitrogen) and mounted with DAPI antifade (#P36931, Invitrogen) to outline plasma membrane and nuclei, respectively. Intracellular protein colocalizations were acquired under laser scanning confocal microscopy (Leica TCS SP5, Leica Microsystems), and quantitative analyses were performed using Fiji ImageJ (National Institute of Health, Bethesda, MD, USA) software.[392]

2.2.12. Transmission Electron Microscopy (TEM)

Human explanted myocardial specimens were collected transmurally as described above. The tissues (<1mm^3) were promptly fixed in 2% glutaraldehyde with a physiological pH and 360 mOsm osmolarity at 37℃. After stored in 4℃ fridges overnight, the specimens were post-fixed in 1.5% $K_4Fe(CN)_6$ and 2% osmium tetroxide (OsO_4) followed by complete washing with 0.1M sodium cacodylate (pH 7.2) and 0.1M sodium acetate (pH 5.2) buffers. Next, the post-fixative samples were immersed in solution of 2% uranyl acetate (UA) and 0.1M sodium acetate (pH 5.2) for high-contrast en bloc staining. Samples were dehydrated with graded ethanol and acetone solutions, immediately followed by infiltration with Spurr's Resin (Leica Electron Microscopy Sciences, Hatfield, PA, USA). After 24 hours, two resin blocks per sample were sectioned with an ultramicrotome diamond knife along the longitudinal axis of myofilaments to produce four non-consecutive ultrathin sections (70μm), which were further post-stained with 4% UA and 4% lead citrate.

Four 100 μm^2 regions were randomly selected to obtain n=1 image at 2000X resolution, n=4 images at 4000X resolution, and n=6 images at 10000X resolution per sections for a total of 44 images per sample (H7650, Hitachi, Tokyo, Japan). Two investigators independently evaluated cardiomyocytes for the presence and severity of intramitochondrial inclusions, mitochondrial cristae quality as well as sarcomeric ultrastructural integrity (ImageJ software, National Institute of Health, Bethesda, MD, USA). Each mitochondrial long axis, short axis and cross-sectional surface area were measured. The cross-sectional area was defined as the region enveloped by the mitochondria outer membrane, and mitochondrial long axis was defined as the longest distance

between two points on the outer membrane, while short axis was defined as the shortest distance perpendicular to the long axis. We established a scoring system in which a higher score signified a greater severity of dysfunction and based on the collective score of individual mitochondria, each heart specimen was ranked as healthy or varying degree (mild, moderate, or severe) of abnormalities (**Table 4.1**). For consistency, sarcomere or mitochondria whose outer membrane was cut off by the image field of view were excluded from analysis. Blinded assessment of all images was randomly carried out in triplicate by two examiners, and a third adjudicator was involved should any discrepancies arise between the individual assessments.

2.2.13. Cardiac Magnetic Resonance Imaging (CMR)

Frozen myocardium from the middle of interventricular septum were adopted to evaluate the tissue iron content by CMR mappings.[393] Based on LV iron level, n=10 and n=4 samples were retrospectively included in the NFC group and each HF subgroup, respectively. However, the subsequent sample preparation, image acquisition, and analytical processing were conducted in a double-blinded manner. After rapid thawing (15 seconds) on ice, each frozen specimen was cut into cuboids with an approximate dimension of 10mm x 10mm x 5mm (length x width x thickness) with smooth edges. They were then immersed in sufficient 0.9% saline solution to gently equilibrate the tissues to RT (21°C) avoiding possible interferences from temperature,[393] and the fresh saline solution was replaced every 10 minutes for a total of three times. To eliminate artifacts from air bubbles, the final saline buffer (50ml) was simultaneously prepared by heating the 50ml conical tube in a water bath for 30 minutes, followed by thorough sonication (FS30H, Fisher Scientific, MA, USA) for additional 30 minutes at RT. Similarly, the tapping water filling the ultrasonic bath was replaced every 10 minutes in order to equilibrate the heated buffer solution back to RT without time delay. A 10ml Pyrex® glass beaker (CLS100010, Aldrich, MO, USA) was assembled into the conical tube, where the prepared tissue was surrounded by homogenous deaired buffer solution and well situated at the bottom center with muscle fiber orientation in parallel to the magnetic field. All measurements were completed in duplicate.

CMR experiments were performed on a 3T MRI scanner (MAGNETOM Prisma; Siemens Healthcare; Erlangen, Germany) with body coil excitation and a 2.5 cm surface coil for signal reception. Longitudinal relaxation time (T_1) images were acquired with a saturation-recovery

gradient-echo pulse sequence with the following parameters: 10 slices (no gap), 1 mm slice thickness, 30 mm by 60 mm field of view, 128 phase-encoding and 256 readout points for 0.23 mm in-plane spatial resolution. Saturation-recovery images with a recovery time of TS = 1000 ms and full recovery were used to calculate T_1 in each pixel. Transverse relaxation time (T_2) images were acquired with a spin-echo sequence with identical spatial coverage and resolution as the T_1 acquisition, with echo-times of TE=11 ms in steps of 11 ms to 88 ms. T_2* images were acquired with a multi-echo gradient-echo sequence with identical spatial coverage and resolution as the T_1 and T_2 acquisitions, with echo-times of TE=3.26 ms in steps 6.28 ms to 47.22 ms. Mono-exponential recovery was assumed for calculation of T_1, T_2 and T_2* (signal (TS)=1-exp(-TS/T_1) for saturation recovery imaging and signal(TE)=exp(-TE/T_2) and signal (TE)=exp(-TE/T_2*) for T_2 and T_2* multi-echo imaging) with pixel-by-pixel relaxation maps generated for all samples. Averaged relaxation values (measured in msec) from all pixels within each tissue sample were automatically selected for analyses; all measurements were completed in duplicate.

2.2.14. Bulk RNA Sequencing

Transcriptome sequencing, including sample preparation, library construction, and Illumina sequencing were carried out by Novogene Corporation Inc. (California, USA). The reported methods below were modified based on the standard procedures provided by Novogene.

RNA Extraction and RT-PCR. Total RNA isolation was performed by Trizol-chloroform extraction method[192] on an RNA dedicated bench. Briefly, ice-cold Trizol (1ml) was added to an eppendorf tube containing 40-60mg heart tissue, followed by homogenization with a metal bead at 25rpm for 3 mins. The homogenization was further repeated twice at 25rpm for 2 mins, and the homogenates were incubated at RT for 5 mins, and then centrifuged at 12,000g for 10 mins at 4℃. 200µl chloroform was added to a new eppendorf tube containing the supernatant collected from the centrifugation, followed by vigorous shaking for 15 secs and incubation at RT for 2-3 mins. Next, centrifuged again at 12,000g for 10 mins at 4℃, and the upper colorless phase was transferred to a new eppendorf tube with addition of 500µl isopropanol per tube. The lysates were thoroughly mixed by inverting several times, and then incubated at -20℃ overnight. After 24 (-72) hrs, centrifuged at 12,000g for 10 mins at 4℃, and the supernatant was completely discarded. 1ml ethanol (75%) was added by pipetting gently until the pellet was dislodged, and finally,

centrifuged at 7,500g for 10 mins at 4°C. After the supernatant was carefully removed, dissolved the air-dried (5-10 mins) pellet with 12-20µl RNase-free H_2O.

Isolated RNA (1µg) was reversed transcribed with random primers (Invitrogen), followed by cDNA synthesis using SuperScript® II Reverse Transcriptase (Invitrogen). Real-time quantitative PCR was applied using TaqMan premixed assays (ThermoFisher Scientific™) for gene expressions in the human heart tissues. All procedures were strictly carried out on ice.

RNA Quantitation and Qualification. RNA degradation and contamination was firstly monitored on 1% agarose gels. The RNA purity was checked using the NanoPhotometer® spectrophotometer (Implen, CA, USA), while the RNA integrity and quantitation were further assessed using the RNA Nano 6000 Assay Kit of the Bioanalyzer 2100 system (Agilent Technologies, CA, USA).

Quality Control and Library Construction. Quality control (QC) was performed at each step from RNA sample preparation to final data analyses, including total RNA purification and qualification, mRNA enrichment, double-stranded cDNA synthesis, end repair by polyA or adaptor addition, fragments selection and real-time quantitative PCR, library construction and quality assessment, transcriptome sequencing and reference genome mapping.

A total amount of 1µg RNA per sample specimen was used as input material for RNA preparation. Sequencing libraries were generated using NEBNext® Ultra™ RNA Library Prep Kit for Illumina® (NEB, USA) as per manufacturer's recommendations and index codes were added to attribute sequences to each sample. mRNA was purified from total RNA using poly-T oligo-attached magnetic beads.

Clustering and Sequencing Depth. The clustering of the index-coded samples was performed on a cBot Cluster Generation System using PE Cluster Kit cBot-HS (Illumina) based on manufacturer's suggestions. Following cluster generation, the library preparations were sequenced on the Illumina HiSeq platform (NovaSeq 6000). Paired-end read length of 150bp was generated, with a total sequencing depth of 30M pair reads per biological sample.

Raw Data Processing. Raw data (reads) of FASTQ format were firstly processed through fastp. In this step, clean data were obtained by removing reads containing adapter and poly-N

sequences and reads with low quality from raw data. Q20, Q30, and GC content of the clean data were calculated. All downstream analyses were based on the clean data with high quality.

Mapping to Reference Genome. Reference genome and gene model annotation files were accessible from genome website (NCBI/UCSC/Ensembl). Paired-end reads were aligned to the reference genome using the Spliced Transcripts Alignment to a Reference (STAR) software, which was based on a previously undescribed RNA-seq alignment algorithm that used sequential maximum mappable seed search in uncompressed suffix arrays followed by seed clustering and stitching procedure. STAR demonstrated better alignment precision and sensitivity than other RNA-seq aligners for both experimental and simulated data.

Gene Expression Normalization and Unit. FeatureCounts was applied to count the read numbers mapped of each gene. Then RPKM of individual gene was calculated based on the length of the gene and reads count mapped to this gene. **RPKM**, Reads Per Kilobase of exon model per Million mapped reads, considers the effect of sequencing depth and gene length for the reads count at the same time, and is currently the most commonly applied method for estimating gene expression levels[193].

Differentially Expressed Genes (DEG) Analysis. Differential expression analysis between two conditions/groups with three or more biological replicates per condition was performed using DESeq2 R package. DESeq2 provides statistical routines for determining differential expression in digital gene expression data using a negative binomial distribution-based model. The resulting *p values* were adjusted using the Benjamini and Hochberg's approach for controlling the False Discovery Rate (FDR). Genes with an adjusted $p\ value < 0.05$ found by DESeq2 were assigned as differentially expressed.

Differential expression analysis of two conditions without biological replicates was performed using the edgeR R package. The read counts of each sequenced library were adjusted by Trimmed Mean of M values (TMM) through one scaling normalized factor before differential gene expression analysis. The *p values* were adjusted using the Benjamini and Hochberg methods. Corrected $p\ value\ of\ 0.005$ and $|\log_2^{(\text{Fold Change})}|$ of 1 were set as the threshold for significantly differential expression.

Functional Enrichment Analyses. Shared functions among genes were searched by integrating the biological knowledge from various manually-curated biological ontologies[194]. Gene Ontology (GO) annotates genes to biological processes (BP), molecular functions (MF), and cellular components (CC) in a directed acyclic graph structure. Kyoto Encyclopedia of Genes and Genomes (KEGG) annotates genes to high-level functional pathways. Reactome annotates genes to pathways and reactions in human biology. The Human Disease Ontology (DO) annotates genes to pathways and DisGeNET annotates genes to pathways.

GO Enrichment Analysis. Gene Ontology, http://www.geneontology.org/, is a major bioinformatics classification system to unify the presentation of gene properties across all species. GO enrichment analysis of differentially expressed genes was implemented by the clusterProfiler R package. GO terms with corrected $p\ value < 0.05$ were considered significantly enriched by differential expressed genes.

KEGG Pathway Enrichment Analysis. KEGG is a database resource for understanding high-level functions and utilities of the biological system, such as cells and organisms, from molecular-level information, especially large-scale molecular datasets generated by genome sequencing and other high-throughput experimental technologies (http://www.genome.jp/kegg/). clusterProfiler was applied to examine the statistical enrichment of differential expression genes in KEGG pathways. KEGG terms with adjusted $p\ value < 0.05$ were considered significant enrichment.

Reactome Enrichment Analysis. Reactome (https://reactome.org/) is an open-source, peer-reviewed and manually-curated pathway database, providing knowledge on signaling and metabolic molecules involved in biopathological reactions. We used clusterProfiler for statistical Reactome enrichment of differential expression genes. Most importantly, clusterProfiler applies biological term classification and enrichment analyses to gene cluster comparison, helping to better understand higher order functions of biological system. In general, Reactome terms with adjusted $p\ value < 0.05$ were considered significant enrichment.

DO Enrichment Analysis. The Human Disease Ontology (DO, http://www.disease-ontology.org) is a community driven standards-based ontology that provides the disease interface between data resources through ongoing support of disease terminology needs, which is associated with human disease and gene function. We used an R package called clusterProfiler for statistical

DO enrichment of differential expression genes. DO terms with adjusted *p value* < *0.05* were considered significant enrichment.

DisGeNET Enrichment Analysis. The DisGeNET (https://www.disgenet.org) remains the discovery platform which represents one of the largest publicly available databases of genes and variants related to human diseases. We also used clusterProfiler in R for statistical DisGeNET enrichment of differential expression genes. DisGeNET terms with adjusted *p value* < *0.05* were considered significant enrichment.

Alterative Splicing Analysis. Alternative splicing (AS) analysis was performed by the software rMATS, a statistical method for robust and flexible detection of differential AS from replicate RNA-Seq metadata. It identifies alternative splicing events corresponding to all major types of alternative splicing patterns and calculates the *p value* and *FDR* for differential splicing, which include exon skipping (SE), alternative 5' splice sites (A5SS), alternative 3' splice sites (A3SS), mutually exclusive exons (MXE), and retained introns (RI).

Gene Mutation Analysis. Picard tools and Samtools were used to sort, mark duplicated reads and reorder the bam alignment results of each sample. Then, HaplotypeCaller in GATK software was used to perform variant discovery. Raw VCF files were filtered with GATK standard filter method and other parameters (cluster: 3.0; WindowSize: 35.0; QD < 2.0 or FS > 30.0). Finally, ANNOVAR was used to functionally annotate genetic variants detected from diverse genomes against UCSC Genome Browser, dbSNP database, the 1000 Genomes Project and so on.

2.2.15. Global- and Phospho-Proteomic Mapping

Human Heart Tissue Preparation. Human heart explants were procured as described above, and further processed with minor modifications[195, 196]. Briefly, snap-frozen tissue (50mg) was mechanically homogenized in 1ml of 8M urea solution supplemented with protease (cOmplete™, Sigma) and phosphatase (PhosSTOP™, Roche) inhibitors cocktail, followed by centrifugation at 13,000g for 10 mins at 4°C. After collecting the supernatant, centrifugation was repeated in the same manner until there was no visible pellet. The supernatant now containing all intracellular proteins without interferences from cellular debris, fibrotic clots, and contractile

apparatus components (which may cause ion suppression) were snap-frozen in liquid nitrogen and then at -80℃ freezers for downstream mass spectrometry analyses.

Protein Digestion and Quantitation. A total of 100μg protein per biological replicate was used, following quantitation of the protein concentration (μg/μl) by Bradford assay. As we reported before[195, 196], a final concentration of 2.5mM DTT was added to each homogenate for 1 hr at RT to for optimal protein purification, and then a final concentration of 5mM iodoacetamide was added to each homogenate for alkylation and incubated in the dark for 30mins at RT. The homogenates were diluted in 50mM ammonium bicarbonate which brought the urea concentration below 1M, followed by addition of sequencing-grade trypsin (Promega) in a 1:20 protein:protein ratio for overnight digestion at 37℃. Formic acid (to a final concentration of 1%) was subsequently added to sample solutions for blocking trypsin activities. All digested peptide fragments were isolated and desalted with C18 TopTips (Glygen), and then dried to completion by SpeedVac (ThermoFisher Scientific™). Finally, all prepared samples were resuspended in 80% acetonitrile (ACN) with 0.1% triflouroacetic acid (TFA) before subjected to HILIC-HPLC fractionation and TMT labeling.

TMT Labeling. 100μg total protein (per TMT label), as determined by Bradford assay, were labeled with TMT10-plex reagents according to the manufacturer's instructions (ThermoFisher Scientific™)[195, 196]. In brief, dried peptides from individual sample were resuspended in 100μl of triethylammonium bicarbonate (Sigma), with addition of corresponding TMT labels which were firstly suspended in 41μl of ACN. The subsequent labeling reaction was developed for 1 hr at RT and was ended by quenching with 8μl of 5% hydroxylamine (Sigma). Samples from same group were pooled together, and the combined samples were dried to completion by SpeedVac and was further resuspended in 80% ACN with 0.1% TFA for HILIC fractionation.

Chromatographic Fractionation and Phosphopeptide Enrichment. HILIC fractionations were performed using the 2.0 X 150mm X 5μm particle TSKgel Amide-80 column (Tosoh Biocience) and Agilent 1200 HPLC system (Agilent Technologies, CA, USA). Two mobile phases, namely, buffer A containing 98% ACN, 0.1% TFA and buffer B consists of 2% ACN and 0.1% TFA, were applied, and a total of 1mg digested peptides were loaded onto the column at a flow rate of 250 μl/min. The liquid chromatography was set up as we previously reported[195, 196]:

1) a 3 min loading in 20% buffer B; 2) a gradient of 20-40% buffer B for 27 mins; 3) a gradient of 40–100% buffer B for 3 mins; 4) 100% buffer B for 5 mins; 5) a gradient of 100–20% buffer B for 2 mins; and finally, 6) 20% buffer B for 10 mins. The eluted samples were further fractionated into 1.5ml tubes at 2 min intervals, and then dried to completion. 10% of each fraction was reserved for global proteomic analysis.

Phosphopeptide enrichment from the remaining HILIC fractions was conducted using TiO2-coated Mag Sepharose beads (GE Life Sciences) as per the manufacturer's instructions. Briefly, individual HILIC fraction was dried to completion by SpeedVac (ThermoFisher Scientific™) and then was resuspended in 200µl of binding buffer (1M glycolic acid, 80% ACN and 5% TFA), followed by 1 hr incubation with the prepared magnetic beads. Next, it was washed once with 500µl binding buffer and additional three times with washing buffer (80% ACN and 1% TFA), and then eluted in 100µl 5% ammonium hydroxide solution for a total of three times. Eluted phosphopeptides were immediately dried to completion and resuspended in 20µl 1% formic acid prior to liquid chromatography–mass spectrometry analysis. Resuspended peptides and phosphopeptides from individual HILIC fraction were analyzed in technical duplicates, respectively.

Liquid Chromatography-Mass Spectrometry. The liquid chromatographic component was composed of a reverse-phase Thermo Acclaim PepMap pre-column (2cm in length, 75µm in diameter, 3µm C18 beads) and a Thermo PepMap RSLC C18 analytical column (50cm in length, 75µm in diameter, 2µm C18 beads) connected with an Easy-nLC 1200 system (ThermoFisher Scientific™)[195, 196]. The gradient (3 hr) was made of buffer A (5% ACN, 0.1% formic acid) and buffer B (85% ACN, 0.1% formic acid) and had a flow rate of 220 nl/min. Prior to each injection, the equilibration was achieved with 100% buffer A on both the pre (20µl) and analytical (3µl) columns, followed by the nanoflow gradient as previously reported: 5–35% buffer B for 156 mins, 35–100% buffer B for 9 mins and 100% buffer B for 15 mins. The peptides and phosphopeptides injected into the Q Exactive HF mass spectrometer (ThermoFisher Scientific™) were directly ionized by the EasySpray ion source (ThermoFisher Scientific™). For each selected MS1 full scan mass spectrum in profile, MS2-dependent scans were acquired by HCD fragmentation with normalized collision energy (32%). Full scan settings were documented as previously reported: 1.2 x 10^5 resolution, maximum injection time (50ms), ion packet setting for automatic gain control

(3 x 10^6), and a range of 350-1450 m/z. Similarly, MS2 scan settings were as follows: 6 x 10^4 resolution, maximum injection time (100ms), ion packet setting for automatic gain control (1 x 10^5), and a fixed first mass at 100 m/z with 1.2 m/z isolation window. Unassigned parent ions with charge states > 6 were excluded from MS2 analysis, and with dynamic exclusion range set at 20s. Identical liquid chromatography and mass spectrometry settings and procedures were applied to both proteomic (unenriched) and phosphoproteomic (phosphopeptide-enriched) fractions.

MS Data Processing and Analysis. MaxQuant software (v.1.6.2.10, www.coxdocs.org/doku.php?id=maxquant:start) were used for analyzing all raw MS data files against the online human protein sequence database (http://www.uniprot.org/taxonomy/9606) with the application of "Reporter ion MS2" 10-plex TMT settings[195, 196]. With a reporter-ion tolerance at 0.003, our standardized approach allowed for two missed trypsin-cleavage sites and variable modifications for protein phosphorylation at residues of S, T, and Y, N-terminal acetylation, methionine oxidation, asparagine and glutamine deamidation as previously reported. Carbamidomethylation was set as a fixed modification at cysteine residues. A *FDR = 1%* was adopted for filtering candidate peptides and phosphopeptides by searching of a reverse-sequence decoy database.

MaxQuant output files were further processed by Perseus (v.1.6.0.7) and Bioconductor packages in R Studio. The output files including report ion (TMT-labeled data) intensities of protein groups and phosphorylation sites (Ser, Thr, Tyr) firstly underwent $\log_2$-transformation and quartile-normalization by applying "width adjustment" in Perseus[197], and their identifications were ensured by filtering the entries that corresponded to reverse database identifications, potential contaminants, and those with single site identification. Singly or multiply phosphorylated phosphopeptides were reported as separate entries despite their identified values of identical phosphorylation sites. Following normalization individually, proteomic and phosphoproteomic datasets of each sample were combined to construct the merged datasets at both gene and protein levels (which may have multiple entries due to multiple identified phosphorylation sites on identical phosphoproteins), for downstream unsupervised principal component analyses (PCA, all data), and hierarchical clustering ($p<0.05$, all data). Merged datasets were further trimmed by removing phosphorylation sites with <0.7 localization probability as well as duplicate entries at the gene levels to ensure only the most significantly altered protein and phosphorylation sites were

kept. Subsequently, the processed merged datasets were subjected to independent biological pathway enrichment by GSEA[198] or gProfiler[199] using custom databases containing annotated GO terms (including BP, MF, and CC) and other curated pathways. Enriched gene sets were expected to have 10 to 500 associated components, with both *p value* and *FDR* less than 0.1. Hierarchical clustering was performed in Perseus (v.1.6.0.7). Euclidian distance without constraints on row and/or column clustering was adopted after preprocessing data by *k*-means, 10 iterations, and a maximal number of 300 clusters.

Targeted Kinase Motif Prediction. Significantly altered phosphorylation sites (two-tailored Student's t-test, $p<0.05$) between individual comparisons were annotated using the liner motifs function in Perseus which centered the sequencing window around the modified phosphorylation sites for identification of corresponding kinases[195-197].

Pathway Enrichment Analysis and Network Biology Visualization. Enriched gene-sets using ENSEMBL ID as a unique identifier were uploaded to gProfiler, a widely accepted web server (https://biit.cs.ut.ee/gprofiler/gost), for functional pathway enrichment analysis[194, 200]. Significantly upregulated and downregulated gene-sets from all three omics datasets (transcriptome, proteome, phosphoproteome) were inputted separately, for exploration of over- and down-represented biological pathways (more than would be expected by chance) associated with the inputted query gene list between individual comparison. g:GOSt tool was applied against homo sapiens (human) for query gene list which was ranked in order by significance level in decreasing manner. g:SCS (default) or Benjamini-Hochberg FDR method with user-defined threshold at 0.05 was selected as appropriate for multiple testing correction, and all annotated genes were mapped to well-known databases including GO, KEGG, Reactome, WikiPathways, Human Protein Atlas, Human Phenotype (HP) Ontology. The enrichment output is presented as publication-ready Manhattan plot and extensive tables with detailed information about individual biological pathway (BP) term and associated gene lists between comparisons.

The statistically enriched and large-size biological pathways were further assembled into functionally related groups using the Enrichment Map tool (http://baderlab.org/Software/EnrichmentMap)[201] to visually cluster similar BP terms under major biological themes in CytoScape[194, 202]. The cutoffs of *p-value*, *FDR Q-value* were both set at 1.0 by default, and overlap coefficient was tuned at 0.5 as similarity cutoff. Individual node (colored

by enrichment scores) represented the biological pathways, while the edge indicates the connection (i.e., shareable genes) between different pathways and its size was determined by the number of common genes shared between connected pathways. AutoAnnotate plugin (https://autoannotate.readthedocs.io/en/latest/) was further applied in CytoScape to automatically cluster similar networks using clusterMaker2 and then add a concise semantic summary (enclosing shape and label) of all the BP terms attached to the nodes within each new cluster via WordCloud, while maintaining the relationship between multiple sets of annotations for any single network[203]. Large network containing many clusters can be collapsed for simplified view and better interpretation.

2.2.16. Statistical Analysis

No statistical algorithms were applied to predetermine the sample size. Our experiments were conducted in a randomized manner, whereas the investigators were blinded in sample allocation and outcome assessments.

Data Reporting. Shapiro-Wilk test and Levene test were firstly applied to check the normality of data distribution and homogeneity of variance, respectively. Continuous variables were reported as medians with interquartile ranges (median, Q1-Q3) for clinical parameters, or means ± standard deviations (mean ± SD) for experimental measurements. Categorical data were summarized as numbers with percentages (integer, %). One-way ANOVA (followed by Tukey or Bonferroni post-hoc analysis), or independent sample t-test was used to compare continuous variables between subgroups, while Mann-Whitney U test or Kruskal Wallis test was applied for non-parametric comparisons as appropriate. All categorical data were analyzed by Chi-squared test or Fisher's exact test where applicable.

Data Presentation. Continuous datasets were visualized by box plots with overlapping data points, or bar charts (upper line of the bar represents mean value) in a consistent manner. Pearson's correlation or Spearman rank correlation was used as applicable to evaluate the statistical association between variables of interest, including parametric and non-parametric variates, respectively. Multiple linear regression models were performed as applicable to estimate the relationship between two or more explanatory variables and the dependent variable, including the

logistic regression algorithm for binary outcome prediction. Data visualization and graphical representation was performed on Origin for Windows, Version 2018b (OriginLab Corp., M.A., USA), and GraphPad Prism for Windows, Version 9.3.0 (GraphPad Software, C.A., USA). IBM SPSS Statistics for Windows, Version 21 (IBM Corp., N.Y., USA) was used for data analyses and narrative interpretation. A two-tailed $p\ value < 0.05$ was considered statistically significant.

Chapter 3

Overview of Research Programs & Protocols

The Human Explanted Heart Program:

A Translational Bridge for Cardiovascular Medicine

Hao Zhang[1,2], Anissa Viveiros[2,3], Anish Nikhanj[1,2], Quynh Nguyen[1,2], Kaiming Wang[1,2], Wei Wang[2,4], Darren H. Freed[2,4], John C. Mullen[2,4], Roderick MacArthur[2,4], Daniel H. Kim[1,2], Wayne Tymchak[1,2], Consolato M. Sergi[2,5], Zamaneh Kassiri[2,3], Shaohua Wang[2,4] and Gavin Y. Oudit[1,2,#]

[1]Division of Cardiology, Department of Medicine, [2]Mazankowski Alberta Heart Institute, [3]Department of Physiology, [4]Division of Cardiac Surgery, Department of Surgery, [5]Division of Anatomical Pathology, Department of Laboratory Medicine & Pathology, Faculty of Medicine & Dentistry, University of Alberta, Edmonton, Alberta, Canada

A version of this chapter has been published as: ***Zhang H**, Viveiros A, Nikhanj A, Nguyen Q, Wang K, Wang W, Freed DH, Mullen JC, MacArthur R, Kim DH, Tymchak W, Sergi CM, Kassiri Z, Wang S, and Oudit GY. The Human Explanted Heart Program: A translational bridge for cardiovascular medicine. Biochimica et Biophysica Acta (BBA)-Molecular Basis of Disease. 2021;1867:165995.* This chapter has been modified from the article above.

3.1 Abstract

The progression of cardiovascular research is often impeded by the lack of reliable disease models that fully recapitulate the pathogenesis in humans. These limitations apply to both i*n vitro* models such as cell-based cultures and *in vivo* animal models which invariably are limited to simulate the complexity of cardiovascular disease in humans. Implementing human heart tissue in cardiovascular research complements our research strategy using preclinical models. We established the Human Explanted Heart Program (HELP) which integrates clinical, tissue and molecular phenotyping thereby providing a comprehensive evaluation into human heart disease. Our collection and storage of biospecimens allow them to retain key pathogenic findings while providing novel insights into human heart failure. The use of human non-failing control explanted hearts provides a valuable comparison group for the diseased explanted hearts. Using HELP we have been able to create a tissue repository which have been used for genetic, molecular, cellular, and histological studies. This review describes the process of collection and use of explanted human heart specimens encompassing a spectrum of pediatric and adult heart diseases, while highlighting the role of these invaluable specimens in translational research. Furthermore, we highlight the efficient procurement and bio-preservation approaches ensuring analytical quality of heart specimens acquired in the context of heart donation and transplantation.

Highlights

1. HELP - The largest research-integrated human heart transplant platform in Canada.

2. Sizable specimen inventory of HELP enables research on a spectrum of heart diseases.

3. Systematic review of the methodology for HELP biobank management.

4. Detailed evaluation on use of human hearts in translational cardiovascular medicine.

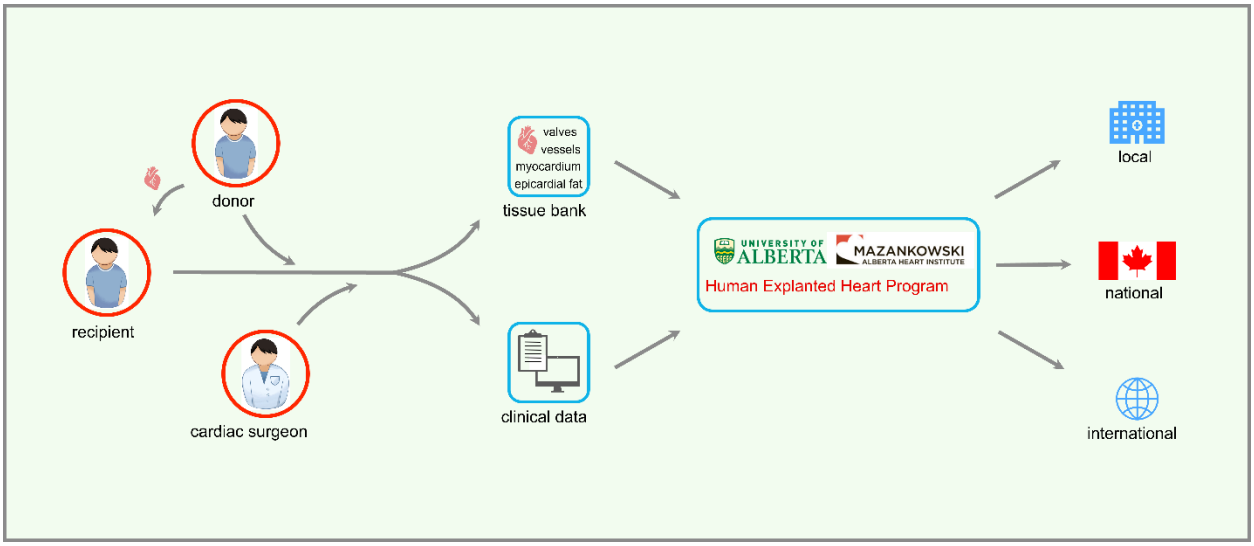

Figure 3.1. Schematic illustration of the Human Explanted Heart Program (HELP). HELP serves as an integrative program that brings together clinicians and researchers aiming to unravel the underpinnings of cardiovascular disease and discover novel therapeutics. Our biobank contains tissue collections covering all sections of the explanted heart. A comprehensive review of the research participant clinical profile is also integrated into the analysis while complementary academic partnerships enabled us to broaden and diversify our approach to human heart disease.

3.2. Introduction

Cardiovascular diseases (CVD) remains the number one cause for mortality worldwide[204], which is projected to grow within the next decades resulting in enormous medical and societal burdens[2]. Heart failure (HF) is the final stage of structural and functional myocardial impairment due to varying etiologies[205]. It is characterized by activation of signaling pathways resulting in pathological remodeling, increased myocardial fibrosis, altered electrophysiology, and defective metabolite regulation leading to systolic and diastolic dysfunction[6-8, 206-210]. While medical and device therapies are effective against HF, many patients still progress to end-stage HF requiring left ventricular assist device (LVAD) and heart transplantation[211-214]. However, organ supply from optimal donors severely limits transplantation as a therapeutic option, which causes high waitlist mortality[215-219]. Therefore, there is an urgent need for tailored and improved pharmacotherapies for HF.

Human heart biospecimens remain high on the agenda for mechanistic studies and drug discovery and validation when studying multifaceted human CVD[220-223]. A biobank is a bio-depository that encompasses the collection and storage of biologic samples and associated biological and clinical data to be used for research[224-226]. Importantly, biobanking enables bi-directional approaches to discover novel targets for HF prospectively, or retrospectively verify existing hypotheses derived from previous experimental models. In this review, we outline the methodology and classification of our heart biobank, and we also illustrate the utility of our program for current and future applications to better elucidate the mechanism for human heart disease and to drive drug discovery.

3.3. Human Explanted Heart Program: Overview & Background

3.3.1. Tissue Biobanking

The Mazankowski Alberta Heart Institute (MAHI) administers an extensive research-integrated human heart transplant program – the Human Explanted Heart Program (HELP). Established in 2010, HELP is a research partnership between basic scientists, clinicians, and clinician-scientists of the MAHI at the University of Alberta. The primary objective of this program was to serve as an integrative and sustainable platform for discovery, innovation, and improved patient care. Fundamental to this approach is the consistent collection of human explanted heart tissues over the past decade, such that our biobank now contains a breadth of heart diseases, which fosters ongoing collaborations[26, 129, 227-234]. Our biobank contains samples obtained from over 450 specimens with diverse phenotypes coupled with comprehensive clinical phenotypes. We have implemented quality control measures involving tissue collection, processing, biopreservation, and biobanking.

As of May 2020, the HELP heart biobank is primarily comprised of specimens representative of four categories: adult (n=219) and pediatric (n=58) failing native hearts, non-failing control hearts (NFC; n=48), and left ventricular apical cores (n=136; **Fig. 3.2A**). Specimen procurement is an ongoing effort, and as such our inventory continues to increase. For the adult cohort, dilated cardiomyopathy (DCM) remained the most common etiology, followed by coronary artery disease (CAD). Likewise, apical cores were collected from patients with similar

etiologies at the time when they received left ventricular assist device (LVAD) as a bridge to heart transplant (**Fig. 3.2A**). Yet often, DCM in our inventory remains idiopathic or familial; we have collected a decent amount of specimens with identified cause(s) impairing the myocardium. Specifically, it includes alcohol abuse, exposure to toxins (i.e., illicit drugs) or heavy metals, anticancer chemotherapies (i.e., Adriamycin), certain infectious diseases (i.e., viral myocarditis) and systemic conditions (e.g., transfusion iron overload, peri-partum CM, diabetic and thyroid diseases). As for the pediatric specimens, congenital heart defects (CHD) constitute 40% of the collection with hypoplastic left heart syndrome (HLHS) and tetralogy of Fallot being the primary diagnoses (**Fig. 3.2A**). In addition to the HF specimens, HELP biobank has also compiled an inventory of the non-failing control (NFC) hearts that serve as the "control" group in the context of cardiovascular research. The NFCs consisted of non-diseased hearts from brain-dead donors obtained through the Human Organ Procurement and Exchange (HOPE) program, which were found unsuitable for transplantation due to various reasons but primarily due to blood type (ABO) and/or human leukocyte antigen (HLA) mismatch. Furthermore, the donor allografts were evaluated and stratified as ideal and marginal based on the reason the organ was declined for transplantation including assessment of clinical parameters (see section 2.2 for more discussion; **Fig. 3.2A**; **Fig. 3.3A**).

As of May 2020, over a total of 25,000 tissue samples from over 400 patients with HF, and over 50 healthy organ donors have been collected, catalogued, and stored in the HELP biobank. Data collection from these hearts is based on the anatomic structure of the whole heart. Each heart was dissected into the left and right atria, left and right ventricles, interventricular septum, apex, coronary arteries, aorta, bicuspid and tricuspid valves, as well as the epicardial adipose tissue (**Fig. 3.2B**). We tailored our approach to the collection of myocardial samples and the dissection and collection of the myocardium was different based on ischemic versus non-ischemic etiologies. The myocardial specimens from the ischemic group were taken based on the position relative to the infarct area, while the myocardium from patients without myocardial infarction (MI) was procured based on anatomical location (basal, mid and apical regions) (**Fig. 3.2B-C**). The full-thickness biopsies of the myocardium and other structures were further divided longitudinally, followed immediately by freezing in liquid nitrogen as tissue samples and as tissue freezing medium (TFM)-embedded specimens. Samples were also collected for histological analysis and electron microscopy by being fixed in formalin or 2% glutaraldehyde, respectively.

A

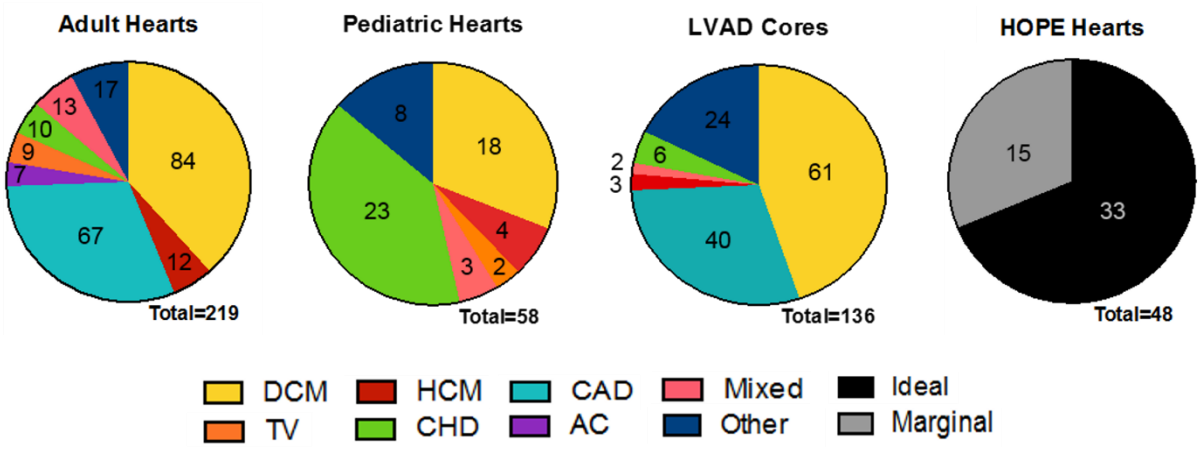

B

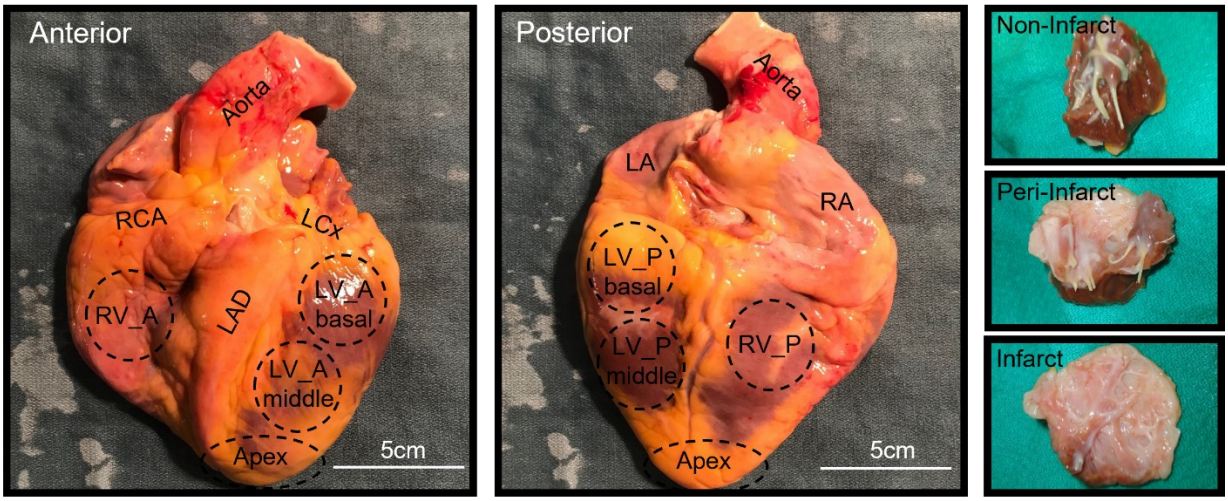

C

Non-Ischemic

Myocardium	**RV**	Anterior		Frozen 2xOCT Formalin EM
		Posterior		
	LV	Anterior	Basal	
			Middle	
		Posterior	Basal	
			Middle	
	Septum			
	Apex			

Ischemic

Myocardium	**RV**	Anterior	Frozen 2xOCT Formalin EM
		Posterior	
	LV*	Infarct	
		Peri-Infarct	
		Non-Infarct	
	Septum		
	Apex		

Non-Ischemic and Ischemic

Atria	**RA**	Free Wall	Frozen 2xOCT Formalin EM
	LA	Free Wall	
		Appendage	
Arteries	**Large Vessels**	Aorta	Frozen OCT Formalin
	Coronary Arteries	RCA	
		LAD	
		LCx	
Valves	**Mitral Valve**	Anterior	
		Posterior	
	Aortic Valve	NCC/RCC/LCC	
EAT	**RV**		
	LV		

Figure 3.2. Schematic of the collection and dissection of the explanted heart tissue. A. Etiology of heart disease in explanted hearts and apical cores. Numbers represent total hearts collected within that group as of May, 2020. Mixed etiology describes patients that fit into multiple categories, such as DCM with CAD; other etiology describes conditions that do not fall into these categories, for example chemotherapy-induced and restrictive cardiomyopathies. B. Visual representation of the non-ischemic explanted heart sample collection (left) and the resultant tissue samples for the ischemic group (right). C. The range of distinct sample sections collected for each explanted heart with the myocardium collected differently according to the infarct area. DCM: dilated cardiomyopathy; CAD: coronary artery disease; HCM: hypertrophic cardiomyopathy; TV: transplant vasculopathy; CHD: congenital heart defects; AC: arrhythmogenic cardiomyopathy; LAD: left anterior descending artery; LCX: left circumflex artery; RCA: right coronary artery; LCC/RCC/NCC: left/right/non-coronary cusp, EAT: epicardial adipose tissue; OCT: optimal cutting temperature-mounted; EM: electron microscope.

3.3.2. Source of Explanted Failing and Donor Hearts

The failing explanted hearts in our collection comprise of the native hearts of transplant recipients. Therefore, our HELP inventory of specimens reflects the diagnoses seen in patients with advanced HF who are eligible for heart transplant (**Fig. 3.2A**; **Fig. 3.3A**)[217, 235]. The high prevalence of cardiac diseases, together with improved survival in patients from advancements in medical and device therapies, have ultimately increased the number of patients with advanced HF. This has induced a supply-demand imbalance for cardiac transplantation, with the number of recipients far exceeding the number of available donor hearts (**Fig. 3.3A**). In Canada, for example, the annual number of HF patients (both adult and pediatric) on the waiting lists increased by almost three-fold from n=47 adult and n=6 pediatric in 2006 to n=122 adult and n=35 pediatric patients in 2018, according to the latest administrative data available from the longitudinal national database of the Canadian Organ Replacement Register (**Fig. 3.3B**)[236-238]. However, the number of heart transplants has climbed relatively slowly for adult patients with an upsurge only in the recent five years, and has even decreased for pediatric patients during the past thirteen years (**Fig. 3.3B-C**)[236-238].

To be eligible for heart transplantation, patients must pass rigorous criteria and thorough assessments, including considerations for relative or absolute contraindications (**Fig. 3.3A**)[217, 239, 240]. Following that, there are two types of assessments to guide the pre-transplant referral. The first includes compatibility tests for matching, such as blood types (e.g., ABO, Rh) and

histocompatibility (i.e., HLA), whereas the second involves cardiopulmonary stress testing and prognostic assessments of HF survival (**Fig. 3.3A**)[217, 240]. The other source of failing hearts (n=9) in the HELP inventory is from patients who required re-transplantation due to transplant vasculopathy[232]. Heart transplantation cannot exist without organ donors. Occasionally, donor hearts are rejected for transplantation resulting in the organs being offered for research, thus our NFC collection via the HOPE program. This is a provincial organ procurement agency that facilitates the donation, allocation and recovery of the organs for transplantation, but also works jointly with HELP to coordinate the procurement of clinically exempted NFC hearts.

Following the procurement of donor organs, we classify the hearts into "ideal" or "marginal", taking account of cardiac and extracardiac factors that prevented the donor hearts for being transplanted[241-244]. To illustrate, a series of cardiac and clinical screenings (i.e., 12-lead electrocardiogram and echocardiogram) are performed routinely on the potential donors. Ideal donor hearts may be rejected from transplantation for extracardiac reasons (such as failed compatibility tests, mismatched donor-recipient size) and/or logistical limitations (i.e., extended cold ischemia time; **Fig. 3.3A**)[241-243, 245, 246]. For the NFC classified as marginal hearts, cardiac (e.g., mild systolic dysfunction) and baseline clinical (namely advanced age and diabetes) conditions are contradindications for heart transplantation (**Fig. 3.3A**)[241-243, 245, 246] in compliance to the nation-wide organ sharing and allocation agreement[217, 235].

A. Transplant Listing Criteria and Imbalanced Donor-Recipient Matching

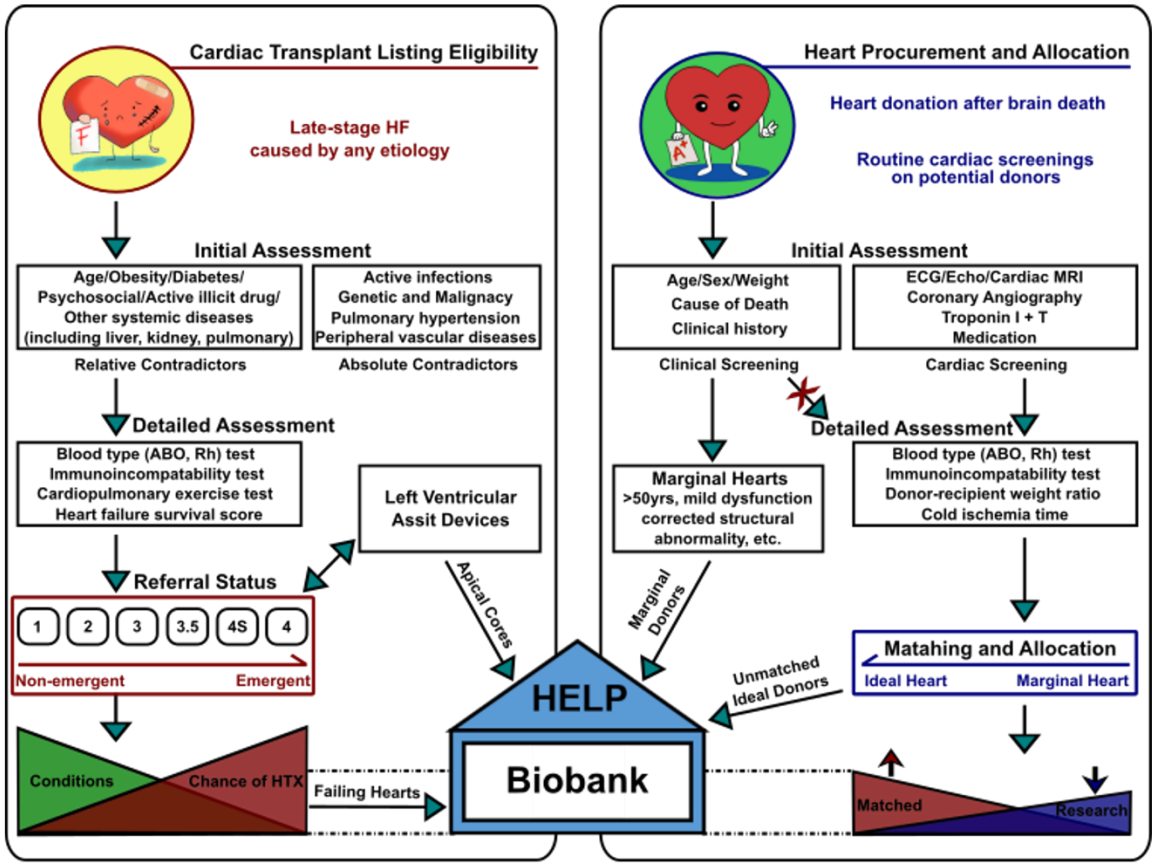

B. Pan-Canada Annual Heart Transplants, Adult vs. Pediatrics, 2006 to 2018

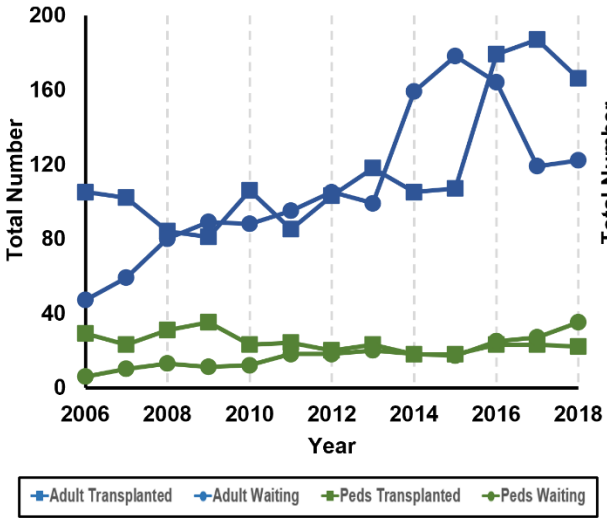

C. Annual Total Heart Transplants, Alberta vs. Canada, 2014 to 2018

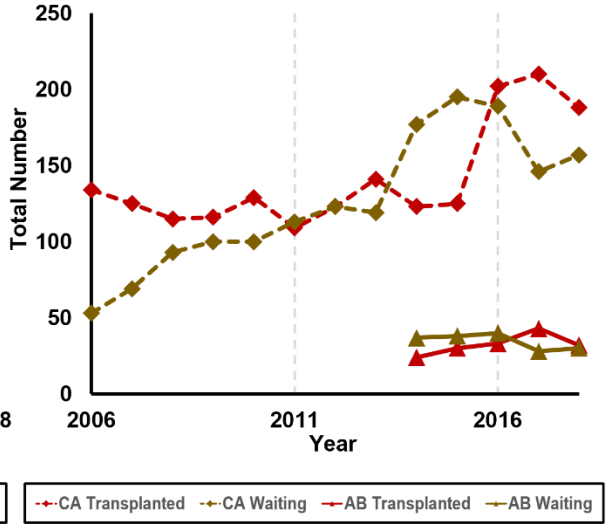

Figure 3.3. Transplant listing criteria and the relation to the Human Explanted Heart Program. A. Conceptual diagram depicting the heart transplant listing eligibilities for both recipients (left) and donors (right), and the sources of failing and nonfailing hearts for HELP biobank. Left: Flow chart illustrating the eligibility, detailed evaluations, and referral status for being listed as heart transplant candidates. Right: The inclusion criteria, specific assessments, and types of donor hearts are delineated. Note that transplantations were limited by the scarcity of matched ideal donor hearts, with the potential to improve by extending the clinical acceptance of donor hearts. HELP biobank: Our heart pools are composed of native failing hearts from transplant recipients, the apical core from patients receiving an LVAD, and non-failing (namely marginal, and unmatched ideal) hearts. B. Imbalanced heart donor-recipient matching in Canada. The HF population was divided into adult (blue lines) and pediatric (green lines) subpopulations; accordingly, the statistics recorded the annual numbers of patients needing heart transplants (round marker) and the ones got transplanted (square marker) from 2006 to 2018. C. Clinical potentials of expanded application of "marginal hearts". Annual total numbers of HF patients (including adult and pediatrics) were collected at both national (dash lines) and provincial (solid lines) levels. The data from 2014 to 2018 demonstrated the advantageous outcomes in terms of increased heart transplant cases (red lines) and simultaneously reduced number of patients awaiting (brown lines) at the national level, while the heart transplant rate remained relatively stable in Alberta during the past five years. Statistics were obtained from the Canadian Organ Replacement Register affiliated with the Canadian Institute for Health Information [39, 40]. CA: Canada; AB: Alberta.

3.4. Human Explanted Heart Procurement: Technical Features and Quality Control

3.4.1. Before Collection

The HELP program encompasses Albertans and a wide coverage of out-of-province patients, including Saskatchewan, Manitoba, and northeastern British Columbia. Informed consent and/or assent were obtained from the patients (or power of attorney) in situations when patients were unable to consent or for pediatric patients less than seven years old. The HELP conforms to the ethical principles of the Declaration of Helsinki and has been approved by the institutional review committee and Health Research Ethics Board (HREB) at the University of Alberta. As for the non-diseased heart donors, informed consent was acquired from the family via the institutional HOPE protocol.

The pre-collection preparation involved extensive labeling of aluminum foil in which dissected biopsies were wrapped and stored in -80°C freezers or liquid N_2, followed by aliquoting of different fixative solutions (e.g., formalin, 2% glutaraldehyde) for preserving tissues. This procedure was conducted by two trainees in the Alberta Cardiovascular and Stroke Research Center (ABACUS). The core laboratory within the ABACUS facility is a dedicated resource, which has allowed us to successfully launch this translational research project. The ABACUS facility has sufficient supplies and equipment to enable tissue collection, including a clean working bench with at least two scalpels, scissors, and forceps, as well as one reusable coronary artery probe with a bendable tip (d~2mm, for tracing the coronary arteries), metal plate, dissection block and surgical towels. Moreover, ABACUS is equipped with a large liquid N_2 tank, ice maker machine, 4°C fridge, and two freezers with the temperature set to either -80°C or -20°C. This setup is paramount to the rapid heart dissection and subsequent storage to maintain tissue integrity.

3.4.2. During Collection

Two trainees with medical training background were on call 24/7 with the cardiac surgical team to procure each consecutively explanted heart. Trainees were informed about the transplant as soon as a donor heart became available, and they would be present on site to receive the explanted heart within 10 minutes of its explantation. Details of the dissection procedure varied slightly depending on the four collection types as indicated in the subsequent sections:

***Failing Hearts**:* Before excision, the beating hearts were perfused with ice-cold standard cardioplegic solution via the aortic root after cross-clamping of the aorta by the operating surgeons. The hypothermic cardioplegic solution containing high potassium washed out the remaining blood within the coronaries circulation and maintained the excised heart at a low metabolic state. Importantly, it prevented further myocardial injury during the temporary ischemic period. Once removed, the hearts were placed in a container with cold saline, surrounded by ice, for immediate transportation to the ABACUS core laboratory, which is directly connected to the cardiac operating theaters. The hearts were then immediately dissected and processed by two trainees within 10 minutes while maintained cooled on ice, after a prompt heart weight measurement and macroscopic examination (Fig. 3.4 and 3.5). One trainee led the systematic dissection while the

other processed the collected tissues. The overall integrity of the removed native heart was maintained to obtain a conventional pathological assessment.

Generally, all sections of the heart were harvested, including myocardium, coronary arteries, valves, larger vessels, and adipose tissues as described earlier in Section 2.1 (**Fig. 3.2B**; **Fig. 3.4**). Methodically, the myocardium was dissected into right and left atrium (both anterior and posterior walls) and its appendage, interventricular septum, left and right ventricles (anterior and inferolateral walls) and apex. The coronary arteries were divided into the left coronary arteries, left anterior descending artery and left circumflex artery, and right coronary artery. The valves included both atrioventricular (i.e., tricuspid and mitral) and semilunar (e.g., aortic and pulmonary) valves. Larger vessels contained ascending aorta, aortic arch and its branches (e.g., brachiocephalic trunk, left common carotid artery and left subclavian artery) and the descending aorta, when available. Lastly, the adipose tissues were procured from the epicardium from the left and right ventricles and around the epicardial coronary arteries. The ventricular free walls were collected based on either the physiological anatomy (apical, mid and basal segments) for the non-ischemic failing hearts and healthy donor hearts, or location relative to the pathological affected area (infarcted, peri-infarcted and non-infarcted regions) for hearts with CAD (**Fig. 3.4A-C**).

The tissue size that was obtained varied depending on the heart weight and shape, but the anatomical positions from where the tissues were captured remained consistent among samples. For instance, positions at approximately one-third and two-thirds below the aortic valves are where we captured the basal and middle ventricular free walls, respectively. As for the major coronary arteries, they were dissected with caution from the explanted hearts, and the vessels were dissected longitudinally to expose the endoluminal surface and cross-sectional landscape. Atherosclerotic lesions were identified and scored by inspecting through a dissecting microscope, and arteries would then be divided into 1.0- to 2.0-cm segments macroscopically designated as disease or disease-free segments. All samples were obtained as transmural biopsies and were further divided to be immediately flash-frozen or TFM-embedded frozen in liquid nitrogen. Meanwhile, the remaining full-thickness pieces were fixed in 10% formalin (containing approximate 4% formaldehyde) or 2% glutaraldehyde for long-term storage. As a bridge to transplantation, the LVAD-supported hearts were also collected when patients received heart transplantation. A 1.0-cm rim of fibrotic myocardium around the apical VAD insertion site was removed and discarded.

These tissues offered the opportunity to study the effects of mechanical unloading on failing hearts (Fig. 3.4D) [233].

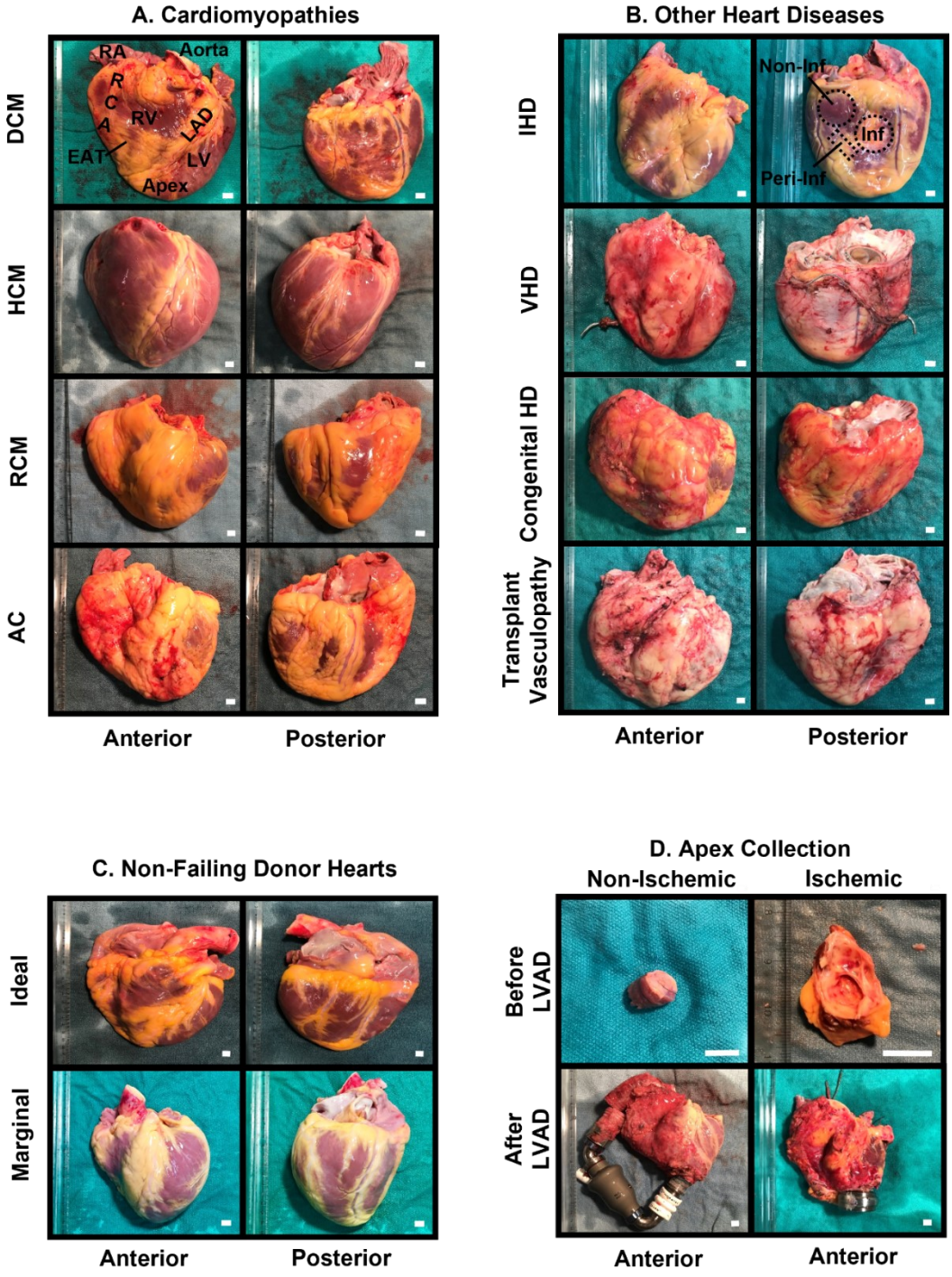

Figure 3.4. Adult human explanted heart gallery. A. Adult failing hearts with various types of cardiomyopathies including dilated cardiomyopathy (DCM), hypertrophic cardiomyopathy (HCM), restrictive cardiomyopathy (RCM) and arrhythmogenic cardiomyopathy (AC). B. Other etiologies that led to end-stage HF including ischemic heart disease (IHD), valvular heart disease (VHD), congenital heart

defects (CHD) and transplant vasculopathy. C. Unmatched ideal hearts, and marginal hearts were harvested into our non-failing control pool. Age and gender-matched selection was adopted while seeking the best reference group in our research. D. Apex during LVAD insertion and native failing heart following transplant were both procured. Scale bar=1 cm.

Non-Failing Hearts: The tissues were obtained in a similar fashion as noted above from organ donors deemed unsuitable for transplantation via the HOPE program. These hearts had no evidence of major functional or structural impairment and received 1 liter of cold Celsior® cardioplegic solution into the coronary system following cross-clamping of the aorta (**Fig. 3.4C**). The excised donor hearts were placed in cold saline immediately following explanation and transported in ice-cool containers to the ABACUS core laboratory.

LVAD Apical Cores: As an integral part of the clinical care of HF patients[213, 247-249], MAHI contains one of the largest VAD program in North America and involves both pediatric and adult patients (**Fig. 3.2A**). At the time of implantation of the LV apical inflow cannula, the apex was collected and divided into two halves: one frozen in liquid nitrogen and the other half further divided into two sections as formalin-fixed for pathological assessment and TFM-embedded for histological staining (**Fig. 3.4D**).

Pediatric Failing Hearts: A meticulous examination of the heart anatomy was conducted before each collection, as CHD were the leading causes of HF in pediatric cases, and they were characterized by various structural anomalies (**Fig. 3.5**). We have also collected some unique pediatric hearts with novel etiologies including Kawasaki disease. The tissues were also procured by two experienced team members within 10 minutes.

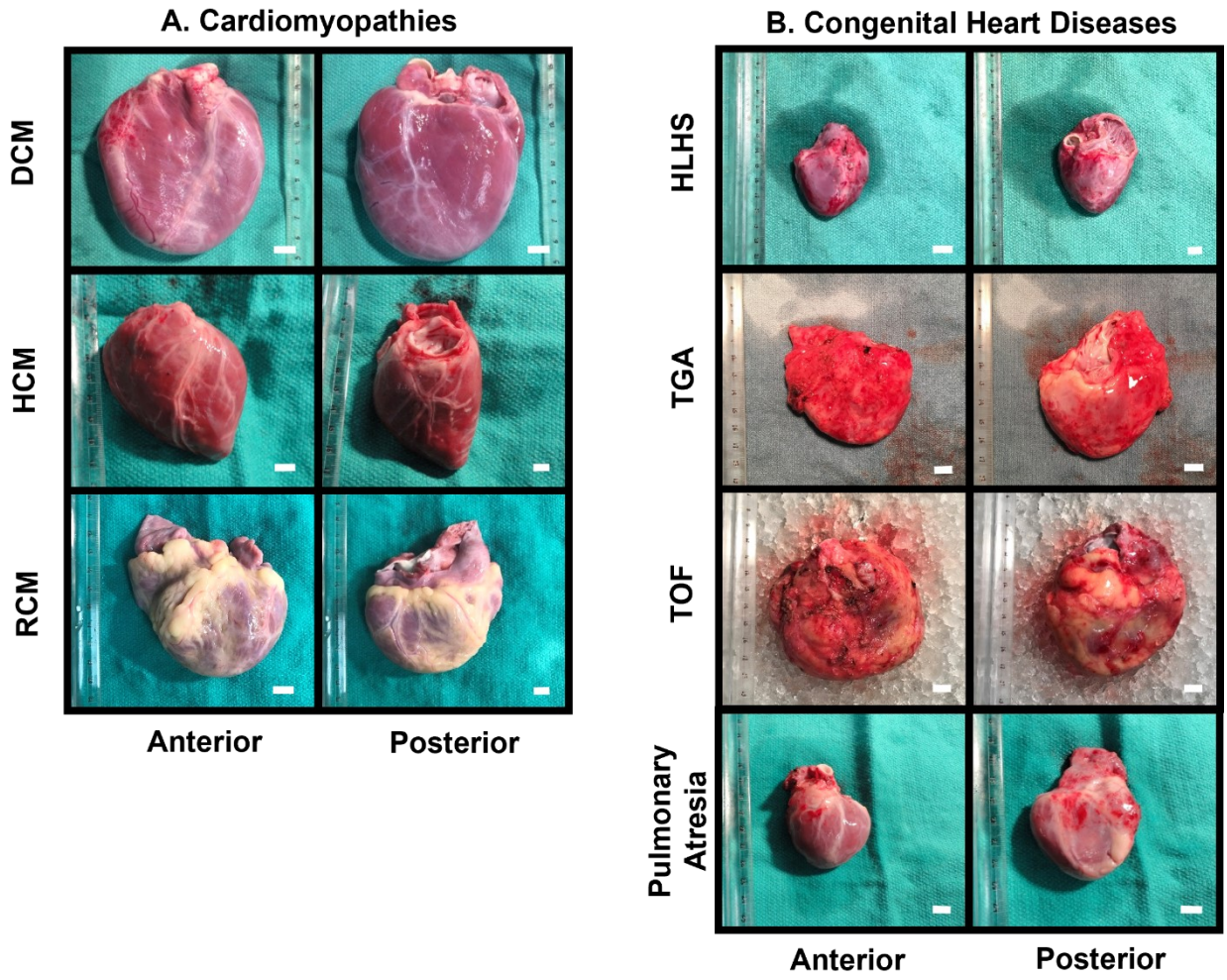

Figure 3.5. Pediatric human explanted heart gallery. A. The common types of cardiomyopathies contributing to pediatric HF such as dilated cardiomyopathy (DCM), hypertrophic cardiomyopathy (HCM), and restrictive cardiomyopathy (RCM). B. Congenital heart diseases with a variety of etiologies, such as hypoplastic left heart syndrome (HLHS), transposition of great artery (TGA), Tetralogy of Fallot (TOF), and pulmonary atresia. Scale bar = 1 cm.

3.4.3. Cellular Manipulation

Cryopreserved tissue has its limitation by virtue of the heterogeneous nature (as a mixture of diverse cell types) and the inability to perform experiments to examine specific cellular mechanisms or signaling pathways upon genetic or pharmacological manipulation. Alternatively, primary cells, which are derived and separated from tissue, provide an ideal model to assess the effects of drug candidates or chemical compounds in a specific cell type, such as cardiomyocytes,

cardiofibroblasts and vascular smooth muscle cells. Further, adenoviral-based techniques can be utilized to inform potential candidates for gene therapy[26, 231, 250-253].

Enzymatic tissue digestion is commonly applied to isolate human cardiomyocytes and cardiofibroblasts with satisfactory yield and viability. Excised myocardial tissue were submerged in the cold formulated Krebs-Henseleit solution that supported cell growth[254]. Cardiomyocytes were separated using a modified five-step isolation procedure as previously described[26, 254-261], which successfully yield viable rod-shaped atrial and/or ventricular cardiomyocytes. The isolation of cardiofibroblasts was performed according to previously described methodology with slight modifications[26, 250, 260, 262]. In brief, 1-gram myocardium from the ventricular or atrial free walls of the explanted failing and non-failing hearts were carefully chopped into several hundred pieces and minced, followed by washing in Ca^{2+}-free buffer (pH 7.4, RT, 9mins), and enzymatic digestion in collagenase buffer with the addition of collagenase II (275 u/ml), protease XXIV (1.2 u/ml), and (S)-(-)-blebbistatin (25 μM) at 37°C. Next, the digested cell suspension was filtered, and the cardiomyocyte-containing homogenate was centrifuged at 20g for 3 minutes to pellet the cardiomyocytes and harvest cardiofibroblasts in the supernatant fraction simultaneously[26, 258-260]. This step was repeated for multiple times under carbogen (95%O_2/5% CO_2), and cell suspensions were removed by gauze filtration. Cardiomyocytes were identified by α-sarcomeric actin and F-actin staining[26]. To enrich for cardiofibroblasts, the suspension was centrifuged for 10 min at 300g, and the resulting pellet was re-suspended in Dulbecco's modified Eagle's medium (DMEM) and centrifuged twice before seeded into pre-warmed culture dishes[26, 262]. Fibroblast-specific markers, such as vimentin and discoidin domain receptor 2, can be used to identify cardiofibroblasts while α-smooth muscle actin staining is a reflection of the myofibroblast phenotype[26, 263]. Despite the short-lived lifespan of primary cultures, overexpression or selective knockout/knockdown of specific genes using adenoviral vector allows for the manipulation of the isolated primary cells and to examine the genotype-phenotype association[26, 255, 256, 264].

3.4.4. After Collection

A tissue-based diagnosis in human heart failure has been shown to be more accurate than the clinical-based diagnosis. In fact, in both American and Canadian based studies, there is 17% clinical misdiagnosis rate with the omission of the patients with CAD, and there was a 30%

misdiagnosis rate for non-ischemic cardiomyopathy[265, 266]. Considering this, all obtained explanted hearts underwent a thorough pathological examination by our co-investigator, who is a board-licensed cardiac pathologist on a routine basis. A close correlation with the clinical features of every patient would be available, including a comparison with the clinical diagnosis.

Clinical Database. Clinical phenotyping is another essential part of our program. The primary investigators (practicing clinicians) have collected a detailed clinical profile of our patients undergoing heart transplant and/or LVAD insertions via chart review. Our extensive database included demographics, comorbidities, medications, risk factors, electrophysiology, and imaging (e.g., echocardiography, cardiac magnetic resonance imaging, diagnostic coronary angiogram). Right heart catheterization data was obtained to evaluate the degree of pulmonary hypertension, pulmonary capillary wedge pressure (LV filling pressure), and the relationship between RV and LV function. The information collected best represents the patient medical condition at the time the heart tissue was acquired. A secured, uniform coding system and strict encryption were employed to maintain confidentiality.

3.4.5. Quality Control for Biobanking Management.

Quality control ensures transparency, traceability, and reproducibility across multiple heart collections, which is of pivotal importance in translational research to minimize introducing new variables and given the vast heterogeneity between individuals. We reiterated that the quality assurance standards were strictly implemented throughout the whole process, from preparation to experimentation.

Firstly, uniform coding (A=adult, P=pediatric, L=LV apical core, and H=non-diseased controls) and acronym (Ant=anterior side, Post=posterior side, Mid=middle wall, Base=basal wall, App=appendage, etc.) minimized the systematic errors that could result from mislabeling or misidentification. Temperature and cold ischemia time were the other two critical variables that were rigorously controlled. In addition, refrigerant cold packs were usually avoided as the solidification of fundamental cytoplasm at a temperature below the freezing point of water was presumed to damage the living tissue cells[267, 268]. By maintaining hypothermic conditions, this procedure curtails analytical artifacts from potential proteolytic degradation and unstable post-

translational modifications[269-272], in conjunction with swift translocation (~1-2 minutes) and rapid processing (<10 minutes) after removal (**Fig. 3.6A**).

Secondly, we have gained plenty of experience to optimize the bio-preservation methods for subsequent quality-assured histopathological imaging (**Fig. 3.6B**). For example, OCT blocks were suspended on top of liquid nitrogen, after embedding the tissues in the cassettes with full TFM immersion, resulting in a slower freezing process without promoting crystallization or matrix cracking inside the tissues (**Fig. 3.6B**). For another, all the tissues were entirely soaked with different fixative buffers and nicely embedded in color-coded blocks for sectioning and mounting for immunofluorescent and immunohistochemical examinations (**Fig. 3.6B-C**); other details are omitted for the consideration of a concise body of work.

Thirdly, standard operating procedures for handling the frozen human heart specimens for RNA and protein extractions were well established. Cross-contamination between samples was avoided by decontaminating the cutting tools with 75% ethanol, followed by 10% bleach. To reduce the unpredictable impacts of warmth, samples were processed frozen with surrounding liquid nitrogen. Aliquots were prepared each time to avoid multiple freezing-thawing cycles, yet the total cycle times were tracked using the archival system that we developed for documenting sample usage, sharing, and retrieving information. Moreover, all frozen samples were safely stored in the cryogenic storage facility consisting of six -85℃ freezers and five liquid nitrogen tanks with a real-time temperature monitoring system (**Fig. 3.6D**).

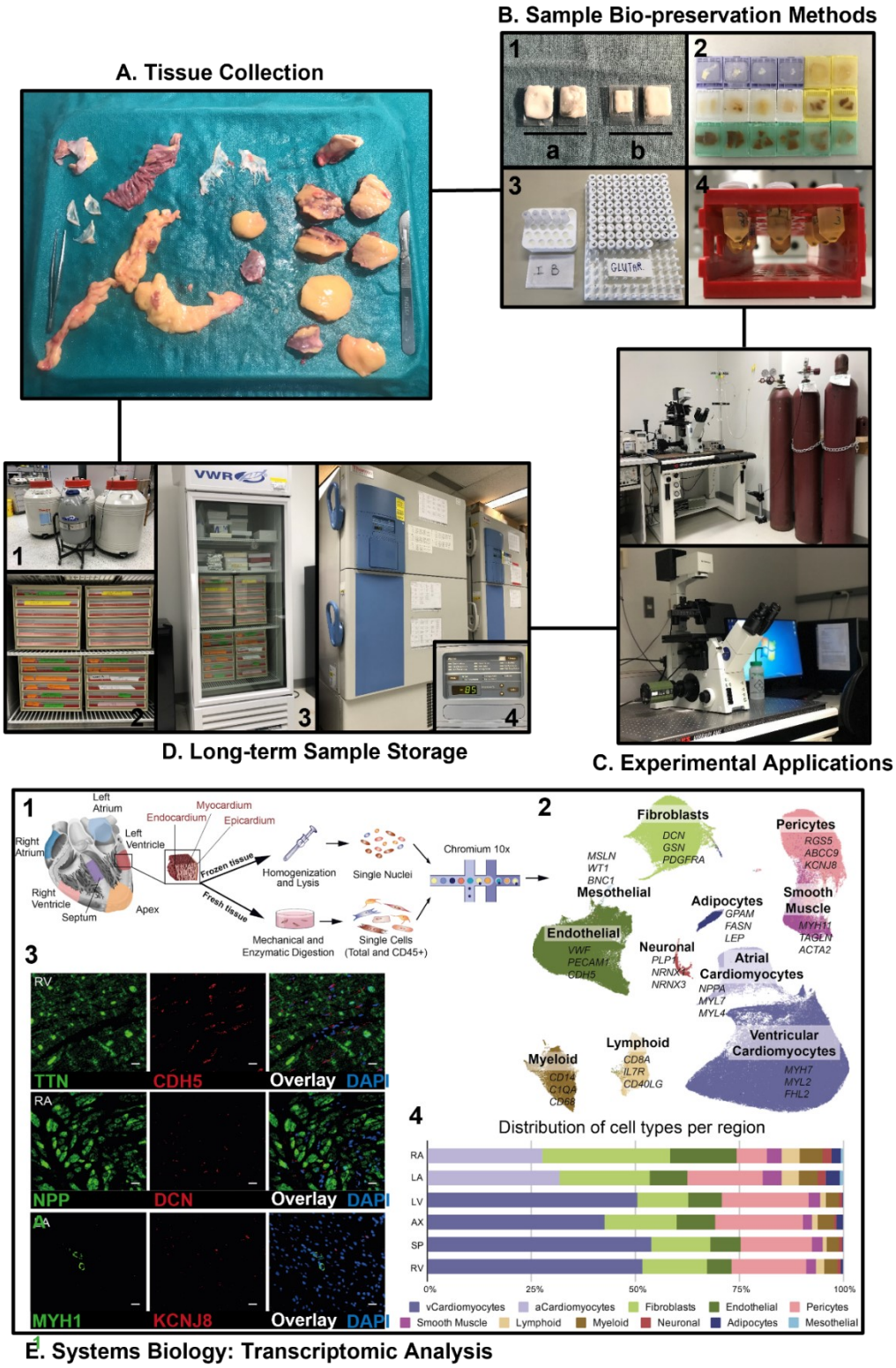

Figure 3.6. Quality control practices to manage and maintain the HELP biobank, and experimental applications. A. A visual representation of the dissected pieces of explanted heart tissues on a metal plate full of ice. B. Representative pictures showing optimized biopreservation methods leading to appropriately

prepared TFM sample (1), paraffin-embedded blocks were systematically color-coded based on the structures (2), buffers for isolating cardiac cells or fixing tissues for histological examination (3), and embedded myocardial samples for ultrastructural study using an electron microscope (4). C. Experimental applications on the heart samples such as immunofluorescent light microscopy and confocal microscopy. D. A capture of the cryogenic long-term storage facility for appropriate depositing of different tissue samples. E. Systems biology analysis using advanced multi-omics techniques. Tissue sampling and processing (1), transcriptome from cells and nuclei delineating whole cardiac cell profiles by UMAP (2), spatial visualization of cell types probed by RNAscope (3), distribution of specific cell population after subclustering analysis (4). Modified from Litvinukova et al.[183] and reproduced with permission from *Nature*.

3.5. Use and Application of the Explanted Heart Samples

The HELP program has offered the unique opportunity to study the correlates of tissue mechanisms in the context of the broader clinical phenotype of each patient. Specifically, we were able to acquire bio-molecular data from diseased myocardial samples to formulate and test hypotheses informed by our ongoing translational studies (i.e., sexually dimorphic responses post-MI, age-dependent or development-specific pathogenesis underlying DCM). Conversely, findings deciphered from the explanted hearts would be applied to gene-based approaches (e.g., adenovirus vector-mediated methods) and/or genetic models to manipulate specific pathways and to examine its downstream effects. As such, this bi-directional approach to translation research truly bridges a critical link to both basic science and to clinical medicine.

3.5.1. Systems Biology

Multi-omics approaches, including genomics, transcriptomics, proteomics, and metabolomics were integrated into our analysis on the explanted human heart tissues. Compared with conventional techniques, systems biology provide a non-biased approach for the identification of novel tissue biomarkers and pathways implicated in CVD[273-275]. In this context, the multi-omics platform would facilitate the generation of a navigated “roadmap” connecting genotype to phenotype with potential clinical applicability for CVD patients.

Genomic Analyses. The polygenetic nature of end-stage HF makes an unbiased, genome-wide analysis a useful tool to identify the underlying basis of heart disease[276-279]. Slow progress has been made on understanding the genetic underpinnings of complex CVD due to confounding factors like extrinsic variables and genetic variation in susceptibility to disease[278]. Current technique for genotyping is based on gene panel based testing in which a predefined set of genes are examined in the diseased specimens. However, more advanced testing using whole-genome sequencing (WGS), for example, maps the entire genome, while whole-exome sequencing (WES) focuses on all the exon (protein-coding) regions in a genome. Though there has been a recent explosion in the number of genes responsible for cardiomyopathies, genotype-phenotype correlations are generally lacking, and studies on the underlying biological mechanisms for numerous mutations and gene variants need to be conducted[280].

Transcriptomic Analyses. The study of transcriptome examines all sets of transcribed RNA molecules from protein-coding messenger RNA (mRNA) to noncoding RNAs such microRNA and long non-coding RNA (lncRNA). The realization of genome-wide profiling of heart diseases necessitates the incorporation of transcriptomic analysis as an integral part, as incomplete interpretation arises without transcription linking genetic information and proteomic expression[275, 281]. With regard to techniques, there are two approaches applied most frequently: hybridization-based microarrays and RNA-sequencing (RNA-Seq). Microarrays are tools that detect the expression of thousands of genes using chips that contain pre-determined probes[282], and hybridization happens when the complementary DNA (reversely transcribed from mRNA) binds to the DNA probes yielding a specific fluorescent color and gene expression is represented as the color intensity after normalized to the corresponding controls[283]. As for analysis on a more global scale, RNA-Seq is more readily employed, where high-throughput sequencing methods (i.e., next-generation sequencing technologies) are used to provide insights into the transcriptomes of explanted heart tissue in an unbiased manner including single-cell and single-nucleus analyses[284-286]. In addition, RNA-Seq analysis provides an improved and expanded RNA profiling with higher specificity and sensitivity, especially for less abundant transcripts. RNA expression profiling has provided new insight into disease pathogenesis including transcriptome signatures of DCM hearts with ventricular arrhythmia[26, 287-290]; however, full knowledge of the broader repertoire of healthy hearts' molecular and genetic landscape is fundamental in this endeavor. To achieve that, we profiled both cells and nuclei from six distinct cardiac anatomical regions (apex, septum, left/right

atria and ventricles) of the non-failing donor hearts, and constructed a most comprehensive transcriptome atlas as the reference framework to advance mechanistic exploration into heart diseases (**Fig. 3.6E**)[26, 234, 288-291].

Proteomic Analyses. Proteomics offer the capability to capture protein structures from whole proteome sequencing, identify post-translationally modified peptides and monitor the subcellular protein-protein interactions[292-295]. Among them, post-translational modifications, including phosphorylation, glycosylation, acetylation and ubiquitination add further diversity to the proteome, which may offer a targetable approach to HF management including the identification of novel biomarkers and therapeutic targets[296].

Metabolomics and Correcting Metabolic Defects. Dysregulated metabolism contributes to the progression of myocardial dysfunction in obesity, diabetes and HF in part due to changes in mitochondrial dynamics post-MI, or varied epigenomic remodeling (e.g., histone modification, DNA methylation, non-coding RNAs in obese-induced cardiomyopathy)[210, 231, 297, 298]. A switch in energy supply from glucose metabolism to fatty acid β-oxidation occurs in heart disease[210], and accordingly, inhibiting fatty acid β-oxidation and stimulating the use of other fuels such as glucose and ketones is a promising therapeutic approach in HF[210, 299]. Pyruvate dehydrogenase kinase isozyme 4 and malonyl-CoA decarboxylase inhibitors are being developed as novel therapies[300], which can be readily tested in human HF cardiomyocytes to examine changes in metabolism. Our metabolomics approach showed elevated branch chain amino acids levels in explanted failing human hearts indicating impaired cardiac branch chain amino acid catabolism in human heart failure, while enhancing branch chain amino acids oxidation improved cardiac function in the failing heart[301].

3.5.2. Reverse Remodeling of the Failing Human Heart: Impact of LVAD Therapy

Extensive studies alleged the beneficial adaptive or reverse remodeling upon LVAD implantation, but several questions remain unanswered such as identification of markers of recovery, genetic basis underlying disparate outcomes among patients, and longitudinal effects of mechanical circulatory support[233, 254, 256, 302-306]. The HELP program offers the ability to investigate them comprehensively on a large scale. We would prioritize the apical tissue taken at the time of LVAD

insertion and compare with the LV myocardium procured from the same patient undergoing subsequent transplantation. In addition, genetic or proteomic markers underlying RV failure, a persistent limitation of current LVAD therapy[307], would also be incorporated into our analysis.

3.6. Targeted Approaches of the HELP Program

3.6.1. Enhancing Angiotensin-Converting Enzyme 2 and Apelin Pathways as Potential Novel Therapy for Human HF

Activation of the systemic RAS and the generation of angiotensin II (Ang II) by angiotensin-converting enzyme (ACE) is major driver of cardiovascular diseases[308-310]. In contrast, ACE2 functions as a pleiotropic monocarboxypeptidase, which generates Ang 1-7 from Ang II[311-313] leading to activation of the widely expressed Mas receptor in the CV system[250, 313, 314]. ACE2 is the receptor for the SARS-CoV-2 and is associated with myocarditis, microvascular dysfunction, LV dysfunction in COVID-19 patients[310, 315, 316]. Therapeutic strategies focus on maintaining the balance between the two arms by either enhancing ACE2 (e.g., administration of recombinant human ACE2, rhACE2) or suppressing Ang II actions (i.e. blockade of AT_1R, or ACE inhibition) in the context of HF, whereby we have gained substantial understandings from rodent models combined with human tissue explants[250, 310, 317-321]. Interestingly, an alternative ACE-independent pathway for converting Ang I to Ang II was found in the heart driven by the serine proteinase, chymase family[322]. In accordance, there is incomplete suppression of plasma Ang II levels in patients who took ACE inhibitors chronically[323-325], and using the HELP platform we demonstrated increased chymase protein levels and activity in explanted DCM hearts which likely contributed to the elevated tissue Ang II despite ACE inhibition[326].

Apelin is an endogenous family of peptides which binds and activate the G protein-coupled receptor, apelin receptor[327]. Similar to the AT_1R, the apelin receptor is highly expressed in the cardiovascular system[327] and the apelin axis is proposed to have the opposite effects to the Ang II/AT_1R pathway[328]. Apelin mediates a positive inotropic effect and by activating eNOS results in mild vasodilation and afterload reduction[329, 330]. Loss of apelin could lead to increased mortality, greater adverse remodeling post-MI, exacerbated myocardial damage in response to myocardial ischemia-reperfusion injury, and higher susceptibility to vascular events such as abdominal aortic

aneurysm and peripheral arterial diseases[253, 331, 332]. Apelin levels are decreased in the coronary arteries from explanted hears with myocardial infarction[333] but increased in aortic samples obtained from patients with aortic aneurysm[253]. The metalloprotease, neprilysin, is a major physiological enzyme, apart from ACE2, that degraded apelin peptides and inactivated the apelinergic system providing important insight into the therapeutic benefit of sacubitril/valsartan therapy in HF[327, 334]. Enhancing the apelin/apelin receptor axis has emerged as the novel pathway for the treatment of cardiovascular diseases, such as obesity-associated cardiac hypertrophy and contractile dysfunction[335].

3.6.2. Correcting the Dysregulated Extracellular Matrix (ECM): role of TIMPs

At the tissue level, cardiomyocytes are surrounded and supported by the ECM, which maintains stability and the architectural integrity of the myocardium. The matrix metalloproteinases (MMPs) are the predominant proteases that regulate the ECM homeostasis by degrading the ECM proteins. This process can be blocked physiologically by the tissue inhibitor of metalloproteinases (TIMPs)[336-340]. Maladaptive myocardial remodeling is characterized by an overall imbalance in ECM turnover, which can result in excess accumulation or disruption of the ECM structural proteins, mainly collagens, leading to impaired systolic performance and diastolic dysfunction in failing hearts[129, 340-342]. In addition, insufficient ECM remodeling can lead to LV dilation and rupture, resulting in a high proportion of early sudden death post-MI[343-345]. Myocardial TIMP-1, TIMP-3 and TIMP-4 were reduced in patients having CAD and DCM[346, 347], while TIMP2 markedly increased in later-stage DCM patients[348].

Despite similar phenotypes characterized as systolic dysfunction and eccentric ventricular dilation, pediatric DCM are distinct from adult DCM. Accordingly, there are no proven effective therapies for HF in pediatric patients with DCM[124, 349]. We discovered disparate remodeling patterns of the fibrillar and non-fibrillar ECM components, such as glycosaminoglycans and proteoglycan that exists between the pediatric and adult DCM groups[129]. This finding may underlie the pathological basis for differential fibrotic reverse remodeling and distinct affinity to the transforming growth factor-β pathway[129], which provides insights as to why pediatric HF patients were less responsive to HF therapies based on clinical trials in adults. The use of explanted failing

hearts from children and adults provides an important opportunity to examine the ECM remodeling and its relationship with advanced HF.

3.7. Future Directions of HELP Program

3.7.1. Investigation of Inherited Cardiomyopathies

Our large and diverse collection of samples gives us the opportunity to investigate the pathophysiology and genetics associated with various cardiomyopathies[350-353]. We have the unique access to LVAD cores and explanted hearts of patients diagnosed with Fabry disease (FD), muscular dystrophy (MD) and other types of genetic cardiomyopathies. FD is an X-linked recessive lysosomal storage disorder, identifiable by the accumulation of glycosphingolipids, leading to multisystem disease[354]. Cardiac complications associated with FD include arrhythmias, LV hypertrophy, and diastolic dysfunction; progression of heart disease in FD results in HFpEF[354, 355]. Assessment of human heart tissue through histological staining and genetic sequencing will provide critical insights into the adverse remodeling pathways associated with FD as well as the HFpEF phenotype. MD describes a family of inherited neuromuscular diseases with systemic manifestations[351]. Heart disease, characterized by cardiomyopathy and arrhythmias, is recognized as the primary cause of morbidity and mortality in these patients[356-358]. At the cellular level, Duchenne MD and limb-girdle MD are characterized by the absence or dysfunction of critical cytoskeletal proteins, which leaves cardiomyocytes vulnerable to contractile and shearing forces[356]. Importantly, the correlation of our tissue findings to clinical characteristics could serve to improve patient prognosis through a precision medicine-based approach.

3.7.2. Epicardial Adipose Tissue and Its Relationship with Heart Disease

Adipose tissue of the heart can be divided into two distinct subsets: the epicardial adipose tissue (EAT) and the pericardial adipose tissue (PAT). The EAT is a visceral fat depot with anatomic proximity to the myocardium, located between the visceral pericardium and myocardium[359-362]. In fact, the close relationship between the myocardium and EAT is exemplified in that they share a common microcirculation. Healthy EAT accounts for approximately 15% of total cardiac mass

and primarily resides in the atrioventricular and interventricular grooves (**Fig. 3.4C**). However, in diseased states, EAT volume increases and expands to cover the ventricles and the entire epicardial surface[359, 362, 363] (**Fig. 3.4A-B**). Physiologically, the EAT maintains fatty acid (FA) homeostasis to both mobilize FA for oxidation, which in general meets 50-70% of the metabolic demand of the heart, as well as sequester excess FA to circumvent lipotoxicity[363, 364]. Further, at physiological volumes, the EAT secretes anti-inflammatory cytokines and adipokines, including adiponectin, leptin, and apelin[365]. However, the pathological progression of CAD and HF is associated with a shift in the EAT secretasome, favoring a proinflammatory cytokine profile and excess release of FA[360, 362, 365, 366]. Importantly, cardiac adipose tissue is limited in laboratory mice, and when present is restricted to the atrioventricular groove[227, 367]. Therefore, this highlights the utility of our program to obtain and study EAT from explanted human hearts, offering an optimal platform to study EAT tissue and to unravel its close connection with human heart disease.

3.7.3. Cardiac Electrophysiology and Ventricular Optical Mapping

Ventricular arrhythmias and sudden cardiac death account for 50% of the mortality in patients with advanced HF[368]. Our studies have provided an improved understanding of the mechanism of ventricular fibrillation and the role of signaling pathways and late sodium current[369, 370]. The MiCAM Ultima camera system incorporates novel image sensors with high-speed image acquisition while retaining maximal quantum efficiency, and the high signal-to-noise ratio allows for detection of activation times from the first derivative of optical signals during ventricular fibrillation without spatial averaging. We have recently described the genetic and electrophysiological characteristics of a patient with familial Long QT syndrome caused by missense mutations in *KCNH2*[371]. The ability to characterize the electrophysiological changes at a cellular level coupled with the optical mapping of the electrical activation of the whole heart will offer unique insights into the mechanism of ventricular arrhythmias.

3.8. Conclusions

There are limitations at different stages of the HELP and HOPE programs that need to be acknowledged. Prior to collection, we are limited both by the time of organ procurement and the

general heterogeneity of patients. HOPE donors spend an average of 4 days in hospital prior to the declaration of brain death while receiving ongoing therapy. The issue of heterogeneity is intrinsic to working with human samples; comorbidities, lifestyle, and pharmaceutical interventions in HF may affect experimental results. However, access to clinical data allows us to assess specimens and perform subsequent subgrouping. Further, the pathological effects of the adrenergic storm (associated with brain death) on the donor hearts can alter the tissue characteristics in the NFC hearts we have collected. Indeed, some of the data acquired from the control group might not be true representatives of the healthy heart *in vivo*. Following collection, the challenge of working exclusively with frozen clinical specimens or short-lived primary cardiomyocytes limits the analysis and exploration of dynamic biological mechanisms, which could be unraveled when combined with animal models. Lastly, our patient cohorts were all at end-stage HF and thus we captured a single time point of the entire disease course. Therefore, despite the limitations of our program, our human explanted heart tissue biobank constitutes a unique platform for cardiovascular translational research.

Chapter 4

Myocardial Iron Deficiency and Mitochondrial Dysfunction

In Advanced Heart Failure in Humans

Myocardial Iron Deficiency and Mitochondrial Dysfunction In Advanced Heart Failure in Humans

Hao Zhang MD[1,2], K. Lockhart Jamieson PhD[3], Justin Grenier MSc[2,4], Anish Nikhanj MSc[1,2], Zeyu Tang MD[1,2], Faqi Wang PhD[1,2], Shaohua Wang MD MSc[2,5], Jonathan G Seidman PhD[6], Christine E. Seidman MD[6,7], Richard Thompson PhD[2,4], John M. Seubert PhD[2,3] and Gavin Y. Oudit MD PhD[1,2,#]

[1]Division of Cardiology, Department of Medicine, [2]Mazankowski Alberta Heart Institute, [3]Department of Pharmacology, [4]Department of Biomedical Engineering, [5]Division of Cardiac Surgery, Department of Surgery, Faculty of Medicine and Dentistry, University of Alberta, Edmonton, AB, CA. [6]Department of Genetics, Harvard Medical School, Boston, MA, USA. [7]Cardiovascular Division, Brigham and Women's Hospital, Boston, MA, USA

A version of this chapter has been published as: ***Zhang H**, Jamieson KL, Grenier J, Nikhanj A, Tang Z, Wang F, Wang S, Seidman JG, Seidman CE, Thompson RB, Seubert JM, and Oudit GY. Myocardial iron deficiency and mitochondrial dysfunction in advanced heart failure in humans. Journal of the American Heart Association. 2022;e022853. DOI:10.1161/JAHA.121.022853.* This chapter has been modified from the article above.

4.1. Abstract

Background. Myocardial iron deficiency (MID) in heart failure (HF) remains largely unexplored. We aim to establish defining criterion for MID, evaluate its pathophysiological role, and evaluate the applicability of monitoring it non-invasively in human explanted hearts.

Methods and Results. Biventricular tissue iron levels were measured in both failing (n=138) and non-failing control (NFC, n=46) explanted human hearts. Clinical phenotyping was complemented with comprehensive assessment of myocardial remodeling and mitochondrial functional profiles, including metabolic and oxidative stress. Myocardial iron status was further investigated by cardiac magnetic resonance (CMR) imaging. Myocardial iron content in the left ventricle (LV) was lower in HF versus NFC [121.4 (88.1-150.3) vs. 137.4 (109.2-165.9) μg/g dry weight], which was absent in the right ventricle (RV). With *a priori* cutoff of 86.1 μg/g d.w. in LV, we identified 23% of HF patients with MID (HF-MID) associated with higher NYHA class and worsened LV function. Respiratory chain and Krebs cycle enzymatic activities were suppressed and strongly correlated with depleted iron stores in HF-MID hearts. Defenses against oxidative stress were severely impaired in association with worsened adverse remodeling in iron-deficient hearts. Mechanistically, iron uptake pathways were impeded in HF-MID including decreased translocation to the sarcolemma, while transmembrane fraction of ferroportin positively correlated with MID. CMR with T2* effectively captured myocardial iron levels in failing hearts.

Conclusions. MID is highly prevalent in advanced human HF and exacerbates pathological remodeling in HF driven primarily by dysfunctional mitochondria and increased oxidative stress in the LV. CMR demonstrates clinical potential to non-invasively monitor MID.

4.2. Clinical Perspective

What is New?

- Myocardial iron deficiency is common in explanted failing human hearts with either dilated cardiomyopathy or coronary artery disease.
- Myocardial iron deficiency correlated with greater adverse myocardial remodeling, oxidative stress and suboptimal mitochondrial structure and function.
- Myocardial iron deficiency correlated with reduced levels of iron importers, transferrin receptor-1 and divalent metal transporter-1, and increased levels of the sole iron exporter, ferroportin, in the sarcolemma.

What Are the Clinical Implications?

- Magnetic resonance imaging can detect myocardial iron deficiency.
- Iron supplementation in patients with myocardial iron deficiency, in the absence of major systemic iron deficiency and anemia, is a potential therapy for patients with advanced heart failure.

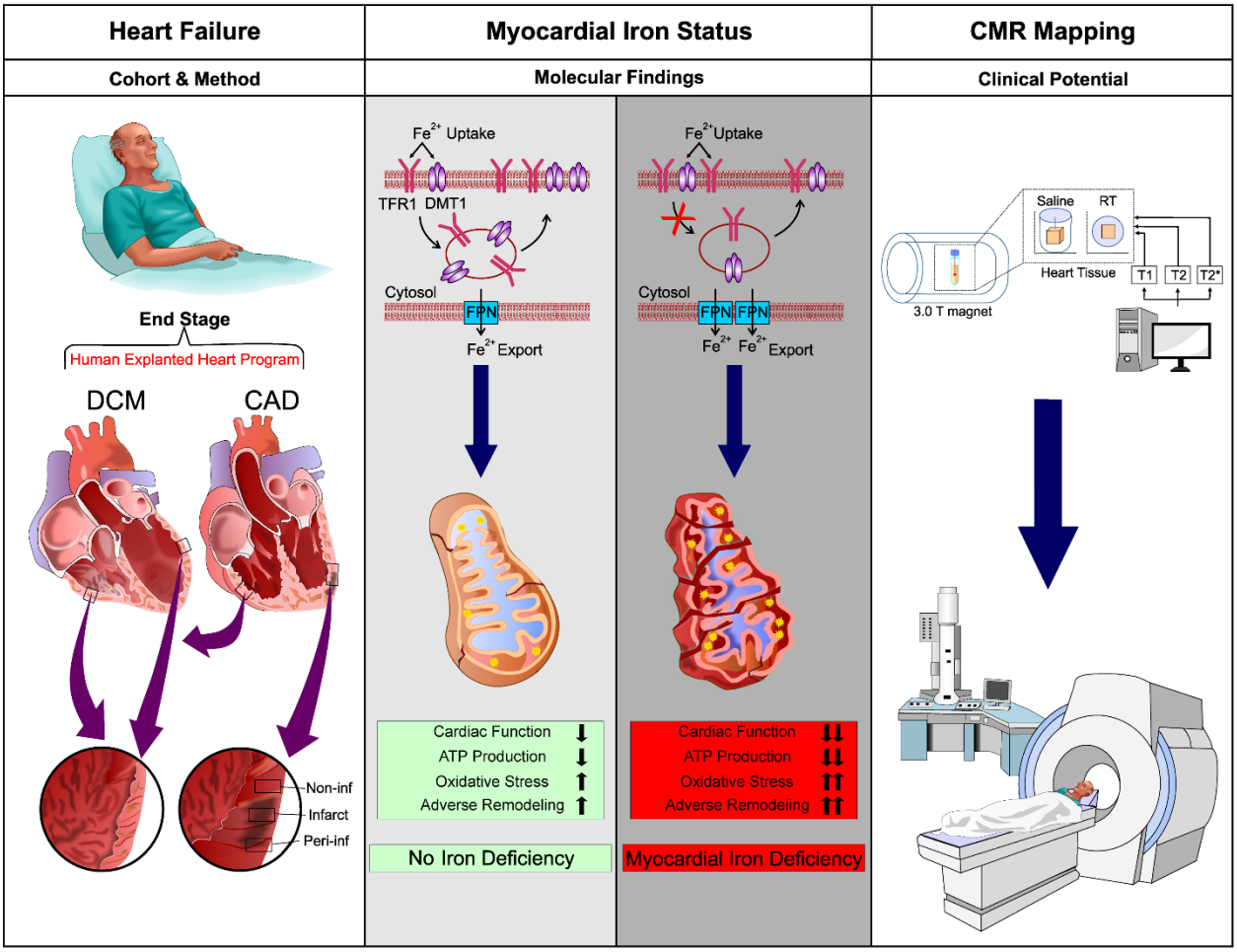

Figure 4.1. Schematic illustration of the research study and technical highlights.

4.3. Introduction

Heart failure (HF) remains extremely prevalent on a global scale with high morbidity and mortality[10, 372]. Comorbid conditions in patients with advanced HF not only complicate the presentation and treatment, but also play an instrumental role in progression of HF[373]. Thus, management of comorbidities is gaining equal importance to treating the primary cause of HF itself[10, 374]. Iron deficiency (ID) is the commonest malnutrition globally, and often co-exists with HF irrespective of the presence of abnormal blood cell indices (i.e., anemia)[375, 376]. Conventionally, systemic iron deficiency (SID), defined as either absolute deficit with serum ferritin <100 μg/L or functional insufficiency combining serum ferritin 100-300 μg/L and transferrin saturation <20%, represents ID in the context of HF[28, 95, 373, 376]. Prior studies have demonstrated the detrimental

impact of SID on patients' physical capacity and clinical outcomes[27, 375], whereas iron supplementations exhibited substantial benefits constituting a promising therapeutic target[10, 374, 377]. However, the diagnosis of SID is solely relied on circulating hematopoietic markers, and screening for SID in HF patients without anemia remains uncommon. Emerging evidence has highlighted the presence of myocardial iron deficiency (MID) in several HF cohorts, and consistently revealed a weak association with systemic iron status[60, 80, 378].

The heart has the highest metabolic demand and is fueled largely by mitochondrial activity[379-381]. Iron is an important micronutrient whose role extends beyond oxygen transport and erythropoiesis to cellular energetics in mitochondria and oxidative stress homeostasis[382]. Mechanistically, intracellular iron availability is maintained by iron trafficking pathways including uptake, utilization, storage, and excretion of the iron by cardiomyocytes[383]. While systemic iron regulation is a critical determinant of erythropoiesis and anemia, homeostatic iron levels in the heart are controlled at the tissue level[47, 57]. However, the direct burden of MID in patients with HF is unknown. As such, elucidating the prevalence and mechanism of MID, and its impact on mitochondrial function and anti-oxidative protection directly from the human failing myocardium is clearly warranted.

Accordingly, we studied the burden of MID in the largest cohort of explanted human hearts to date and determined its pathophysiological implications on the failing hearts. Furthermore, we explored the suitability of using quantitative parametric mapping with cardiac magnetic resonance (CMR) as a non-invasive imaging modality to assess myocardial iron levels. Our results revealed a high prevalence of MID in diseased human explanted hearts which correlated with worsened clinical status and adverse remodeling. We showed greater mitochondrial damage and loss of function in the setting of MID, which was associated with overall reduced expressions of major iron importers. Magnetic resonance imaging provided a useful tool to assess myocardial iron levels, possibly guiding a precision medicine-based approach to iron supplementation therapy. Taken together, our data revealed that MID is highly prevalent in advanced HF and worsens mitochondrial function, and thereby identifying an unappreciated role for correcting MID in patients with HF.

4.4. Methods

The data that support the findings of this study are available from the corresponding author upon reasonable request.

4.4.1. Human Explanted Hearts: Tissue Procurement and Preparation

Heart specimens from the non-failing control (NFC, n=46) and adult failing hearts (HF, n=138) were procured from the Human Organ Procurement and Exchange (HOPE) program and Human Explanted Heart Program (HELP), respectively. Our diseased cohort consisted of patients with end-stage HF secondary to coronary artery disease (CAD, n=67) or dilated cardiomyopathy (DCM, n=71) who underwent heart transplantation. The NFC hearts were obtained from brain dead donors with no past history of major comorbidities or cardiovascular diseases, and antemortem echocardiography demonstrated normal ejection fraction of the left and right ventricles as well as normal LV dimensions[179-183]. Informed consents were obtained from all patients and both programs conformed to the ethical principles of the Declaration of Helsinki, and were approved by the institutional review committee and Health Research Ethics Board at the University of Alberta, Edmonton, Canada. Clinical data was obtained by chart review.

Heart tissue procurement strictly followed our well-established protocols[179-183]. Transmural myocardial samples from both ventricles were obtained by avoiding the epicardial fat and scar tissues. For this study, mid-anterior ventricular walls from both LV (approximately two-thirds below the aortic valves) and right ventricle (RV, approximately two-thirds below the tricuspid valves) were procured from the NFC and DCM failing hearts, whereas peri-infarcted and non-infarcted regions from LV were collected from failing hearts with CAD involving the left anterior descending artery (LAD). All the full-thickness specimens were snap-frozen and/or OCT-mounted frozen in liquid nitrogen, and then stored in the -80℃ freezers for subsequent molecular and histochemical analyses[182].

4.4.2. Tissue Iron Level Measurement

Chamber- and etiology-specific myocardial tissue iron levels were directly measured by inductively-coupled plasma resonance mass spectrometry as previously described at the

Department of Pathology and Laboratory Medicine, London Health Sciences Center and St. Joseph's Health Care, London, Western Ontario[17, 26, 188]. Measurement of myocardial iron content was carried out from both ventricles in non-ischemic DCM and NFC hearts, while the levels from peri- and non-infarction regions in LV were anatomized in relation to LAD blockade. Tissue samples were analyzed in triplicate and the average values were reported in this study.

4.4.3. Spectrophotometric Assays for ETC Enzymes

Supernatant from the left ventricle (LV) homogenate was used to assess the electron transport chain (ETC) enzyme activity of NADH:ubiquinone oxidoreductase (COX I), succinate dehydrogenase (SDH, COX II), decylubiquinol cytochrome c oxidoreductase (COX III), NADH cytochrome c oxidoreductase (COX I + III), succinate cytochrome c reductase (COX II + III), cytochrome c oxidase (COX IV) and citrate synthase (CS)[384]. Enzyme activity ($nmol \cdot min^{-1} \cdot mg^{-1}$) was normalized to volume and protein concentration, following protein determination with Bradford assay. Furthermore, the reaction specificity was assured by subtracting the inhibitor-resistant activity from the total enzymatic activity, which were conducted in parallel. The inhibitor for COX I (1mM rotenone), COX II (1M malonate), COX III (1mg/ml antimycin A), COX I + III (1mM rotenone), COX II + III (1M malonate), and COX IV (10mM KCN) were added to each corresponding reaction mixture prepared separately[384]. Measurements were performed in triplicate.

4.4.4. Spectrophotometric Assays for Antioxidant Enzymes

Sample homogenates from flash-frozen LV tissues were prepared as previous described and all measurements were repeated in duplicate and the average value was used[26, 385].

CAT Enzyme Assay. Catalase (CAT) activity was measured according to the method described previously with minor modification[386, 387]. Specific activity (units/mg) was defined as the rate of H_2O_2 consumption per minute per milligram of protein sample.

SOD Enzyme Assay. Superoxide dismutase (SOD) activity was assayed based on the competition for O_2^- between (ferri-)cytochrome c and SOD following its spontaneous dismutation with minor modifications[189, 386]. One unit of activity was defined as the amount of SOD required to inhibit the initial reduction rate of ferri-cytochrome c by 50%. Mitochondrial SOD (SOD2,

Mn/Fe-SOD) activity was determined by adding 100mM KCN to a matched reaction mixture prepared from the same sample. The overall Cu/Zn-SOD activities from cytosol (SOD1) and extracellular matrix (SOD3) were completely inhibited by the KCN (100mM) added[388].

GPX Enzyme Assay. Glutathione peroxidase (GPX) activity was measured based on the oxidation of reduced glutathione (GSH) by GPX coupled to the disappearance of NADPH catalyzed by glutathione reductase (GR)[386, 388]. The rate of NADPH oxidation was monitored spectrophotometrically at 340nm. Briefly, two assays (A & B) were prepared each containing 0.1M K_2HPO4/1mM EDTA (pH 7.0), 10mM L-glutathione reduced (G4251, Sigma, MO, USA), 2.4unit/ml glutathione reductase (G3664, Sigma, MO, USA). The non-enzymatic and H_2O_2-independent NADPH depletion were subtracted from the total GPX activity, by comparing the absorbance changes after addition of H_2O_2 in the assays. Activities were normalized to the added lysate volume and protein concentration.

4.4.5. Measurement of Myocardial Oxidative Stress

Malondialdehyde Assay. Myocardial malondialdehyde (MDA) levels were assayed using a commercially available colorimetric kit in accordance with the manufacturer's instructions (Abcam, ab233471). The total concentration of free MDA (μM/mg) was determined by reference to the MDA standard curve correcting for the sample lysate dilution as well as total amount of protein loaded[26, 190]. Each sample was measured in duplicate, with the average value reported.

Glutathione Recycling Assay. Total myocardial glutathione, including the reduced (GSH), and oxidized (GSSG) forms, and their redox ratio (GSH:GSSG) were quantitated by the enzymatic recycling method with minor modification[188, 385, 389]. Each sample was analyzed in triplicate, and the average value was finally adopted in our study.

Dihydroethidium Staining and Densitometry. In situ generation of reactive oxygen species (ROS) was determined by incubating the 5-10 um cryosections with dihydroethidium dye (DHE, D1168, Invitrogen), following the application of TrueBlack Lipofuscin Quencher (#23007, Biotium). The superoxide, as the redox indicator, was fluorescently visualized red within nucleus under Olympus IX81 fluorescence microscope. Quantitative measurements of DHE fluorescence intensity, corrected by the average pixel intensity from the background, were further carried out using MetaMorph software (Basic version, 7.7.0.0, Molecular Devices, *Inc*.)[26, 190, 314, 390, 391].

4.4.6. Subcellular Fractionation and Western Blot

Subcellular fractionations were carried out as previously described with modifications[191]. The purity of each fraction was further validated by using anti-rabbit TLR-4 (Santa Cruz, sc-10741; membrane marker), anti-rabbit Caspase-3 (Cell Signaling, 9662S; cytosolic marker) and anti-rabbit Histone H3 (Cell Signaling, 4499s; nuclear marker)[333]. Western blot was performed on flash snap-frozen human myocardium tissues as we previously published[191, 333]. The below primary antibodies were used: anti-rabbit TFR-1 (Cell Signaling, 13208s); anti-rabbit FPN (Novus, NBP1-21502); anti-rabbit FTN (Abcam, ab75973); anti-mouse DMT-1 (Abcam, ab55735), followed by incubation with HRP-conjugated secondary antibodies at 1/5000 dilution (Cell Signaling). The total protein loadings were visualized by MemCode™ reversible stain (24585, Thermo Scientific™) as a loading control. Fiji ImageJ software (NIH, Bethesda, MD, USA) was used for band intensity quantitation.

4.4.7. Histological Analysis and Confocal Microscopy

The 5μm thick sections of the formalin-fixed paraffin-embedded tissue were stained with picrosirius red (PSR) and Masson's trichrome stain for morphometric analyses as described previously[26, 188]. From each heart, n=2 sections were stained with n=20-25 random images analyzed from each section in a blinded manner. Cardiomyocyte cross-sectional area was evaluated as using fluorescence wheat-germ agglutinin staining previously published[26, 179, 191]. From each heart, n=2 sections (including one technical control) were examined, with n=20-25 random images captured from each section in a blinded manner. Within each image, n=25 cardiomyocytes were unbiasedly sampled from whole regions (four corners & center) into our analyses.

Non-specific autofluorescences (mainly lipofuscin) from the human OCT-embedded blocks were eliminated by applying TrueBlack® Lipofuscin Quencher (#23007, Biotium) to the cryosections, followed by standardized tissue fixation, deparaffinization, antigen retrieval and permeabilization. The sections were then incubated with primary antibodies overnight as per manufacturer instructions, followed by incubation with fluorochrome conjugated secondary

antibodies (Invitrogen, USA). Intracellular protein colocalizations were acquired under laser scanning confocal microscopy (Leica TCS SP5, Leica Microsystems), and quantitative analyses were performed using Fiji ImageJ software[191].

4.4.8. Transmission Electron Microscopy (TEM)

Fresh transmural myocardium from LV (<1 mm^3) were promptly fixed in 2% glutaraldehyde upon explantation. The post-fixative samples were immersed in solution of 2% uranyl acetate (UA) and 0.1M sodium acetate (pH 5.2) for high-contrast *en bloc* staining, followed by dehydration using graded ethanol and acetone solutions, and immediate infiltration with Spurr resin (Leica Electron Microscopy Sciences, Hatfield, PA, USA). Two resin blocks per sample were sectioned along the longitudinal axis of myofilaments to produce four non-consecutive ultrathin sections (70 μm), which were further post-stained with 4% UA and 4% lead citrate.

Four 100 μm^2 regions were randomly selected to obtain n=1 image at 2000X, n=4 images at 4000X, and n=6 images at 10000X resolutions per section for a total of 44 images per sample (H7650, Hitachi, Tokyo, Japan). We established a scoring system evaluating the presence and severity of intramitochondrial inclusions, mitochondrial cristae quality as well as sarcomeric integrity, in which a higher score signified a greater severity of dysfunction (**Table 4.1**). Blinded assessment of all images was randomly carried out in triplicate by two examiners, and a third adjudicator was involved should any discrepancies arise between the grading.

Table 4.1. Qualitative Scoring Criteria for Mitochondrial Ultrastructural Morphology and Architecture for Intra-mitochondrial Inclusion (A) and Cristae (B)

A.		**Percentage of Individual Mitochondrial Inclusion Scores**		
		% Mitochondria with score = 0	% Mitochondria with score = 1-2	% Mitochondria with score = 3
Overall Patient Score	Healthy	>75%	<5%	<5%
	Mild	<75%	<5%	<5%
	Moderate	<75%	>5%	<5%
	Severe	X	X	>5%

B.		**Percentage of Individual Mitochondrial Cristae Scores**		
		% Mitochondria with score = 0	% Mitochondria with score = 1-2	% Mitochondria with score = 3
Overall Patient Score	Healthy	>80%	<10%	<5%
	Mild	<80%	<10%	<5%
	Moderate	<80%	>10%	<5%
	Severe	X	X	>5%

Intramitochondrial inclusions score of 0 indicates no inclusions, and scores 1-3 represent the presence of mitochondrial inclusions with increasing severity. Patients with >5% mitochondria having a score of 3 are considered severe regardless of other factors. Mitochondria cristae quality score of 0 indicates healthy cristae, and scores 1-3 represent decreasing cristae quality. Patients with >5% mitochondria having a score of 3 are considered severe regardless of other factors.

4.4.9. Cardiac Magnetic Resonance Imaging (CMR)

Frozen myocardium from the middle of interventricular septum were adopted to evaluate the tissue iron content by CMR mappings. Based on LV iron level, n=10 and n=4 samples were retrospectively included in the NFC group and each HF subgroup, respectively. However, the subsequent sample preparation, image acquisition, and analytical processing were conducted in a double-blinded manner. Possible interferences from specimen dimension, environment temperature or surrounding buffer heterogeneity were eliminated by strictly following same sample preparation[392].

CMR experiments were performed on a 3T MRI scanner (MAGNETOM Prisma; Siemens Healthcare; Erlangen, Germany) with body coil excitation and a 2.5 cm surface coil for signal reception. Longitudinal relaxation time (T_1) images were acquired with a saturation-recovery gradient-echo pulse sequence with the following parameters: 10 slices (no gap), 1 mm slice thickness, 30 mm by 60 mm field of view, 128 phase-encoding and 256 readout points for 0.23 mm in-plane spatial resolution. Saturation-recovery images with a recovery time of TS = 1000 ms and full recovery were used to calculate T_1 in each pixel. Transverse relaxation time (T_2) images were acquired with a spin-echo sequence with identical spatial coverage and resolution as the T_1 acquisition, with echo-times of TE=11 ms in steps of 11 ms to 88 ms. T_2* images were acquired with a multi-echo gradient-echo sequence with identical spatial coverage and resolution as the T_1 and T_2 acquisitions. Averaged relaxation values (measured in msec) from all pixels within each tissue sample were automatically selected for analyses; all measurements were completed in duplicate.

4.4.10. Statistical Analysis

The normality of data distribution and homogeneity of variance were firstly assessed by Shapiro-Wilk test and Levene test, respectively. Continuous variables were presented as medians with interquartile ranges (median, Q1-Q3) for clinical parameters, or means ± standard deviations (mean ± SD) for experimental measurements. Categorical data were summarized as numbers with percentages (integer, %). One-way ANOVA (followed by Tukey post-hoc analysis), or

independent sample t-test was used to compare continuous variables between groups, while Mann-Whitney U test or Kruskal Wallis test was applied for non-parametric comparisons as appropriate. All categorical data were analyzed by Chi-squared test or Fisher's exact test where applicable. Continuous datasets were visualized by box plots with overlapping data points, or bar charts (upper line of the bar represents mean value) in a consistent manner. Pearson's correlation or Spearman rank correlation was used to evaluate the statistical association between variables of interest, including parametric and non-parametric variates, respectively. Multiple linear regression models were performed to estimate the relationship between two or more explanatory variables and the dependent variable, including the logistic regression algorithm for binary outcome prediction.

Briefly, multiple linear regression model was performed (**Table 4.2**) to explore the estimated coefficients of multiparametric cardiac magnetic resonance mappings (CMR, including T1, T2, and T2*) and HF etiology in predicting myocardial iron content. In this model, the myocardial iron level was the outcome variable, whereas the three CMR mapping sequences (measured in msec) and one etiological category (1: non-failing control; 2: heart failure) were the predictor variables. The "Enter" method (direct entry) was accepted for the variable selection in this linear regression model. Data visualization and graphical representation was performed on Origin for Windows, Version 2018b (OriginLab Corp., M.A., USA). IBM SPSS Statistics for Windows, Version 21 (IBM Corp., N.Y., USA) was used for data analysis and narrative interpretation. A two-tailed p value < 0.05 was considered statistically significant.

Table 4.2. Multiple Linear Regression Model: Estimated Coefficients of CMR Mappings

Multiple Linear Regression Model		Unstandardized Coefficients		Standardized Coefficients	t	Sig.	95% Confidence Interval for B	
		B	S.E.M.	Beta			Lower Bound	Upper Bound
CMR[a]	T1	-0.014	0.133	-0.019	-0.106	0.916	-0.287	0.258
	T2	1.700	1.824	0.349	0.932	0.359	-2.031	5.432
	T2*	-3.838	2.178	-0.607	-1.762	0.089	-8.291	0.616
	Etiology[b]	-39.330	22.306	-0.378	-1.763	0.088	-84.950	6.291
	(Constant)	322.849	151.773		2.127	0.042	12.438	633.260

Dependent Variable: Myocardial Iron Level. a: Measured in Millisecond (msec). b: Non-failing Control (label = 1); Heart failure (label = 2). A multiple linear regression was performed, where the myocardial iron level is the outcome variable and the three multiparametric cardiac magnetic resonance mapping (CMR, including T1, T2, and T2*) and one etiological category (1:non-failing control; 2: heart failure) are the predictor variable. The "Enter" method (direct entry) was adopted for the variable selection in the linear regression model. Results show that the overall model could significantly predicted the myocardial iron content by CMR sequences and HF etiology, with $F(4,29)=3.705$ ($p<0.05$, $r=0.581$; **Fig. 4.7D**). However, only T2* ($\beta=-0.607$, $p=0.089$) and etiology ($\beta=-0.378$, $p=0.088$) are marginally significant predicting variables, whereas T1/T2 does not significantly contribute to the prediction model. More specifically, the myocardial iron levels are predicted to be larger with lower T1 and/or T2* mappings and among healthy individuals. IBM SPSS Statistics for Windows, version 21 (IBM Corp., N.Y., USA) was used for data analysis and narrative interpretation.

4.5. Results

4.5.1. Prevalence of Myocardial Iron Deficiency and Its Association with Clinical Characteristics in Patients with End-Stage Heart Failure

We examined the chamber-specific myocardial iron levels in explanted human hearts which included a total of 46 non-failing donor hearts and 138 failing hearts with a primary etiology of DCM (n=71) or CAD (n=67) (**Table 4.3; Table 4.4**). The LV had higher myocardial iron content than the RV in both NFC [LV: 137.4 (109.2-165.9) versus RV: 95.1 (77.6-121.5) µg/g dry weight, $p<0.001$] and HF [LV: 121.4 (88.1-150.3) compared to RV: 96.40 (73.5-120.0) µg/g d.w., $p<0.001$] groups (**Fig. 4.2A**). Surprisingly, iron level decreased only in the LV of HF patients ($p=0.015$) with similar changes seen between the two etiological cohorts, while no difference was observed in the RV between NFC and HF groups ($p=0.648$) indicating MID is a major insult to the systemic ventricle (**Fig. 4.2A)**. Accordingly, we defined MID with *a priori* threshold < 86.1 µg/g d.w. in LV, based on its distinct distribution pattern between non-diseased and failing hearts (**Fig. 4.2B**). Our tissue-based approach clearly separated NFC from the HF cohort resulting in n=32 (23%) failing hearts classified as iron-deficient for the first time (**Fig. 4.2B**). Our analyses also revealed that MID is LV-specific and subsequent molecular investigations were all performed using LV samples.

Our NFC group consisted of 46 donors (male: 50%), with a median age of 47.0 years (28.0-56.5), heart weight of 350.0 grams (312.0-427.0), and LV ejection fraction (LVEF) of 60% (52.5-62.5%) in the absence of major comorbidities and cardiovascular diseases. The HF-MID had comparable demographics, comorbid and cardiovascular history, hemodynamic parameters and medical therapy as the HF patients with normal myocardial iron levels (HF-NID, **Table 4.3**). We found no correlations between myocardial iron content and hemoglobin (r=0.017, $p=0.84$), serum ferritin (r=0.028, $p=0.82$) and systemic iron levels (r=0.173, $p=0.23$) in the HF cohorts indicating that in the absence of distinct systemic iron deficiency (SID) and severe anemia, MID is a highly localized to the heart (**Fig. 4.3**). Importantly, HF-MID patients had remarkably higher NYHA class (II/III/IV, HF-MID: 0/15.6/84.4 vs. HF-NID: 7.5/34.9/57.5 %, $p=0.017$), and worsened myocardial remodeling and systolic function as reflected by greater lowering in LVEF [HF-MID: 17.1 (11.5-29.1) vs. HF-NID: 20.4 (15.0-31.3) %, $p=0.04$] and larger increase in LV internal dimensions at end-systole [LVIDs, HF-MID: 58.0 (47.0-67.0) vs. HF-NID: 50.0 (38.3-60.8) mm, $p=0.03$] and

end-diastole [LVIDd, HF-MID: 67.0 (51.5-71.5) vs. HF-NID: 58.0 (50.3-67.0) mm, *p*=0.03] (**Fig. 4.2C**).

Table 4.3. Baseline Clinical Characteristics of Patients with Normal Myocardial Iron Levels (NID) versus Myocardial Iron Deficiency (MID)

	HF-NID (N=106)	**HF-MID (N=32)**	**p-value**
Clinical			
Age (years)	54.5 (47.0-61.75)	54.5 (41.8-60.3)	0.904
Sex, Male	92 (87)	24 (75)	0.110
Etiology, DCM	53 (50)	18 (56)	0.535
BMI (kg/m^2)	26.3 (24.2-30.2)	27.7 (24.6-30.6)	0.631
Physical assessment			
SBP (mmHg)	100.0 (88.0-120.0)	100.0 (90.0-115.0)	0.865
DBP (mmHg)	64.0 (56.0-72.0)	63.0 (51.5-73.0)	0.535
Electrocardiography			
QRS Duration (ms)	122.0 (92.0-151.0)	136.0 (104.8-164.0)	0.180
AF	19 (18)	8 (24)	0.377
LBBB	12 (11)	3 (10)	0.757
Echocardiography			
LA Volume Index (ml/m^2)	43.5 (32.6-61.9)	47.3 (30.0-57.8)	0.944
LVPWT (mm)	8.9 (8.0-10.0)	8.5 (8.2-10.0)	0.952
RVSP (mmHg)	35.8 (26.6-47.9)	34.1 (28.2-37.2)	0.298
TAPSE (mm)	1.4 (1.0-1.8)	1.4 (1.1-1.8)	0.952
RVd Basal (cm)	4.2 (3.6-4.9)	4.2 (3.9-4.8)	0.484
Blood Parameters			
Ferritin (µg/L)	142.5 (61.3-309.0)	91.0 (47.0-151.0)	0.103
Serum Iron (µmol/L)	10.0 (8.5-13.0)	10.5 (6.3-14.0)	0.667

TIBC (μmol/L)	54.0 (47.0-63.0)	61.0 (53.3-72.0)	0.093
sTF (%)	19.5 (13.8-27.3)	17.0 (9.3-19.8)	0.150
Hemoglobin (g/L)	128.5 (111.0-140.0)	125.5 (108.5-135.3)	0.424
MCV (fL)	90.0 (86.0-95.0)	89.5 (86.8-92.3)	0.757
MCHC (g/L)	336.0 (330.0-342.0)	332.5 (322.5-338.5)	0.067
eGFR (ml/min/1.73m^2)	55.0 (41.0-70.0)	58.5 (47.0-76.8)	0.384
Devices			
Pacemaker	65 (61)	21 (66)	0.660
ICD/BiV-ICD	86 (81)	27 (84)	0.676
VAD	67 (63)	20 (63)	0.942
Medications			
ACEi/ARB	81 (76)	28 (88)	0.177

DCM=dilated cardiomyopathy; BMI=body mass index; SBP=systolic blood pressure; DBP=diastolic blood pressure; NYHA=New York Heart Association Functional Classification; AF=atrial fibrillation; LBBB=left bundle branch block; LVPWT=left ventricular posterior wall thickness; RVSP=right ventricular systolic pressure; TAPSE=tricuspid annular plane systolic excursion; RVd Basal=basal right ventricular diameter; TIBC=total iron binding capacity; sTF=saturation of transferrin; MCV=mean corpuscular volume; MCHC=mean corpuscular hemoglobin concentration; eGFR=estimated glomerular filtration rate based on MDRD equation; BiV-ICD=bi-ventricular implantable cardioverter-defibrillator; ACEi = angiotensin converting enzyme inhibitors; ARB=angiotensin receptor blockers. Categorical variables reported by count with percentage in parenthesis: sex, etiology, diagnosis of AF and LBBB, device implantation, and medications. Continuous variables reported by median with interquartile range in parenthesis: age, BMI, physical assessment, QRS duration, echocardiography, and blood parameters.

Table 4.4. Basic Clinical Profile of Patients with End-stage Heart Failure Secondary to Dilated Cardiomyopathy (DCM) and Coronary Artery Disease (CAD)

	End-stage HF (N=138)	**DCM (N=71)**	**CAD (N=67)**	**p-value**
Demographic				
Age (years)	54.5 (47.0-61.0)	50.0 (40.0-58.5)	57.0 (48.5-63.0)	<0.001**
Sex, Male	116 (84)	59 (83)	57 (85)	0.751
Heart Weight (gram)	465.0 (374.5-563.0)	476.0 (374.5-546.0)	443.0 (375.5-564.8)	0.928
Comorbidities				
CVD	21 (15)	12 (17)	9 (13)	0.571
PVD	12 (9)	4 (6)	8 (12)	0.189
COPD/Asthma	46 (33)	22 (31)	24 (36)	0.547
DM2	36 (26)	11 (15)	25 (37)	0.004**
Dyslipidemia	41 (30)	12 (17)	29 (43)	<0.001**
Thyroid Disease	22 (16)	14 (20)	8 (12)	0.212
Kidney Disease	74 (54)	39 (55)	35 (52)	0.751
Liver Disease	24 (17)	13 (18)	11 (16)	0.769
Obesity	88 (64)	40 (56)	48 (72)	0.061
PAH	37 (27)	22 (31)	15 (22)	0.254
Hypertension	33 (24)	12 (17)	21 (31)	0.047*

Electrocardiography				
PR Interval (ms)	171.0 (146.0-202.0)	172.0 (148.5-199.0)	168.0 (144.0-205.0)	0.555
QRS Duration (ms)	124.0 (93.0-154.0)	134.0 (102.0-162.0)	112.0 (88.5-148.0)	0.049*
AF	26 (19)	16 (23)	10 (15)	0.253
IVCD	35 (25)	22 (31)	13 (19)	0.118
LBBB	14 (10)	10 (14)	4 (6)	0.115
RBBB	23 (17)	8 (11)	15 (22)	0.080
Blood Parameters				
Ferritin (μg/L)	133.0 (56.0-276.0)	135.0 (62.5-276.0)	110.4 (53.0-261.8)	0.484
Serum Iron (μmol/L)	10.0 (7.0-13.5)	10.0 (6.0-14.0)	11.0 (8.6-12.0)	0.764
TIBC (μmol/L)	54.0 (48.0-67.0)	57.0 (50.0-65.0)	54.0 (47.3-71.5)	0.795
sTF (%)	19.0 (11.3-26.5)	16.0 (11.0-25.0)	20.0 (15.0-27.0)	0.401
Hemoglobin (g/L)	127.0 (109.5-139.0)	133.0 (114.0-142.5)	119.0 (102.0-130.5)	0.001**
MCV (fL)	90.0 (86.0-94.0)	90.0 (86.0-95.0)	90.0 (86.0-93.0)	0.624
MCHC (g/L)	336.0 (328.3-342.0)	336.0 (327.5-341.5)	335.0 (330.0-342.5)	0.465
BNP (pg/ml)	989.0 (485.0-1749.0)	942.0 (494.0-1731.0)	994.5 (476.5-3084.5)	0.624
NT-proBNP (pg/ml)	3671.0	3785.0	2800.0	0.208

	(2677.0-7777.0)	(2889.5-8087.0)	(1037.8-5100.8)	
C-reactive Protein (mg/L)	6.5 (3.0-31.8)	7.2 (3.6-42.3)	6.1 (2.6-19.7)	0.472
Creatinine (μmol/L)	121.0 (95.3-150.0)	120.0 (96.5-147.0)	121.0 (93.5-152.5)	0.920
eGFR (ml/min/1.73m^2)	55.0 (41.2-73.5)	55.0 (44.0-75.0)	56.0 (40.0-72.0)	0.529
Medications				
ACEi/ARB	109 (79)	67 (94)	42 (63)	<0.001**
Beta Blocker	112 (81)	61 (86)	51 (76)	0.141
Diuretics	110 (80)	57 (80)	53 (79)	0.864
MRA	80 (58)	48 (68)	32 (48)	0.018*
Digoxin	31 (22)	20 (28)	11 (16)	0.098
Antiplatelet	81 (59)	35 (49)	46 (69)	0.021*
Anticoagulation	97 (70)	54 (76)	43 (64)	0.127
Statin	76 (55)	28 (39)	48 (72)	<0.001**
Antiarrhythmic	61 (44)	37 (52)	24 (36)	0.054

BMI=body mass index; BSA=body surface area; HR=heart rate; SBP=systolic blood pressure; DBP=diastolic blood pressure; NYHA=New York Heart Association Functional Classification; CVD=cerebrovascular diseases; PVD=peripheral vascular diseases; COPD=chronic obstructive pulmonary diseases; DM2=type 2 diabetes mellitus; PAH=pulmonary artery hypertension; AF=atrial fibrillation; IVCD=intraventricular conduction delay; LBBB=left bundle branch block; RBBB= right bundle branch block; TIBC=total iron binding capacity; sTF=saturation of transferrin; MCV=mean corpuscular volume; MCHC=mean corpuscular hemoglobin concentration; BNP=brain natriuretic peptide; NT-proBNP=N-terminal pro b-type natriuretic peptide; eGFR=estimated glomerular filtration rate based on MDRD equation; ACEi=angiotensin converting enzyme inhibitors; ARB=angiotensin receptor blockers; MRA=mineralocorticoid receptor antagonists. Data are presented as means ± standard deviations, medians (with lower and upper quartiles), or numbers (with percentages), where appropriate. Chi-square test, one-

way ANOVA (followed by Tukey post hoc analysis) or Mann-Whitney U test were used as appropriate to compare the variables between groups. A two-tailed p value < 0.05 was considered statistically significant, as indicated by an asterisk. *$p<0.05$; **$p<0.01$. Categorical variables reported by count with percentage in parenthesis: sex, comorbidities, diagnosis of AF, IVCD, LBBB and RBBB, and medications. Continuous variables reported by median with interquartile range in parenthesis: age, heart weight, PR interval and QRS duration, and blood parameters.

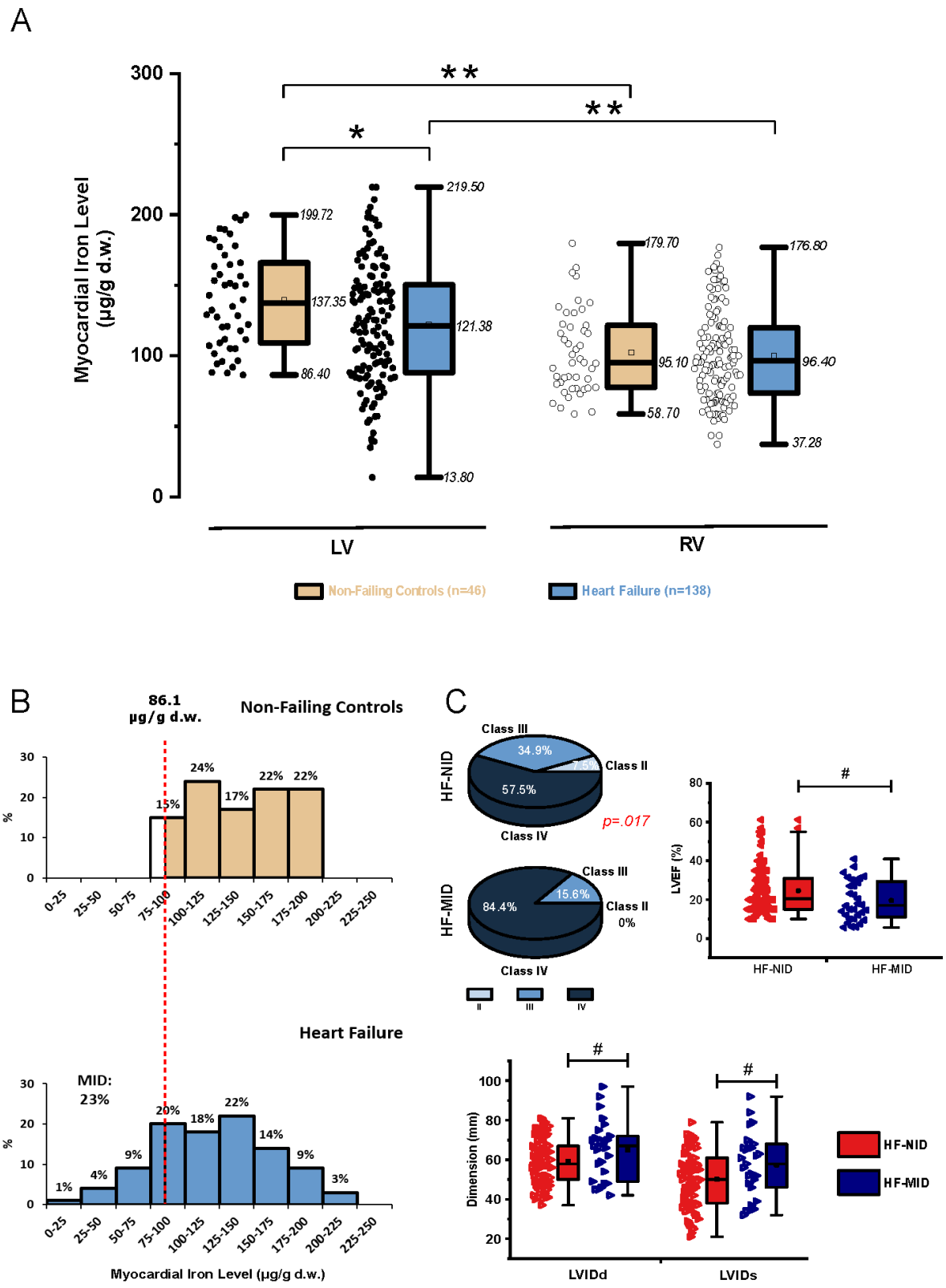
A
Myocardial Iron Level (µg/g d.w.)
300
200
100
0
**
**
*
199.72
137.35
86.40
219.50
121.38
13.80
179.70
95.10
58.70
176.80
96.40
37.28
LV
RV
Non-Failing Controls (n=46)
Heart Failure (n=138)
B
86.1 µg/g d.w.
Non-Failing Controls
%
30
20
10
0
15%
24%
17%
22%
22%
0-25
25-50
50-75
75-100
100-125
125-150
150-175
175-200
200-225
225-250
Heart Failure
MID: 23%
1%
4%
9%
20%
18%
22%
14%
9%
3%
Myocardial Iron Level (µg/g d.w.)
C
HF-NID
Class III
34.9%
Class II
57.5%
Class IV
p=.017
HF-MID
Class III
15.6%
84.4%
Class II
0%
Class IV
II
III
IV
LVEF (%)
80
60
40
20
0
#
HF-NID
HF-MID
Dimension (mm)
100
80
60
40
20
#
#
LVIDd
LVIDs
HF-NID
HF-MID

Figure 4.2. Myocardial iron deficiency in failing explanted human hearts with chamber-specific features of iron levels. A. Myocardial iron levels in the left (LV) and right ventricles (RV) in non-failing control (NFC, n=46) and explanted failing hearts (HF, n=138). B. Distribution of myocardial iron levels and the definition of myocardial iron deficiency (MID) with a cutoff value of 86.1 μg/g dry weight separating out 23% of HF patients. C. NYHA classification, LVEF, LVIDs and LVIDd in HF-NID (n=106) versus HF-MID (n=32). NYHA: New York Heart Association; LVEF: LV ejection fraction; LVIDd: LV end-diastolic internal diameter; LVIDs: LV end-systolic internal diameter; HF-NID: HF patients without myocardial iron deficiency; HF-MID: HF patients with myocardial iron deficiency. *$p<0.05$, **$p<0.01$ compared with NFC; $^{\#}p<0.05$, $^{\#\#}p<0.01$ compared with HF-NID.

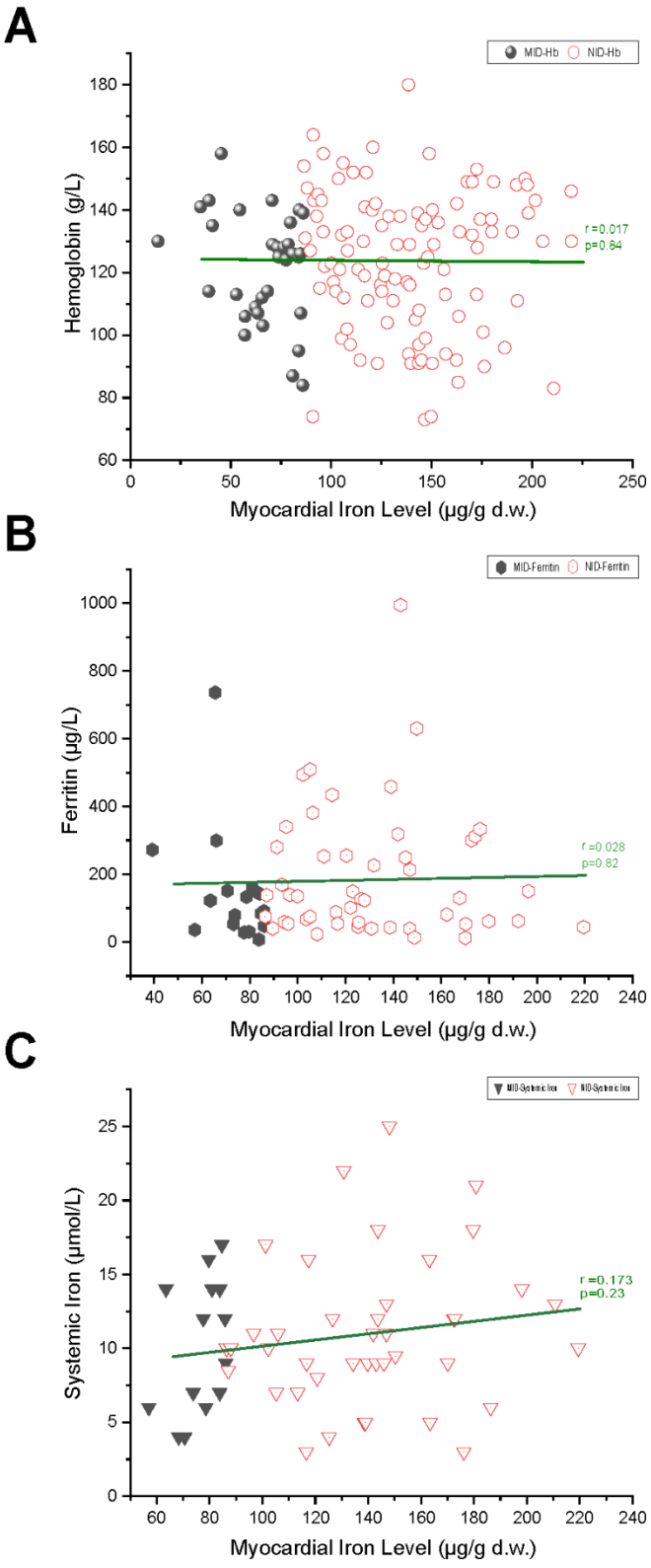
A
MID-Hb
NID-Hb
Hemoglobin (g/L)
Myocardial Iron Level (µg/g d.w.)
r=0.017
p=0.84
B
MID-Ferritin
NID-Ferritin
Ferritin (µg/L)
Myocardial Iron Level (µg/g d.w.)
r=0.028
p=0.82
C
MID-Systemic Iron
NID-Systemic Iron
Systemic Iron (µmol/L)
Myocardial Iron Level (µg/g d.w.)
r=0.173
p=0.23

Figure 4.3. Lack of correlation between myocardial iron levels and systemic hemoglobin (A), ferritin (B), and serum iron (C) levels in HF cohorts, based on linear regression analysis. MID: myocardial iron deficiency, n=32; NID: no myocardial iron deficiency, n=106.

4.5.2. Myocardial Iron Deficiency is Linked to Adverse Myocardial Remodeling and Mitochondrial Dysfunction

We next examined the cellular and subcellular characteristics of the explanted failing hearts (LV) to correlate the effects of MID on adverse myocardial remodeling. Increased myocardial hypertrophy and interstitial fibrosis are prominent features of heart diseases[393, 394]. Cardiomyocyte size assessed by WGA staining displayed greater increase in the failed hearts regardless of cardiac iron status compared to NFC (NFC: 239.6±46.4 vs. HF: 670.0±248.6 μm^2, $p<0.001$), which was consistent with our gravimetric analysis of the explanted hearts (NFC: 363.0±74.3 vs. HF: 472.4±130.0 gram, $p<0.001$) (**Fig. 4.4A-C; Fig. 4.5A**). Meanwhile, PSR staining captured strikingly higher fibrosis in the failing hearts which was further exacerbated in the HF-MID group (**Fig. 4.4D-E; Fig. 4.5B**), and it was confirmed by classic Masson's trichrome staining (**Fig. 4.5C**). Next, we developed a comprehensive scoring system evaluating cardiomyocyte ultrastructure, presence and severity of intramitochondrial inclusions and mitochondrial cristae quality **(Table 4.1)**. Myofilament disarray and severe lysis were identified in the HF-MID group in both DCM and CAD samples, in comparison with NFC (**Fig. 4.4F; Fig. 4.5D-E**). Qualitative assessment of the mitochondria using TEM showed severe distortion of cristae and increased inclusion bodies in the HF-MID group with occasional mitochondrial lysis (**Fig. 4.6**). These features demonstrated exacerbation of the adverse remodeling in the explanted failing human hearts with MID.

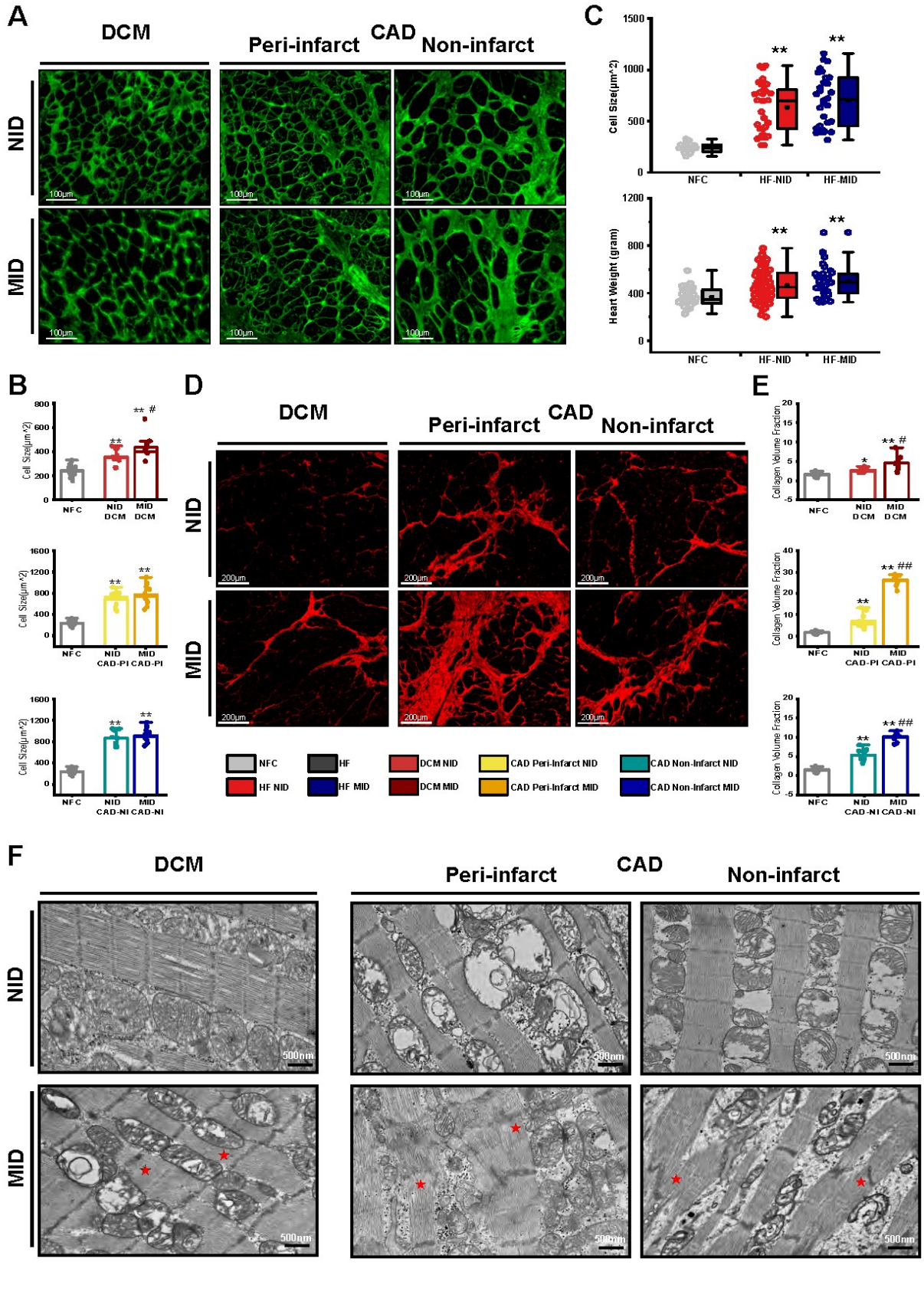
A
DCM
CAD
Peri-infarct
Non-infarct
NID
MID
100μm
C
Cell Size(μm^2)
Heart Weight (gram)
NFC
HF-NID
HF-MID
B
D
E
Collagen Volume Fraction
NID DCM
MID DCM
NID CAD-PI
MID CAD-PI
NID CAD-NI
MID CAD-NI
200μm
NFC
HF
HF NID
HF MID
DCM NID
DCM MID
CAD Peri-Infarct NID
CAD Peri-Infarct MID
CAD Non-Infarct NID
CAD Non-Infarct MID
F
500nm

Figure 4.4. Adverse myocardial remodeling in failing hearts is exacerbated by myocardial iron deficiency. A-C Representative wheat germ agglutinin staining (scale bar = 100 μm) (A), cardiomyocyte cross-sectional area across diseased subgroups (n=20 for NFC, n=10 for each HF subgroup) (B), and heart weight (n=46 for NFC; n=106 for HF-NID and n=32 HF-MID groups) (C) showing greater hypertrophy in the explanted failed hearts compared with non-failing controls (NFC). D-E Representative picrosirius red staining (D) and relative quantification (E) of myocardial fibrillar content exhibiting significantly higher fibrosis in the iron-deficient failing hearts. n=20 for NFC, n=10 for each HF subgroup. F. Representative TEM images illustrating myofilament disarray, derangement and lysis in the HF subgroups identified from both DCM and CAD samples (scale bar = 500 nm; asterisks represent areas with severe alterations). NFC: non-failing controls; DCM: dilated cardiomyopathy; CAD-PI: peri-infarcted from coronary artery disease; CAD-NI: non-infarcted from coronary artery disease; NID: no myocardial iron deficiency; MID: myocardial iron deficiency; TEM: transmission electron microscopy. *$p<0.05$, **$p<0.01$ compared with NFC; $^{\#}p<0.05$, $^{\#\#}p<0.01$ compared with HF-NID.

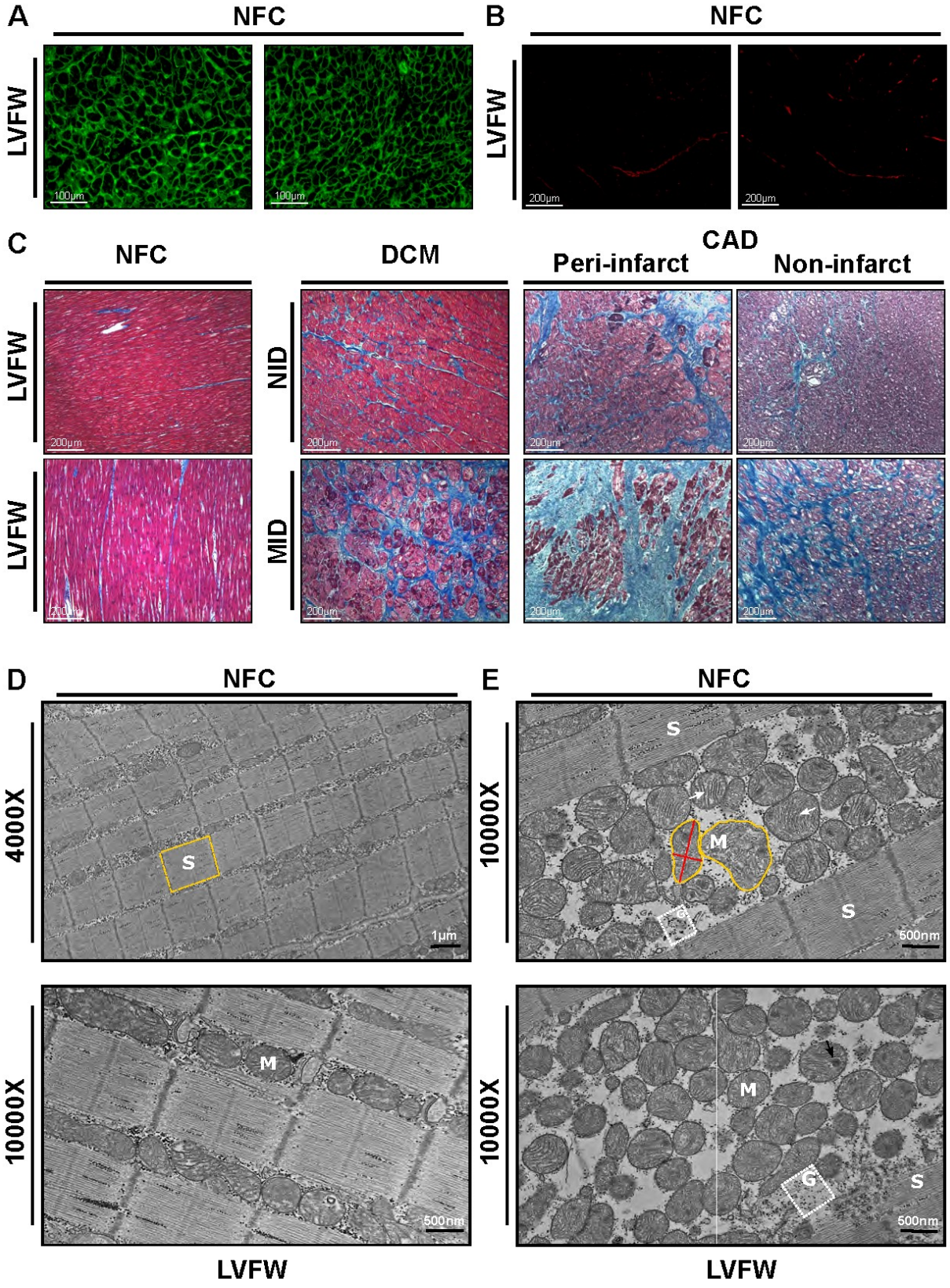
A
NFC
LVFW
100μm
100μm
B
NFC
LVFW
200μm
200μm
C
NFC
DCM
CAD
Peri-infarct
Non-infarct
LVFW
NID
LVFW
MID
200μm
D
NFC
4000X
S
1μm
10000X
M
500nm
LVFW
E
NFC
10000X
S
M
G
S
500nm
10000X
M
G
S
500nm
LVFW

Figure 4.5. Representative histological staining and transmission electron microscopy (TEM) on normal myocardium. A-B. Representative wheat germ agglutinin staining (A, scale bar = 100 μm) and picrosirius red staining (B, scale bar = 200 μm) of normal myocardium (NFC). C. Masson's trichrome staining (scale bar = 200 μm) confirmed exacerbated interstitial fibrosis in the HF subgroups with MID. D-E. TEM images captured from NFC at different magnifications illustrating pristine and well-aligned sarcomeric and mitochondrial ultrastructure; scale bar = 1 μm (4000X) or 500 nm (10000X). S: sarcomere; M: mitochondrion; G: cytoplasmic granules; DCM: dilated cardiomyopathy; CAD: coronary artery disease; LVFW: left ventricle free wall.

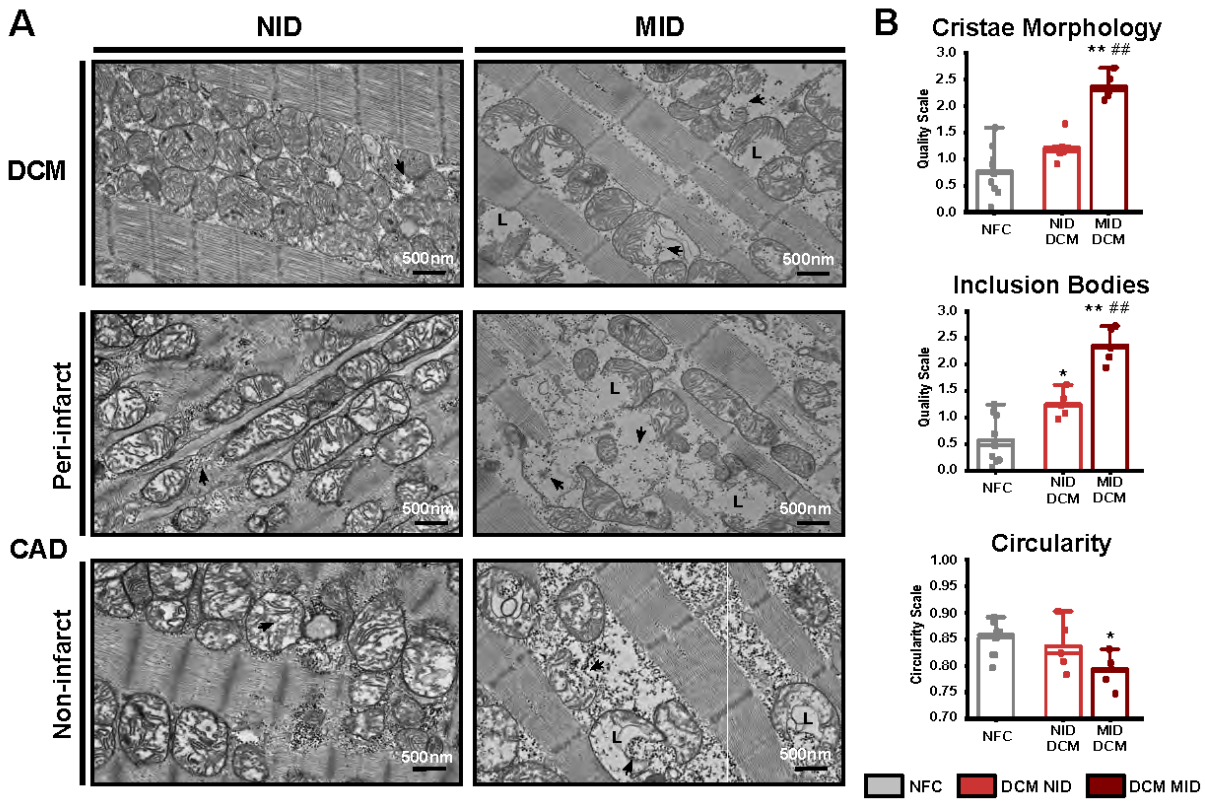

Figure 4.6. Mitochondrial morphological alterations worsened by iron deficiency in failing explanted hearts. Representative TEM images illustrating worsened intra-mitochondrial ultrastructural derangements in iron-deficient failing hearts captured from samples with both DCM and CAD (A) with qualitative quantification shown from the DCM subgroups (B) demonstrating predominant changes in cristae structures and increased presence of inclusion bodies in the MID subgroup with occasional mitochondrial lysis. n=10 for NFC; n=5 each for DCM-NID and DCM-MID groups. Scale bar = 500 nm. Mito: mitochondria; DCM: dilated cardiomyopathy; CAD-PI: peri-infarcted from coronary artery disease; CAD-NI: non-infarcted from coronary artery disease; NID: no myocardial iron deficiency; MID: myocardial iron deficiency; TEM: transmission electron microscopy. Arrows indicate inclusion bodies. *p<0.05, **p<0.01 compared with NFC; $^{\#}$p<0.05, $^{\#\#}$p<0.01 compared with HF-NID.

A central role of iron relates to the superoxide dismutase (SOD) family which provides a key defense against superoxide radicals (O_2^-) produced in the mitochondria as a byproduct of the respiratory chain activity (**Fig. 4.7A**). We assessed total SOD and mitochondria-specific (SOD2) enzymatic activities. While the enzymatic activities of total (NFC: 127.4±22.1 vs. HF: 131.8±71.2 unit/mg protein/min, *p=0.786*) and mitochondrial (NFC: 69.9±16.8 vs. HF: 72.5±50.8 unit/mg protein/min, *p=0.822*) isoforms were comparable between the two groups, we further identified a marked suppression of their ROS-scavenging capacities in the HF-MID group (**Fig. 4.7B**), with concordant changes seen across all etiological subgroups (**Fig. 4.7C-D**). In contrast, functional activities of two downstream antioxidant enzymes, catalase (CAT) and glutathione peroxidase-1 (GPX1), were not affected by myocardial iron levels (**Fig. 4.8A-B**). Overall, myocardial reduced glutathione (GSH) levels and GSH to oxidized glutathione (GSSG) ratio were further decreased in iron-deficient failing hearts (**Fig. 4.7E-F**) likely due to the loss of SOD-related antioxidant protections[26, 388]. While markedly elevated oxidative stress within failing myocardium was delineated by DHE staining, the corresponding densitometric analyses confirmed higher level of superoxide associated with myocardial iron insufficiency across all subgroups (**Fig. 4.7G-I**). Additionally, we observed aggravated lipid peroxidation profiles specifically in iron-deficient failing hearts, consistent with increased oxidative damage in these hearts (**Fig. 4.7J-K**).

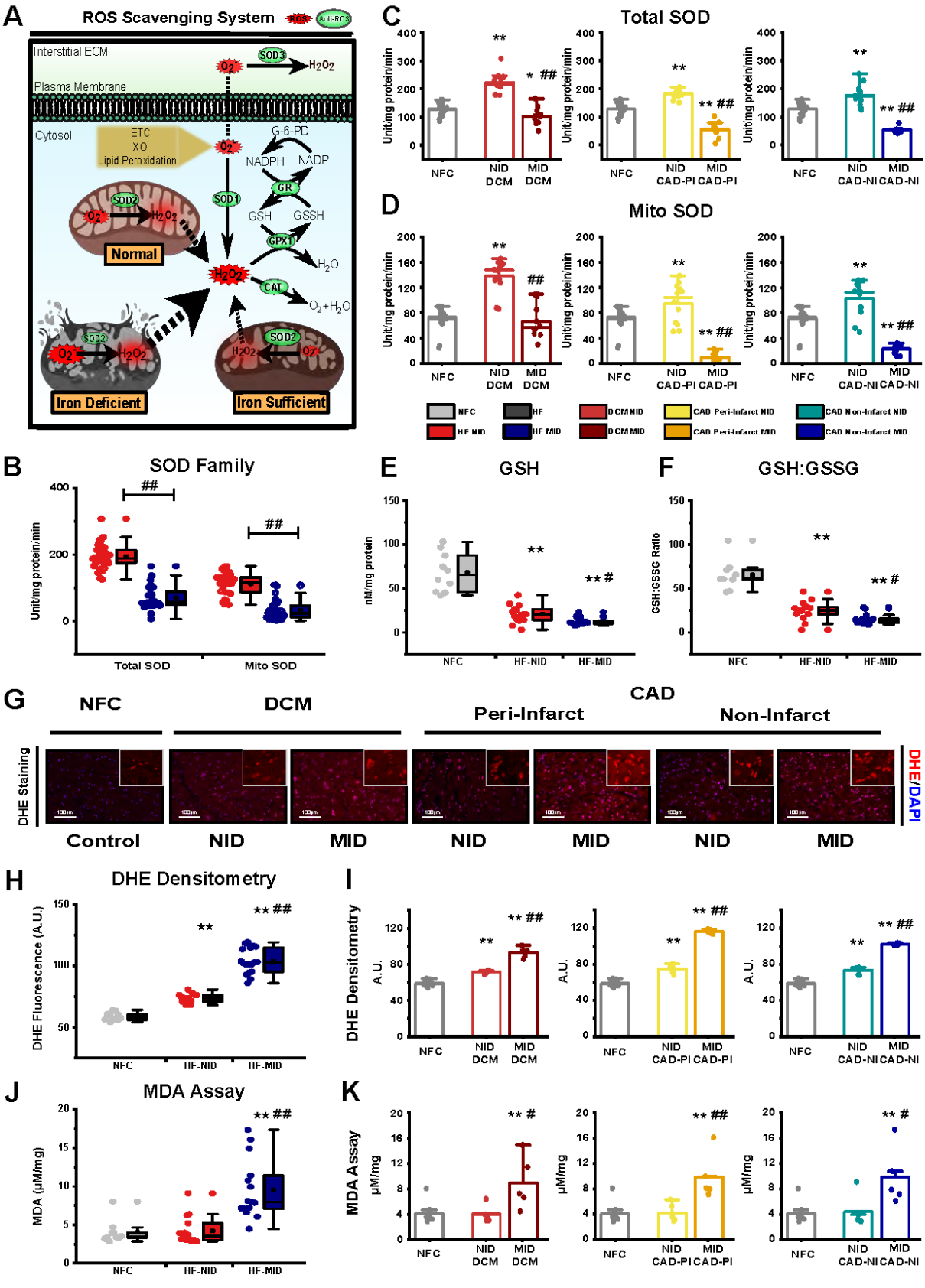
A
ROS Scavenging System
ROS
Anti-ROS
Interstitial ECM
Plasma Membrane
Cytosol
ETC
XO
Lipid Peroxidation
SOD3
SOD2
SOD1
G-6-PD
NADPH
NADP
GR
GSH
GSSH
GPX1
CAT
Normal
Iron Deficient
Iron Sufficient
B
SOD Family
Unit/mg protein/min
Total SOD
Mito SOD
C
Total SOD
D
Mito SOD
Unit/mg protein/min
NFC
NID DCM
MID DCM
NID CAD-PI
MID CAD-PI
NID CAD-NI
MID CAD-NI
NFC
HF
DCM NID
DCM MID
CAD Peri-Infarct NID
CAD Peri-Infarct MID
CAD Non-Infarct NID
CAD Non-Infarct MID
HF NID
HF MID
E
GSH
nM/mg protein
HF-NID
HF-MID
F
GSH:GSSG
GSH:GSSG Ratio
G
NFC
DCM
CAD
Peri-Infarct
Non-Infarct
DHE Staining
DHE/DAPI
Control
NID
MID
H
DHE Densitometry
DHE Fluorescence (A.U.)
I
DHE Densitometry
A.U.
J
MDA Assay
MDA (μM/mg)
K
MDA Assay
μM/mg

Figure 4.7. Greater oxidative stress in iron deficient failing explanted hearts. A. Schematic of the mitochondrial function and role of iron in enzymes involved in oxidative stress. B-D Superoxide dismutase (SOD) activity assays showing overall reduced myocardial antioxidant capacity based on total (B, C) and mitochondrial (B, D) SOD activities. n=20 for NFC; n=12 for each HF subgroup with n=36 for HF-MID and HF-NID, respectively. E-F Reduced glutathione (GSH, E) and reduced/oxidized glutathione (GSH/GSSG, F) ratio in HF samples further exacerbated in the MID group. n=10 NFC; n=18 each for HF-NID and HF-MID groups. G-I Representative dihydroethidium-stained images (G) and corresponding densitometries (H, I) delineating the markedly elevated oxidative stress (reflected as the total superoxide levels) in the failing human hearts, which was further inflamed by myocardial iron insufficiency. n=12 for NFC; n=6 for each HF subgroup with n=18 for HF-MID and HF-NID, respectively. Scale bar = 100 μm. J-K Quantitative colorimetry of the total free malondialdehyde levels highlighting the aggravated lipid peroxidation in iron-deficient failing myocardium (J), which could consistently be alleviated by restoring iron levels in HF patients with DCM or CAD (K). n=10 for NFC; n=5 for each HF subgroup with n=15 for either HF-MID or HF-NID. DCM: dilated cardiomyopathy; CAD-PI: peri-infarcted from coronary artery disease; CAD-NI: non-infarcted from coronary artery disease; NID: no myocardial iron deficiency; MID: myocardial iron deficiency. *$p<0.05$, **$p<0.01$ compared with NFC; $^{\#}p<0.05$, $^{\#\#}p<0.01$ compared with HF-NID.

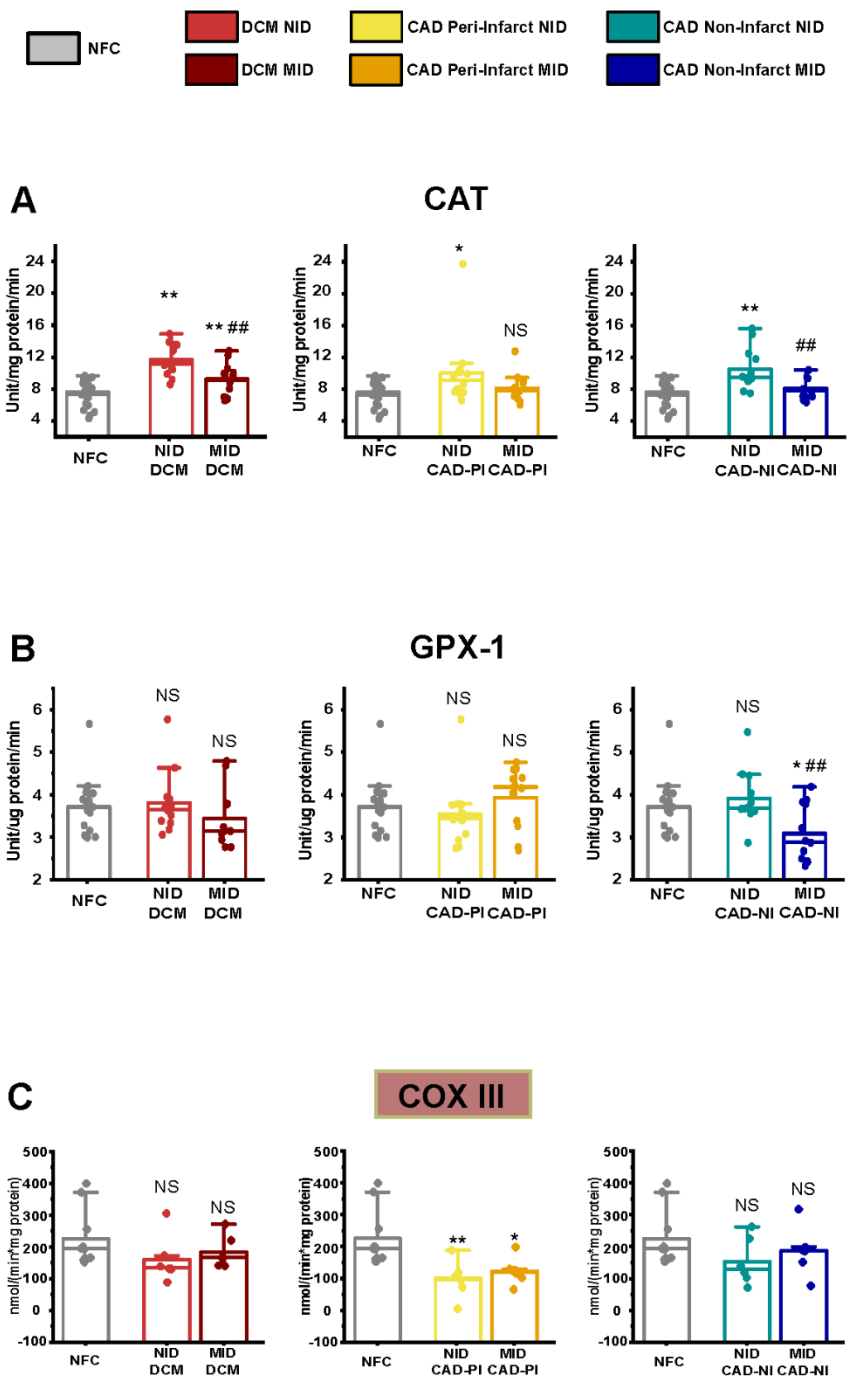

Figure 4.8. Enzymatic activities of antioxidant enzymes including catalase (CAT, A) and glutathione peroxidase (GPX-1, B) and election transport chain complex III (COX III, C) in HF subgroups in comparison with non-failing controls (NFC). A-B. Enzymatic activities of antioxidant enzymes including

catalase (A), glutathione peroxidase (GPX-1, B) in HF subgroups in comparison with non-failing controls (NFC). n=20 for NFC; n=12 for each HF subgroup. C. Enzymatic activity of election transport chain complex III (COX III) in HF subgroups compared NFC. n=10 for NFC; n=6 for each HF subgroup. DCM: dilated cardiomyopathy; CAD-PI: peri-infarcted from coronary artery disease; CAD-NI: noninfarcted from coronary artery disease; NID: no myocardial iron deficiency; MID: myocardial iron deficiency.

Iron is a component of iron-sulfur (Fe-S) clusters in the electron transport chain (ETC) pathways, which in combination with increased oxidative stress and ultrastructural abnormalities, implicates dysfunctional respiratory and metabolic activities in the mitochondria (**Fig. 4.9A**). Complex-specific activity assays showed a selective loss of complex I, II, IV (**Fig. 4.9B-C**) and citrate synthase (CS, **Fig. 4.9D-E**) activities in HF-MID with no decline in complex III functional activity (**Fig. 4.8C**). Moreover, the enzyme activities of ETC complex I (r=0.54, $p<0.001$), II (r=0.41, $p=0.012$) and IV (r=0.47, $p=0.004$) and CS (r=0.59, $p<0.001$) within the citric acid cycle correlated positively with myocardial iron levels in failing hearts, providing further evidence for a direct relationship between myocardial iron status and mitochondrial enzyme activities (**Fig. 4.9F**). These results demonstrated that lowered myocardial iron in human hearts was closely associated with unfavorable myocardium remodeling, and could further exacerbate oxidative stress and deplete respiratory chain activity in the setting of advanced HF.

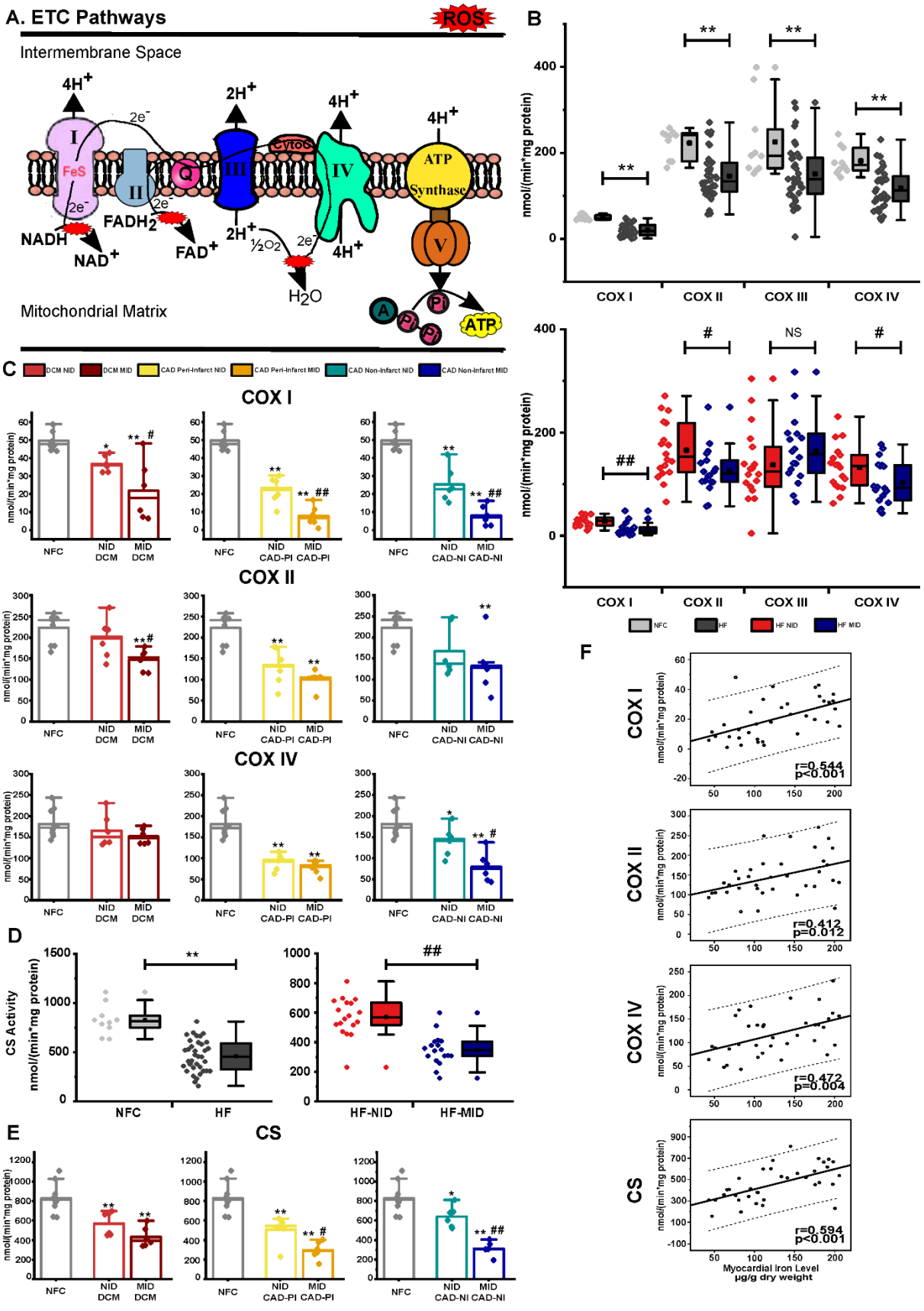
A. ETC Pathways
ROS
Intermembrane Space
Mitochondrial Matrix
B
COX I
COX II
COX III
COX IV
nmol/(min*mg protein)
NFC
HF
HF NID
HF MID
C
DCM NID
DCM MID
CAD Peri-Infarct NID
CAD Peri-Infarct MID
CAD Non-Infarct NID
CAD Non-Infarct MID
NID DCM
MID DCM
NID CAD-PI
MID CAD-PI
NID CAD-NI
MID CAD-NI
D
CS Activity
HF-NID
HF-MID
E
CS
F
r=0.544 p<0.001
r=0.412 p=0.012
r=0.472 p=0.004
r=0.594 p<0.001
Myocardial Iron Level µg/g dry weight

Figure 4.9. Assessment of electron transport chain pathway and the impact of myocardial iron deficiency. A. Schematic of the electron transport chain (ETC) for ATP production and its role in the generation of reactive oxygen species (ROS). B-C Reduction in enzymatic activities of complex I, II, III, and IV in HF samples (top panel) with greater functional decrease seen in complex I, II and IV in HF-MID (bottom panel) (B), which were further stratified based on etiologies (C). A greater reduction in complex I and II activities were observed in DCM and CAD samples with MID, while reduced complex IV activity was restricted to iron-deficient samples with CAD. n=10 for NFC, n=36 for HF; n=6 for each HF subgroup with n=18 for HF-MID and HF-NID, respectively. D-E Decreased citrate synthase (CS) activity in HF samples (left panel) compared to NFC, and it was exacerbated in HF samples with MID (right panel) (D), which was primarily driven by lowered CS activity in the iron-depleted peri-infarct and non-infarct regions from CAD (E). n=10 for NFC, n=36 for HF; n=6 for each HF subgroup with n=18 for HF-MID and HF-NID, respectively. F. Linear regression analyses showing the strong dependence of complex I, II, IV, and CS enzyme activities on myocardial iron levels within HF cohort. n=36 for each enzyme, and dotted lines represent 95% confidence interval. COX I-IV: complexes I-IV; DCM: dilated cardiomyopathy; CAD-PI: peri-infarcted from coronary artery disease; CAD-NI: non-infarcted from coronary artery disease; NID: no myocardial iron deficiency; MID: myocardial iron deficiency. *$p<0.05$, **$p<0.01$ compared with NFC; $^{\#}p<0.05$, $^{\#\#}p<0.01$ compared with HF-NID.

4.5.3. Role of Iron Trafficking System in Myocardial Iron Deficiency

Myocardial iron homeostasis is orchestrated by a tightly controlled regulatory system involving transcriptional control of the iron regulatory protein (IRP-1/-2) axis and corresponding changes in key iron transporters, namely transferrin receptor-1 (TFR-1), divalent metal transportort-1 (DMT-1) and ferroportin (FPN) (**Fig. 4.10A**)[47, 382]. We showed that total levels of TFR-1 and DMT-1 were reduced in HF-MID compared to iron-sufficient failing hearts by 54.3% and 31.4%, respectively, while the overall level of FPN remained unchanged between two groups (**Fig. 4.10B; Fig. 4.11**). Next, we investigated the intracellular translocation of iron transporters between cytosolic and plasma membrane compartments respectively (**Fig. 4.10C-K**), following our validated subcellular fractionation protocol (**Fig. 4.12A-B**). Likewise, our immunoblotting analysis of major iron importers demonstrated that HF-MID had significantly reduced membrane and cytosolic levels of both TFR-1 (**Fig. 4.12C, 4.13**) and DMT-1 (**Fig. 4.12D, 4.14**) when compared to their iron-sufficient counterparts. Interestingly, there was relatively increased

expression of FPN on sarcolemma without noticeable change seen in the cytosolic fraction (**Fig. 4.12E, 4.15**) of iron-deficient failing myocardium. The subcellular distribution and shift of iron transporters was further examined across all HF subgroups (**Fig. 4.10C-K**) and similar findings of TFR-1 (**Fig. 4.10C-D; Fig. 4.13**), DMT-1 (**Fig. 4.10F-G; Fig. 4.14**) and FPN **(Fig. 4.10I-J; Fig. 4.15**) were observed in DCM and CAD samples with MID, indicating that restricted iron uptake with concomitant iron efflux can underlie the basis of MID in failing hearts. We next used immunofluorescent staining of the iron transporters in DCM and CAD samples to confirm the subcellular location and concordance of changes seen in the Western blot analysis (**Fig. 4.10E, 4.10H, 4.10K; Fig. 4.16**). Collectively, our results demonstrated a differential subcellular regulation of iron transporters in MID characterized by reduced membrane and cytosolic levels of iron uptake transporters, TFR-1 and DMT-1, and increased levels of the iron exporter, FPN, in the membrane.

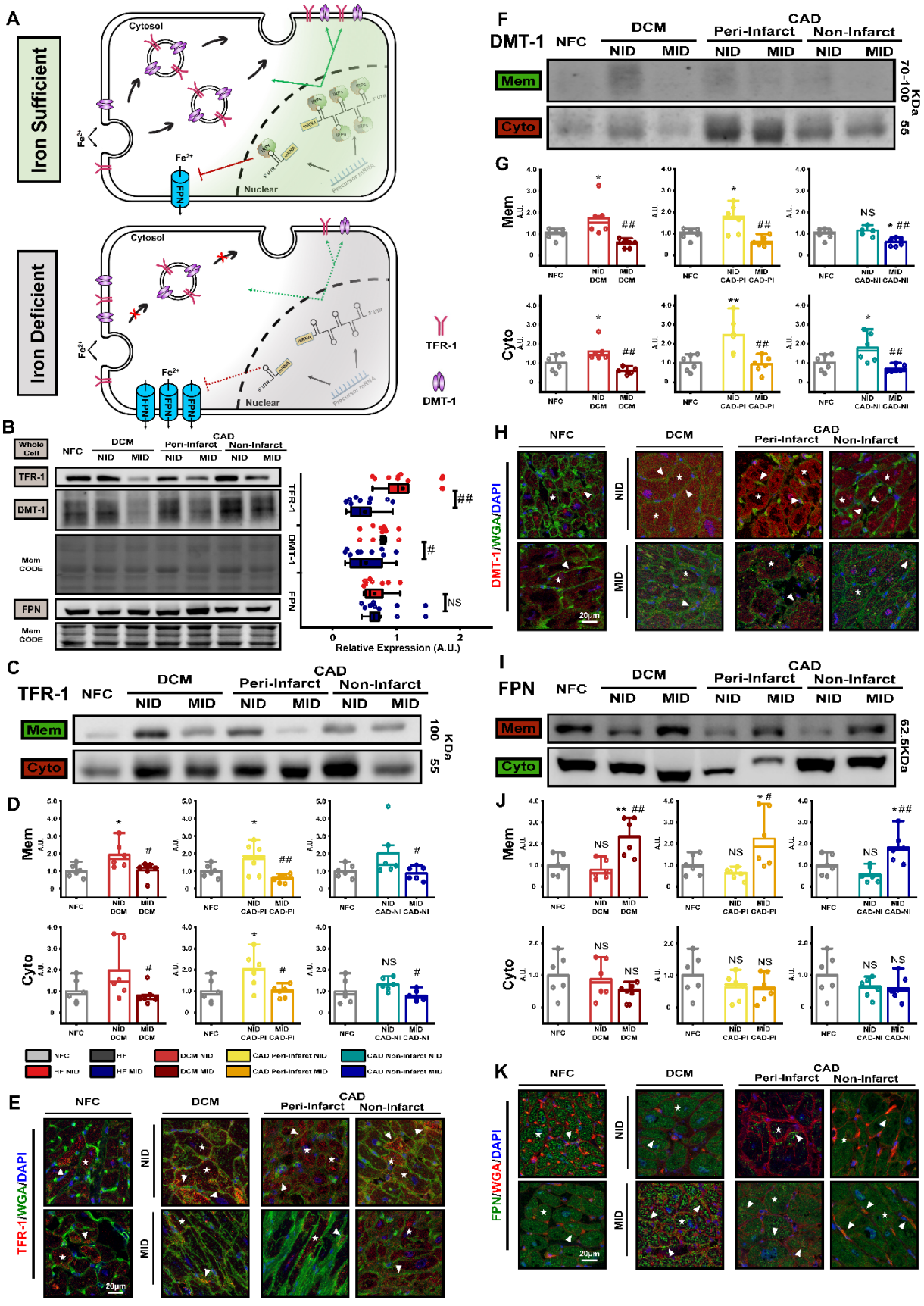
A
Iron Sufficient
Iron Deficient
Cytosol
Nuclear
Fe2+
FPN
TFR-1
DMT-1
B
Whole Cell
Mem CODE
NFC
DCM
CAD
Peri-Infarct
Non-Infarct
NID
MID
Relative Expression (A.U.)
C
TFR-1
Mem
Cyto
100
55
KDa
D
Mem
Cyto
A.U.
NFC
HF
DCM NID
CAD Peri-Infarct NID
CAD Non-Infarct NID
HF NID
HF MID
DCM MID
CAD Peri-Infarct MID
CAD Non-Infarct MID
E
TFR-1/WGA/DAPI
20μm
F
DMT-1
70-100
55
G
H
DMT-1/WGA/DAPI
I
FPN
62.5KDa
J
K
FPN/WGA/DAPI

Figure 4.10. Assessment of iron transporters using immunoblotting analysis and immunofluorescence staining with confocal microscopy. A. Schematic of the key iron transporters and the role of the iron regulatory proteins in a cardiomyocyte. B. Immunoblotting analysis (left panel) and quantification (right panel) of the total transferrin receptor 1 (TFR-1), divalent metal transporter 1 (DMT-1), and ferroportin (FPN) levels showing overall decreased TFR-1 and DMT-1 expressions in HF-MID, after normalized to NFCs. n=3 for each HF subgroup with n=9 for HF-MID and HF-NID, respectively. C-E Subcellular immunoblotting analysis with representative bands (C) and quantification (D) of TFR-1 showing overall reduced expressions in both membrane and cytosolic fractions in samples with MID, which was confirmed by immunofluorescence staining (E). F-H Similarly, subcellular immunoblotting analysis with representative bands (F) and quantification (G) of DMT-1 showing overall reduced expressions in both membrane and cytosolic fractions in HF subgroups with MID, which was supported by immunofluorescence staining (H). I-K Subcellular western blot analysis (I) and quantification (J) of FPN, and immunofluorescence staining (K) showing its relative increase in membrane fraction but not in cytosol in samples with MID. Mem: membrane; Cyto: cytosol; DCM: dilated cardiomyopathy; CAD-PI: peri-infarcted from coronary artery disease; CAD-NI: non-infarcted from coronary artery disease; NID: no myocardial iron deficiency; MID: myocardial iron deficiency; WGA=wheat germ agglutinin; DAPI=4′,6-diamidino-2-phenylindole. Arrowheads indicated membrane colocalization while asterisks refer to the cytosolic location of the proteins. n=10 for NFC; n=6 each for HF subgroups for all subcellular immunoblotting analyses. *$p<0.05$, **$p<0.01$ compared with NFC; $^{\#}p<0.05$, $^{\#\#}p<0.01$ compared with HF-NID.

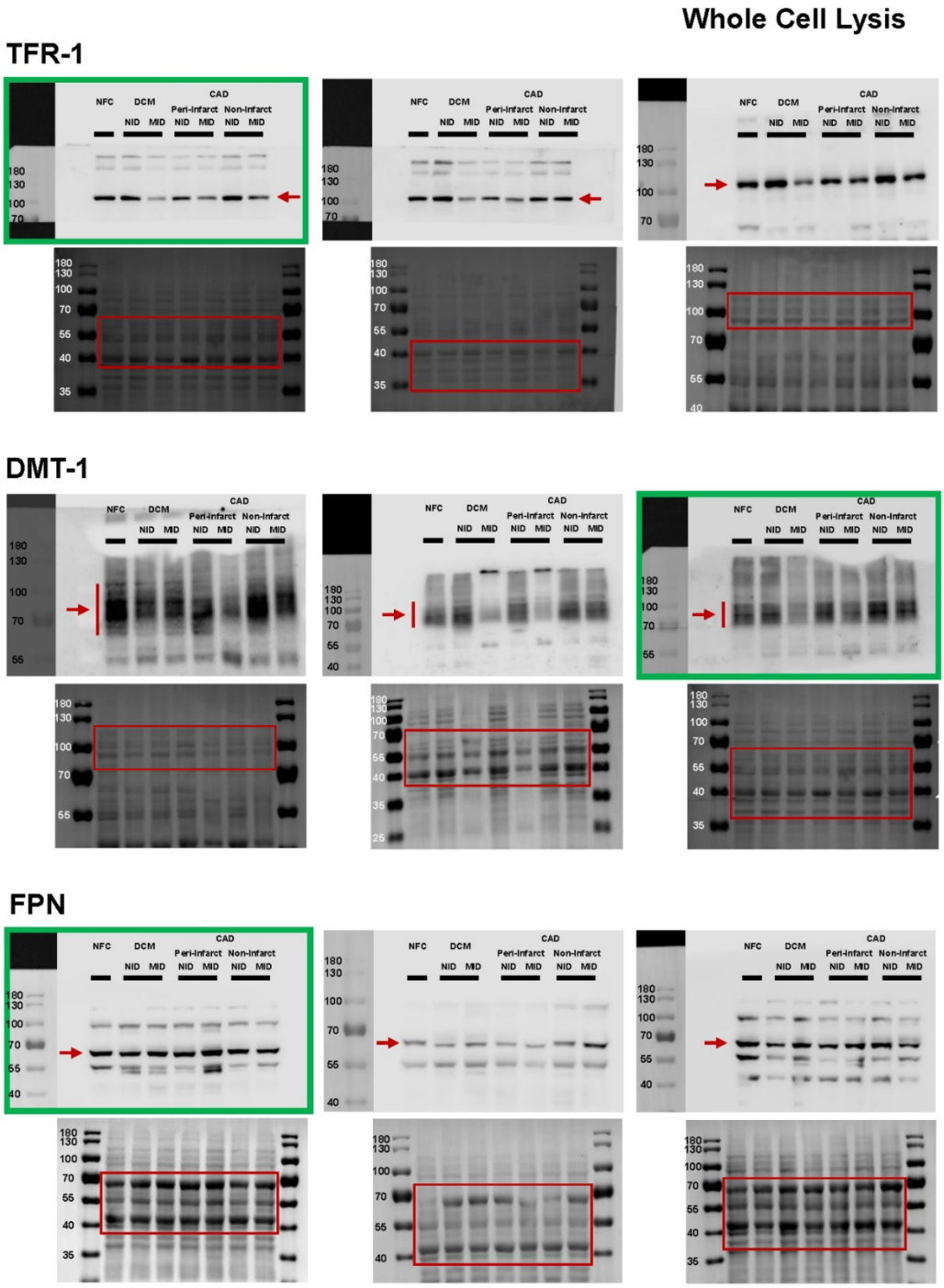

Figure 4.11. Original immunoblots of iron transporters using whole cell lysates that correspond to the protein quantitation in Figure 4.10B. TFR-1: transferrin receptor 1; DMT-1: divalent metal transporter 1; FPN: ferroportin. Arrowheads indicated the probed proteins with targeted molecular weight (TFR-1: 100 KDa, DMT-1: 70-100 KDa, FPN: 62.5 KDa), whereas red rectangular boxes showed the part of MemCode that were analyzed for protein abundance normalization. The blots selected as representative in Figure 4.10B were outlined with a green border.

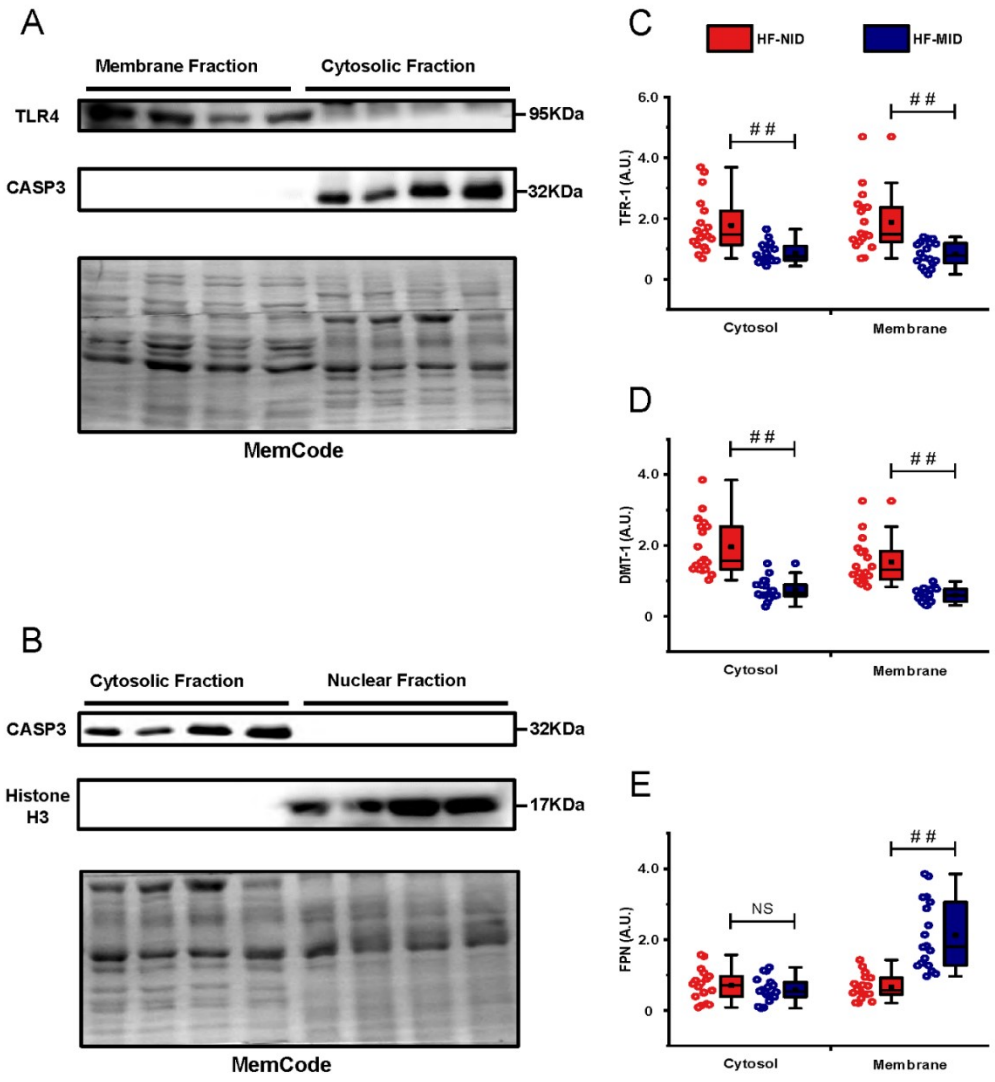

Figure 4.12. Western blot analysis demonstrating the validity of our tissue fractionation methods including membrane versus cytosolic (A), cytosolic versus nuclear (B) fractionations by established compartment-specific markers. C-E: Subcellular expression comparisons of TFR-1 (C), DMT-1 (D), and FPN (E) between HF-MID and HF-NID groups, respectively. TLR4: toll-like receptor 4; CASP3: caspase 3. MemCode represents the total protein loading on PVDF membrane. NID: no myocardial iron deficiency; MID: myocardial iron deficiency. n=6 for each HF subgroup.

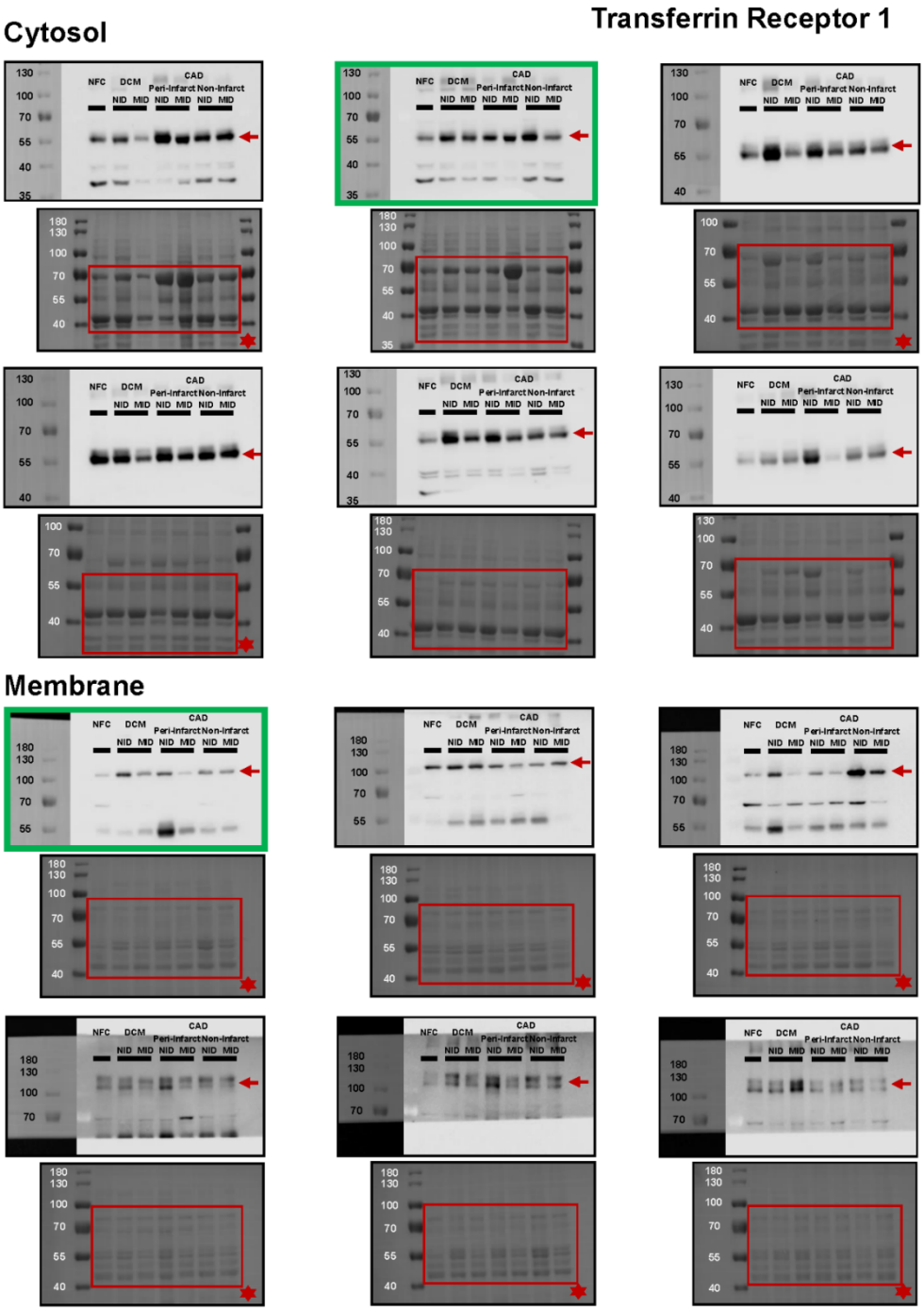

Figure 4.13. Original immunoblots of cytosolic and membrane TFR-1 that correspond to the protein quantitation in Figure 4.10D. TFR-1: transferrin receptor 1. Arrowheads indicated the TFR-1 molecular weight across cytosolic (55 KDa) and membrane (100 KDa) fractions, respectively. Rectangular boxes showed the part of MemCode that were analyzed for abundance normalization, whereas red asterisks indicated those underwent additional membrane stripping and downstream protein redetection (i.e., DMT-1). The blots selected as representative in Figure 4.10C were outlined with a green border.

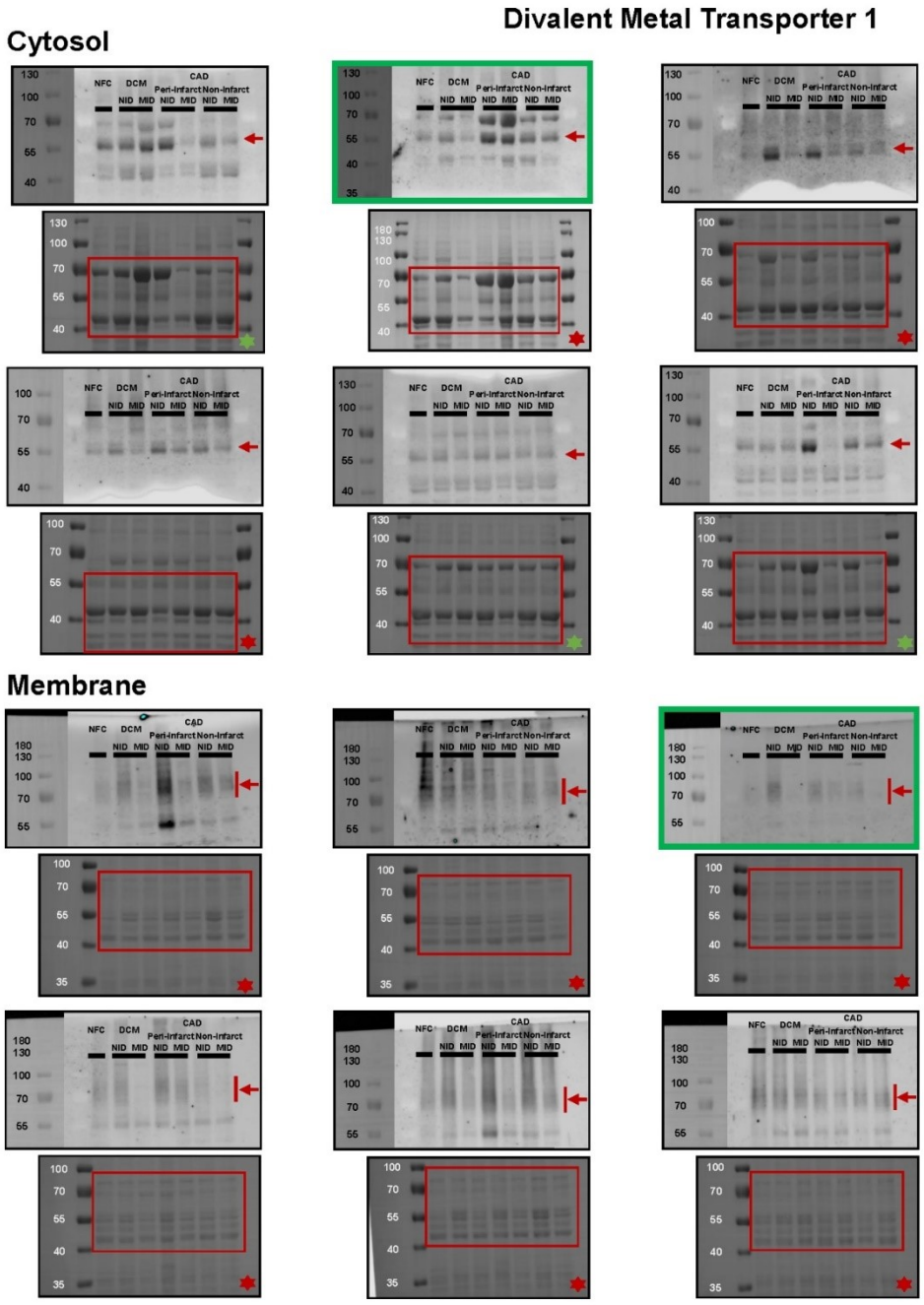

Figure 4.14. Original immunoblots of cytosolic and membrane DMT-1 that correspond to the protein quantitation in Figure 4.10G. DMT-1: divalent metal transporter 1. Arrowheads indicated DMT-1 molecular weight across cytosolic (55 KDa) and membrane (70-100 KDa) fractions. Rectangular boxes showed the part of MemCode that were analyzed for abundance normalization, whereas colored asterisks indicated those underwent additional membrane stripping and downstream protein redetection: red asterisks represented the shared MemCode as total protein loading for both TFR-1 and DMT-1 quantification, while green asterisks for DMT-1 and FPN quantification. The blots selected as representative in Figure 4.10F were outlined with a green border.

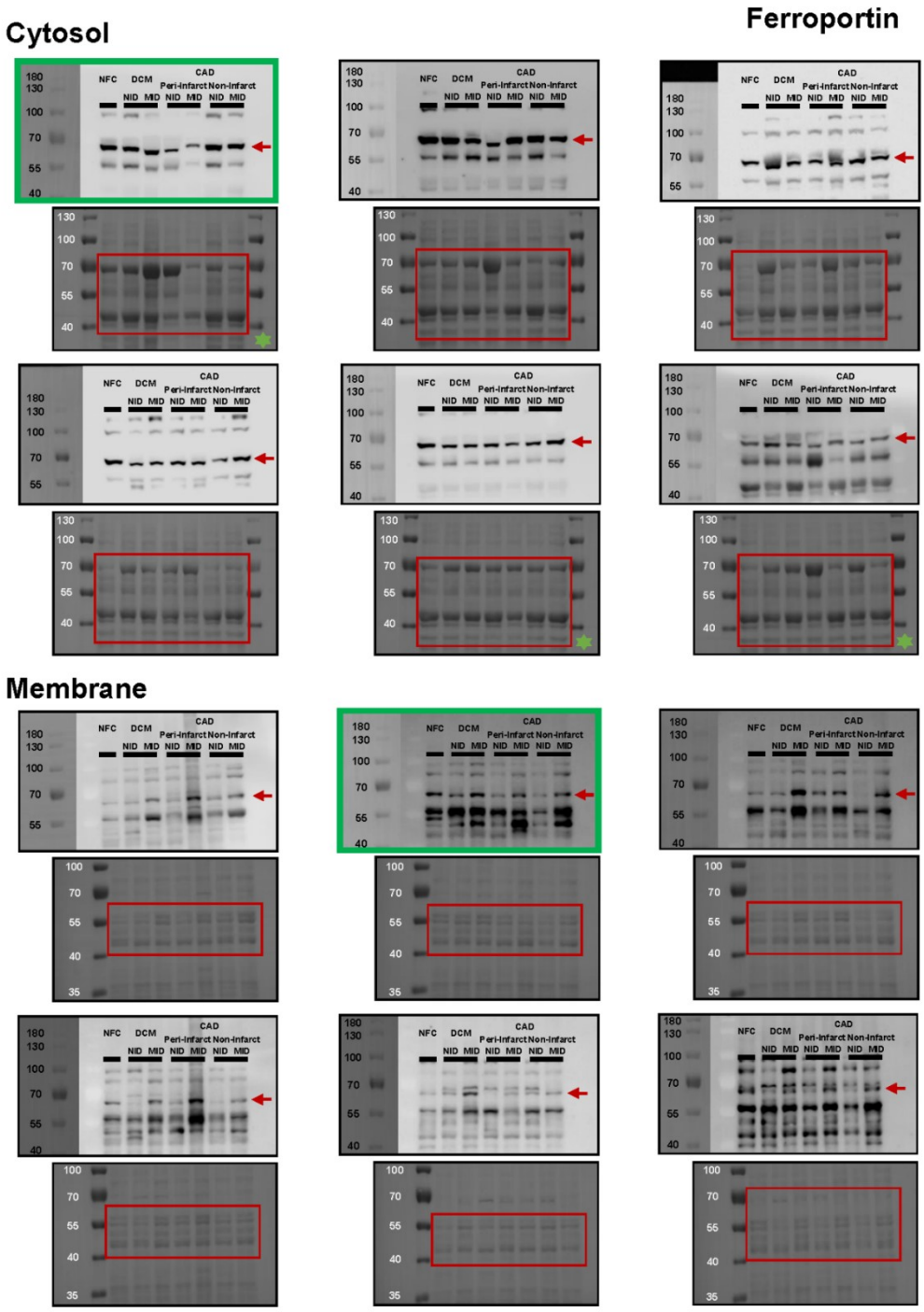

Figure 4.15. Original immunoblots of cytosolic and membrane FPN that correspond to the protein quantitation in Figure 4.10J. FPN: ferroportin. Arrowheads demonstrated the FPN's unaltered molecular weight in both cytosolic and membrane (62.5 KDa) fractions. Rectangular boxes showed the part of MemCode that were analyzed for abundance normalization, whereas green asterisks indicated those underwent additional membrane stripping and downstream protein redetection (i.e., DMT-1). The blots selected as representative in Figure 4.10I were outlined with a green border.

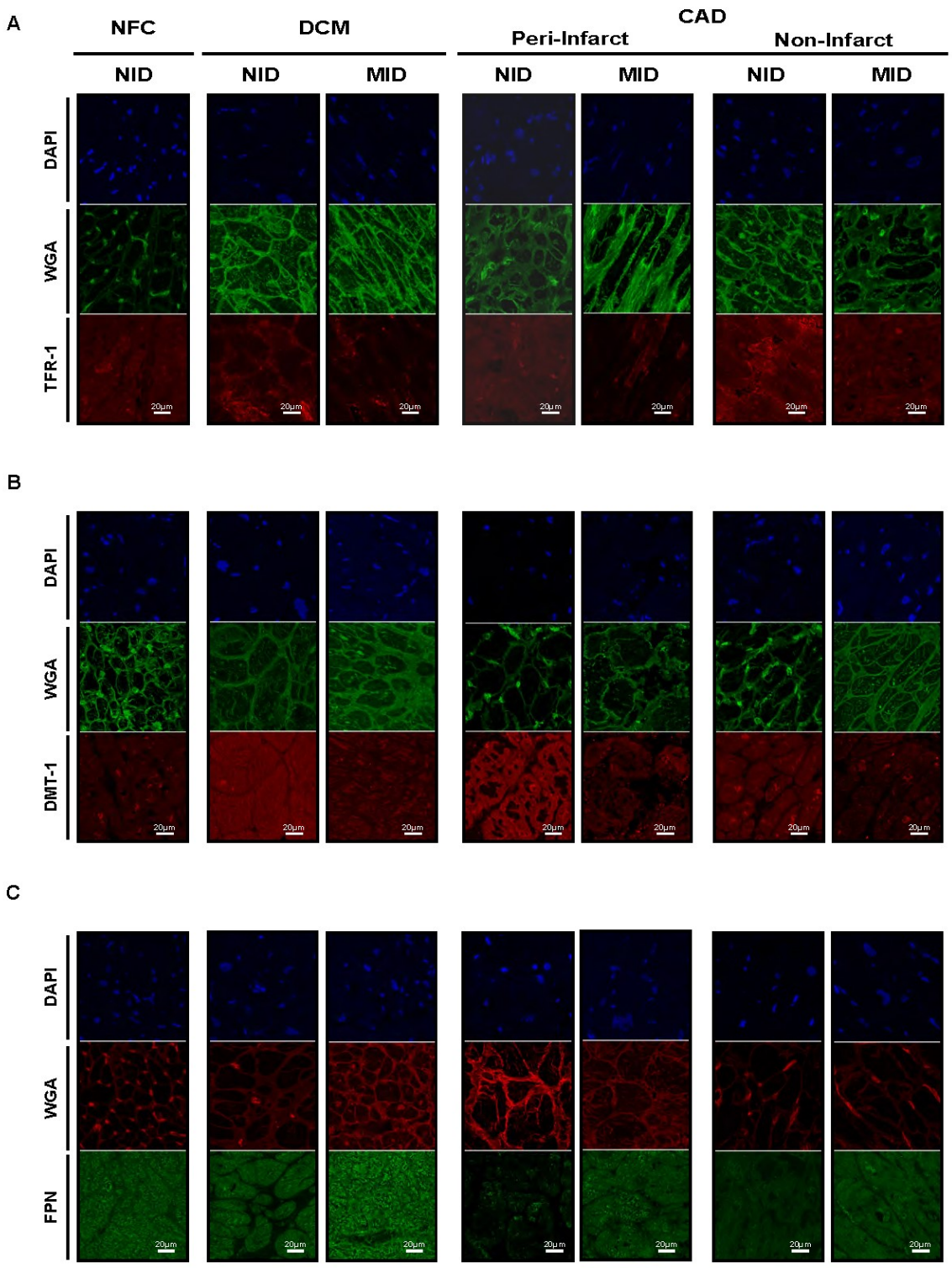

Figure 4.16. Original immunofluorescent images of separated channels that constitute the representative composites of individual iron transporter, including TFR-1 (A, red), DMT-1 (B, red), and FPN (C, green). TFR-1: transferrin receptor 1; DMT-1: divalent metal transporter 1; FPN: ferroportin.

4.5.4. Myocardial Iron Levels Assessed by Cardiac Magnetic Resonance Imaging

In the absence of overt SID, we evaluated quantitative imaging using CMR relaxation time constants as a non-invasive assessment of myocardial iron status. In our study, we explored the feasibility of applying T1, T2 and T2* evaluations in tissue samples using CMR technique (**Fig. 4.17A**). Our analyses showed that significantly elevated T2 (**Fig. 4.17B**) and T2* values (**Fig. 4.17C**) were featured in iron-deficient failing hearts, with similar changes seen between healthy control and diseased groups. However, T1 signal did not exhibit such distinct alteration (**Fig. 4.17B**). Multivariate analysis incorporating T1, T2, T2* and etiology showed moderate predictability of myocardial iron levels providing a reliable and non-invasive methodology to determine myocardial iron levels (**Fig. 4.17D; Table 4.2**). These results demonstrated the ability of CMR to detect and accurately reflect myocardial iron levels as a promising clinical surrogate in patients with advanced HF.

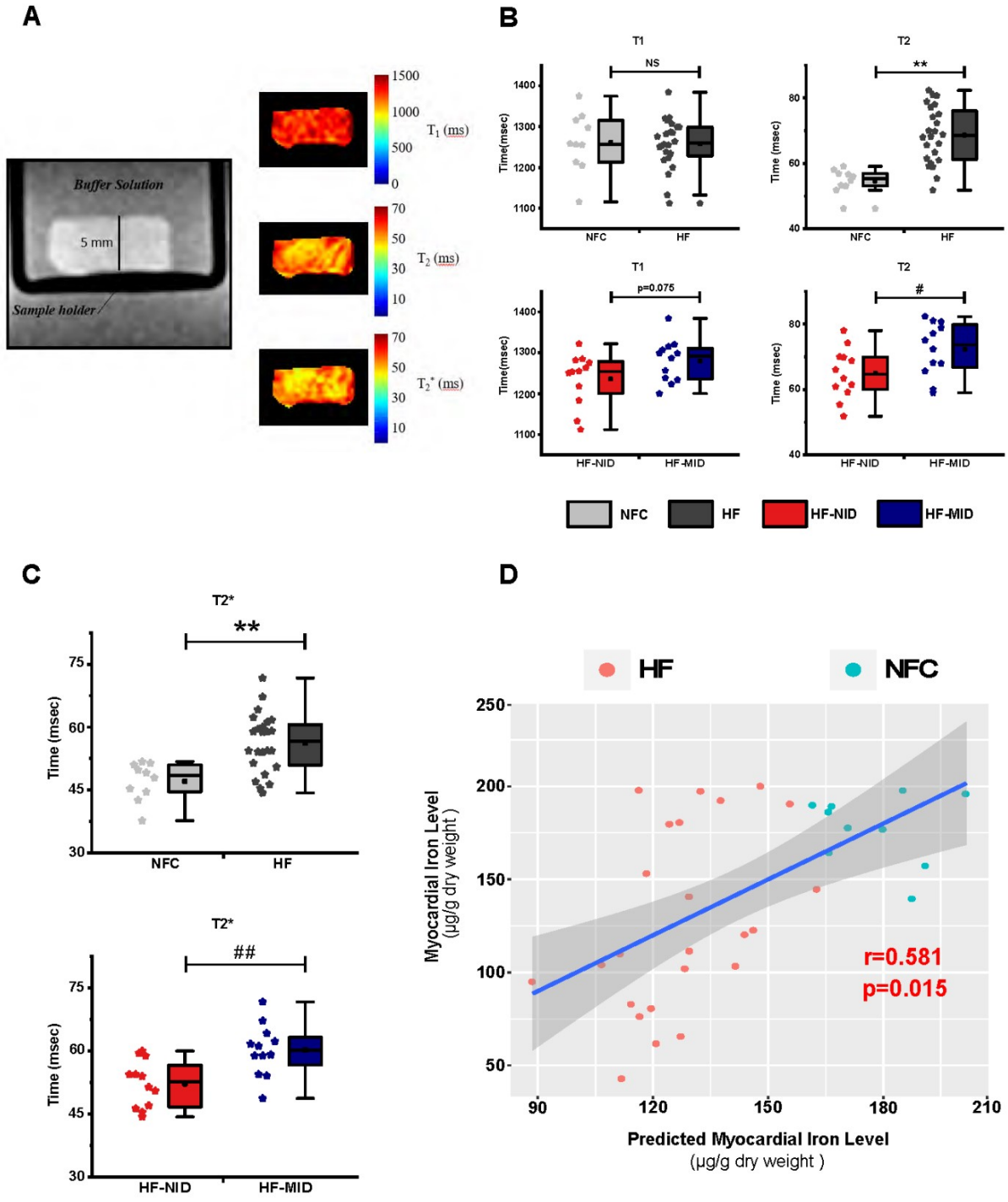

Figure 4.17. Magnetic resonance imaging of explanted human heart samples in relation to myocardial iron levels. A-C Typical parametric maps (T1, T2 and T2*) from a representative sample are illustrated (A) allowing for the quantitative assessment using T1 and T2 (B) and T2* values (C) in non-failing controls

(NFC) and HF subgroups consist of DCM and CAD. D. Multiple linear regression analysis using T1, T2, T2* and etiology as covariates showing a moderately strong relationship with myocardial iron levels (r=0.581; p=0.015; n=34). NID=no iron deficiency; MID=myocardial iron deficiency. n=10 for NFC, n=24 for HF; n=4 for each HF subgroup with n=12 for HF-MID and HF-NID, respectively. *p<0.05, **p<0.01 compared with NFC; #p<0.05, ##p<0.01 compared with HF-NID.

4.6. Discussion

Elucidating and treating comorbidities in patients with HF remains a pivotal approach to minimize morbidity and mortality. While systemic iron deficiency and anemia in acute and chronic HF patients are associated with worsened clinical outcome, iron supplementation in these patients improved prognosis[59, 95, 373, 395, 396]. Current guidelines for the diagnosis and treatment of HF clearly endorse a class I recommendation of iron deficiency and anemia screening in all patients[10, 374]. Given that the dominant mechanism of iron regulation occur at the tissue level, myocardial iron homeostasis can be uncoupled from systemic iron profile[28, 58, 59]. However, the primary determinant of the myocardial iron levels in failing human hearts remains unexplored. Our prospective human explanted heart program has provided a valuable resource with extensive collection of explanted human heart specimens and clinical phenotypes, thereby facilitating the examination of myocardial iron regulation in relation to advanced HF[182, 183]. We performed the largest translational study examining myocardial iron levels directly from the LV and RV of explanted human hearts in patients with DCM or CAD.

Our results established that MID in advanced failing hearts is associated with greater adverse remodeling including interstitial fibrosis and cardiac hypertrophy, as well as worsened LVEF and NYHA classification. Interestingly, myocardial iron levels in RV were coherently lower compared to LV regardless of etiology, and the lack of MID in the RV indicated divergent adverse remodelling progression in those HF patients[397]. We also showed that LV-specific MID was associated with further suppressed ROS-scavenging capacity, excessive oxidative stress, and impaired mitochondrial respiratory function and altered ultrastructure integrity. While our results were correlative in nature, they were consistent with prior studies directly linking iron deficiency to impaired human cardiomyocyte function and mitochondrial respiration[380, 398]. Human embryonic stem cell-derived cardiomyocytes depleted of iron affected mitochondrial function

through reduced activity of the Fe-S cluster-containing complexes I, II and III with reduced ATP levels and contractile force[380]. Fe-S clusters are ubiquitous cofactors composed of iron and inorganic sulfur, which are required for the proper function of Fe-S proteins involved in a wide range of biological activities, including electron transport in respiratory chain, micronutrient (i.e., iron) sensing, DNA repair and a key component of antioxidant enzymes.

The steady-state level of myocardial iron is maintained by the concerted action of major iron importers, TRF-1 and DMT-1, and the sole iron exporter, FPN[57, 72, 83, 382, 399]. The expressions of TRF-1 and DMT-1 are positively regulated by the nuclear transcriptional factors, IRP-1 and IRP-2, and cardiac selective disruption in the IRP-1/-2 axis led to MID and cardiac dysfunction[47, 57]. **S**urprisingly, there was reduced membrane translocation of TRF-1 and DMT-1 likely a result of the defective IRP-1/-2 pathway in HF-MID, which clearly was inadequate to restore myocardial iron status. Disruption in IRP-1/-2 action would conversely lead to increased translation of FPN mRNA. Indeed, we observed relatively increased membrane fractions of FPN facilitating iron efflux from the failing cardiomyocytes, which is supported by findings in a genetic murine model[399]. Suppression of FPN in the membrane compartment provides a promising foundation for correcting MID in patients with advanced HF.

The exact mechanisms by which HF patients develop MID are not completely understood. An interplay between increased sympathetic activation and iron deficiency was recently observed in patients with chronic HF, suggesting the latter could be more than a comorbidity but a critical component leading to HF[400]. Our data supported the hypothesis that iron deficiency is an integral pathophysiology promoting the progression to advanced HF, and that low iron storage in HF patients is independently associated with escalated rates of mortality and re-hospitalizations[401]. In addition, our results were consistent with clinical trial findings showing that the treatment of iron deficiency irrespective of anemia was beneficial[396]. Regulation of skeletal muscle energetics also represents an important mechanism by which iron supply confers benefits in HF in addition to its central role in myocardial iron homeostasis[402].

Different therapeutic possibilities embrace iron replacement by oral or intravenous routes. Several clinical trials with intravenous iron in chronic HF patients with SID, have demonstrated equally efficacious and similar favorable safety profiles following correction of iron levels, irrespective of anemia[377, 402]. Thus, iron status should be assessed in symptomatic HF patients both

with or without anemia, and treatment of iron deficiency warrants consideration in clinical practice[396]. The use of CMR to diagnose myocardial iron-overload is a valid and established technique[403]. Our ability to extend the evaluation of myocardial iron levels using CMR to iron-deficient hearts provides a unique tool to potentially diagnose and monitor HF patients with MID. Our findings illustrate the potential for precision medicine and correction of MID, especially given the widespread clinical availability of parametric mapping with CMR and its assessment of myocardial iron levels[392, 403-405]. Animal models with selective MID and cardiac dysfunction are corrected by the intravenous administration of iron supporting the distinct possibility of this approach in patients[57]. In patients with heart failure and iron deficiency, intravenous ferric carboxymaltose administration changed T2* and T1 cardiac MRI parameters indicative of myocardial iron repletion, further supporting the utility of cardiac MRI to monitor myocardial iron deficiency and its response to therapy[405].

4.7. Conclusions and Limitations

There are a few limitations of our study that need to be acknowledged. First, our investigation was cross-sectional and all patients included were at end-stage HF, and thus we captured a single time point of the entire disease course thereby limiting the ascertainment of causative relationship when interpreting the experimental results. Secondly, while our non-failing control hearts demonstrated no evidence of adverse remodeling characteristic of heart failure, they do not represent the true normal myocardium in vivo for reasons including, but not limited to, antemortem medications and metabolic alteration in relation to initial injuries, and postmortem adrenergic storm associated with brain death. In order to minimize these limitations, we used a large number of samples coupled with a comprehensive profile of clinical parameters including comorbidities, past medical history, and treatments, which were integrated into specimen assessment, subgrouping, and data interpretation.

Chapter 5

Multi-Omics Profiling of Pediatric Dilated Cardiomyopathy:

A Focus on Metabolism Phenotypic Switching

Multi-Omics Profiling of Pediatric Dilated Cardiomyopathy: A Focus on Metabolism Phenotypic Switching

Hao Zhang MD[1,2,*], Uros Kuzmanov PhD[3,4,*], Kemar B. Joseph MD[5], Anissa Viveiros MSc[1,2], Yuri Kim MD PhD[5], Sarah Morton MD PhD[6], Simon Urschel[2,7], John M. Seubert PhD[2,8], Shaohua Wang MD MSc[2,9], Jonathan G Seidman PhD[10], Christine E. Seidman MD[10,11], Anthony Gramolini PhD[3,4], and Gavin Y. Oudit MD PhD[1,2,#]

[1]Division of Cardiology, Department of Medicine, [2]Mazankowski Alberta Heart Institute, Faculty of Medicine & Dentistry, University of Alberta, Edmonton, Alberta, CA. [3]Department of Physiology, [4]Translational Biology and Engineering Program, Ted Rogers Center for Heart Research, Faculty of Medicine, University of Toronto, Toronto, Ontario, CA. [5]Division of Cardiology, Massachusetts General Hospital, [6]Department of Neonatology, Boston Children's Hospital, Harvard Medical School, Boston, Massachusetts, USA. [7]Division of Pediatric Cardiology, Department of Pediatrics, [8]Department of Pharmacology, [9]Division of Cardiac Surgery, Department of Surgery, Faculty of Medicine & Dentistry, University of Alberta, Edmonton, Alberta, CA. [10]Department of Genetics, [11]Cardiovascular Division, Brigham and Women's Hospital, Harvard Medical School, Boston, Massachusetts, USA

[*] Denotes equal contributions; # Denotes corresponding author

A version of this chapter will be submitted to a peer-reviewed journal for consideration of publication as: ***Zhang H**, Kuzmanov U, Joseph KB, Viveiros A, Kim Y, Morton S, Urschel S, Seubert JM, Wang S, Seidman JG, Seidman CE, Gramolini A, and Oudit GY. Multi-omics profiling of pediatric dilated cardiomyopathy: A focus on metabolism phenotypic switching.* This chapter has been modified from the article above.

5.1. Abstract

Background. Dilated cardiomyopathy (DCM) remains the leading cause of heart transplantation in children. Despite similar phenotypic features and genetic etiologies, medications routinely prescribed to adult heart failure (HF) patients are not as effective in children. Behind this, the mechanistic explanations are largely unknown. Indeed, few pioneering studies have shown that pediatric DCM (P-DC) demonstrated disparate remodeling patterns from their adult counterparts (A-DC), a full-repertoire characterization of the molecular processes implicated in P-DC does not exist, which impedes the development of children-appropriate HF therapies.

Methods and Results. Explanted failing hearts from adults and children with DCM, and age-matched non-cardiomyopathic (NC) controls were used in the study. To fully characterize the gene expressional profiles, (phospho-)protein abundances and perturbed signaling dynamics at an early symptomatic stage of DCM progression, we hereby reported an integrative system biology strategy based on state-of-the-art analyses of bulk-RNA sequencing and global and phospho-proteomic profiling at the tissue level, which was further complemented with single-cell/-nucleus transcriptomics (sc/snRNA-Seq) delineating the full landscape of cellular heterogeneity with diverse developmental origins and specialized properties. Notably, divergent transcriptome and (phospho-)proteome profiles were uncovered between pediatric and adult patients, and we demonstrated, by validation of a plethora of in vitro molecular experiments, that electron transport chain (ETC) pathway was prominently disrupted in P-DC likely due to oxidative stress-induced cardiolipin peroxidation. Premature mitochondrial failure characterized the early presentation of disease in kids.

Conclusions. Our opportune implementation of comparative multi-omics approach illustrated a navigated “roadmap” connecting tissue and clinical phenotyping, and for the first time systematically revealed the whole compositional patterns specific to P-DC, potentiating the development of robust biosignatures that can possibly differentiate them from adult counterparts. Further, our study provided new insights into pathological mechanisms implicated in pediatric cardiac disease that could serve as a test bed for prospective drug screening.

5.2. Clinical Perspective

What is New?

- Pediatric DCM is a pathologically distinct entity from their adult counterparts.
- Pediatric DCM demonstrates minimal adverse tissue remodeling with maintained contractile properties, the primary targets of adult HF therapies.
- Pediatric DCM exhibits remarkably dysfunctional mitochondrial electron carriers, namely, complex I, imputable to oxidative stress-induced cardiolipin peroxidation and remodeling.
- Divergent tissue phenotypes, including thousands of coding RNA, proteins, phosphoproteins, and phosphorylation sites, are fully characterized in pediatric failing hearts by systems biology.

What Are the Clinical Implications?

- Pediatric DCM is a clinically distinct entity with unique underlying pathogeneses warrants tailored interventions rather than simple extrapolation from the adults.
- Defective mitochondrial respiration and bioenergetics, characterized by functional impairment of electron transporting carriers and superoxide dismutases, in the absence of major adult-dominant cardiac remodeling, remains a potential target to treat pediatric patients with advanced HF.
- Mitochondria-specific compounds that improve electron transporting efficiency by ameliorating oxidative damage via MnSOD, or stabilizing inner membrane via cardiolipin, warrant future investigations.

5.3. Introduction

Heart failure (HF) remains a global epidemic affecting both adults and children (0-18 years old) which is projected to continue growing rapidly within the next decade imposing tremendous medical and societal burdens[372, 406]. Statistically, over 6 million adults in North America alone carry a diagnosis of HF as of today, with an estimated increase in prevalence by 46% until 2030[372]; however, the overall epidemiology of pediatric HF is limited. In adults, HF represents the final phase of cardiac structural and functional impairments primarily due to coronary artery diseases and cardiomyopathies (CMs)[205], whereas in the pediatric population, it often carries heterogeneous genetic underpinnings and demonstrates age-dependent intrinsic features driven by developmental and pathological factors[407]. For instance, pediatric HF may present as early as at birth due to congenital structural malformations[408], or develop at any later stage of childhood as a result of primary CMs[122].

Dilated cardiomyopathy (DCM) represents the most common cause of end-stage HF with reduced ejection fraction (HF-rEF) in adult and pediatric (>1 year) patients awaiting cardiac transplantation. Despite similar phenotypes characterized as systolic dysfunction and eccentric ventricular dilation, pediatric DCM (P-DC) are pathologically distinct entities with causes largely idiopathic, and with age- and development-specific features in the heart. While a plethora of studies have investigated the pathogenesis of adult DCM (A-DC) leading to targetable anti-remodeling therapies, few have been successfully translated from P-DC. And due to the paucity of large-scale clinical trials in pediatrics, current pharmaceutical recommendations for children and adolescents with HF are primarily extrapolated from adults[121, 122], which could be problematic. Indeed, recent randomized trials using the beta-blocker Carvedilol, and ACE inhibitor Enalapril, both failed to show definite improvements or benefits of these drugs as observed in their adult counterparts[123, 124]. These striking results clearly indicate the disparate pathophysiology underlying children's failing hearts, which warrants focused examination especially given their inferior prognoses of transplant-free or survival rate at 5 years[125, 409]. In addition, the age of pediatric patients was reported to be associated with a higher risk of pump failure death and life-threatening arrhythmias[409], whereas younger patients with less LV dilation at diagnosis independently predicted structural and functional recovery within 2 years of presentation[410].

Typically, DCM is considered an insult predominantly impacting the left ventricle (LV), marked by a spectrum of adverse remodeling progressions. It involves structural, functional, electrophysiological, and metabolic alterations predisposing to irreversibly advanced HF[117, 119, 393]. There is a growing body of literature unveiling the unique course of disease implicated in P-DC from various physiological aspects, namely, differential adrenergic adaptation and fibrotic pattern, that could possibly explain their differed responsiveness to adult HF therapies[126-128]. Our recent work assessing the fibrillar and nonfibrillar extracellular matrix (ECM) components and associated regulatory factors also confirmed the divergent remodeling within the pediatric dilated hearts[129]. Nevertheless, the whole picture of the mechanistic basis of P-DC has not yet been fully charted, because of the limited number of comparative studies between pediatric and adult DCM cohorts conducted so far. Major restraints include the extreme rarity of clinical specimens from pediatrics, and the lack of reliable preclinical models that can approximate developmental traits in kids.

Here, implementing state-of-the-art integrative omics on the explanted human heart tissues plays an unprecedented role in fully recapitulating the maturation-related complexities in the pediatric falling hearts[178]. Our cutting-edge omics platform enabled comprehensive profiling of transcriptomic biomarkers implicated explicitly in the P-DC cohorts, following normalization to contemporaneous non-cardiomyopathic controls (NC)[411]. Since protein abundance does not always correlate with the expression of RNA[292, 412], we further profiled global- and phospho-proteome within early affected hearts by comparing them to the adult counterparts (A-DC)[275, 413, 414]. In our study, we highlighted hundreds of differentially expressed coding transcripts, proteins, and phosphoproteins between P-DC and A-DC, in a greater context of thousands of co-expressed genes and downstream cardiac proteins. Dysregulated phosphorylation sites were mapped after affinity capture and identification of 3397 unique phosphopeptides in fractionated myocardium homogenates within failing systemic ventricles. Global statistical enrichment analyses of the differential transcriptional and translational patterns revealed selective perturbation of biological pathways involved in cytoskeleton organization and muscle contraction, cellular respiration and metabolism, immune response, regulation of reactive oxygen species (ROS) and cell death, intracellular signaling transduction and ECM remodeling. Notably, single-cell and single-nucleus RNA sequencing (scRNA-seq and snRNA-seq, respectively) and multiplex single-molecule fluorescence in situ hybridization (smFISH) enabled deeper identification of the cellular composition of failing ventricles from both groups, and highlighted the heterogeneities of relevant

cardiac cells (cardiomyocytes, fibroblasts, endothelial cells, lymphoid and myeloid cells) with distinct developmental origins and specialized properties. Phenotype-specific analyses of cell-to-cell interactions and spatial relationships further characterized the early symptomatic stage of DCM progression at the single cell resolution.

5.4. Methods

The data supporting this study's findings are available from the corresponding author upon reasonable request.

5.4.1. Human Explanted Heart Specimens

Study Design. The Mazankowski Alberta Heart Institute (MAHI) administers the largest research-integrated Human Explanted Heart Program (HELP) nationwide, which encompasses a sizable collection of diseased human explanted heart tissues associated with biomedical database[178]. In parallel, we have compiled an inventory of non-failing or non-cardiomyopathic (NC) hearts via the Human Organ Procurement and Exchange (HOPE) program that serve as the "control" group for adults or pediatrics in our study. Informed consents were obtained from all patients or their power of attorney. Both programs conformed to the ethical principles of the Declaration of Helsinki, and were approved by the institutional review committee and Health Research Ethics Board at the University of Alberta, Edmonton, Canada. Clinical data were obtained by chart review.

Pathologic heart specimens were procured ethically from adult and prepubertal pediatric patients with idiopathic or familial DCM undergoing cardiac transplantation (**Fig. 5.1A**). Patients with any secondary etiologies underlying cardiomyopathies, namely, coronary artery disease, myocarditis, cardiac sarcoidosis, amyloidosis, peripartum or chemical-induced (including alcohol) cardiomyopathy, congenital heart defects, neuromuscular dystrophies, mitochondrial or metabolic disorders, were excluded from this study. Both diseased groups demonstrated comparable age and sex distributions and had significantly reduced LV ejection fractions (LVEF) with no prior implant history of mechanical unloading devices (**Table 5.1, 5.2**). Age-matched NC hearts were obtained

as controls from either deceased adult donors without cardiovascular history, or prepubertal children with hypoplastic left heart syndrome (HLHS) showing LVEF>60% (**Table 5.1, 5.2**). Briefly, the adult controls consisted of pristine hearts from brain-dead donors which were declined for transplantation primarily due to blood type (ABO) and/or human leukocyte antigen (HLA) mismatch[178, 415], whereas pediatric control samples were collected from the left ventricle of HLHS following successfully staged reconstructions. Despite the underdeveloped nature of pediatric control specimens, it did not demonstrate cardiomyopathic pathogeneses as investigated (**Fig. 5.1B, 5.2**), thus constituting a scientifically reasonable control group given the extreme paucity of true pediatric non-failing hearts (see Limitations for more discussion). We excluded potential interferences from sex and growth hormones by incorporating prepubertal children subjects with similar sex distribution (**Fig. 5.1C**).

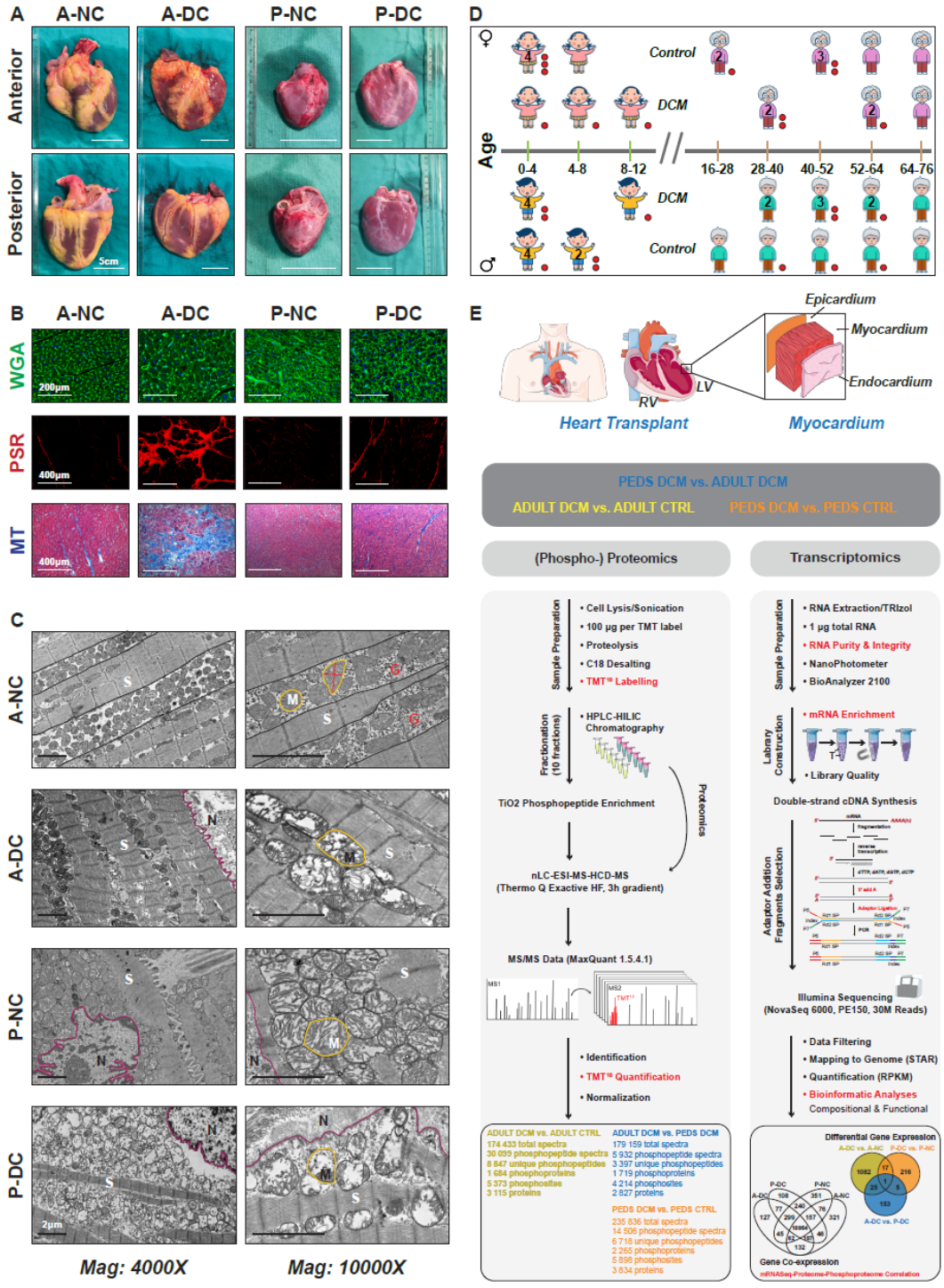

Figure 5.1. Overview of transcriptomic and phosphoproteomic workflows. A. Representative anterior and posterior views of human explanted hearts. Overall, heart size between adults and children differed tremendously. Extensive epicardial adipose tissue were noted only in the adults including the diseased and nondiseased hearts, whereas such areal distribution of the epicardial fat was strikingly minimal in the kids. Images (scale bar: 5cm) reproduced with permission from Zhang H et al.; heart weights are summarized in

Figure 5.2. B. Absence of adverse myocardial remodeling in pediatric dilated failing hearts, with representative images of wheat germ agglutinin (WGA: green, scale bar: 200 μm), picrosirius red (PSR: red, scale bar: 400 μm), and Mason's trichrome staining (MT: blue, scale bar: 400 μm). For their corresponding quantifications, refer to Figure 5.2. C. Representative high-magnification TEM images illustrating severe myofilament disarray, ultrastructural derangement and mitochondrial lysis in both young and adult HF subgroups (scale bar = 2 μm). G: glucose; M: mitochondrion; N: nucleus; S: sarcomere; purple line outlines nuclear membrane while the red represents long and short axis of the mitochondrion. D. Infographic displays diseased and nondiseased sample donors (top: female; bottom: male) from different age groups (left: young; right: aged) that were included in the study. Statistically, n=8 young (3 female; 5 male) and n=13 aged (5 female; 8 male) patients with dilated cardiomyopathy, and n=11 young (5 female, 6 male) and n=12 aged (7 female, 5 male) non-failing heart donors were recruited. Samples contributed to both RNA-Seq and (phospho-)proteomic datasets are marked with red circles (n=6 biological replicates per subgroup). Detailed demographics and clinical information are available in **Table 5.1** and **5.2**, respectively. E. Transmural myocardial specimen from the mid-anterior LV free wall (approximately two-thirds below the aortic valves) without epicardial fat and scar tissues, were analyzed with our well-established techniques combining quantitative precision LC-MS/MS and poly-A enriched NGS platforms. LC-MS/MS: liquid chromatography with tandem mass spectrometry; NGS: next generation (m)RNA sequencing (RNA-Seq). DCM: dilated cardiomyopathy; A-DC: adult dilated cardiomyopathy; A-NC: adult non-DCM control; P-DC: pediatric dilated cardiomyopathy; P-NC: pediatric non-DCM control; LV/RV: left/right ventricle; HPLC-HILIC: high performance liquid chromatography-hydrophilic interaction liquid chromatography; nLC-ESI-MS-HCD-MS: nano liquid chromatography-electrospray ionization tanden mass spectrometry-high collision dissociation mass spectrometry; TEM: transmission electron microscopy. Panel E was partly generated using Servier Medical Art, licensed under a Creative Commons Attribution 3.0 unported license.

Table 5.1. Baseline Clinical Characteristics of Adult (A-DC) and Pediatric (P-DC) Patients with End-Stage Heart Failure Secondary to Dilated Cardiomyopathy

	A-NC (N=12)	**A-DC (N=13)**	**P-NC (N=11)**	**P-DC (N=8)**
Demographics				
Age (years)	48.0 (35.3-54.0)	51.0 (39.0-60.0)	0.8$^{***, \dagger\dagger\dagger}$ (0.4-2.8)	2.6$^{***, \dagger\dagger\dagger}$ (1.5-9.1)

Sex, Male	5 (42)	8 (62)	6 (55)	5 (63)
BSA (m^2) [§]	1.9 (1.7-2.0)	1.9 (1.8-2.0)	0.4[***, †††] (0.3-0.6)	0.5[***, †††] (0.4-1.4)
Heart Weight (gram)	316.0 (304.5-345.0)	480.0[***] (376.0-546.0)	77.0[***, †††] (54.0-122.5)	145.5[***, †††] (120.0-212.8)
Physical Assessment				
SBP (mmHg)	na	102.0 (93.8-111.0)	94.0 (88.0-111.5)	97.0 (92.5-109.8)
DBP (mmHg)	na	64.0 (52.8-72.8)	54.5 (47.0-73.3)	61.5 (49.3-74.5)
Comorbidities				
PAH	0 (0)	3 (23)	0 (0)	2 (25)
Dyslipidemia	0 (0)	2 (15)	0 (0)	0 (0)
Thyroid Disease	0 (0)	5 (38)	0 (0)	0 (0)
Kidney Disease	0 (0)	8 (62)	0 (0)	0 (0)
Electrocardiography				
LBBB	0 (0)	3 (23)	0 (0)	0 (0)
RBBB	0 (0)	0 (0)	0 (0)	0 (0)
QRS Duration (ms)	na	120.0 (97.0-140.0)	81.0[††] (72.0-89.0)	106.0[#] (88.5-115.0)
Echocardiography				
LVEF (%)	>57.5 (50.0-60.0)	24.8[***] (17.4-30.6)	>60[††] (42.6-65.6)	24.8[***, ##] (18.3-29.6)
LVIDd (mm)	na	63 (59.5-67.3)	27.0[††] (26.5-27.5)	55.5[##, †] (43.5-58.5)
LVIDs (mm)	na	56.0 (49.3-63.8)	21.5[††] (18.8-24.3)	46.0[#, †] (36.5-48.0)
RV Systolic Dysfunction [§]	na	0	1.5	2

		(0.0-1.0)	(1.0-2.8)	(1.5-2.0)
Blood Parameters				
Hemoglobin (g/L)	na	125.0 (113.0-130.0)	144.5[†] (124.0-153.8)	108.5[##] (100.0-115.5)
Creatinine (μmol/L)	na	120.0 (95.0-150.0)	32.0[†] (27.0-46.5)	32.0[†] (18.0-49.8)
eGFR (ml/min/1.73m^2)	na	44.0 (41.0-56.7)	81.5[†] (71.8-86.3)	117.0[#, †] (101.0-150.0)
Devices				
Pacemaker	0 (0)	4 (31)	0 (0)	0 (0)
ICD/BiV-ICD	0 (0)	11 (85)	0 (0)	0 (0)
VADs	0 (0)	0 (0)	0 (0)	0 (0)
Medications				
ACEi/ARB	na	11 (85)	6 (55)	5 (63)
Beta Blockers	na	10 (77)	2 (18)[†]	6 (75)[#]
Diuretics	na	11 (85)	7 (64)	7 (88)
MRA	na	7 (54)	1 (9)[†]	3 (38)
Antiarrhythmic	na	3 (23)	1 (9)	1 (13)

BSA=body surface area ([§]Mosteller formula for pediatrics); SBP=systolic blood pressure; DBP=diastolic blood pressure; PAH=pulmonary artery hypertension; LBBB=left bundle branch block; RBBB=right bundle branch block; LVEF=LV ejection fraction; LVIDd=LV end-diastolic internal diameter; LVIDs=LV end-systolic internal diameter; [§] scoring for RV Systolic dysfunction: none=0, trivial=1, mild=2, moderate=3, severe=4; eGFR=estimated glomerular filtration rate based on MDRD equation; BiV-ICD=bi-ventricular implantable cardioverter-defibrillator; ACEi=angiotensin converting enzyme inhibitors; ARB=angiotensin receptor blockers; MRA=mineralocorticoid receptor antagonists. Categorical variables reported by count with percentage in parenthesis: sex, diagnosis of comorbidities, LBBB, RBBB, device implantations, and medications. Continuous variables reported by median with interquartile range in parenthesis: age, BSA, heart weight, physical assessments, QRS duration, echocardiography, and blood

parameters. Chi-squared test, independent sample t-test or one-way ANOVA (followed by Tukey post hoc analysis), Kruskal Wallis or Mann-Whitney U test was used as appropriate to compare the variables between groups. A two-tailed *p<0.05* was considered statistically significant. *p<0.05, **p<0.01, ***p<0.001 compared to A-NC; #p<0.05, ##p<0.01, ###p<0.001 compared to P-NC; †p<0.05, ††p<0.01, †††p<0.001 compared to A-DC.

Table 5.2. Additional Clinical Profiling of Adult (A-DC) and Pediatric (P-DC) Patients with End-Stage Heart Failure Secondary to Dilated Cardiomyopathy

	A-NC (N=12)	**A-DC (N=13)**	**P-NC (N=11)**	**P-DC (N=8)**
Demographics				
Ethnicity White/Black/Asian/Other	10/0/1/1 (84/0/8/8)	13/0/0/0 (100/0/0/0)	9/1/1/0 (82/9/9/0)	5/0/1/2 (63/0/12/25)
Blood type A/B/AB/O, Rh(D)+	na	4/3/2/4, 8 (31/23/15/31, 62)	6/0/1/4, 9 (55/0/9/36, 82)	4/1/0/3, 8 (50/13/0/37, 100)
Physical Assessment				
Weight (kg)	74.0 (62.8-80.0)	75.0 (71.5-81.0)	8.1$^{***, \dagger\dagger\dagger}$ (4.8-15.4)	12.0$^{***, \dagger\dagger\dagger}$ (8.6-50.2)
Height (cm)	171.0 (165.0-175.0)	170.0 (168.0-173.0)	74.0$^{***, \dagger\dagger\dagger}$ (57.0-92.5)	84.0$^{***, \dagger\dagger\dagger}$ (75.5-152.5)
Comorbidities				
CVD	0 (0)	1 (8)	0 (0)	0 (0)
PVD	0 (0)	0 (0)	0 (0)	0 (0)
Diabetes Mellitus (II)	0 (0)	0 (0)	0 (0)	0 (0)
Liver Disease	0 (0)	2 (15)	0 (0)	1 (13)
Obesity	2 (17)	6 (46)	0 (0)	0 (0)
Hypertension	1 (8)	2 (15)	0 (0)	1 (13)

Smoker	3 (25)	4 (31)	0 (0)	0 (0)
COPD/Asthma	2 (17)	3 (23)	1 (9)	1 (13)
Electrocardiography				
QTI	na	452.0 (396.0-478.0)	325.0†† (287.0-360.0)	378.0 (375.3-407.0)
IVCD	0 (0)	3 (23)	0 (0)	1 (13)
Medications				
Digoxin	na	4 (31)	4 (36)	2 (25)
Antiplatelet	na	6 (46)	0 (0)	0 (0)
Anticoagulation	na	8 (62)	1 (9)††	0 (0)
Statin	na	5 (38)	0 (0)	0 (0)
PPI	na	8 (62)	2 (18)†	3 (38)
Vitamin D	na	7 (54)	6 (55)	6 (75)

CVD=cerebrovascular diseases; PVD=peripheral vascular diseases; COPD=chronic obstructive pulmonary diseases; AF=atrial fibrillation; QTI=QT interval; IVCD=intraventricular conduction delay; PPI= proton pump inhibitors. Categorical variables reported by count with percentage in parenthesis: demographics, diagnosis of comorbidities, IVCD, and medications. Continuous variables reported by median with interquartile range in parenthesis: physical assessments and QT interval. Chi-squared test, independent sample t-test or one-way ANOVA (followed by Tukey post hoc analysis), Kruskal Wallis or Mann-Whitney U test was used as appropriate to compare the variables between groups. A two-tailed $p<0.05$ was considered statistically significant. *p<0.05, **p<0.01, ***p<0.001 compared to A-NC; #p<0.05, ##p<0.01, ###p<0.001 compared to P-NC; †p<0.05, ††p<0.01, †††p<0.001 compared to A-DC.

Tissue Procurement and Preparation. Heart tissue procurement strictly followed our well-established protocols[129, 178, 415, 416]. For this study, transmural myocardium from the mid-anterior LV free wall (approximately two-thirds below the aortic valves) of individual heart was captured

by avoiding the epicardial fat and scar tissues (**Fig. 5.1D**). All the full-thickness specimens were snap-frozen or OCT-mounted frozen in liquid nitrogen within 10 minutes following explantation, and then stored in -80°C freezers for subsequent molecular and histochemical analyses (**Fig. 5.1D**).

5.4.2. Tissue Genotyping and Pathologic Variants Analysis

Genomic DNA was isolated from the frozen LV specimens using Genomic DNA Extraction Kit (Qiagen) followed by whole genome sequencing (WGS) on Illumina NovaSeq instruments. All sequencing reads were aligned to GRCh37 (hg 19) using BWA-MEM[184]. Single nucleotide variants (SNVs) and small indels were identified using the HaplotypeCaller from Genome Analysis Tool Kit (GATK; version 3.8)[185]. dbNSFP[186], gnomAD (version 2.1)[187], and SnpEff (version 4.3t , bundled with GRCh37.75) were applied for annotating variant call format files.

5.4.3. Histopathological Analysis

Myocardial Fibrosis. The excised transmural biopsies were immediately fixed in 10% buffered formalin (containing 4% formaldehyde) followed by embedding in paraffin. Thin sections (5μm) of the tissue were stained with picro-sirius red (PSR) and Masson's trichrome for morphometric analysis. The tissue sections were first deparaffinized in xylene and alcohol grades, then rehydrated in water and subjected to respective staining protocols as described previously[26, 188, 415]. The fibrotic pattern was assessed by visualization under a bright field microscope (DM 4000 B, Leica), together with fibrillar content quantification under Olympus IX81 fluorescence microscope. Image analysis was performed on MetaMorph software (Basic version 7.7.0.0, Molecular Devices, Inc). From each heart, n=2 sections were stained with n=20-25 random images analyzed from each section in a blinded manner. Within each image, the fraction of total collagen volume relative to the whole image field was calculated.

Cardiomyocyte Hypertrophy. Cardiomyocyte morphology was evaluated fluorescently by applying wheat germ agglutinin (WGA) staining on the optimal cutting temperature (OCT) compound-mount (TFM, General Data Company) tissue blocks, which were snap frozen in liquid nitrogen as previously published[26, 129, 191, 415]. Briefly, cryo-sectioned slices (5-10μm) were fixed with 4% paraformaldehyde for 20 mins followed by rehydration in 1X PBS for 30 mins at RT.

Sections were permeabilized using 100% precool methanol (-20°C) for 10mins, and then blocked with 4% BSA for 1 hr at RT. After rigorous washings, the sections were incubated with WGA (1:200, W11261, Invitrogen) for 30 mins at RT followed by application of 20µl/section DAPI gold anti-fade mountant (#P36931, Invitrogen). The cardiomyocyte membranes were visualized under Olympus IX81 fluorescence microscope and analyzed by MetaMorph software (Basic version 7.7.0.0, Molecular Devices, Inc). From each heart, n=2 sections (including one technical control) were examined, with n=20-25 random images captured from each section in a blinded manner. Within each image, n=25 cardiomyocytes were unbiasedly sampled from the whole regions (four corners & center) into our analyses.

Autofluorescence Quench and Confocal Microscopy. Non-specific lipofuscin autofluorescences of the human OCT-embedded blocks were significantly eliminated by applying TrueBlack® Lipofuscin Quencher (#23007, Biotium) to the cryosections for 5 mins at RT. Standardized tissue fixation, deparaffinization, antigen retrieval, and permeabilization were performed as described above[415]. The sections were gently washed with 1XPBS for 3 times, blocked with 5% serum for 1 hr at RT, and then incubated with primary antibody overnight in a humidified hood at 4°C, as per manufacturer instructions. The sections were further incubated with Alexa Fluor 594-conjugated secondary antibodies (Invitrogen, USA) against the host species of individual primary antibody for 2 hrs at 37°C. Lastly, Alexa Fluor 488-conjugated WGA (W11261, Invitrogen), mounted with DAPI antifade (#P36931, Invitrogen), was applied to outline plasma membrane and nuclei, respectively. Intracellular protein colocalizations were acquired using laser scanning confocal microscopy (Leica TCS SP5, Leica Microsystems), and quantitative analyses were carried out using Fiji ImageJ (National Institute of Health, Bethesda, MD, USA) software [191, 415].

5.4.4. Whole Transcriptomic Sequencing

A schematic of the experimental workflows was depicted in **Fig. 5.1C-D**, which included transcriptomic, phosphoproteomic and proteomic mappings on the human explanted hearts. We primarily focused on the subgroup comparisons between **A-DC versus P-DC, A-DC versus A-NC, and P-DC versus P-NC**. Transcriptome sequencing, including sample preparation, library construction, and Illumina sequencing were carried out by Novogene Corporation Inc. (California,

USA). The below reported methods were modified based on the standard procedures provided by Novogene.

RNA Extraction and RT-PCR. Total RNA isolation was performed by Trizol-chloroform extraction method[192] on an RNA dedicated bench. Briefly, ice-cold Trizol (1ml) was added to an eppendorf tube containing 40-60mg heart tissue, followed by homogenization with a metal bead at 25rpm for 3 mins. The homogenization was further repeated twice at 25rpm for 2 mins, and the homogenates were incubated at RT for 5 mins, and then centrifuged at 12,000g for 10 mins at 4℃. 200µl chloroform was added to a new eppendorf tube containing the supernatant collected from the centrifugation, followed by vigorous shaking for 15 secs and incubation at RT for 2-3 mins. Next, centrifuged again at 12,000g for 10 mins at 4℃, and the upper colorless phase was transferred to a new eppendorf tube with addition of 500µl isopropanol per tube. The lysates were thoroughly mixed by inverting several times, and then incubated at -20℃ overnight. After 24 (-72) hrs, centrifuged at 12,000g for 10 mins at 4℃, and the supernatant was completely discarded. 1ml ethanol (75%) was added by pipetting gently until the pellet was dislodged, and finally, centrifuged at 7,500g for 10 mins at 4℃. After the supernatant was carefully removed, dissolved the air-dried (5-10 mins) pellet with 12-20µl RNase-free H_2O.

Isolated RNA (1µg) was reversed transcribed with random primers (Invitrogen), followed by cDNA synthesis using SuperScript® II Reverse Transcriptase (Invitrogen). Real-time quantitative PCR was applied using TaqMan premixed assays (ThermoFisher Scientific™) for gene expressions in the human heart tissues. All procedures were strictly carried out on ice.

RNA Quantitation and Qualification. RNA degradation and contamination was firstly monitored on 1% agarose gels. The RNA purity was checked using the NanoPhotometer® spectrophotometer (Implen, CA, USA), while the RNA integrity and quantitation were further assessed using the RNA Nano 6000 Assay Kit of the Bioanalyzer 2100 system (Agilent Technologies, CA, USA).

Library Construction. A total amount of 1μg RNA per sample specimen was used as input material for RNA preparation. Sequencing libraries were generated using NEBNext® Ultra™ RNA Library Prep Kit for Illumina® (NEB, USA) as per manufacturer's recommendations.

Clustering and Sequencing Depth. The clustering of the index-coded samples was performed on a cBot Cluster Generation System using PE Cluster Kit cBot-HS (Illumina) based on manufacturer's suggestions. Following cluster generation, the library preparations were sequenced on the Illumina HiSeq platform (NovaSeq 6000). Paired-end read length of 150bp was generated, with a total sequencing depth of 30M pair reads per biological sample.

Quality Control and Raw Data Processing. Quality control (QC) was performed at each step from RNA sample preparation to final data analyses, including total RNA purification and qualification, mRNA enrichment, double-stranded cDNA synthesis, end repair by polyA or adaptor addition, fragments selection and real-time quantitative PCR, library construction and quality assessment, transcriptome sequencing and reference genome mapping. Raw data (reads) of FASTQ format were firstly processed through fastp. In this step, clean data were obtained by removing reads containing adapter and poly-N sequences and reads with low quality from raw data. Q20, Q30, and GC content of the clean data were calculated. All downstream analyses were based on the clean data with high quality.

Mapping to Reference Genome. Reference genome and gene model annotation files were accessible from genome website (NCBI/UCSC/Ensembl). Paired-end reads were aligned to the reference genome using the Spliced Transcripts Alignment to a Reference (STAR) software, which was based on a previously undescribed RNA-seq alignment algorithm that used sequential maximum mappable seed search in uncompressed suffix arrays followed by seed clustering and stitching procedure. STAR demonstrated better alignment precision and sensitivity than other RNA-seq aligners for both experimental and simulated data.

Gene Expression Normalization and Unit. FeatureCounts was applied to count the read numbers mapped of each gene. Then RPKM of individual gene was calculated based on the length of the gene and reads count mapped to this gene. **RPKM**, Reads Per Kilobase of exon model per Million mapped reads, considers the effect of sequencing depth and gene length for the reads count at the same time, and is adopted for estimating gene expression levels[193].

Differentially Expressed Genes (DEG) Analysis. Differential expression analysis between two conditions/groups with three or more biological replicates per condition was performed using DESeq2 R package. DESeq2 determines differential expression in digital gene expression data by a negative binomial distribution-based model. The resulting *p values* were adjusted using the Benjamini and Hochberg's approach for controlling the False Discovery Rate (FDR). Genes with an adjusted $p\ value < 0.05$ found by DESeq2 were assigned as differentially expressed.

Differential expression analysis of two conditions without biological replicates was performed using the edgeR R package. For individual library, the read counts were adjusted by Trimmed Mean of M values (TMM) through one scaling normalized factor before conducting any differential gene expression analysis. The *p values* were adjusted using the Benjamini and Hochberg methods. Corrected $p\ value\ of\ 0.005$ and $|\log_2^{(\text{Fold Change})}|$ of 1 were set as the threshold for significantly differential expression.

Functional Enrichment Analyses. Shared functions among genes were searched by integrating the biological knowledge from various manually-curated biological ontologies[194]. Gene Ontology (GO) annotates genes to biological processes (BP), molecular functions (MF), and cellular components (CC) in a directed acyclic graph structure. Kyoto Encyclopedia of Genes and Genomes (KEGG) annotates genes to high-level functional pathways. Reactome annotates genes to pathways and reactions in human biology. The Human Disease Ontology (DO) annotates genes to pathways and DisGeNET annotates genes to pathways.

GO Enrichment Analysis. Gene Ontology, http://www.geneontology.org/, is a major bioinformatics classification system to unify the presentation of gene properties across all species. GO enrichment analysis of differentially expressed genes was implemented by the clusterProfiler

R package. GO terms with corrected *p value < 0.05* were considered significantly enriched by differential expressed genes.

KEGG Pathway Enrichment Analysis. KEGG is a database resource for understanding high-level functions and utilities of the biological system, such as cells and organisms, from molecular-level information, especially large-scale molecular datasets generated by genome sequencing and other high-throughput experimental technologies (http://www.genome.jp/kegg/). clusterProfiler was applied to examine the statistical enrichment of differential expression genes in KEGG pathways. KEGG terms with adjusted *p value < 0.05* were considered significant enrichment.

Reactome Enrichment Analysis. Reactome (https://reactome.org/) is an open-source, peer-reviewed and manually-curated pathway database, providing knowledge on signaling and metabolic molecules involved in biopathological reactions. We used clusterProfiler for statistical Reactome enrichment of differential expression genes. Most importantly, clusterProfiler applies biological term classification and enrichment analyses to gene cluster comparison, helping to better understand higher order functions of biological system. In general, Reactome terms with adjusted *p value < 0.05* were considered significant enrichment.

DO Enrichment Analysis. The Human Disease Ontology (DO, http://www.disease-ontology.org) is a community driven standards-based ontology that provides the disease interface between data resources through ongoing support of disease terminology needs, which is associated with human disease and gene function. We used an R package called clusterProfiler for statistical DO enrichment of differential expression genes. DO terms with adjusted *p value < 0.05* were considered significant enrichment.

DisGeNET Enrichment Analysis. The DisGeNET (https://www.disgenet.org) remains the discovery platform which represents one of the largest publicly available databases of genes and variants related to human diseases. We also used clusterProfiler in R for statistical DisGeNET enrichment of differential expression genes. DisGeNET terms with adjusted *p value < 0.05* were considered significant enrichment.

5.4.5. Proteomic and PhosphoProteomic Mapping

Human Heart Tissue Preparation. Human heart explants were procured as described above, and further processed with minor modifications[195, 196]. Briefly, snap-frozen tissue (50mg) was mechanically homogenized in 1ml of 8M urea solution supplemented with protease (cOmplete™, Sigma) and phosphatase (PhosSTOP™, Roche) inhibitors cocktail, followed by centrifugation at 13,000g for 10 mins at 4℃. After collecting the supernatant, centrifugation was repeated in the same manner until there was no visible pellet. The supernatant now containing all intracellular proteins without interferences from cellular debris, fibrotic clots, and contractile apparatus components (which may cause ion suppression) were snap-frozen in liquid nitrogen and then at -80℃ freezers for downstream mass spectrometry analyses.

Protein Digestion and Quantitation. A total of 100µg protein per biological replicate was used, following quantitation of the protein concentration (µg/µl) by Bradford assay. As we reported before[195, 196], a final concentration of 2.5mM DTT was added to each homogenate for 1 hr at RT to for optimal protein purification, and then a final concentration of 5mM iodoacetamide was added to each homogenate for alkylation and incubated in the dark for 30mins at RT. The homogenates were diluted in 50mM ammonium bicarbonate which brought the urea concentration below 1M, followed by addition of sequencing-grade trypsin (Promega) in a 1:20 protein:protein ratio for overnight digestion at 37℃. Formic acid (to a final concentration of 1%) was subsequently added to sample solutions for blocking trypsin activities. All digested peptide fragments were isolated and desalted with C18 TopTips (Glygen), and then dried to completion by SpeedVac (ThermoFisher Scientific™). Finally, all prepared samples were resuspended in 80% acetonitrile (ACN) with 0.1% triflouroacetic acid (TFA) before subjected to HILIC-HPLC fractionation and TMT labeling.

TMT Labeling. 100µg total protein (per TMT label), as determined by Bradford assay, were labeled with TMT10-plex reagents according to the manufacturer's instructions (ThermoFisher Scientific™)[195, 196]. In brief, dried peptides from individual sample were resuspended in 100µl of triethylammonium bicarbonate (Sigma), with addition of corresponding

TMT labels which were firstly suspended in 41µl of ACN. The subsequent labeling reaction was developed for 1 hr at RT and was ended by quenching with 8µl of 5% hydroxylamine (Sigma). Samples from same group were pooled together, and the combined samples were dried to completion by SpeedVac and was further resuspended in 80% ACN with 0.1% TFA for HILIC fractionation.

Chromatographic Fractionation and Phosphopeptide Enrichment. HILIC fractionations were performed using the 2.0 X 150mm X 5µm particle TSKgel Amide-80 column (Tosoh Biocience) and Agilent 1200 HPLC system (Agilent Technologies, CA, USA). Two mobile phases, namely, buffer A containing 98% ACN, 0.1% TFA and buffer B consists of 2% ACN and 0.1% TFA, were applied, and a total of 1mg digested peptides were loaded onto the column at a flow rate of 250 µl/min. The liquid chromatography was set up as we previously reported[195, 196]: 1) a 3 min loading in 20% buffer B; 2) a gradient of 20-40% buffer B for 27 mins; 3) a gradient of 40–100% buffer B for 3 mins; 4) 100% buffer B for 5 mins; 5) a gradient of 100–20% buffer B for 2 mins; and finally, 6) 20% buffer B for 10 mins. The eluted samples were further fractionated into 1.5ml tubes at 2 min intervals, and then dried to completion. 10% of each fraction was reserved for global proteomic analysis.

Phosphopeptide enrichment from the remaining HILIC fractions was conducted using TiO2-coated Mag Sepharose beads (GE Life Sciences) as per the manufacturer's instructions. Briefly, individual HILIC fraction was dried to completion by SpeedVac (ThermoFisher Scientific™) and then was resuspended in 200µl of binding buffer (1M glycolic acid, 80% ACN and 5% TFA), followed by 1 hr incubation with the prepared magnetic beads. Next, it was washed once with 500µl binding buffer and additional three times with washing buffer (80% ACN and 1% TFA), and then eluted in 100µl 5% ammonium hydroxide solution for a total of three times. Eluted phosphopeptides were immediately dried to completion and resuspended in 20µl 1% formic acid prior to liquid chromatography–mass spectrometry analysis. Resuspended peptides and phosphopeptides from individual HILIC fraction were analyzed in technical duplicates, respectively.

Liquid Chromatography-Mass Spectrometry. The liquid chromatographic component was composed of a reverse-phase Thermo Acclaim PepMap pre-column (2cm in length, 75µm in diameter, 3µm C18 beads) and a Thermo PepMap RSLC C18 analytical column (50cm in length, 75µm in diameter, 2µm C18 beads) connected with an Easy-nLC 1200 system (ThermoFisher Scientific™)[195, 196]. The gradient (3 hr) was made of buffer A (5% ACN, 0.1% formic acid) and buffer B (85% ACN, 0.1% formic acid) and had a flow rate of 220 nl/min. Prior to each injection, the equilibration was achieved with 100% buffer A on both the pre (20µl) and analytical (3µl) columns, followed by the nanoflow gradient as previously reported: 5–35% buffer B for 156 mins, 35–100% buffer B for 9 mins and 100% buffer B for 15 mins. The peptides and phosphopeptides injected into the Q Exactive HF mass spectrometer (ThermoFisher Scientific™) were directly ionized by the EasySpray ion source (ThermoFisher Scientific™). For each selected MS1 full scan mass spectrum in profile, MS2-dependent scans were acquired by HCD fragmentation with normalized collision energy (32%). Full scan settings were documented as previously reported: 1.2 x 10^5 resolution, maximum injection time (50ms), ion packet setting for automatic gain control (3 x 10^6), and a range of 350-1450 m/z. Similarly, MS2 scan settings were as follows: 6 x 10^4 resolution, maximum injection time (100ms), ion packet setting for automatic gain control (1 x 10^5), and a fixed first mass at 100 m/z with 1.2 m/z isolation window. Unassigned parent ions with charge states > 6 were excluded from MS2 analysis, and with dynamic exclusion range set at 20s. Identical liquid chromatography and mass spectrometry settings and procedures were applied to both proteomic (unenriched) and phosphoproteomic (phosphopeptide-enriched) fractions.

MS Data Processing and Analysis. MaxQuant software (v.1.6.2.10, www.coxdocs.org/doku.php?id=maxquant:start) were used for analyzing all raw MS data files against the online human protein sequence database (http://www.uniprot.org/taxonomy/9606) with the application of "Reporter ion MS2" 10-plex TMT settings[195, 196]. With a reporter-ion tolerance at 0.003, our standardized approach allowed for two missed trypsin-cleavage sites and variable modifications for protein phosphorylation at residues of S, T, and Y, N-terminal acetylation, methionine oxidation, asparagine and glutamine deamidation as previously reported. Carbamidomethylation was set as a fixed modification at cysteine residues. A *FDR = 1%* was

adopted for filtering candidate peptides and phosphopeptides by searching of a reverse-sequence decoy database.

MaxQuant output files were further processed by Perseus (v.1.6.0.7) and Bioconductor packages in R Studio. The output files including report ion (TMT-labeled data) intensities of protein groups and phosphorylation sites (Ser, Thr, Tyr) firstly underwent log_2-transformation and quartile-normalization by applying "width adjustment" in Perseus[197], and their identifications were ensured by filtering the entries that corresponded to reverse database identifications, potential contaminants, and those with single site identification. Singly or multiply phosphorylated phosphopeptides were reported as separate entries despite their identified values of identical phosphorylation sites. Following normalization individually, proteomic and phosphoproteomic datasets of each sample were combined to construct the merged datasets at both gene and protein levels (which may have multiple entries due to multiple identified phosphorylation sites on identical phosphoproteins), for downstream unsupervised principal component analyses (PCA, all data), and hierarchical clustering ($p<0.05$, all data). Merged datasets were further trimmed by removing phosphorylation sites with <0.7 localization probability as well as duplicate entries at the gene levels to ensure only the most significantly altered protein and phosphorylation sites were kept. Subsequently, the processed merged datasets were subjected to independent biological pathway enrichment by GSEA[198] or gProfiler[199] using custom databases containing annotated GO terms (including BP, MF, and CC) and other curated pathways. Enriched gene sets were expected to have 10 to 500 associated components, with both *p value* and *FDR* less than 0.1. Hierarchical clustering was performed in Perseus (v.1.6.0.7). Euclidian distance without constraints on row and/or column clustering was adopted after preprocessing data by *k*-means, 10 iterations, and a maximal number of 300 clusters.

Targeted Kinase Motif Prediction. Significantly altered phosphorylation sites (two-tailored Student's t-test, $p<0.05$) between individual comparisons were annotated using the liner motifs function in Perseus which centered the sequencing window around the modified phosphorylation sites for identification of corresponding kinases[195-197].

Pathway Enrichment Analysis and Network Biology Visualization. Enriched gene-sets using ENSEMBL ID as a unique identifier were uploaded to gProfiler, a widely accepted web server (https://biit.cs.ut.ee/gprofiler/gost), for functional pathway enrichment analysis[194, 200]. Significantly upregulated and downregulated gene-sets from all three omics datasets (transcriptome, proteome, phosphoproteome) were inputted separately, for exploration of over- and down-represented biological pathways (more than would be expected by chance) associated with the inputted query gene list between individual comparison. g:GOSt tool was applied against homo sapiens (human) for query gene list which was ranked in order by significance level in decreasing manner. g:SCS (default) or Benjamini-Hochberg FDR method with user-defined threshold at 0.05 was selected as appropriate for multiple testing correction, and all annotated genes were mapped to well-known databases including GO, KEGG, Reactome, WikiPathways, Human Protein Atlas, Human Phenotype (HP) Ontology. The enrichment output is presented as publication-ready Manhattan plot and extensive tables with detailed information about individual biological pathway (BP) term and associated gene lists between comparisons.

The statistically enriched and large-size biological pathways were further assembled into functionally related groups using the Enrichment Map tool (http://baderlab.org/Software/EnrichmentMap)[201] to visually cluster similar BP terms under major biological themes in CytoScape[194, 202]. The cutoffs of *p-value*, *FDR Q-value* were both set at 1.0 by default, and overlap coefficient was tuned at 0.5 as similarity cutoff. Individual node (colored by enrichment scores) represented the biological pathways, while the edge indicates the connection (i.e., shareable genes) between different pathways and its size was determined by the number of common genes shared between connected pathways. AutoAnnotate plugin (https://autoannotate.readthedocs.io/en/latest/) was further applied in CytoScape to automatically cluster similar networks using clusterMaker2 and then add a concise semantic summary (enclosing shape and label) of all the BP terms attached to the nodes within each new cluster via WordCloud, while maintaining the relationship between multiple sets of annotations for any single network[203]. Large network containing many clusters can be collapsed for simplified view and better interpretation.

5.4.6. Ultra-Structural and Functional Analysis

Transmission Electron Microscopy. Human explanted myocardium were collected transmurally and processed as previously reported[415]. Briefly, fresh tissues (<1mm^3) were promptly fixed in 2% glutaraldehyde with a physiological pH and 360 mOsm osmolarity at 37℃. After overnight storage in 4℃, the specimens were post-fixed in 1.5% $K_4Fe(CN)_6$ and 2% osmium tetroxide (OsO_4) and then completely washed with 0.1M sodium cacodylate (pH 7.2) and 0.1M sodium acetate (pH 5.2) buffers. High-contrast en bloc staining was performed by immersing the post-fixative samples in solution of 2% uranyl acetate (UA) and 0.1M sodium acetate (pH 5.2), followed by dehydration using graded ethanol and acetone solutions and immediate infiltration with Spurr's Resin (Leica Electron Microscopy Sciences, Hatfield, PA, USA) for 24 hours. Two resin blocks per sample were sectioned along the longitudinal axis of myofilaments using a ultramicrotome diamond knife, and four non-consecutive ultrathin sections (70μm) were further post-stained with 4% UA and 4% lead citrate.

Four 100 μm^2 regions were randomly selected to obtain n=1 image at 2000X resolution, n=4 images at 4000X resolution, and n=6 images at 10000X resolution per section for a total of 44 images per sample (H7650, Hitachi, Tokyo, Japan). Two investigators independently evaluated cardiomyocytes for the presence and severity of intramitochondrial inclusions, mitochondrial cristae quality as well as sarcomeric ultrastructural integrity (ImageJ software, National Institute of Health, Bethesda, MD, USA). We have previously established a scoring system[415] which comprehensively evaluates mitochondrial morphology and architecture and ranks each specimen as healthy or with varying degree (mild, moderate, severe) of abnormalities. Blinded assessment of all images was randomly carried out in triplicate by two investigators, and a third adjudicator was involved should any discrepancies arise between the individual assessments. For consistency, sarcomere or mitochondria whose outer membrane was cut off by the image field of view were excluded from analysis.

Spectrophotometric Assays for ETC Enzymes. LV tissues were homogenized in ice-cold homogenization buffer (20mM Tris, 40mM KCl, 2mM EGTA, pH=7.4, with 50mM sucrose added upon homogenization). The homogenates were centrifuged at 600g for 10 minutes at 4°C to remove cellular debris. Supernatant was collected for assessing the enzymatic activity of

NADH:ubiquinone oxidoreductase (COX I), succinate dehydrogenase (SDH, COX II), decylubiquinol cytochrome c oxidoreductase (COX III), NADH cytochrome c oxidoreductase (COX I + III), succinate cytochrome c reductase (COX II + III), cytochrome c oxidase (COX IV) and citrate synthase (CS)[384, 415].

Enzyme activity (nmol·min^{-1}·mg^{-1}) was normalized to volume and protein concentration, following protein determination with Bradford assay. Specifically, it is calculated based on the following equation: enzyme activity = (△Absorbance/min x 1000)/[(extinction coefficient x volume of sample loaded in ml) x (protein concentration of sample in mg/ml)]. The reaction specificity was ensured by subtracting the inhibitor-resistant activity from the total enzymatic activity for individual ETC enzyme, which was conducted in parallel. The inhibitor of COX I (1mM rotenone), COX II (1M malonate), COX III (1mg/ml antimycin A), COX I + III (1mM rotenone), COX II + III (1M malonate), and COX IV (10mM KCN) was added to each corresponding reaction mixture prepared, respectively[384, 415]. Each sample was assayed in triplicate.

5.4.7. Immunoblotting Analysis

Fractionation and Western Blot. Subcellular fractionations were performed with minor modifications [191, 415]. LV tissues (~50-80mg) were mechanically homogenized (20 rpm/min, 2 mins, 4℃) in 500µl radioimmunoprecipitation assay (RIPA, 50 mM Tris-HCl, 150mM NaCl and 1mM EDTA, pH=7.4) buffer supplemented with 1X protease inhibitor cocktail (Roche). The homogenate was centrifugated (2900 g, 20 mins, 4℃) to precipitate the crude nuclear from the cytosolic and membrane proteins (first supernatant). The pellet was gently washed and homogenized again using the aforementioned method, followed by a second homogenization (25 rpm/min, 3 mins, 4℃) in 200µl commercial RIPA buffer (ThermoFisher, 25mM Tris-HCl, 150mM NaCl, 1% NP-40, 1% sodium deoxycholate and 0.1% SDS) with addition of 1X protease inhibitor cocktail (Roche), which produced pure nuclear fraction. The first supernatant was further ultra-centrifuged (29000 g, 45 mins, 4℃) to pellet the membrane and simultaneously harvest cytosolic components from the second supernatant. The purity of each fraction was further validated by using anti-rabbit TLR-4 (Santa Cruz, sc-10741; membrane marker), anti-rabbit Caspase-3 (Cell Signaling, 9662S; cytosolic marker) and anti-rabbit Histone H3 (Cell Signaling, 4499s; nuclear marker)[333, 415].

For mitochondrial fractionation, frozen LV tissues were ground and homogenized in fractionation buffer with recipe of 250mM sucrose, 10mM Tris-HCL, 1mM EDTA, 1mM sodium orthovanadate, 1mM sodium fluoride, 10μg/L aproptinin, 2μg/L leupeptin, and 100μg/L pepstatin[417]. The homogenate was first centrifuged (700g, 10 mins, 4°C) to remove any cellular debris. The supernatant was then decanted and centrifuged again (10,000g, 20 mins, 4°C) to obtain the "crude" mitochondrial fractions as pellet, which was further resuspended in fractionation buffer. Mitochondrial protein concentrations were calorimetrically determined using the Bio-Rad BCA protein assay kit.

Western blotting was performed on snap-frozen human myocardium tissues[191, 333, 415]. A total of 500μg protein was extracted; and appropriate aliquots of protein (45 - 60μg) were separated on 6% - 20% gradient sodium dodecyl sulfate polyacrylamide gel electrophoresis (SDS-PAGE) and later transferred onto 0.2μm PVDF membranes. They were subject to immunoblotting with the following primary antibodies: anti-mouse NCX1 (Invitrogen, MA3-926); anti-rabbit SERCA2 (Cell Signaling, 9580s); anti-rabbit phosphor-(Ser16)/anti-mouse total PLN (Badrilla, phosphor A010-12, total A010-14); anti-rabbit phosphor-(Thr172)/anti-rabbit total AMPKα (Cell Signaling, phosphor 2531s, total 2532s); anti-rabbit phosphor-(Ser473)/anti-rabbit total AKT (Cell Signaling, phosphor 9271, total 9272); anti-rabbit phosphor-(Thr308)/anti-rabbit total AKT (Cell Signaling, phosphor 9275, total 9272); anti-rabbit phosphor-(Ser9)/anti-rabbit total GSK3β (Cell Signaling, phosphor 9336s, total 9315); anti-rabbit phosphor-(Thr180/Tyr182)/anti-rabbit total p38 MAPK (Cell Signaling, phosphor 9215s, total 9212s); anti-rabbit phosphor-(Thr202/Tyr204)/anti-rabbit total p44/42 MAPK (Erk1/2) (Cell Signaling, phosphor9101Ss, total 9102s); anti-rabbit phosphor-(Thr183/Tyr185)/anti-rabbit total SAPK/JNK (Cell Signaling, phosphor 4668, total 9252), and subsequently incubated with HRP-conjugated secondary antibodies at 1/5000 dilution (Cell Signaling) against the host species of individual primary antibody for 2 hrs at 37°C. All blots were visualized by ImageQuant LAS 4000 (28955810, GE Health Care, Biosciences, Uppsala, Sweden) with band intensity quantitation, and total protein amount were determined by MemCodeTM reversible stain (24585, Thermo ScientificTM) as a loading control for all proteins. The level of phosphorylation was calculated by normalizing signaling intensity of the phosphorylated protein by the band intensity of total protein of interest. To avoid exhausting the samples with limited quantity, certain blots were reprobed with a second targeted (unphosphorylated) protein after incubation in RestoreTM Western Blot Stripping Buffer (ThermoFisher 21059) for 15-30 mins at

RT, followed by vigorous washing using combination of 1X TBST (3rpm, 5mins x3) and 1X TBS (3rpm, 5mins x3), and complete blocking by 5% non-fat milk for 1 hour (3rpm, RT).

5.4.8. Statistical Analysis

No statistical algorithms were applied to predetermine the sample size. Our experiments were conducted in a randomized manner, whereas the investigators were blinded in sample allocation and outcome assessments[415].

Data Reporting. Shapiro-Wilk test and Levene test were firstly applied to check the normality of data distribution and homogeneity of variance, respectively. Continuous variables were reported as medians with interquartile ranges (median, Q1-Q3) for clinical parameters, or means ± standard deviations (mean ± SD) for experimental measurements. Categorical data were summarized as numbers with percentages (integer, %). One-way ANOVA (followed by Tukey or Bonferroni post-hoc analysis), or independent sample t-test was used to compare continuous variables between subgroups, while Mann-Whitney U test or Kruskal Wallis test was applied for non-parametric comparisons as appropriate. All categorical data were analyzed by Chi-squared test or Fisher's exact test where applicable.

Data Presentation. Continuous datasets were visualized by box plots with overlapping data points, or bar charts (upper line of the bar represents mean value) in a consistent manner. Pearson's correlation or Spearman rank correlation was used as applicable to evaluate the statistical association between variables of interest, including parametric and non-parametric variates, respectively. Multiple linear regression models were performed as applicable to estimate the relationship between two or more explanatory variables and the dependent variable, including the logistic regression algorithm for binary outcome prediction. Data visualization and graphical representation was performed on Origin for Windows, Version 2018b (OriginLab Corp., M.A., USA), and GraphPad Prism for Windows, Version 9.3.0 (GraphPad Software, C.A., USA). IBM SPSS Statistics for Windows, Version 21 (IBM Corp., N.Y., USA) was used for data analyses and narrative interpretation. A two-tailed $p\ value < 0.05$ was considered statistically significant.

5.5. Results

5.5.1. Clinical Characteristics of Pediatric and Adult Patients with DCM

Our diseased cohort consisted of eight prepubertal children [P-DC: 5M:3F, 2.6 (1.5-9.1) years] and thirteen adults [A-DC: 8M:5F, 51.0 (39.0-60.0) years] patients with end-stage HF due to idiopathic or familial DCM who underwent heart transplantation at different life stages (**Table 5.1**). Patients with a prior implant of mechanical unloading device, such as ventricular assistant devices, were excluded from our study; regardless of age, LVEF remained comparable between the two failing groups [A-DC: 24.8 (17.4-30.6) % vs. P-DC: 24.8 (18.3-29.6) %] (**Table 5.1**). While both cohorts had a similar prevalence of hypertensive disorders, A-DC demonstrated overall higher rates of comorbid incidents such as renal dysfunctions, and implants of cardiac electrical devices (**Table 5.1, 5.2**). As for HF medications, those receiving the ACE inhibitors (A-DC: 53.8% vs. P-DC: 62.5%), beta-blockers (A-DC: 76.9% vs. P-DC: 75.0%), digoxin (A-DC: 30.8% vs. P-DC: 25.0%) and diuretics (A-DC: 84.6% vs. P-DC: 87.5%) remained comparable between adults and pediatric patients (**Table 5.1, 5.2**). Of note, while angiotensin receptor blockers (30.8%), antiplatelets (46.2%), anticoagulation (61.5%) and anti-statin (38.5%) medications remained common indications among A-DC, none was administered to the pediatrics (**Table 5.1, 5.2**). Interestingly, the anti-arrhythmic drugs (Class I-IV, A-DC: 23.1% vs. P-DC: 12.5%), mineralocorticoid receptor antagonists (MRA, A-DC: 53.8% vs. P-DC:37.5%), and proton pump inhibitors (PPI, A-DC: 61.5% vs. P-DC: 37.5%) were almost double prescribed in A-DC cohorts compared to the young counterparts (**Table 5.1, 5.2**).

Our age- and sex-matched control groups were carefully selected as previously reported[129, 178], and they consisted of eight pediatric [P-NC: 6M:5F, 0.8 (0.4-2.8) years] and twelve adults [A-NC: 5M:7F, 48.0 (35.3-54.0) years] donor hearts, respectively (**Table 5.1**). A-NC were obtained from brain-dead adult donors with no major comorbidities or prior cardiovascular histories, whereas P-NC were procured from contemporaneous prepubertal children with HLHS following successful transplantations. Both controls had maintained ejection function of the left ventricle [LVEF, P-NC: >60% (42.6-65.6) % vs. A-NC: >57.5 (50.0-60.0) %] and importantly, neither demonstrated cardiomyopathic pathogeneses as seen in the diseased groups (**Table 5.1, 5.2**). As such, they constituted scientifically sound and most feasible control models given the extreme rarity of pediatric healthy donor hearts in clinics (see **Limitations** for more discussion).

5.5.2. Disparate Myocardial Adverse Remodeling in Pediatric and Adult DCM Hearts

Adverse remodeling progression in pediatric dilated failing hearts was evaluated by contrasting to adult DCM hearts, after normalization to their age-matched controls, respectively.

Myocardial Hypertrophy. Overall, adults, including both diseased and nondiseased, had appreciably larger size of hearts than the children (**Fig. 5.1A**). Clearly, it was in line with the significant differences in their anthropometrics, namely, height (cm), weight (kg), and body surface area (m2) (**Table 5.1, 5.2**). Our macroscopic examinations of the explanted humans found a remarkable expansion of epicardial adipose tissue (EAT) in adults; however, such areal distribution of epicardial fat was strikingly minimal in kids (**Fig. 5.1A**). Consistently, the whole heart weights of A-DC were significantly heavier than A-NC [A-DC: 480.0 (376.0-546.0) vs. A-NC: 316.0 (304.5-345.0) gram, *p<0.001*, whereas the gravimetric measurements between pediatric subgroups [P-DC: 145.5 (120.0-212.8) vs. P-NC: 77.0 (54.0-122.5) gram, *p=0.370*] were not statistically significant despite a similar tendency as seen in adults (**Table 5.1; Fig. 5.2A**). We further evaluated the cardiomyocyte morphology and cross-sectional area by applying the WGA staining on flash-frozen OCT-mounted tissue blocks[26, 129, 191]. As expected, A-DC had remarkably hypertrophic cardiomyocytes than A-NC (A-DC: 1014.4 ± 160.3 vs. A-NC: 298.9 ± 83.8 μm2, *p<0.001*) (**Fig. 5.1B; 5.2B**), while no statistical significance was detected for the cardiomyocyte dimensions between pediatric subgroups (P-DC: 200.6 ± 107.8 vs. P-NC: 124.8 ± 15.2 μm2, *p=0.628*) (**Fig. 5.1B; 5.2B**) indicating that pediatric dilated failing hearts were less hypertrophic compared to A-DC.

Myocardial Fibrosis. We performed the morphometric assessment of the fibrotic pattern and quantification of the myocardial fibrillar collagen content, including from both interstitial and perivascular space, by applying PSR and Masson's trichrome staining onto the 5μm-section of formalin-fixed paraffin-embedded tissue blocks[26, 188]. PSR staining captured strikingly higher fraction volume of collagen deposition within A-DC (A-DC: 12.1 ± 3.3 vs. A-NC: 2.3 ± 0.7 %, *p<0.001*), but not in P-DC (P-DC: 4.0 ± 2.4 vs. P-NC: 1.5 ± 0.6 %, *p=0.197*), when compared to their corresponding age-matched controls (**Fig. 5.1B; 5.2C**). P-DC displayed minimal interstitial fibrosis as the primary fibrotic pattern, and contrarily, adult DCM hearts demonstrated overall

expanded patches of fibrosis with a significantly higher density of both interstitial and perivascular fibrillar ($p<0.001$), which was further confirmed by Masson's trichrome staining (**Fig. 5.1B**).

Ultrastructural Alterations. While both failing groups displayed severely dilated sarcomeric microstructures in relation to their contemporaneous controls (**Fig. 5.1C**), a greater degree of smear wavy Z lines associated with focal myofibrillar degeneration was only seen in A-DC. Such alterations indicated severe myofilament disarray, suboptimal fractional shortening, and compromised contractile force transmission in the dilated failing hearts, which was consistent with clinical echocardiographic parameters, such as increased LV internal dimensions at both end-systole (LVIDs, $p<0.05$) and end-diastole (LVIDd, $p<0.01$) (**Table 5.1**). Moreover, A-DC demonstrated significantly larger increase in measurements of LVIDs [A-DC: 56.0 (49.3-63.8) vs. P-DC: 46.0 (36.5-48.0) mm, $p=0.026$] and LVIDd [A-DC: 63.0 (59.5-67.3) vs. P-DC: 55.5 (43.5-58.5) mm, $p=0.040$] (**Table 5.1**) indicative of worsened LV dysfunction. The NC hearts also presented more gap junctions (**Fig. 5.1C**).

As for mitochondrial dynamics, irrespective of clinical phenotypes, their intracellular numbers and locations varied dramatically between young and aged groups. Our high-magnification electron microscope has consistently revealed the majority of cellular powerhouses in adult hearts were composed of interfibrillar mitochondria, whereas in the pediatrics, peri-nuclear mitochondria prevailed (**Fig. 5.1C**). Furthermore, the pediatric mitochondria outnumbered with a smaller size of mitochondria in general (**Fig. 5.1C**). Interestingly, we noted the peri-nuclear mitochondria were surrounded by a decent number of electron-dense molecules stained as dark dots, likely an indication of pathologically upregulated glycogen aggregation and initiation of autophagic processes in the pediatric failing hearts[418, 419]. Using our systematic scoring strategy previously reported[415], we further identified a greater number of severely collapsed and deformed mitochondria, featured as lucent swelling appearance, rupture of outer and inner membranes, degradative lysis of cristae, yet with increased aggregates of inclusion bodies, in the failing young group. Our evaluations recapitulated the exacerbated adverse remodeling and autophagic events in both young and adult dilated failing hearts with possibly different underlying mechanisms.

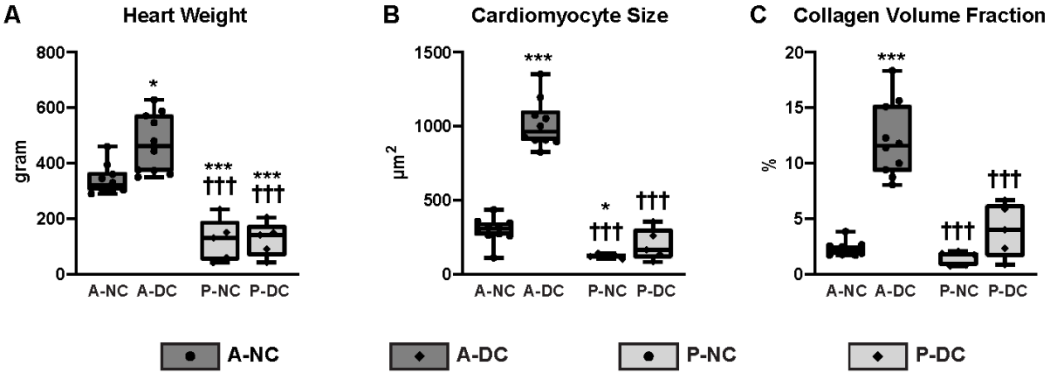

Figure 5.2. Quantifications of Heart Weight, Cardiomyocyte Size, and Collagen Content. A. Quantification of whole heart weights across four groups. n=10 for the adults (A-NC & A-DC), n=5 for pediatric subgroups (P-NC & P-DC), respectively. B. Cardiomyocyte cross-sectional area across four groups. n=10 for the adults (A-NC & A-DC), n=5 for pediatric subgroups (P-NC & P-DC), respectively. C. Relative quantification of myocardial fibrillar content across four groups. n=10 for the adults (A-NC & A-DC), n=5 for pediatric subgroups (P-NC & P-DC), respectively. *p<0.05, **p<0.01, ***p<0.001 compared to A-NC; #p<0.05, ##p<0.01, ###p<0.001 compared to P-NC; †p<0.05, ††p<0.01, †††p<0.001 compared to A-DC.

5.5.3. Transcriptome, Proteome, Phosphoproteome Coverages in Analyzed Comparisons

Global Omics Data Analyses. To achieve a global survey of DCM-related perturbations on cardiac signaling cascades at different development stages (**Fig. 5.1D**), we designed a three-tiered methodology using quantitative proteomic and phosphoproteomic profiling, in complementary with poly-A enriched next-generation RNA sequencing, on explanted human heart samples (**Fig. 5.1E**). For each group, we included n=6 diseased and n=6 age-/sex-matched control samples, which were marked with red circles in **Fig. 5.1D**, in all three sets of comparative analyses: 1) A-DC vs. A-NC; 2) P-DC vs. P-NC; and 3) A-DC vs. P-DC (**Fig. 5.1E**). By contrasting the DCM cohorts to their respective contemporaneous controls, we sought to recognize age as a potential confounding variable while primarily focusing on the third comparison between adult and pediatric patients with DCM.

To further confirm whether pediatric DCM represents a distinctly pathological cohort from the adult DCMs, we performed unsupervised principal component analysis (PCA) as well as

supervised Euclidean distance-based hierarchical clustering on the merged transcriptomic, proteomic, and phosphoproteomic datasets, respectively (**Fig. 5.3, 5.4**). Our findings showed that both adult and pediatric control specimens clearly separated from those presenting pathological conditions, and the segregations were most significant across the proteomic and phosphoproteomic datasets, albeit with a smaller proportion of components. In the direct comparison between adult and pediatric DCM, their class separations on proteome and phosphoproteome were clear and consistent in both PCA (**Fig. 5.3**) and hierarchical clustering analyses (**Fig. 5.4**). However, PCA algorithm showed minor intersection using RNA-Seq data (**Fig. 5.3**), indicating that a shared multigenic pathology may underlie the occurrence of adult and pediatric DCM (refer to **Discussion** for mutation analysis). Indeed, our results confirmed that pediatric DCM is a disparate entity possibly with a more aggressive nature of the disease that drives the early presentation of symptoms.

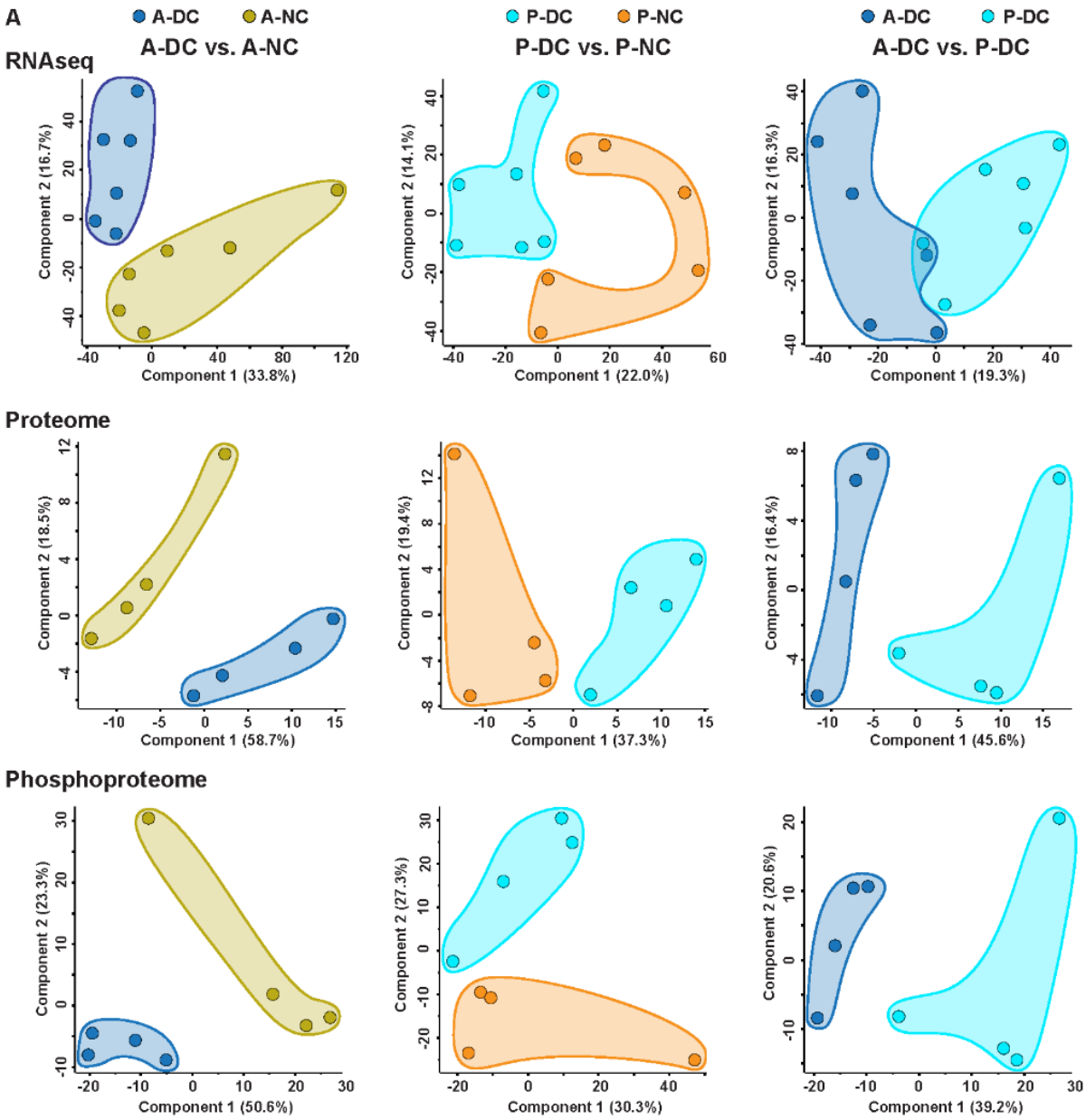

Figure 5.3. Principle component analyses (PCAs) of the (phospho-)proteomic and transcriptomic datasets. Each plot compared the similarity between subgroups. The distance between the dots indicated the similarity of the measured parameters at proteome, phosphoproteome and transcriptome level, respectively: the greater the difference between the measured parameters, the greater the distance between the pooled dots.

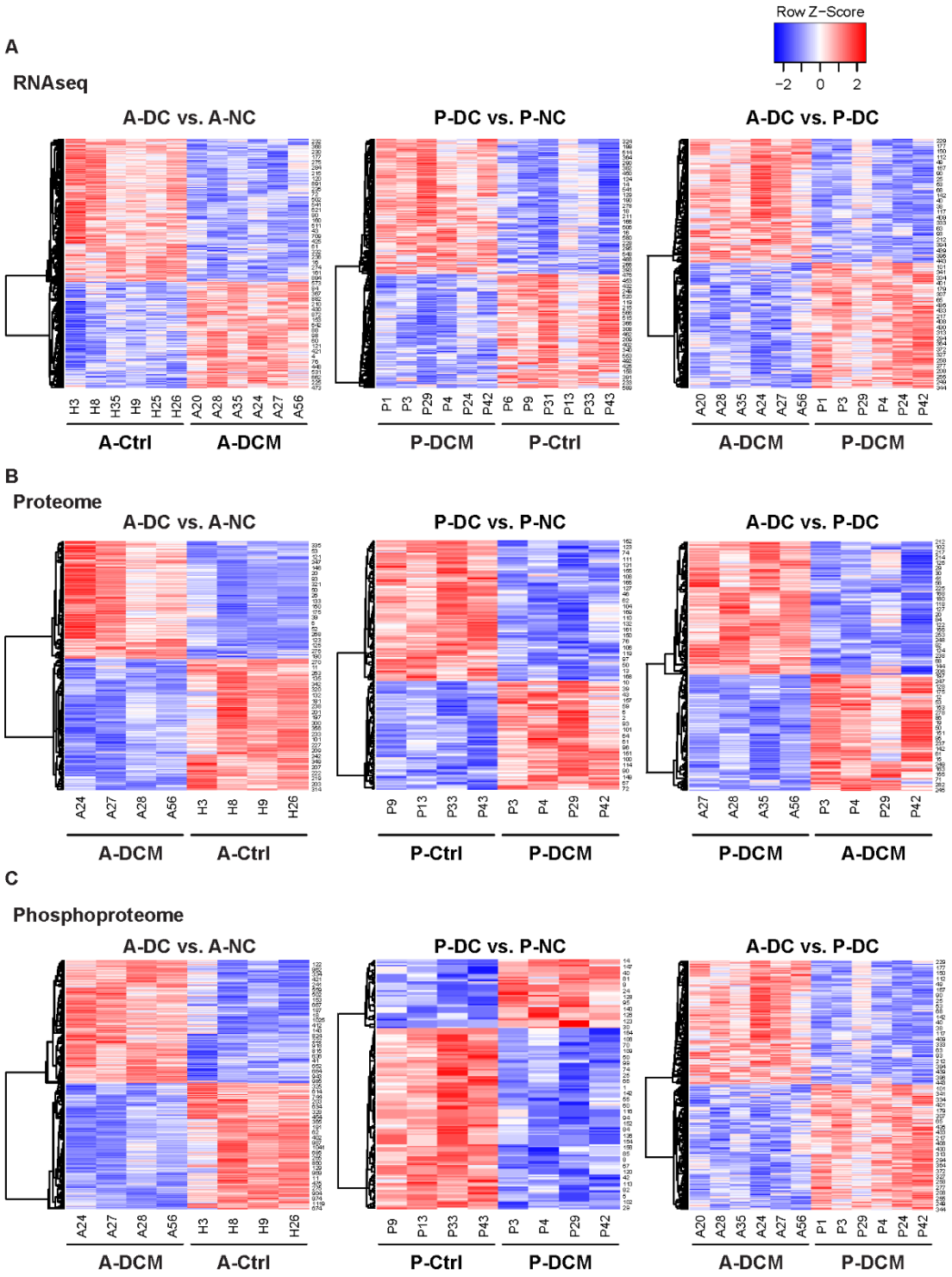

Figure 5.4. Supervised Euclidean distance-based hierarchical clustering on the merged transcriptomic (A), proteomic (B), and phosphoproteomic (C) datasets across comparisons. Each plot compared the similarity between subgroups.

Comparative Proteome and Phosphoproteome Analyses. We applied a phosphoproteomic multiplexing strategy using isobaric chemical-tagged labeling (TMT) to tackle the low yield of phosphoprotein and heterogeneity associated with individual clinical explants (see **Methods** for details). The mixture of negatively charged phosphopeptides was eluted by prefractionation using HILIC, followed by an additional round of affinity enrichment of phosphopeptides using immobilized TiO2 affinity chromatography (**Fig. 5.1E**). Our approach greatly minimized signal suppression caused by an increasing amount of negatively-charged phosphate moiety in the mixture[195].

We mapped a total spectrum of 174433 (A-DC vs. A-NC), 235836 (P-DC vs. P-NC), 179159 (A-DC vs. P-DC), as well as a corresponding phosphopeptide spectra of 30099 (A-DC vs. A-NC), 14506 (P-DC vs. P-NC), 5932 (A-DC vs. P-DC), to the human reference proteome for generating background proteomic and phosphoproteomic datasets (**Fig. 5.1E**). Among them, we identified 3115 proteins, 8847 unique phosphopeptides, and 5373 phosphorylation sites on 1684 phosphoproteins in A-DC, as well as 3834 proteins, 6718 unique phosphopeptides, and 5898 phosphorylation sites on 2265 phosphoproteins in P-DC, relative to their age-matched controls, respectively (**Fig. 5.1E, 5.5A**). We further probed 2827 proteins, 3397 unique phosphopeptides, and 4214 phosphosites on 1719 phosphoproteins in A-DC versus P-DC (**Fig. 5.1E, 5.5A**).

Comparative Transcriptome Analyses. Our tissue-based RNA-Seq identified a comparable total amount of genes across three paired comparisons (A-DC vs. A-NC: 12483; P-DC vs. P-NC: 12602; A-DC vs. P-DC: 12434) (**Fig. 5.1E**). Venn diagrams have presented the total gene counts that were uniquely expressed within each sample type, with overlapping regions showing the number of co-expressed genes between two different sample sources **(Fig. 5.1E**). To our surprise, hundreds of genes were uniquely expressed in a single sample type, whereas the vast majority (over 10 thousand on average) were commonly shared transcripts between the compared groups (**Fig. 5.1E, 5.5B**), and a total of 10954 genes were shared between all compared subgroups (**Fig. 5.1E**). The high throughput but low variability datasets in our multiplexed analyses clearly showed the feasibility of our alternative methods for handling human heart samples with limited protein amounts.

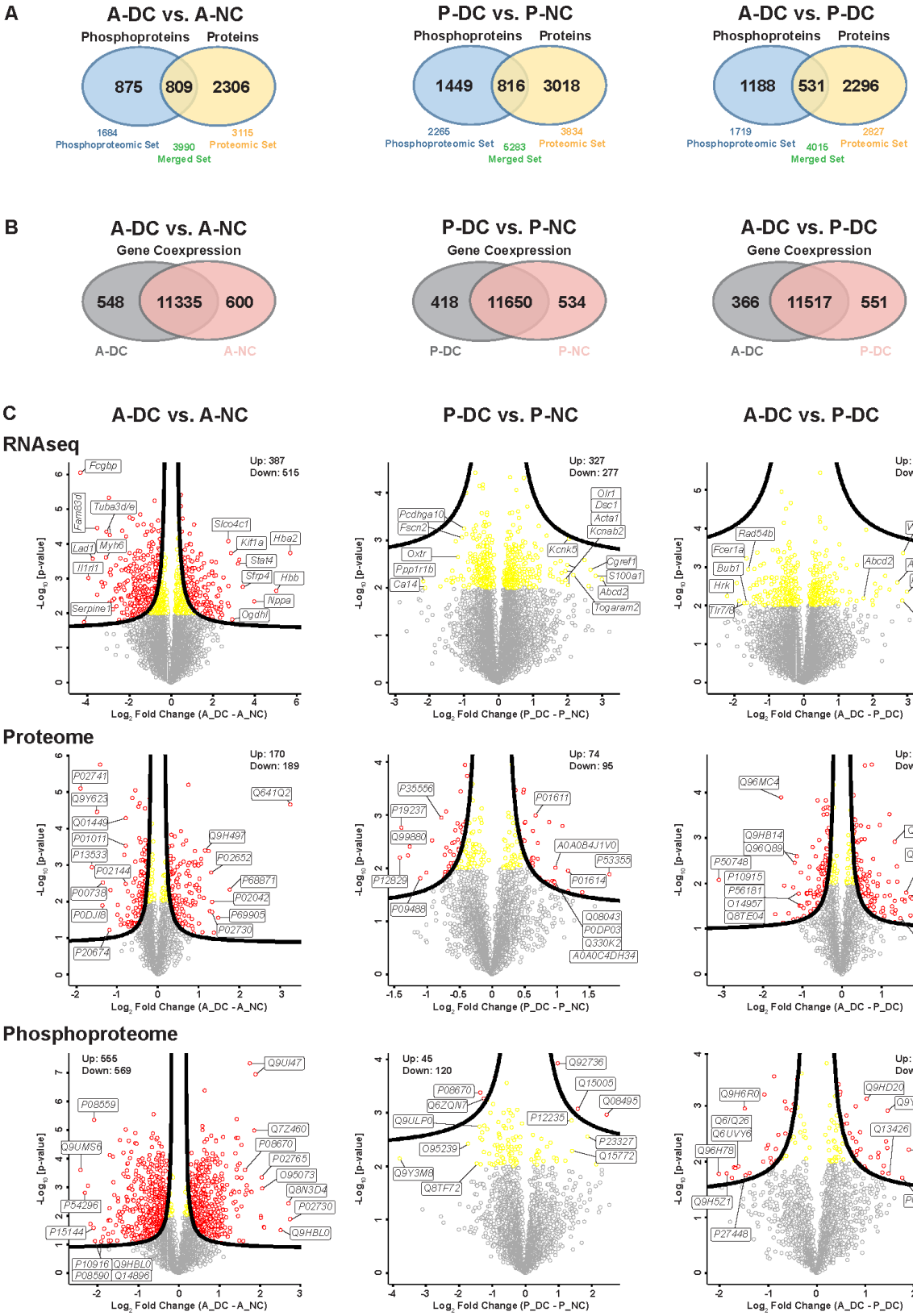
A
A-DC vs. A-NC
Phosphoproteins
Proteins
875
809
2306
1684
Phosphoproteomic Set
3990
Merged Set
3115
Proteomic Set
P-DC vs. P-NC
Phosphoproteins
Proteins
1449
816
3018
2265
Phosphoproteomic Set
5283
Merged Set
3834
Proteomic Set
A-DC vs. P-DC
Phosphoproteins
Proteins
1188
531
2296
1719
Phosphoproteomic Set
4015
Merged Set
2827
Proteomic Set
B
A-DC vs. A-NC
Gene Coexpression
548
11335
600
A-DC
A-NC
P-DC vs. P-NC
Gene Coexpression
418
11650
534
P-DC
P-NC
A-DC vs. P-DC
Gene Coexpression
366
11517
551
A-DC
P-DC
C
A-DC vs. A-NC
P-DC vs. P-NC
A-DC vs. P-DC
RNAseq
Up: 387
Down: 515
Fcgbp
Fam83d
Tuba3d/e
Lad1
Myh6
Il1rl1
Serpine1
Slco4c1
Kif1a
Hba2
Sta14
Sfrp4
Hbb
Nppa
Ogdhl
-Log10 [p-value]
Log2 Fold Change (A_DC - A_NC)
Up: 327
Down: 277
Pcdhga10
Fscn2
Oxtr
Ppp1r1b
Ca14
Olr1
Dsc1
Acta1
Kcnab2
Kcnk5
Cgref1
S100a1
Abcd2
Togaram2
Log2 Fold Change (P_DC - P_NC)
Up: 224
Down: 229
Rad54b
Fcer1a
Bub1
Hrk
Tlr7/8
Wisp2
Abcd2
Alkal2
Fam155b
Nap1l2
Plin1
Log2 Fold Change (A_DC - P_DC)
Proteome
Up: 170
Down: 189
P02741
Q9Y623
Q01449
P01011
P13533
P02144
P00738
P0DJI8
P20674
Q641Q2
Q9H497
P02652
P68871
P02042
P69905
P02730
Log2 Fold Change (A_DC - A_NC)
Up: 74
Down: 95
P35556
P19237
Q99880
P12829
P09488
P01611
A0A0B4J1V0
P53355
P01614
Q08043
P0DP03
Q330K2
A0A0C4DH34
Log2 Fold Change (P_DC - P_NC)
Up: 154
Down: 135
Q96MC4
Q9HB14
Q96Q89
P50748
P10915
P56181
O14957
Q8TE04
Q8IVF4
Q6ZN16
Q9NY74
P33981
Q9Y462
Q9Y6N6
P35968
Log2 Fold Change (A_DC - P_DC)
Phosphoproteome
Up: 555
Down: 569
P08559
Q9UMS6
P54296
P15144
P10916
Q9HBL0
P08590
Q14896
Q9UI47
Q7Z460
P08670
P02765
O95073
Q8N3D4
P02730
Q9HBL0
Log2 Fold Change (A_DC - A_NC)
Up: 45
Down: 120
Q92736
P08670
Q6ZQN7
Q9ULP0
O95239
Q9Y3M8
Q8TF72
Q15005
Q08495
P12235
P23327
Q15772
Log2 Fold Change (P_DC - P_NC)
Up: 144
Down: 75
Q9H6R0
Q6UQ26
Q6UVY6
Q96H78
Q9H5Z1
P27448
Q9HD20
Q9Y2D2
Q13426
Q10570
P51816
Q8NCL4
P0CG31
Log2 Fold Change (A_DC - P_DC)

Figure 5.5. Distinct transcriptome, proteome, and phosphoproteome in pediatric and adult DCM hearts. A. Venn diagram depicting the total number of proteins and phosphoproteins identified in the corresponding proteomic and phosproteomic datasets. B. Venn diagram depicting the total number of gene transcripts that are uniquely expressed in each sample group, with a high degree of coexpression between subgroups. C. Volcano plots showing significantly altered expressions of RNA transcripts, proteins, and phosphoproteins in the combined datasets. Log-transformed p values (t test) associated with individual peptides, phosphopeptides, and poly-A enriched mRNA plotted against log-transformed fold change in abundance between subgroups. Grey circles: hits with no significance; yellow circles: hits with statistical but no biological significance based on a p-value <0.01; red circles: hits with statistical and biological significance based on an Permutation-based FDR q-value<0.05 with an Artificial within groups variance of S0=0.1.

5.5.4. Differential Expression Analysis

Among all identified co-expressed transcripts, including proteins, phosphoproteins, and coding RNA (mRNA), we further performed stratifications based on the differential expression levels between the compared samples, with the overlapping regions indicating the common transcripts across different datasets. Hundreds of statistically significant alterations ($p<0.05$, two-tailored student's t-test) at the levels of mRNA, protein, and phosphorylation site were observed between the experimental and control conditions (**Fig. 5.5C**) and visualized by volcano plots.

Specifically, a total of 902 (387 up-regulated, 515 down-regulated) genes, 359 (170 up-regulated, 189 down-regulated) proteins, 1124 (555 up-regulated, 569 down-regulated) phosphoproteins were selectively regulated in A-DC, whereas in total 604 (327 up-regulated, 277 down-regulated) coding genes, 169 (74 up-regulated, 95 down-regulated) proteins, 165 (45 up-regulated, 120 down-regulated) phosphoproteins were differentially expressed in pediatric diseased conditions, with reference to their controls (**Fig. 5.5C**). Furthermore, 453 (224 up-regulated, 229 down-regulated) genes, 289 (154 up-regulated, 135 down-regulated) proteins, 219 (144 up-regulated, 75 down-regulated) phosphoproteins demonstrated expressional alterations with statistical significance between adult and pediatric diseased conditions (**Fig. 5.5C**). To show the representative genomic, proteomic and phosphoproteomic changes within the individual cohort, we thereby compiled three tables listing the top ten most significantly altered hits from the

comparisons between A-DC versus P-DC (**Table 5.5**), A-DC versus A-NC (**Table 5.3**), and P-DC versus P-NC (**Table 5.4**).

A-DC vs. A-NC. In particular, genes up-regulated in A-DC compared to A-NC mainly included those involved in oxygen and ion transport, oxidant detoxification, cytoskeleton organization and ECM remodeling, cellular metabolism and regulation of cell death, which were well-known hallmarks of chronic HF in adults (**Table 5.3**). Additionally, A-DC demonstrated upregulation of genes involved in immune response signaling such as Wnt/JNK (*NPPA, SFRP4*) and JAK-STAT (*STAT4*) pathways (**Table 5.3**). *SLCO4C1*, an encoding gene of an organic anion transporter for pharmacological substances such as digoxin, was also among the most up-regulated transcripts in adults compared to pediatric patients. On the contrary, cellular adhesion, migration, and matrix association, angiogenesis, oxidative stress clearance, and structural components represented the dysregulated functional pathways associated with those most down-regulated pathological transcripts listed in adult HF patients (**Table 5.3**). Of note, *MYH6*, formerly reported to negatively correlate with cardiomyopathic pathologies progressing to HF[116], and *FAM83D*, *IL1RL1* implicated in pleiotropic MAPK-ERK pathways[420], were all significantly repressed in A-DC compared to controls. The global abundance of proteins including phosphoproteins, consistently mirrored the selective expressional changes of the pathological transcripts identified in A-DC (**Table 5.3**). For instance, hemoglobin subunit alpha (P69905), beta (P68871), and delta (P02042) involved in oxygen transporting and oxidative stress scavenging were all up-regulated in A-DC, whereas down-regulated expressions of myosin isoforms 4 (Q9Y623) and 6 (P13533), and elements that affect Ca^{2+} binding activity (P02741) during contraction, cytochrome c oxidase activity (P20674) during oxidative phosphorylation, and antioxidant protection (P00738) amid acute inflammatory response were all observed in A-DC versus A-NC. All downregulated phosphoproteins in A-DC were involved in regulations of muscle contraction, intermediary metabolism and metalloaminopeptidase and angiogenesis, collectively reflecting an overall severely impaired actomyosin assembly (Q9HBL0, Q14896, P54296, Q9UMS6), contractile property (P08590, P10916), vasculogenesis (P15144), and defective metabolic utilization. Such alterations were further validated by immunoblotting in **Figure 5.6**.

Table 5.3. Top 10 Most Significantly Altered Hits between A-DC versus A-NC

Upregulated in A-DC				
Transcriptome	**Gene**	**Description**	**Log_2**	**$-Log_{10}$**
ENSG00000188536	*HBA2*	Hemoglobin subunit alpha 2	5.69	3.73
ENSG00000244734	*HBB*	Hemoglobin subunit beta	5.01	2.65
ENSG00000175206	*NPPA*	Natriuretic peptide A	3.97	2.34
ENSG00000106483	*SFRP4*	Secreted frizzled related protein 4	3.43	2.76
ENSG00000153446	*C16orf89*	Chromosome 16 open reading frame 89	3.25	3.55
ENSG00000138378	*STAT4*	Signal transducer and activator of transcription	3.20	3.43
ENSG00000197444	*OGDHL*	Oxoglutarate dehydrogenase-like	2.91	1.83
ENSG00000130294	*KIF1A*	Kinesin family member 1A	2.86	3.74
ENSG00000170579	*DLGAP1*	DLG associated protein 1	2.75	2.20
ENSG00000173930	*SLCO4C1*	Solute carrier organic anion transporter family	2.73	2.78
Global Proteome	**Gene**	**Protein Description**	**Log_2**	**$-Log_{10}$**
Q641Q2	*FAM21A/D/C*	WASH complex subunit FAM21A/C	3.25	4.66
P68871	*HBB*	Hemoglobin subunit beta; Spinorphin	1.77	2.33
P69905	*HBA1*	Hemoglobin subunit alpha	1.49	1.55
Q14966	*ZNF638*	Zinc finger protein 638	1.38	1.15
P02042	*HBD*	Hemoglobin subunit delta	1.33	1.99
P00915	*CA1*	Carbonic anhydrase 1	1.33	1.71
P02652	*APOA2*	Apolipoprotein A-II	1.31	2.80
P02730	*SLC4A1*	Band 3 anion transport protein	1.28	1.74
P02765	*AHSG*	Alpha-2-HS-glycoprotein	1.24	3.39
Q9H497	*TOR3A*	Torsin-3A	1.16	3.39
Phosphoproteome	**Gene**	**Description**	**Log_2**	**$-Log_{10}$**
Q8N3D4	*EHBP1L1*	EH domain-binding protein 1-like protein 1	2.74	1.89
P02730	*SLC4A1*	Band 3 anion transport protein	2.70	2.44
Q9HBL0	*TNS1*	Tensin-1	2.50	1.51
P02765	*AHSG*	Alpha-2-HS-glycoprotein	2.05	2.96
O95073	*FSBP*	Fibrinogen silencer-binding protein	2.04	3.35
P02730	*SLC4A1*	Band 3 anion transport protein	2.02	1.99
P16157	*ANK1*	Ankyrin-1	2.01	1.94

Q9UI47	*CTNNA3*	Catenin alpha-3	1.89	6.94
Q7Z460	*CLASP1*	CLIP-associating protein 1	1.85	4.98
P01042	*KNG1*	Kininogen-1; T-kinin; Bradykinin	1.79	2.83
Downregulated in A-DC				
Transcriptome	**Gene**	**Description**	**Log_2**	**$-Log_{10}$**
ENSG00000197616	*MYH6*	Myosin heavy chain 6	-3.12	3.61
ENSG00000101447	*FAM83D*	Family with sequence similarity 83 member D	-3.17	2.86
ENSG00000187922	*LCN10*	Lipocalin 10	-3.28	2.77
ENSG00000106236	*NPTX2*	Neuronal pentraxin 2	-3.33	2.90
ENSG00000177575	*CD163*	CD163 molecule	-3.54	4.46
ENSG00000163814	*CDCP1*	CUB domain containing protein 1	-3.55	2.53
ENSG00000159166	*LAD1*	Ladinin 1	-3.75	3.58
ENSG00000115602	*IL1RL1*	Interleukin 1 receptor like 1	-3.96	3.02
ENSG00000106366	*SERPINE1*	Serpin family E member 1	-4.18	1.74
ENSG00000275395	*FCGBP*	Fc fragment of IgG binding protein	-4.34	6.06
Global Proteome	**Gene**	**Description**	**Log_2**	**$-Log_{10}$**
Q7L3T8	*PARS2*	Probable proline--tRNA ligase	-0.99	1.91
Q9NSC5	*HOMER3*	Homer protein homolog 3	-1.00	1.64
P35637	*FUS*	RNA-binding protein FUS	-1.16	2.31
P20674	*COX5A*	Cytochrome c oxidase subunit 5A,	-1.19	1.22
P00738	*HP; HPR*	Haptoglobin	-1.35	2.51
P0DJI8	*SAA1*	Serum amyloid A-1 protein	-1.36	1.89
Q7Z3D6	*C14orf159*	D-glutamate cyclase,	-1.41	5.76
Q9Y623	*MYH4*	Myosin-4	-1.49	4.46
P13533	*MYH6*	Myosin-6	-1.62	2.94
P02741	*CRP*	C-reactive protein	-1.90	5.10
Phosphoproteome	**Gene**	**Description**	**Log_2**	**$-Log_{10}$**
Q9HBL0	*TNS1*	Tensin-1	-1.72	1.14
Q14896	*MYBPC3*	Myosin-binding protein C,	-1.73	1.84
Q9BX66	*SORBS1*	Sorbin and SH3 domain-containing protein 1	-1.74	1.37
P08590	*MYL3*	Myosin light chain 3	-1.84	1.56
P10916	*MYL2*	Myosin regulatory light chain 2	-2.07	1.12

P08559	*PDHA1/2*	Pyruvate dehydrogenase E1 alpha, somatic	-2.09	5.35
P15144	*ANPEP*	Aminopeptidase N	-2.09	1.59
P52943	*CRIP2*	Cysteine-rich protein 2	-2.17	1.72
P54296	*MYOM2*	Myomesin-2	-2.32	2.80
Q9UMS6	*SYNPO2*	Synaptopodin-2	-2.42	3.60

The present table shows the top 10 most significantly changed hits (based on the order of fold changes), including from transcriptomic, global proteomic, and phosphoproteomic datasets respectively, in the adult dilated failing myocardium (A-DC) following normalization to its control samples (A-NC, as reference group). Gene/protein IDs, gene/protein names, biological annotations, as well as Log_2 [fold-change (A_DC – A_NC)] and $-Log_{10}$ [p-value] were reported where applicable.

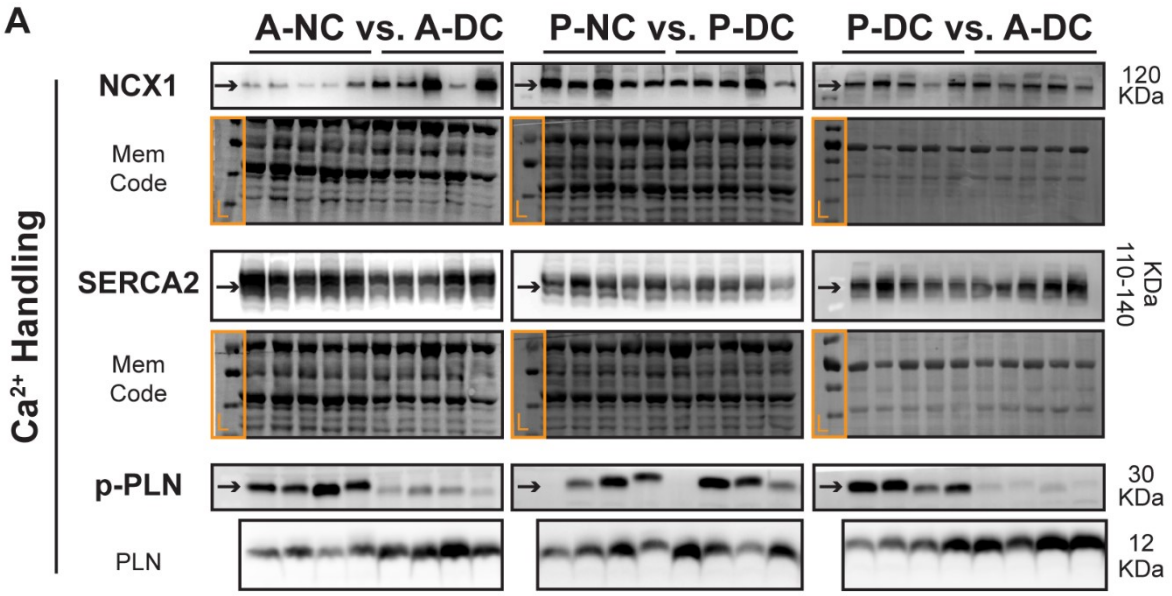

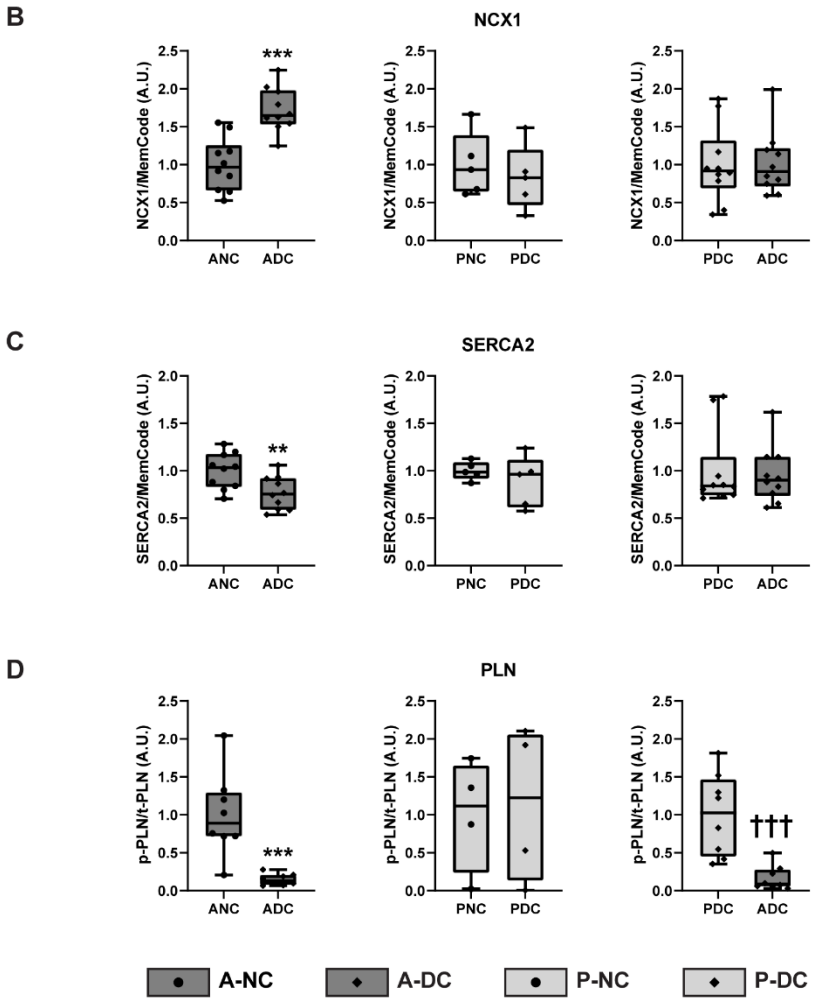

Figure 5.6. Assessment of Ca^{2+} cycling pathways using immunoblotting analyses. Representative blots (A) and corresponding quantifications of the key proteins involved in Ca2+ cycling pathways, including NCX1 (B), SERCA2 (C), and PLN (D), the phosphorylation of which lessens its inhibition on SERCA2. MemCode (total protein loading) was applied for protein normalization for NCX1 and SERCA2, while for the phosphoproteins such as PLN, the total level of paired protein (including phosphorylated and unphosphorylated forms) was alternatively used for determining their phosphorylation fractions. Orange box represented the protein ladder, and arrow indicated the molecular weight (KDa) of the probed proteins. A-DC: adult dilated cardiomyopathy; A-NC: adult non-DCM control; P-DC: pediatric dilated cardiomyopathy; P-NC: pediatric non-DCM control. NCX1: sodium/calcium exchanger 1; SERCA2: sarco(endo)plasmic reticulum calcium-ATPase 2; PLN: phospholamban. For NCX1 and SERCA2, n=10 for each adult subgroup (A-NC vs. A-DC), n=5 for each pediatric subgroup (P-NC vs. P-DC), and n=10 for direct comparison between DCM subgroups (P-DC vs. A-DC), respectively. For PLN, n=8 for each adult subgroup (A-NC vs. A-DC), n=4 for each pediatric subgroup (P-NC vs. P-DC), and n=8 for direct comparison between DCM subgroups (P-DC vs. A-DC), respectively. *p<0.05, **p<0.01, ***p<0.001

compared to A-NC; #p<0.05, ##p<0.01, ###p<0.001 compared to P-NC; †p<0.05, ††p<0.01, †††p<0.001 compared to A-DC.

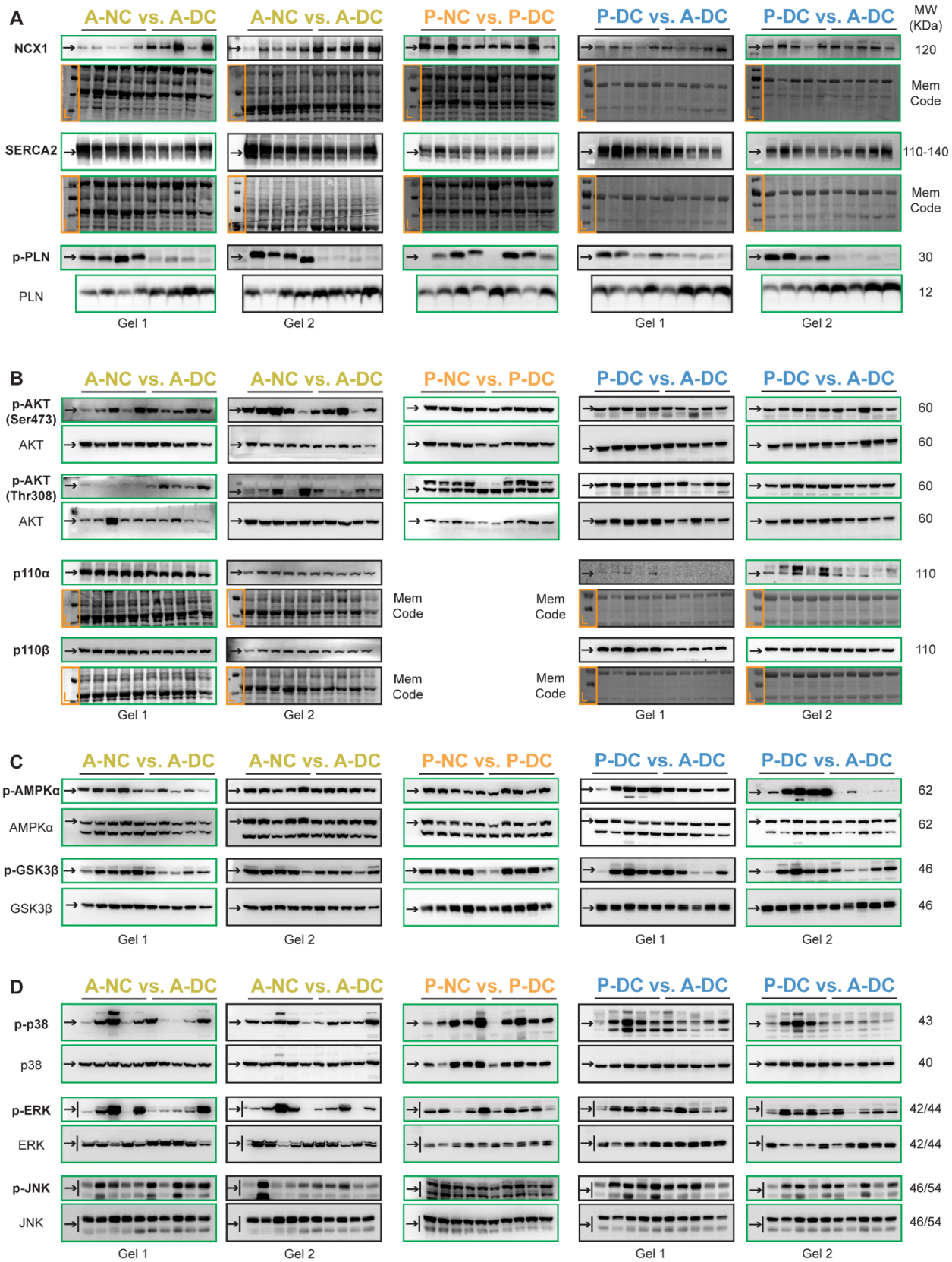

Figure 5.7. Original immunoblots of probed signaling markers that correspond to the protein

quantitation in Figure 5.6 and 5.8-5.9. The blots selected as representatives were outlined with a red border. Orange box represented the protein ladder, whereas arrow indicated the molecular weight (KDa) of the probed proteins. A-DC: adult dilated cardiomyopathy; A-NC: adult non-DCM control; P-DC: pediatric dilated cardiomyopathy; P-NC: pediatric non-DCM control. NCX1: sodium/calcium exchanger 1; SERCA2: sarco(endo)plasmic reticulum calcium-ATPase 2; PLN: phospholamban. AMPKα: AMP-activated protein kinase alpha; GSK3β: glycogen synthase kinase 3 beta; and AKT: protein kinase B; PI3K: phosphoinositide 3 kinases. p38: p38 mitogen-activated protein kinase; ERK: extracellular signal-regulated kinase; and JNK: c-Jun N-terminal kinase.

P-DC vs. P-NC. The top up-regulated genes in P-DC versus P-NC were predominantly involved in redox reactions, Ca^{2+}-dependent intracellular signaling pathways, transcriptional regulation, and nucleosome repair machinery (**Table 5.4**). The downstream proteomic and phosphoproteomic profiling again reflected the transcriptional alterations in P-DC. Importantly, mitochondrial NADH:ubiquinone oxidoreductase complex (Complex I, Q330K2) was among the most significantly altered in P-DC, in addition to other up-regulated proteins such as fatty-acid amide hydrolase 2 (Q6GMR7) and neutral cholesterol ester hydrolase 1 (Q6PIU2) featuring a premature metabolic switch to lipid metabolism associated with defective ETC activities. Furthermore, our phosphoproteomic profiling unveiled elevated phosphorylation levels of sarcoplasmic reticulum histidine-rich calcium-binding protein (P23327), ryanodine receptor 2 (Q92736), and voltage-dependent N-type calcium channel subunit alpha-1B (Q00975) in P-DC, suggesting pediatric dilated failing hearts may have relatively maintained intracellular Ca^{2+} cycling. To validate, we performed immunoblotting analyses on the human heart specimens (**Fig. 5.6, 5.7**) and found that only A-DC demonstrated a significantly increased level of sodium calcium exchanger 1 (NCX1, **Fig. 5.6A, B**) after normalization to the controls, in couple with reduced sarcoplasmic/endoplasmic reticulum calcium ATPase 2 (SERCA2, **Fig. 5.6A, C**) and phosphorylation level of phospholamban (PLN, **Fig. 5.6A, D**). Surprisingly, the phosphorylation level of PLN was remarkably higher (≈5.96 times) in P-DC compared to A-DC directly, while the expressions of NCX1 and SERCA2 did not show a statistical difference.

Table 5.4. Top 10 Most Significantly Altered Hits between P-DC versus P-NC

Upregulated in P-DC				
Transcriptome	**Gene**	**Description**	**Log_2**	**$-Log_{10}$**
ENSG00000173208	*ABCD2*	ATP binding cassette subfamily D member 2	3.00	2.18
ENSG00000211448	*DIO2*	Iodothyronine deiodinase 2	2.81	2.25
ENSG00000138028	*CGREF1*	Cell growth regulator with EF-hand domain 1	2.67	2.39
ENSG00000160678	*S100A1*	S100 calcium binding protein A1	2.61	2.04
ENSG00000116254	*CHD5*	Chromodomain helicase DNA binding protein 5	2.48	2.58
ENSG00000189350	*TOGARAM2*	TOG array regulator of axonemal microtubules 2	2.16	2.27
ENSG00000073282	*TP63*	Tumor protein p63	2.03	3.03
ENSG00000164626	*KCNK5*	Potassium two pore domain channel subfamily K	2.01	2.05
ENSG00000276966	*HIST1H4E*	Histone cluster 1 H4 family member e	1.99	2.48
ENSG00000173391	*OLR1*	Oxidized low density lipoprotein receptor 1	1.93	2.35
Global Proteome	**Gene**	**Description**	**Log_2**	**$-Log_{10}$**
P53355	*DAPK1*	Death-associated protein kinase 1	1.80	1.89
A0A075B6P5	*IGKV2D*	Ig kappa chain V-II region FR/Cum/RPMI 6410	1.17	1.95
Q6SJ93	*FAM111B*	Protein FAM111B	1.17	1.57
Q2PPJ7	*RALGAPA2*	Ral GTPase-activating protein subunit alpha-2	1.09	2.80
Q9BXI3	*NT5C1A*	Cytosolic 5-nucleotidase 1A	0.96	1.74
P08779	*KRT16*	Keratin, type I cytoskeletal 16	0.95	1.76
Q08043	*ACTN3*	Alpha-actinin-3	0.86	1.75
Q330K2	*NDUFAF6*	NADH dehydrogenase (ubiquinone) complex I,	0.81	1.74
Q6GMR7	*FAAH2*	Fatty-acid amide hydrolase 2	0.71	2.18
Q6PIU2	*NCEH1*	Neutral cholesterol ester hydrolase 1	0.70	2.47
Phosphoproteome	**Gene**	**Description**	**Log_2**	**$-Log_{10}$**
Q08495	*DMTN*	Dematin	2.46	2.97
Q6KC79	*NIPBL*	Nipped-B-like protein	2.14	2.04
P23327	*HRC*	Sarcoplasmic reticulum histidine-rich calcium-	1.87	2.56
Q15005	*SPCS2*	Signal peptidase complex subunit 2	1.57	3.07
Q15772	*SPEG*	Striated muscle preferentially expressed protein	1.40	2.28
P12235(6)	*SLC25A4(6)*	ADP/ATP translocase 1/3,	1.40	2.86
Q8N9B5	*JMY*	Junction-mediating	1.21	2.10

Q92736	*RYR2*	Ryanodine receptor 2	0.97	3.93
Q5JV73	*FRMPD3*	FERM and PDZ domain-containing protein 3	0.95	2.09
Q00975	*CACNA1B*	Voltage-dependent N-type calcium channel	0.95	2.15
Downregulated in P-DC				
Transcriptome	**Gene**	**Description**	**Log_2**	**$-Log_{10}$**
ENSG00000070669	*ASNS*	Asparagine synthetase	-1.08	2.25
ENSG00000180914	*OXTR*	Oxytocin receptor	-1.18	2.65
ENSG00000243789	JMJD7	Jumonji domain containing 7	-1.24	2.99
ENSG00000104081	BMF	Bcl2 modifying factor	-1.29	2.22
ENSG00000255423	EBLN2	Endogenous Bornavirus like nucleoprotein 2	-1.33	2.12
ENSG00000161249	DMKN	Dermokine	-1.34	2.36
ENSG00000127578	WFIKKN1	WAP, follistatin/kazal	-1.37	2.21
ENSG00000133134	BEX2	Brain expressed X-linked 2	-1.50	2.16
ENSG00000118298	*CA14*	Carbonic anhydrase 14	-2.12	2.00
ENSG00000131771	*PPP1R1B*	Protein phosphatase 1 regulatory inhibitor subunit	-2.18	2.14
Global Proteome	**Gene**	**Description**	**Log_2**	**$-Log_{10}$**
P05783	*KRT18*	Keratin, type I cytoskeletal 18	-0.72	2.25
Q9Y6M1	*IGF2BP2*	Insulin-like growth factor 2 mRNA-binding	-0.74	1.81
P35556	*FBN2*	Fibrillin-2	-0.78	2.95
O00625	*PIR*	Pirin	-0.92	2.52
Q99983	*OMD*	Osteomodulin	-1.01	1.92
P09488	*GSTM1*	Glutathione S-transferase Mu 1/ 4	-1.10	1.81
Q99880	*HIST1H2BL*	Histone H2B type 1/2	-1.26	2.41
Q5SYE7	*NHSL1*	NHS-like protein 1	-1.29	2.25
P19237	*TNNI1*	Troponin I, slow skeletal muscle	-1.39	2.76
P12829	*MYL4*	Myosin light chain 4	-1.42	2.20
Phosphoproteome	**Gene**	**Description**	**Log_2**	**$-Log_{10}$**
Q6ZQN7	*SLCO4C1*	Solute carrier organic anion transporter family	-1.25	3.27
Q09666	*AHNAK*	Neuroblast differentiation-associated protein	-1.25	2.27
P67809	*YBX1*	Nuclease-sensitive element-binding protein 1	-1.30	2.50
Q8NI08	*NCOA7*	Nuclear receptor coactivator 7	-1.31	2.64
Q9UQL6	*HDAC5*	Histone deacetylase 5	-1.34	2.04

Q9ULP0	*NDRG4*	Protein NDRG4	-1.36	2.53
P08670	*VIM*	Vimentin	-1.39	2.74
Q8TF72	*SHROOM3*	Protein Shroom3	-1.47	2.05
O95239	*KIF4A*	Chromosome-associated kinesin KIF4A	-1.74	2.43
Q9Y3M8	*STARD13*	StAR-related lipid transfer protein 13	-3.80	2.14

The present table shows the top 10 most significantly changed hits (based on the order of fold changes), including from transcriptomic, global proteomic, and phosphoproteomic datasets respectively, in the pediatric dilated failing myocardium (P-DC) following normalization to its control samples (P-NC, as reference group). Gene/protein IDs, gene/protein names, biological annotations, as well as Log_2 [fold-change (A_DC – A_NC)] and $-Log_{10}$ [p-value] were reported where applicable.

A-DC vs. P-DC. Next, we directly compared the transcriptional and expressional profiles of adults and pediatric DCM (**Table 5.5**). Our analyses showed that upregulated transcripts in A-DC were primarily linked to the regulation of fatty acid metabolism (*PLIN1, ABCD2*), cell adhesion and Ca^{2+}-mediated signaling pathways, while most of the downregulated genes in A-DC were involved in innate immune and inflammatory responses including toll-like receptors (TLR, isoforms 3, 4, 7, 8, 9) and tyrosine kinase-mediated signaling pathways. Proteomic profiling confirmed that the majority of upregulated proteins in A-DC, relatively speaking, were associated with ECM remodeling, angiogenesis and glycolipid metabolism, whereas those constituting mitochondrial ETC complexes and implicated in microtubular regulation were downregulated. Consistently, the enriched phosphoproteins in A-DC were principally related to cardiac Ca^{2+} homeostasis and transcriptional regulations on structural components, and the downregulated were implicated in the regulation of myocardial filament, mRNA stability, and MAPK-ERK signaling pathways which were also validated by immunoblotting analyses shown in **Figure 5.7-5.9**.

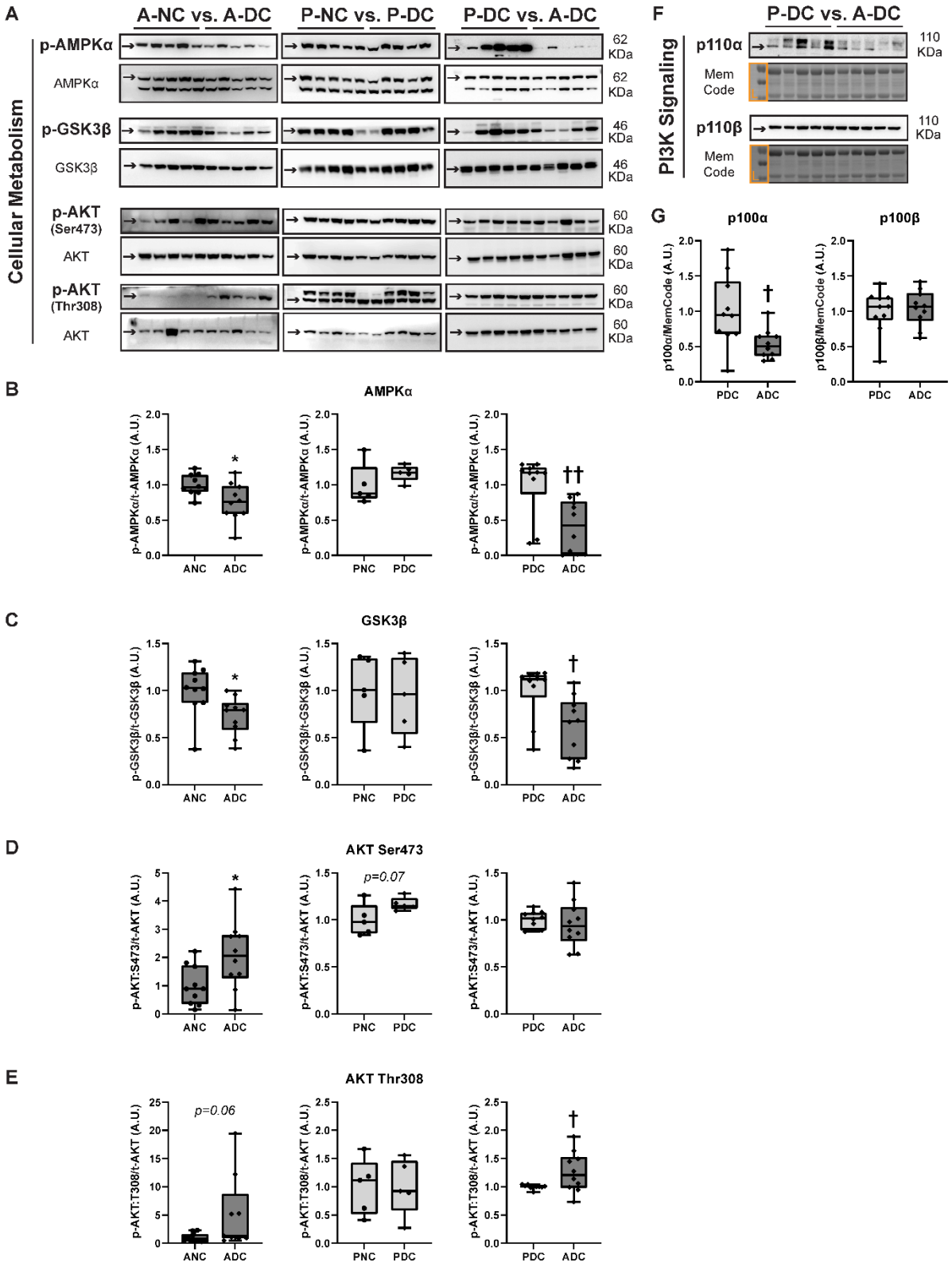

Figure 5.8. Assessment of key metabolic regulatory pathways using immunoblotting analyses. A-E. Representative blots (A) and corresponding quantifications of key phosphoproteins involved in cellular

metabolism, including pAMPKα (B), pGSK3β (C), and pAKT-Ser473/-Thr308 (D-E). Their phosphorylation fractions were calculated relative to the total level of paired proteins (AMPKα, GSK3β, and AKT), respectively. F-G. Representative blots (F) and corresponding quantifications of protein isoforms involved in PI3K pathways, including p100α and p100β (G). MemCode (total protein loading) was applied for protein normalization. Orange box represented the protein ladder, and arrow indicated the molecular weight (KDa) of the probed proteins. A-DC: adult dilated cardiomyopathy; A-NC: adult non-DCM control; P-DC: pediatric dilated cardiomyopathy; P-NC: pediatric non-DCM control. AMPKα: AMP-activated protein kinase alpha; GSK3β: glycogen synthase kinase 3 beta; and AKT: protein kinase B; PI3K: phosphoinositide 3 kinases. n=10 for each adult subgroup (A-NC vs. A-DC), n=5 for each pediatric subgroup (P-NC vs. P-DC), and n=10 for direct comparison between DCM subgroups (P-DC vs. A-DC), respectively. *$p<0.05$, **$p<0.01$, ***$p<0.001$ compared to A-NC; #$p<0.05$, ##$p<0.01$, ###$p<0.001$ compared to P-NC; †$p<0.05$, ††$p<0.01$, †††$p<0.001$ compared to A-DC.

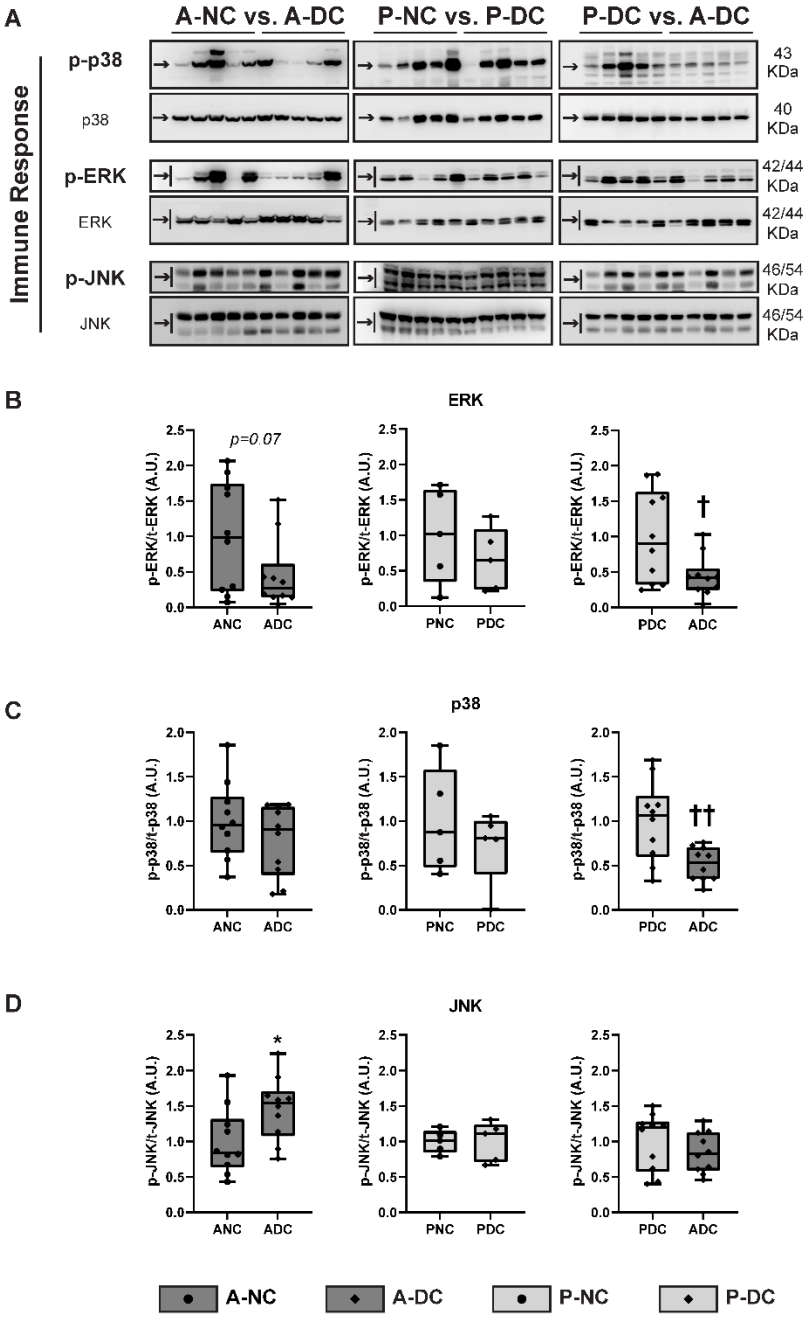

Figure 5.9. Assessment of key immune response pathways using immunoblotting analyses. A-D. Representative blots (A) and corresponding quantifications of key phosphoproteins involved in immune response, including p-p38 (B), p-ERK (C), and p-JNK (D). Their phosphorylation fractions were calculated relative to the total level of paired proteins (P38, ERK, and JNK), respectively. Arrow indicated the molecular weight (KDa) of the probed proteins. A-DC: adult dilated cardiomyopathy; A-NC: adult non-DCM control; P-DC: pediatric dilated cardiomyopathy; P-NC: pediatric non-DCM control. p38: p38 mitogen-activated protein kinase; ERK: extracellular signal-regulated kinase; and JNK: c-Jun N-terminal

kinase. n=10 for each adult subgroup (A-NC vs. A-DC), n=5 for each pediatric subgroup (P-NC vs. P-DC), and n=10 for direct comparison between DCM subgroups (P-DC vs. A-DC), respectively. *p<0.05, **p<0.01, ***p<0.001 compared to A-NC; #p<0.05, ##p<0.01, ###p<0.001 compared to P-NC; †p<0.05, ††p<0.01, †††p<0.001 compared to A-DC.

Table 5.5. Top 10 Most Significantly Altered Hits between A-DC versus P-DC

Upregulated in A-DC				
Transcriptome	**Gene**	**Description**	**Log_2**	**$-Log_{10}$**
ENSG00000186462	*NAP1L2*	Nucleosome assembly protein 1 like 2	3.30	2.24
ENSG00000130054	*FAM155B*	Family with sequence similarity 155 member B	2.99	2.36
ENSG00000064205	*WISP2*	WNT1 inducible signaling pathway protein 2	2.86	3.36
ENSG00000166819	*PLIN1*	Perilipin 1	2.85	2.13
ENSG00000147255	*IGSF1*	Immunoglobulin superfamily member 1	2.70	2.59
ENSG00000189292	*ALKAL2*	ALK and LTK ligand 2	2.48	2.42
ENSG00000242173	*ARHGDIG*	Rho GDP dissociation inhibitor gamma	2.10	2.25
ENSG00000154277	*UCHL1*	Ubiquitin C-terminal hydrolase L1	2.06	2.56
ENSG00000173208	*ABCD2*	ATP binding cassette subfamily D member 2	2.00	2.02
ENSG00000197766	*CFD*	Complement factor D	1.98	2.13
Global Proteome	**Gene**	**Description**	**Log_2**	**$-Log_{10}$**
P33981	*TTK*	Dual specificity protein kinase TTK	2.20	2.04
Q9NY74	*ETAA1*	Ewings tumor-associated antigen 1	1.74	1.70
P52292	*KPNA2*	Importin subunit alpha-1	1.74	1.29
Q6ZN16	*MAP3K15*	Mitogen-activated protein kinase kinase kinase	1.63	1.80
A6NH11	*GLTPD2*	Glycolipid transfer protein domain-containing	1.60	1.64
Q96MY7	*FAM161B*	Protein FAM161B	1.60	1.61
P82094	*TMF1*	TATA element modulatory factor	1.52	1.65
Q9Y6N6	*LAMC3*	Laminin subunit gamma-3	1.49	1.23
P35968	*KDR*	Vascular endothelial growth factor receptor 2	1.45	1.12
P06737	*PYGL*	Glycogen phosphorylase, liver form	1.34	1.15
Phosphoproteome	**Gene**	**Description**	**Log_2**	**$-Log_{10}$**
Q8NCL4	*GALNT6*	Polypeptide N-acetylgalactosaminyltransferase	2.30	1.70

Q13046	*PSG7(1)*	Pregnancy-specific beta-1-glycoprotein 1/7	2.07	1.62
Q00889	*PSG6*	Pregnancy-specific beta-1-glycoprotein 6	2.06	1.65
Q10570	*CPSF1*	Cleavage and polyadenylation specificity factor	2.06	2.46
P51816	*AFF2*	AF4/FMR2 family member 2	1.90	2.21
P0CG31	*ZNF286A(B)*	Zinc finger protein 286A/B	1.76	1.71
Q13426	*XRCC4*	DNA repair protein XRCC4	1.47	1.78
Q9Y2D2	*SLC35A3*	UDP-N-acetylglucosamine transporter	1.46	2.91
P35606	*COPB2*	Coatomer subunit beta'	1.45	2.25
Q9HD20	*ATP13A1*	Manganese-transporting ATPase 13A1	1.42	2.36

Downregulated in A-DC

Transcriptome	Gene	Description	Log_2	$-Log_{10}$
ENSG00000134242	*PTPN22*	Protein tyrosine phosphatase,	-1.44	2.23
ENSG00000111247	*RAD51AP1*	RAD51 associated protein 1	-1.45	2.53
ENSG00000169679	*BUB1*	BUB1 mitotic checkpoint serine/threonine	-1.45	2.04
ENSG00000112655	*PTK7*	Protein tyrosine kinase 7 (inactive)	-1.55	2.44
ENSG00000180071	*ANKRD18A*	Ankyrin repeat domain 18A	-1.61	2.94
ENSG00000101916	*TLR8*	Toll like receptor 8	-1.64	2.07
ENSG00000168329	*CX3CR1*	C-X3-C motif chemokine receptor 1	-1.73	2.06
ENSG00000196664	*TLR7*	Toll like receptor 7	-1.87	2.12
ENSG00000135116	*HRK*	Harakiri, BCL2 interacting protein	-1.93	2.58
ENSG00000121807	*CCR2*	C-C motif chemokine receptor 2	-2.21	2.24
Global Proteome	**Gene**	**Description**	**Log_2**	**$-Log_{10}$**
O14957	*UQCR11*	Cytochrome b-c1 complex subunit 10	-1.06	1.51
P56181	*NDUFV3*	NADH dehydrogenase [ubiquinone]	-1.08	1.51
P10915	*HAPLN1*	Hyaluronan and proteoglycan link protein 1	-1.09	1.78
Q9HB14	*KCNK13*	Potassium channel subfamily K member 13	-1.14	2.60
Q96Q89	*KIF20B*	Kinesin-like protein KIF20B	-1.19	2.45
Q5T749	*KPRP*	Keratinocyte proline-rich protein	-1.24	1.21
Q9H814	*PHAX*	Phosphorylated adapter RNA export protein	-1.36	1.35
Q96MC4	*KIAA1731NL*	Protein DDC8 homolog	-1.54	3.89
Q99880	*HIST1H2BL*	Histone H2B type 1/2	-1.69	1.32
P50748	*KNTC1*	Kinetochore-associated protein 1	-3.12	2.07

Phosphoproteome	Gene	Description	Log_2	$-Log_{10}$
Q0ZGT2	*NEXN*	Nexilin	-1.04	2.23
Q9H3E2	*SNX25*	Sorting nexin-25	-1.11	2.00
O94875	*SORBS2*	Sorbin and SH3 domain-containing protein 2	-1.38	1.80
P27448	*MARK3*	MAP/microtubule affinity-regulating kinase 3	-1.47	1.75
Q9H6R0	*DHX33*	Putative ATP-dependent RNA helicase DHX33	-1.49	2.95
O94875	*SORBS2*	Sorbin and SH3 domain-containing protein 2	-1.61	1.91
Q6UVY6	*MOXD1*	DBH-like monooxygenase protein 1	-1.70	1.90
Q6IQ26	*DENND5A*	DENN domain-containing protein 5A	-1.75	1.70
Q9H5Z1	*DHX35*	Probable ATP-dependent RNA helicase DHX35	-1.86	1.78
Q96H78	*SLC25A44*	Solute carrier family 25 member 44	-2.02	1.78

The present table shows the top 10 most significantly changed hits (based on the order of fold changes), including from transcriptomic, global proteomic, and phosphoproteomic datasets respectively, in the adult dilated failing myocardium (A-DC) in comparison to the reference group (P-DC). Gene/protein IDs, gene/protein names, biological annotations, as well as Log_2 [fold-change (A_DC – A_NC)] and $-Log_{10}$ [p-value] were reported where applicable.

5.5.5. Comparative Functional Pathway Enrichment Analysis and Visualization

Considering the biological complexities underlying a such large number of transcripts that were selectively expressed between adult and pediatric DCM cohorts, we subjected all significantly changed hits as inputs to GO, KEGG, REAC, and Human Protein Atlas (HPA) for functional pathway enrichment analyses on g:Profiler[194]. By default, additional data sources such as WikiPathways, Transfac (TF), and miRTarBase (MIRNA) were also queried for broader coverage and search of over-/down-represented annotations associated with GO functional terms, namely, molecular function (MF), biological process (BP), cellular components (CC), regulatory motifs, and human disease phenotypes.

Comparisons at Transcriptomic Level. Enrichment pathway analyses were performed on transcriptomic datasets for three paired comparisons, which were complemented with downstream proteomic and phosphoproteomic analyses.

A-DC vs. A-NC. A whole list of 387 upregulated genes was subjected to g:GOSt and our enrichment analysis revealed a total of 119 pathways were overrepresented in A-DC versus A-NC, and they were predominantly associated with oxygen, heme, and haptoglobin binding, oxidoreductase activity, and cellular oxidant detoxification involving hydrogen peroxidase (**Fig. 5.10A**). Moreover, cellular compartments namely haptoglobin-hemoglobin complex, collagen-containing ECM and endocytic vesicles were clearly enriched in A-DC compared to A-NC (**Fig. 5.10A**). Similarly, we inputted all 515 downregulated gene transcripts into g:GOSt and a remarkably higher number of pathways (453) were underrepresented in adult diseased hearts in relation to adult controls (**Fig. 5.10A**). Among them, immune response, regulation of ROS clearance (i.e., superoxide metabolism), programmed cell death, cytoskeleton organization, transmembrane signaling receptor activities and angiogenesis represented the most underrepresented hallmarks of DCM in adults (**Fig. 5.10A**). Those statistically enriched biological processes were further clustered into functionally related groups using Enrichment Map tool and consistently revealed the distinct biological themes associated with the aforementioned terms between A-DC versus A-NC (**Fig. 5.11**).

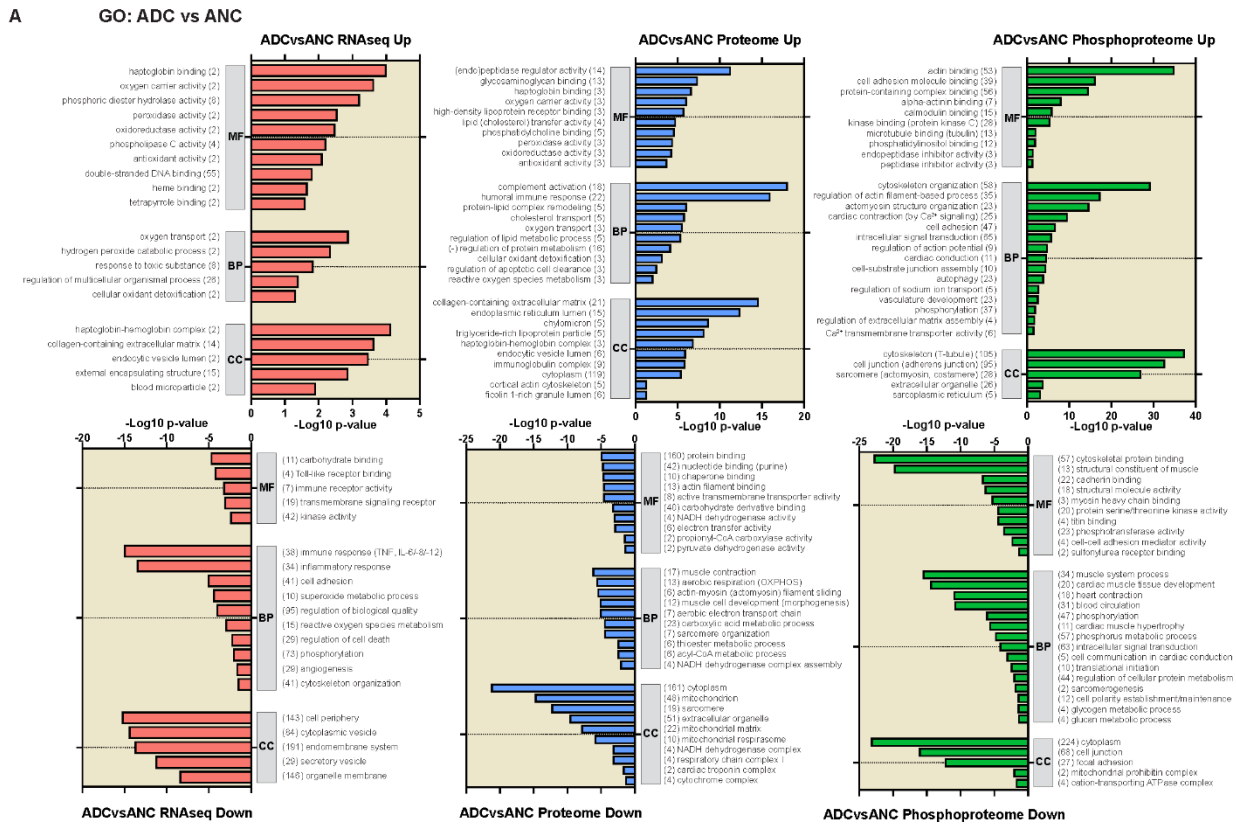

Figure 5.10. Comparative pathway enrichment analyses between A-DC versus A-NC across different datasets, including transcriptome (A), proteome (B), and phosphoproteome (C). Top 20 most over- and down-represented biological pathways were presented.

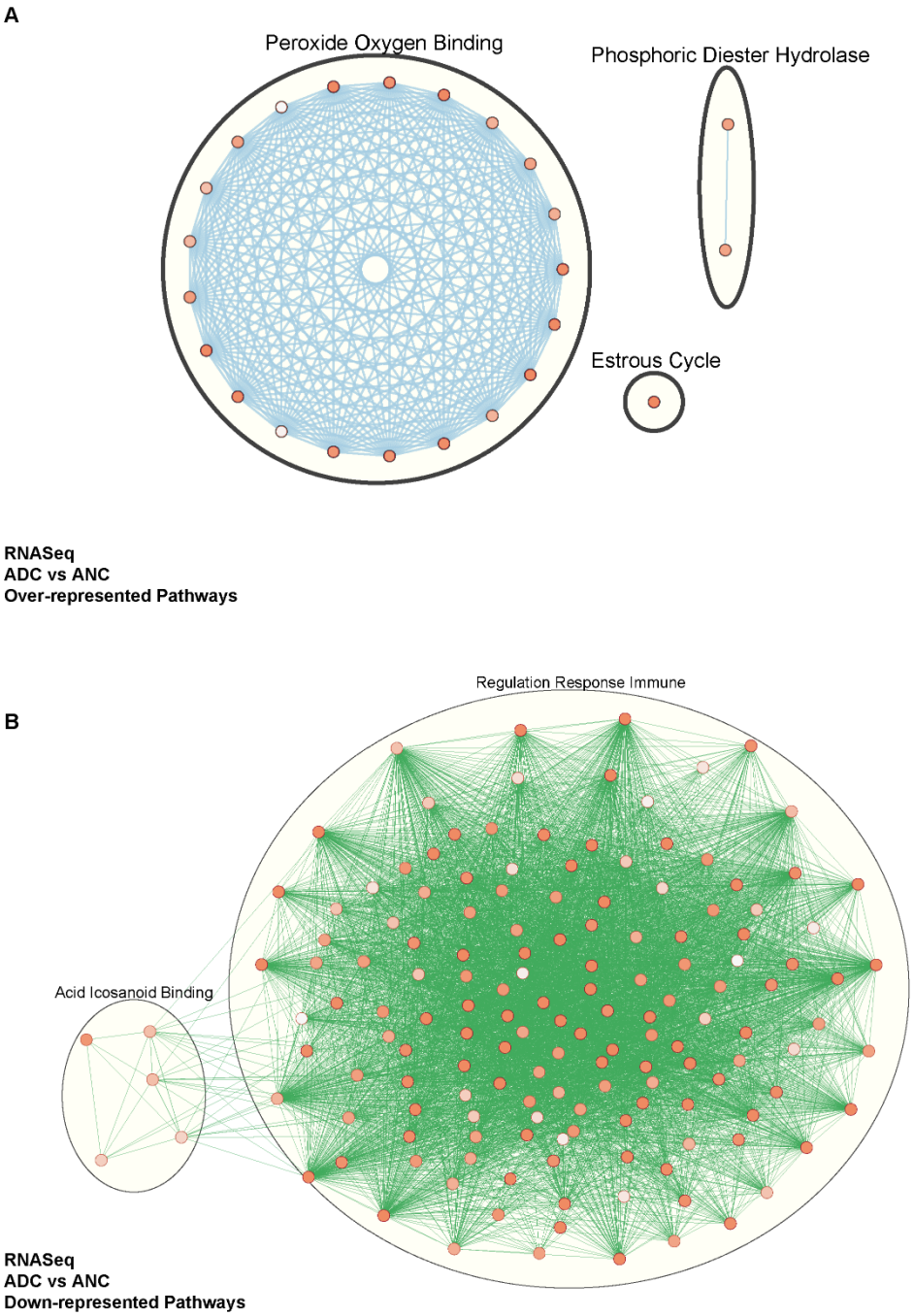

Figure 5.11. Network biology visualization of over- and down-represented functional pathways between A-DC versus A-NC using transcriptomic datasets in CytoScape. Individual node (colored by enrichment scores) represented the biological pathways, while the edge indicated the connection (i.e.,

shareable genes) between different pathways and its size was determined by the number of common genes shared between connected pathways. Blue edge indicated over representation whereas green indicated down representation of the biological pathways between comparisons.

P-DC vs. P-NC. Next, we investigated P-DC by inputting a total of 327 upregulated and 277 downregulated genes (in relation to P-NC), respectively, to g:GOSt (**Fig. 5.12A**). Enriched pathways implicated in molecular function were predominantly involved in regulations of mitochondrial oxidoreductase activities, including NADH dehydrogenase (ubiquinone, GO:0008137; quinone, GO:0050136), NAD(P)H dehydrogenase (quinone, GO:0003955) activities in ETC (GO:0009055), acyl-CoA dehydrogenase (GO:0003955) and nucleoside-triphosphatase (GO:0017111) activities in oxidative phosphorylation (GO:0006119), and ATPase-coupled transmembrane transporter activities (GO:0044769) (**Fig. 5.12A**). As for biological processes, we found concordant changes of functional terms specifically related to metabolic process (GO:0046034) in pediatric failing hearts compared to controls, featuring aerobic respiration (GO:0009060), ATP biosynthetic (GO:0006754), and mitochondrial organization (GO:0007005), translation (GO:0032543) and transport (GO:0006839) (**Fig. 5.12A**). Importantly, P-DC demonstrated significantly enriched pathways related to the respiratory ETC activities (GO:0022904, GO:0042773, GO:0042775, GO:0022900, GO:0019646, GO:0006120), NADH dehydrogenase complex I assembly (GO:0010257, GO:0032981, GO:0033108, GO:0006120) and transmembrane proton transport (GO:0042776, GO:1902600, GO:0015986, GO:0015985) down electrochemical gradient (**Fig. 5.12A**). Of note, fatty acid biosynthesis (GO:0006633) and metabolism (GO:0006631, GO:0044255, GO:0006629, GO:0009062) were overrepresented in P-DC (**Fig. 5.12A**), which indicated an inappropriate metabolic shift to lipid metabolism or utilization possibly underlying early presentation of HF in those children. Mitochondrial skeletons (matrix, envelope, membranes), oxidoreductase complex (complex I), and respirasomes represented the intracellular components that correspond to the pathways most enriched in pediatric failing hearts (**Fig. 5.12A**). Similarly, CytoScape confirmed that mitochondrial electron transporting activity in association with other biological processes such as translation termination and ribonucleoside biosynthetic regulation represented the biological themes that were most enriched in P-DC when compared to P-NC (**Fig. 5.13**).

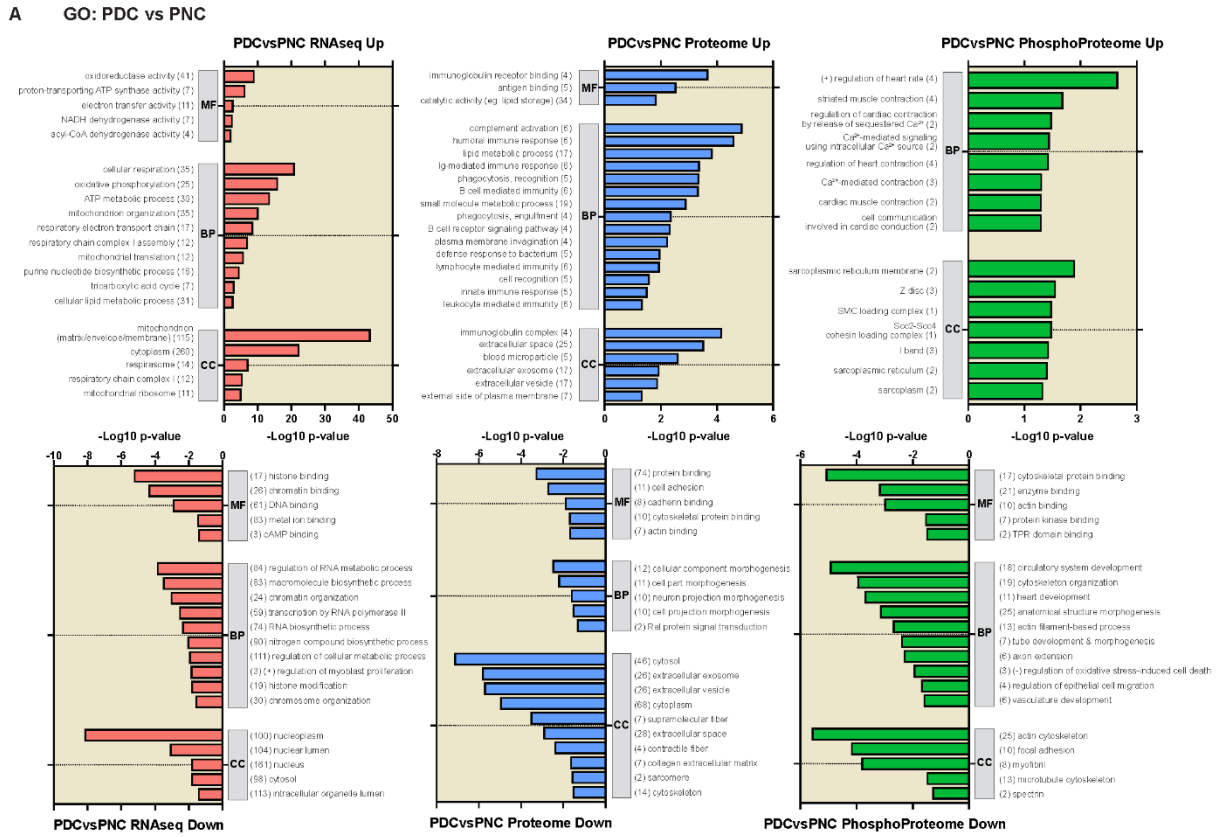

Figure 5.12. Comparative pathway enrichment analyses between P-DC versus P-NC across different datasets, including transcriptome (A), proteome (B), and phosphoproteome (C). Top 20 most over- and down-represented biological pathways were presented.

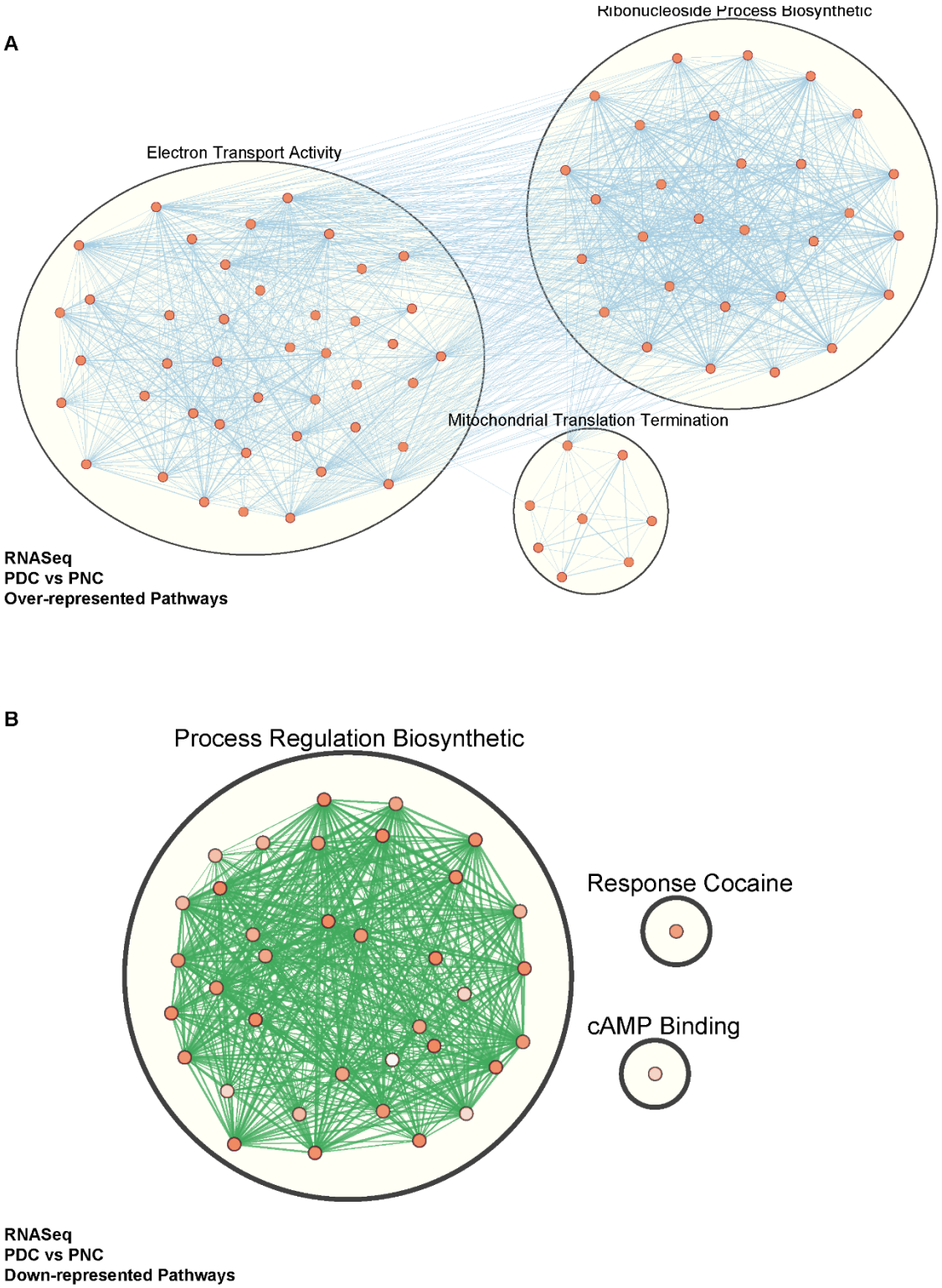

Figure 5.13. Network biology visualization of over- and down-represented functional pathways between P-DC versus P-NC using transcriptomic datasets in CytoScape. Individual node (colored by enrichment scores) represented the biological pathways, while the edge indicated the connection (i.e.,

shareable genes) between different pathways and its size was determined by the number of common genes shared between connected pathways. Blue edge indicated over representation whereas green indicated down representation of the biological pathways between comparisons.

A-DC vs. P-DC. Subsequently, we profiled A-DC by contrasting to P-DC directly, using a total list of 224 upregulated and 229 downregulated genes (**Fig. 5.14A**). A-DC had enriched pathways implicated in protein binding (GO:0005515), oxidoreductase activity (GO:0016491, GO:0016628), and metabolic processes (GO:0044260) (**Fig. 5.14A**), whereas P-DC demonstrated an overall larger number of enriched pathways (402) related to signaling receptor activities (GO:0038023) such as G protein-coupled chemoattractant receptor (GO:0001637, GO:0005096), C-C chemokine receptor (GO:0016493, GO:0019957, GO:0004950) and chemokine binding activity (GO:0019956, GO:0035715, GO:0035716) (**Fig. 5.14A**). Notably, molecular function involving ECM structural constituent (GO:0005201) was overrepresented in P-DC. Various aspects of immune responses (GO:0006955, intersection size: 21) including cellular extravasation (GO:0045123) were among the most underrepresented pathways in adult failing hearts, along with intracellular signaling transduction (GO:0007165, intersection size: 44), cell-cell communications (GO:0007154, intersection size: 46), and cellular adhesion (GO:0007155, intersection size: 19), migration (GO:0016477, intersection size: 18), and motility (GO:0048870, intersection size: 19). Accordingly, endomembrane system (GO:0012505), cytoplasmic lysosomes (GO:0036019), and tertiary secretory granules (GO:0030141, GO:0030667, GO:0070820, GO:0070821) such as ficolin 1-rich granule (GO:0101002, GO:0101003) and nucleoplasm (GO:0005654) were among the most significantly enriched compartments in P-DC. Further, P-DC had relatively enriched pathways related to regulation of primary metabolic processes (GO:0031323, intersection size: 95) explicitly involving nitrogen compound metabolites (GO:0051171, intersection size: 91) than that in A-DC, which was also captured by network biology visualization in **Figure 5.15**.

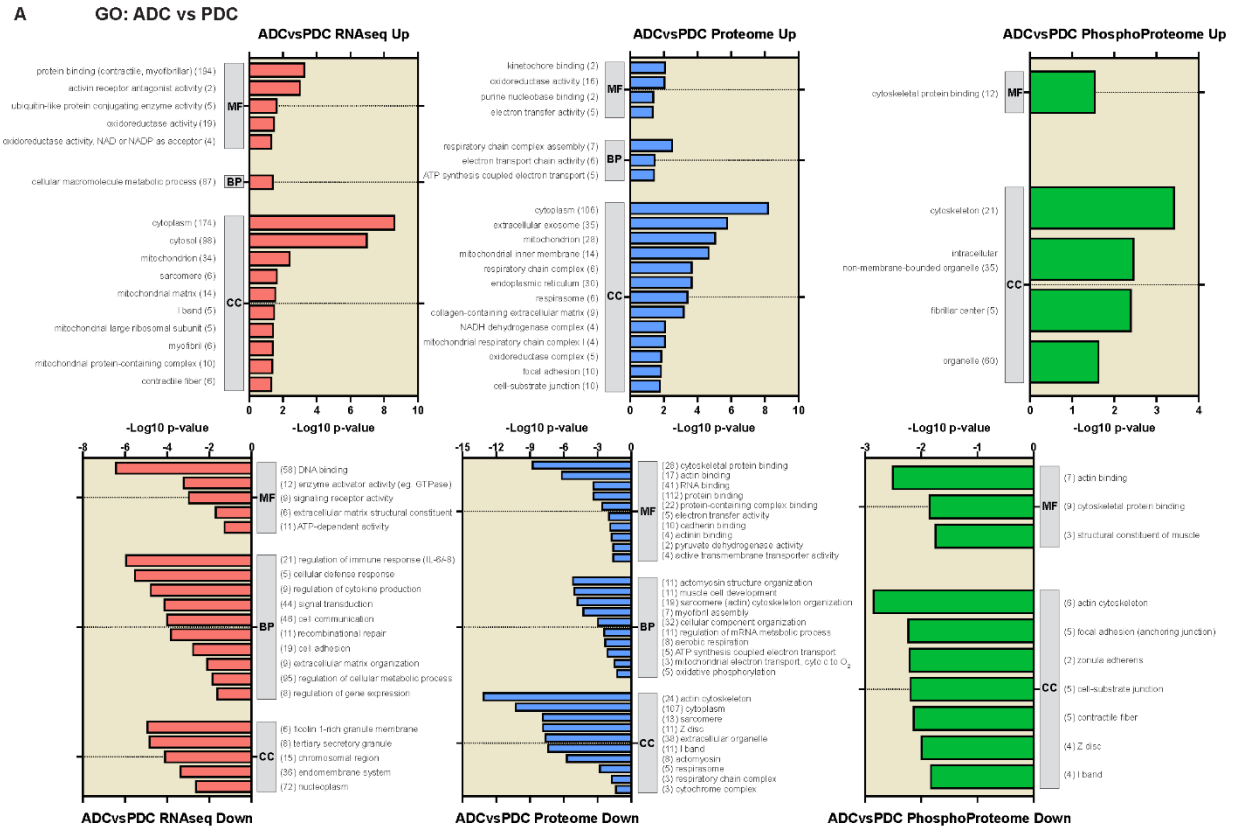

Figure 5.14. Comparative pathway enrichment analyses between A-DC versus P-DC across different datasets, including transcriptome (A), proteome (B), and phosphoproteome (C). Top 20 most over- and down-represented biological pathways were presented.

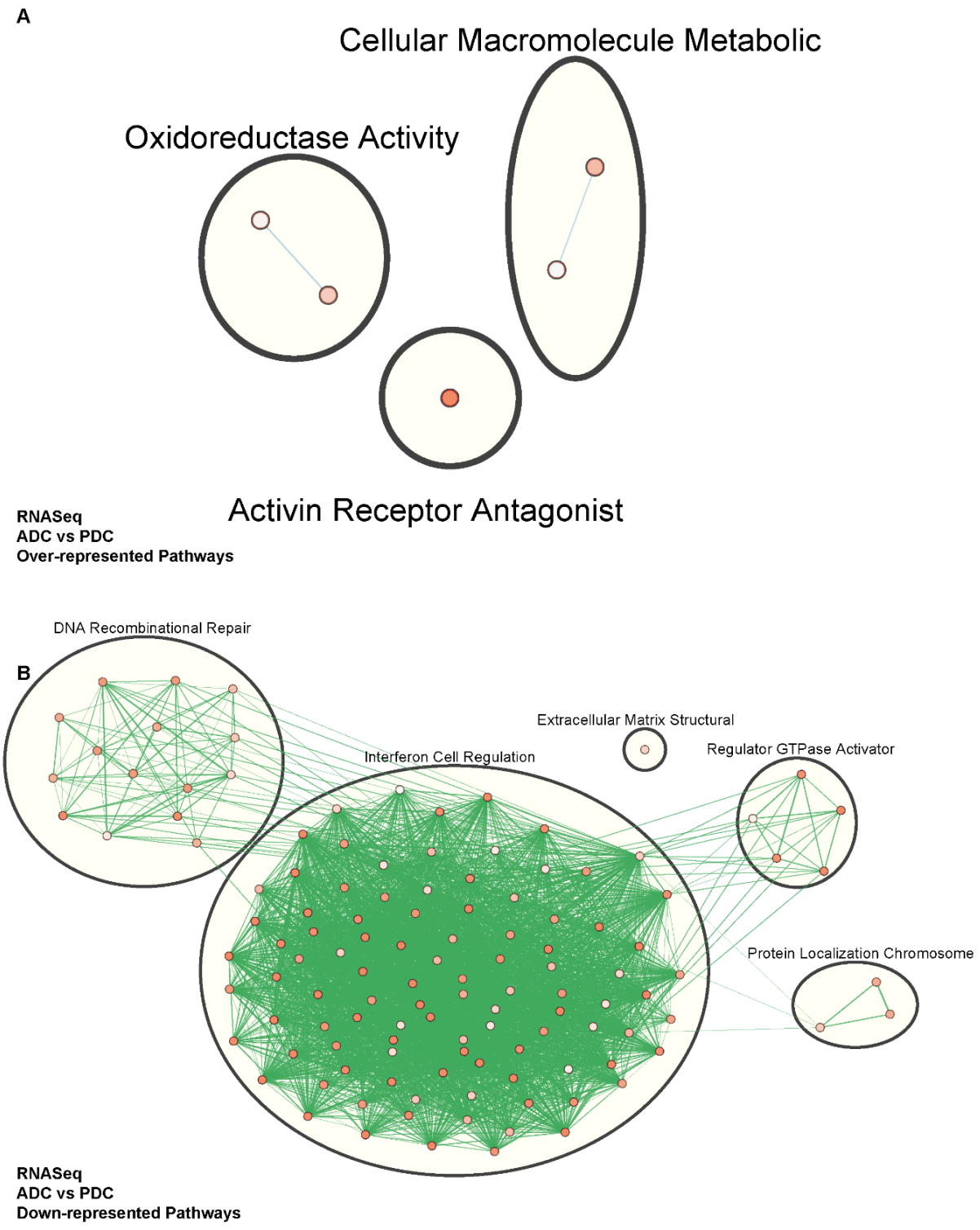

Figure 5.15. Network biology visualization of over- and down-represented functional pathways between A-DC versus P-DC using transcriptomic datasets in CytoScape. Individual node (colored by enrichment scores) represented the biological pathways, while the edge indicated the connection (i.e., shareable genes) between different pathways and its size was determined by the number of common genes

shared between connected pathways. Blue edge indicated over representation whereas green indicated down representation of the biological pathways between comparisons.

Comparisons at Proteomic Level. Our downstream proteomic and phosphoproteomic analyses (**Figure 5.10, 5.12, 5.14**) showed concordant changes with transcriptional findings.

A-DC vs. A-NC. We identified 393 pathways enriched in A-DC following the submission of 164 upregulated genes (corresponding to the proteomic datasets) to g:GOSt, among which oxygen carrier activity (GO:0005344) via haptoglobin (GO:0031720) and hemoglobin (GO:0030492) binding, antioxidant activities (GO:0016209) acting on peroxidase (GO:0004601, GO:0016684) were similarly overrepresented, as compared to A-NC (**Fig. 5.10B**). Interestingly, glycosaminoglycan binding pathway (GO:0005539) was overrepresented in A-DC, and we previously identified, though total glycosaminoglycan content was increased comparably between adult and pediatric failing hearts, its affinity to sequester transforming growth factor-beta was suppressed to a much greater extent in adult failing hearts leading to greater fibrosis in these hearts[129]. In the meantime, underrepresented pathways in A-DC as compared to A-NC were mainly related to contractile constituents (GO:0006936), including myofibril assembly (GO:0030239), actomyosin structure (GO:0031032), sarcomeric organization (GO:0045214), and myocardium morphogenesis (GO:0055008, GO:0060415, GO:0048644) (**Fig. 5.10B**). Of note, pathways involved in ATP metabolic process (GO:0046034), aerobic respiration (GO:0009060), acetyl-CoA metabolic process (GO:0006084, GO:0006637), and pyruvate dehydrogenase activity on acetyl transferring (GO:0004739) were underrepresented in adult failing hearts, as an indication of fetal metabolic phenotype, when compared to the controls. Our network visualization analyses demonstrated concordant changes in enriched biological themes involving defense immune response, ROS balancing, and triglyceride lipoprotein utilization in A-DC versus A-NC (**Fig. 5.16**).

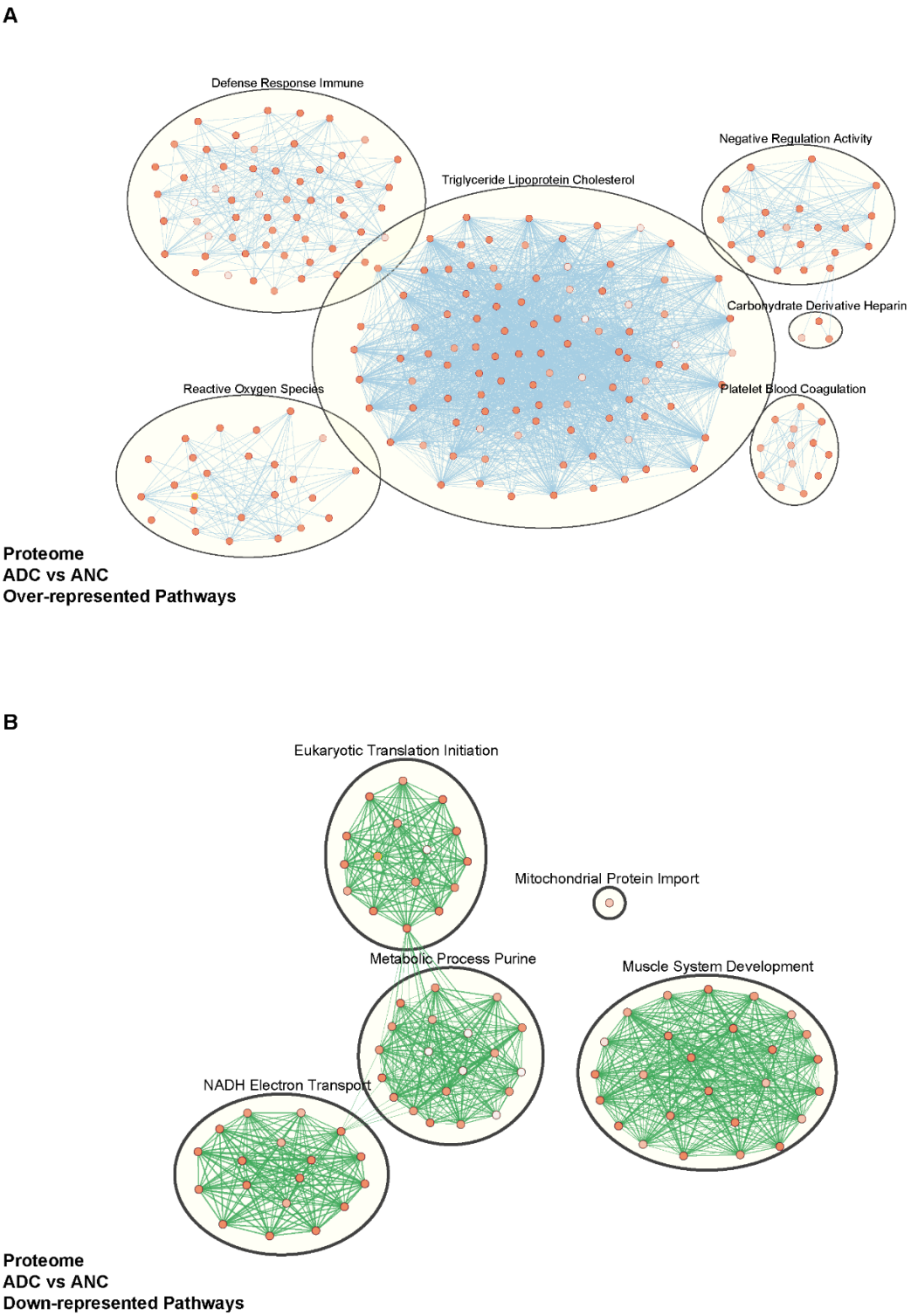

Figure 5.16. Network biology visualization of over- and down-represented functional pathways between A-DC versus A-NC using proteomic datasets in CytoScape. Individual node (colored by enrichment scores) represented the biological pathways, while the edge indicated the connection (i.e., shareable genes) between different pathways and its size was determined by the number of common genes

shared between connected pathways. Blue edge indicated over representation whereas green indicated down representation of the biological pathways between comparisons.

P-DC vs. P-NC. The most predominant overrepresented pathways in P-DC rather than P-NC were related to lipid metabolic process (GO:0006629, GO:0044281, GO:0044255, GO:0003824) and regulation of B cell-mediated immune response (GO:0002455, GO:0006959, GO:0050871) and lymphocyte-mediated immunity (GO:0002449) (**Fig. 5.12B, 5.17**), while underrepresented pathways were mainly associated with binding of cytoskeletal proteins (GO:0008092, GO:0003779) and cadherin (GO:0050839, GO:0045296), cellular morphogenesis (GO:0032989, GO:0032990) including neuron projection (GO:0048812, GO:0048858), and Ral protein signal transduction (GO:0032484) (**Fig. 5.12B, 5.17**).

A

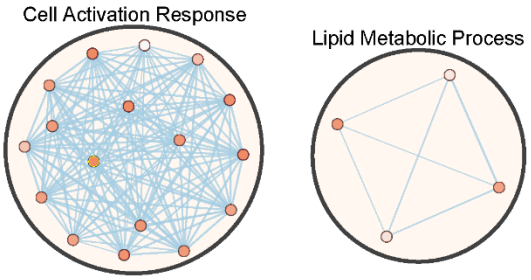

Proteome
PDC vs PNC
Over-represented Pathways

B

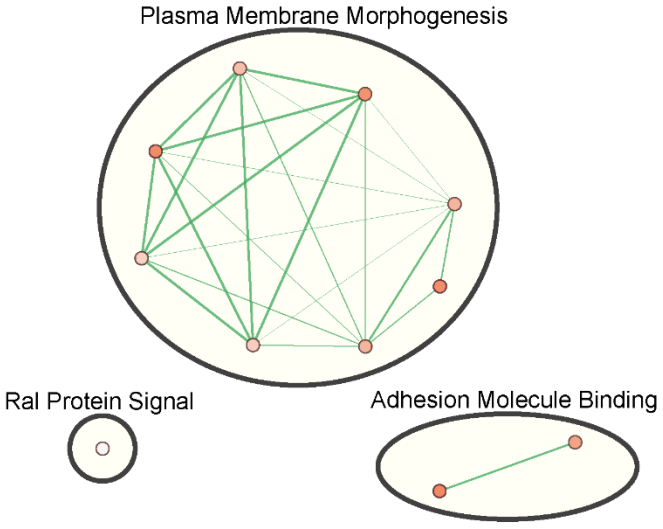

Proteome
PDC vs PNC
Down-represented Pathways

Figure 5.17. Network biology visualization of over- and down-represented functional pathways between P-DC versus P-NC using proteomic datasets in CytoScape. Individual node (colored by enrichment scores) represented the biological pathways, while the edge indicated the connection (i.e.,

shareable genes) between different pathways and its size was determined by the number of common genes shared between connected pathways. Blue edge indicated over representation whereas green indicated down representation of the biological pathways between comparisons.

A-DC vs. P-DC. Through direct comparison between A-DC versus P-DC (**Fig. 5.14B**), we identified enriched pathways in A-DC associated with oxidoreductase activities (GO:0016491) including respiratory electron transferring (GO:0009055, GO:0022904, GO:0042773, GO:0042775) and assembly of complexes (GO:0033108), in particular, complex I (GO:0005747, GO:0045271, GO:0030964), within mitochondrial respirasomes (GO:0070469, GO:0005746). However, P-DC demonstrated a large number of enriched pathways that were mainly involved in assembly, organization and morphogenesis of contractile machineries, regulations of biological quality, and mRNA processing and metabolism (**Fig. 5.14B**), which were consistently reflected by the pathway visualization analyses in **Figure 5.18**.

A

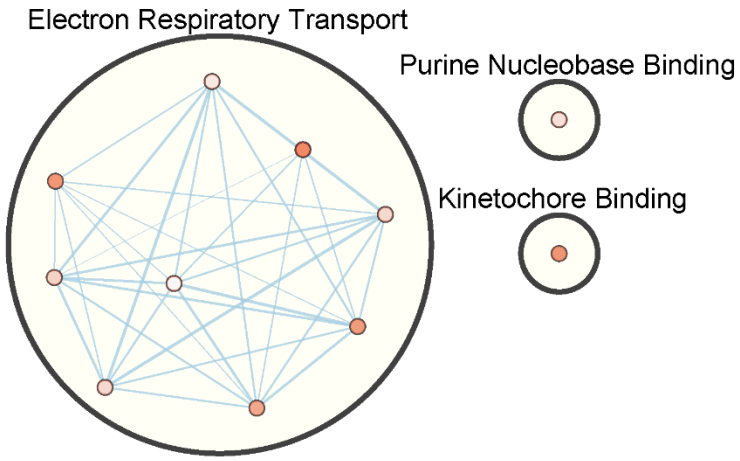

Proteome
ADC vs PDC
Over-represented Pathways

B

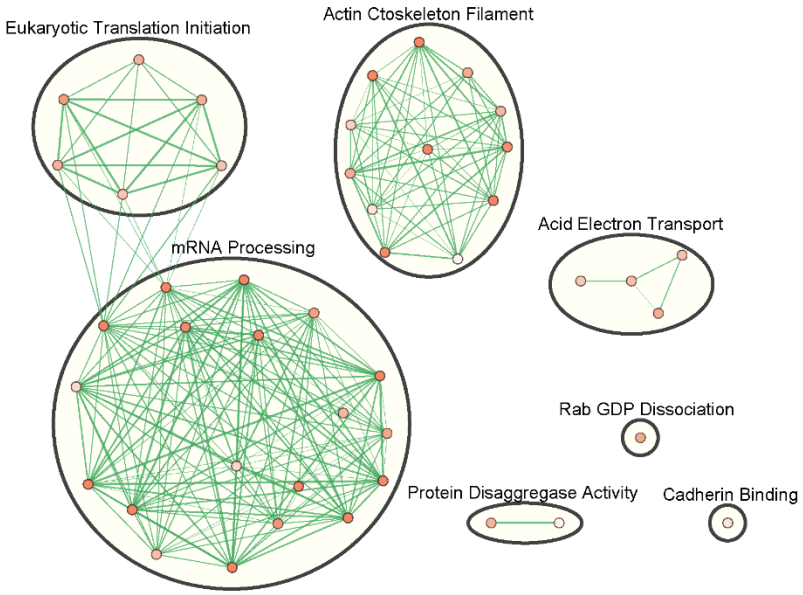

Proteome
ADC vs PDC
Down-represented Pathways

Figure 5.18. Network biology visualization of over- and down-represented functional pathways between A-DC versus P-DC using proteomic datasets in CytoScape. Individual node (colored by enrichment scores) represented the biological pathways, while the edge indicated the connection (i.e.,

shareable genes) between different pathways and its size was determined by the number of common genes shared between connected pathways. Blue edge indicated over representation whereas green indicated down representation of the biological pathways between comparisons.

Comparisons at Phospho-Proteomic Level. Our downstream pathway enrichment analyses using phosphoproteomic datasets for three paired comparisons shed essential insights on the functional profiles within different sample types, which were rather consistent with findings from the upstream analyses and visually summarized by network biology in CytoScape (**Fig. 5.19-5.21**).

A-DC vs. A-NC. We have identified 918 pathways enriched in A-DC as opposed to A-NC by uploading 555 upregulated gene transcripts from the transcriptomic datasets to g:GOSt. Among them, pathways overrepresented in A-DC were mainly associated with binding of cytoskeletal proteins (GO:0008092, intersection size: 79), including actin (GO:0003779, GO:0051015), alpha actinin (GO:0042805, GO:0051393, GO:0051371), calmodulin (GO:0005516) in contraction regulation, ankyrin (GO:0030506), spectrin (GO:0030507), cadherin (GO:0045296), tubulin (GO:0015631), and microtubule (GO:0008017) in mechanoreception, anchoring, and adhesion, and vinculin (GO:0017166) and dystroglycan (GO:0002162) in cell-matrix junctions (**Fig. 5.10C**). In addition, we identified enriched pathways involved in regulation of protein kinase binding (GO:0019901; intersection size: 24) such as protein kinase C (GO:0005080), peptidase inhibitor (GO:0030414) and endopeptidase regulator (GO:0004866, GO:0061135) in post-translational regulations, and enrichment of pathways in phosphatidylinositol binding (GO:0035091) and phosphatidylinositol-4-phosphate binding (GO:0070273) were also noted. The aforementioned molecular functions were further confirmed by functional terms related to biological processes. We identified overrepresented pathways in A-DC associated with cell morphogenesis (GO:0000902, GO:0009653, GO:0003007, GO:0032990), vasculature development (GO:0001944), intracellular signal transduction (GO:0035556, GO:0007165, GO:1902531, GO:0009966) such as phosphorylation (GO:0016310, intersection size: 37), regulation of cardiac conduction (GO:0061337, GO:0086005), and autophagy (GO:0006914, GO:0061919, GO:0010506, GO:0016236). Bundle of His cell to Purkinje myocyte communication (GO:0086073, GO:0086069), regulation of sodium ion transport (GO:0010765, GO:0002028, GO:1902305) and neuron development (GO:0048666) were also over-represented in A-DC (**Fig.**

5.10C). As for the down-represented pathways (729) in A-DC, they were mainly related to contractile protein binding of myosin heavy chain (GO:0032036) and titin (GO:0031432, GO:0070080), and carbohydrate metabolism as indicated by sulfonylurea receptor binding (GO:0017098), an insulin receptor. In addition, we observed a down-representation of pathways in heart cell hypertrophy (GO:0003300, GO:0014897, GO:0014896), and metabolic processes of glycogen (GO:0005977), glycan (GO:0044042, GO:0006073), and amide (GO:0034248). Importantly, cellular components such as mitochondrial prohibitin complex (GO:0035632) and ATPase transport complex (GO:0090533, GO:0098533) were among the most down-regulated terms in A-DC (**Fig. 5.10C**).

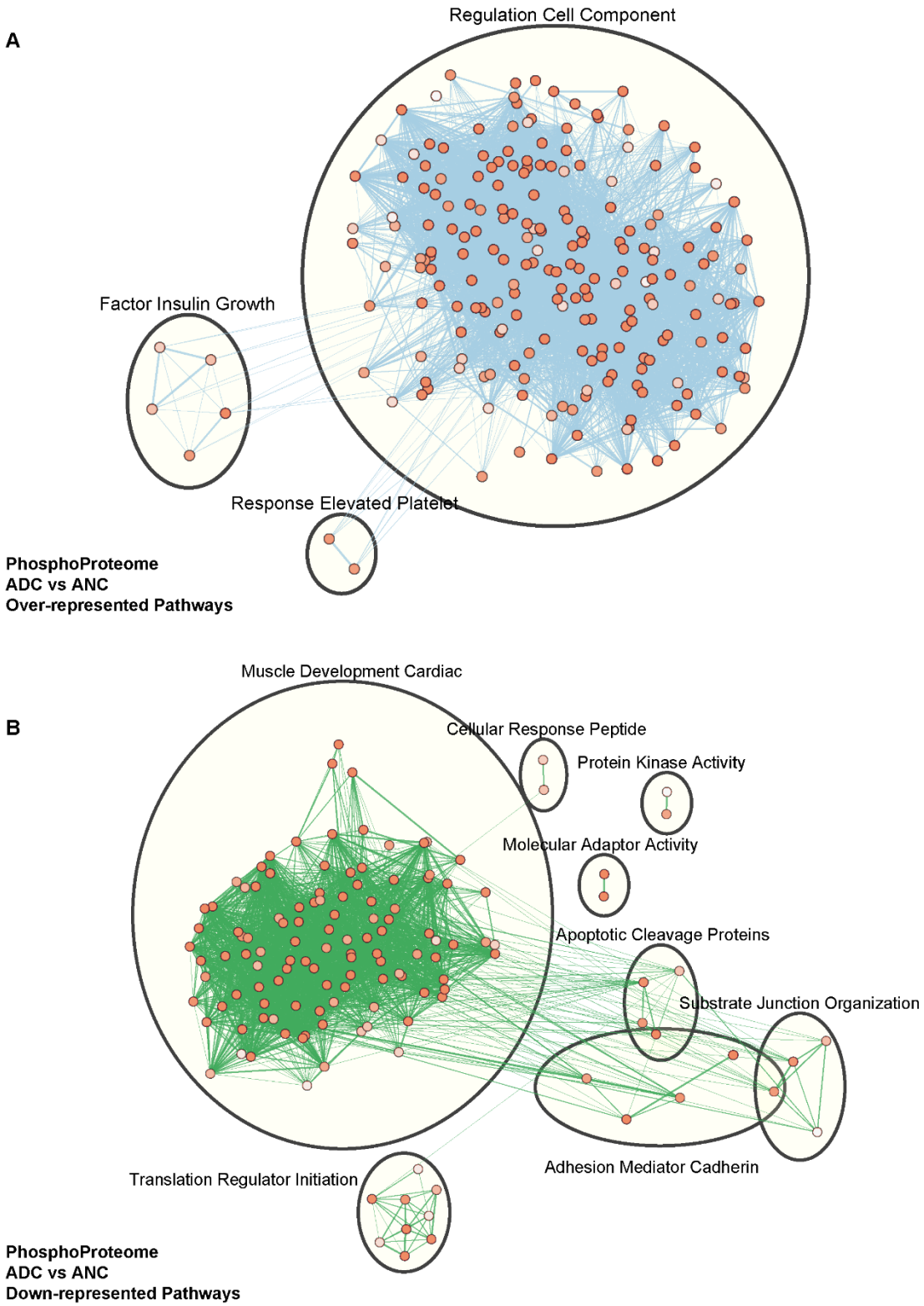

Figure 5.19. Network biology visualization of over- and down-represented functional pathways between A-DC versus A-NC using phosphoproteomic datasets in CytoScape. Individual node (colored by enrichment scores) represented the biological pathways, while the edge indicated the connection (i.e.,

shareable genes) between different pathways and its size was determined by the number of common genes shared between connected pathways. Blue edge indicated over representation whereas green indicated down representation of the biological pathways between comparisons.

P-DC vs. P-NC. P-DC had relatively maintained contractile properties (GO:0006941, GO:0008016) mediated by Ca2+ signaling (GO:0010881, GO:0035584, GO:0019722, GO:0010882), cardiac conduction (GO:0002027, GO:0010460) and intercellular communication (GO:0086064) (**Fig. 5.12C**). Of note, the SMC loading complex and Scc2-Scc4 cohesin loading complex, in addition to the sarcoplasmic reticulum and Z disc, were among the top enriched cellular components in P-DC. Interestingly, neither ETC nor respirasome stood out in the comparative analysis. On the other hand, the number of down-represented pathways (73) in P-DC was relatively more extensive, and they were primarily involved in the development of heart (GO:0032502, GO:0072359, GO:0007507), vasculature (GO:0001944), and neuron including projection extension (GO:1990138), tube morphogenesis (GO:0035239), and axon extension (GO:0048675), migration of epithelial cell (GO:0010632), and regulation of oxidative stress-induced cell death (GO:1903202, GO:1903201) (**Fig. 5.12C**).

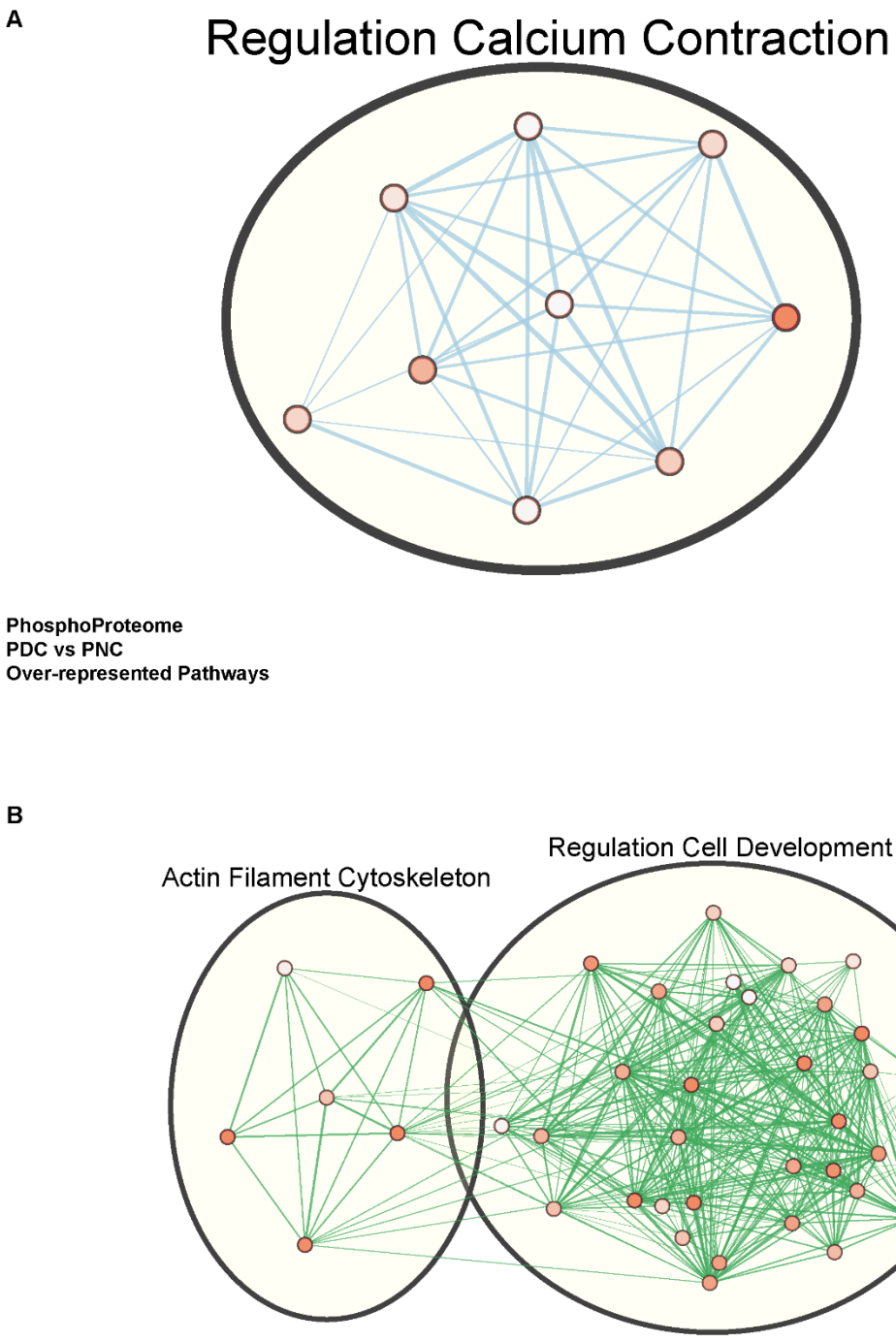

Figure 5.20. Network biology visualization of over- and down-represented functional pathways between P-DC versus P-NC using phosphoproteomic datasets in CytoScape. Individual node (colored by enrichment scores) represented the biological pathways, while the edge indicated the connection (i.e.,

shareable genes) between different pathways and its size was determined by the number of common genes shared between connected pathways. Blue edge indicated over representation whereas green indicated down representation of the biological pathways between comparisons.

A-DC vs. P-DC. Lastly, we investigated into the enrichment of pathways between A-DC and P-DC, and we noted that the output data were quite limited. Only a total of 8 and 12 pathways were over- or down-represented in A-DC, respectively (**Fig. 5.14C**). Among them, the pathways featured as most distinctly altered were involved in contractile processes, such as cytoskeletal protein binding, and myofibrillar assembly. Surprisingly, no metabolic pathways were highlighted at the post-translational level.

A

PhosphoProteome
ADC vs PDC
Over-represented Pathways

B

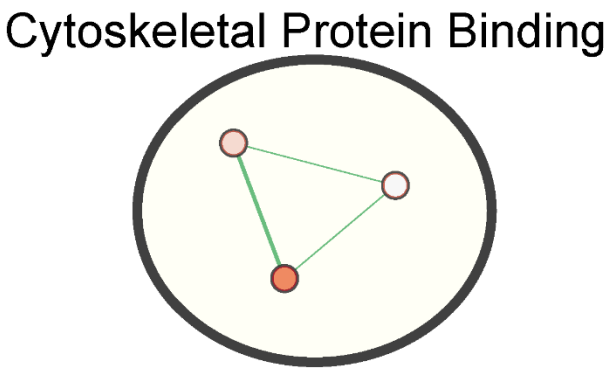

PhosphoProteome
ADC vs PDC
Down-represented Pathways

Figure 5.21. Network biology visualization of over- and down-represented functional pathways between A-DC versus P-DC using phosphoproteomic datasets in CytoScape. Individual node (colored by enrichment scores) represented the biological pathways, while the edge indicated the connection (i.e.,

shareable genes) between different pathways and its size was determined by the number of common genes shared between connected pathways. Blue edge indicated over representation whereas green indicated down representation of the biological pathways between comparisons.

5.5.6. Distinct Metabolic Profiles in P-DC with Defective Complex I and Dysfunctional MnSOD

Humans produce a significant amount of adenosine triphosphate (ATP, ~65kg) daily, and the heart consumes roughly 8% of all ATP generated despite its relatively smaller portion (~0.5%) in whole body weight[421, 422]. Unsurprisingly, the heart, among any other organs, contains the highest content of mitochondria, within which oxidative phosphorylation generates most ATP (~95%) to support the contraction-relaxation cycle and maintenance of membrane transport systems[423, 424]. Ca^{2+} sequestration into the sarcoplasmic reticulum is another big consumer of ATP. Since cardiac energy storage can be quickly exhausted within a few heartbeats, mitochondria must work efficiently to cope with the constantly-changing energy needs imposed by the whole body. Mitochondrial abnormalities and impaired ATP-generating capacity profoundly affect the heart function, and they are believed to link with adverse myocardial remodeling (e.g., myocytes injury) at the tissue level. In addition to being a major source of ROS, damaged mitochondria also promote programmed cell death by releasing cytochrome c to the cytosol and activation of caspases[425]. HF progression is associated with declining mitochondrial capacity that eventually reaches a point after which other compensatory mechanisms can no longer sustain the energy demands[421]. Prior studies in cardiomyopathic failing hearts confirmed remarkable loss of total adenine nucleotide pool including ATP, ADP and AMP, declined creatine kinase activities essential for ATP synthesis, and reduced amount of creatine phosphate and Cr/ATP ratio (a marker of energy metabolism)[299, 423, 424]. Moreover, mitochondrial dysfunction is often associated with patients with renal failure[426] and insulin resistance[427] (comorbidities frequently seen in HF), which highlights the importance of treating mitochondrial impairments in the HF population, possibly through cardiac and extracardiac pathogeneses[421].

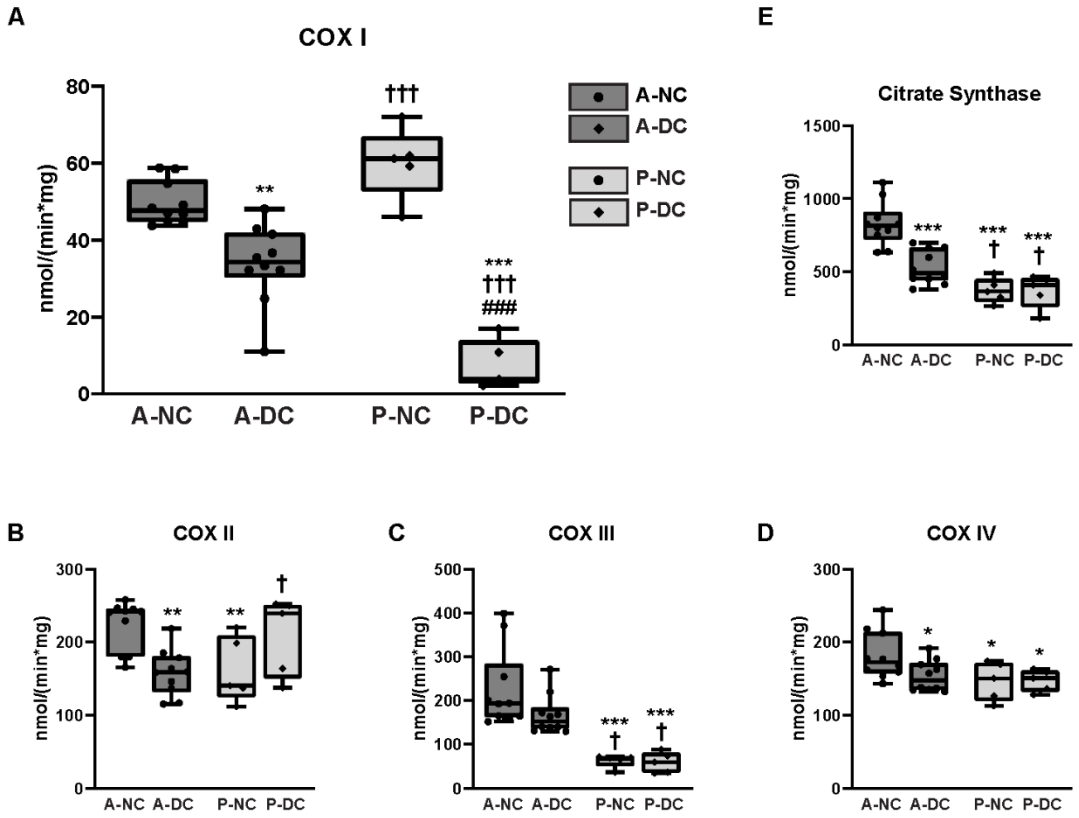

Figure 5.22. Spectrophotometric measurement of electron transport chain enzymatic activities from Complex I to IV, and citrate synthase from Krebs Cycle.

Electron transport chain locates in the inner mitochondrial membranes, and is composed of a series of multimeric protein complexes encoded by both nuclear and mitochondrial DNA. Normal functioning of ETC is essential for fueling various cardiac activities, and its abnormalities have been reported to associate with mitochondrial dysfunction and DCM[428]. Our complex-specific activity assays demonstrated a selective loss of complex I, II, and IV (**Fig. 5.22A-D**) activities in A-DC, with only complex I (NADH ubiquinone oxidoreductase, **Fig. 5.22A**) significantly decreased in P-DC, in comparison to their respective controls. Declined activity of citrate synthase (CS, **Fig. 5.22E**) in the adult failing hearts, further confirmed disrupted intermediary metabolism in A-DC, while it was absent in children's failing hearts in comparison to the controls. Enzymatic activities of complex III (**Fig. 5.22C**), IV (**Fig. 5.22D**) and CS (**Fig. 5.22E**) in the pediatric cohorts were lower than the adults, reflective of an overall smaller functional capacity of citric acid cycling and electron transporting in the children hearts. As the only complex that participates in the citric acid cycle within mitochondrial matrix, complex II (succinate dehydrogenase) is involved in transforming succinate to fumarate and introducing

additional electrons (2) into ETC. Interestingly, the activity of complex II (**Fig. 5.22B**) tended to increase or maintain in the pediatric failing hearts when compared to adult counterparts or P-NC, likely a compensating mechanism as the second entry point of the electron transport pathway, which was clearly inadequate to restore oxidoreduction efficiency in the kids with HF. Given the large-size multiprotein nature of those complexes, we further verified the coding gene and protein expression levels of individual subunit by bulk RNA sequencing and quantitative precision mass spectrometry, respectively. Our results showed the protein expressions of a large proportion of the core (6 out of 14) and supernumerary (8 out of 30) subunits that constitute complex I were significantly decreased in P-DC, while only the genes encoding supernumerary subunits (14 out of 30) were consistently reduced with statistical significance, when compared to A-DC (**Fig. 5.23-5.25**). No remarkable differences in the complex I coding genes were noted in the adult failing hearts, but a few of the subunits including 2 core and 10 supernumerary isoforms showed elevated protein expression when compared to the adult controls (**Fig. 5.23-5.25**). Similarly, we found, at the gene levels (SDHA, SDHB, SDHC, SDHD) of complex II, there was no statistical difference between P-DC versus A-DC, but the protein levels of the succinate dehydrogenase subunits encoded by SDHB (increased) and SDHC (decreased) differed. No statistical differences at the level of coding genes and proteins of complex II were noted between the adult subgroups (**Fig. 5.26-5.28**). As for complex III, none of the 10 coding genes showed any differences between adult subgroups, while 4 subunits (encoded by UQCRC1, CYC1, UQCRFS1, UQCRB) demonstrated significantly reduced protein quantity in A-DC (**Fig. 5.26-5.28**). However, in the pediatric failing hearts, the gene expression level of UQCRC1 and UQCRB (2 out of 10) were significantly lower than those in A-DC, while only CYC1- and UQCRH-coded protein subunits of complex III were lower in P-DC (**Fig. 5.26-5.28**). Further, 4 out of 16 coding genes (COX4I1, COX5A, COX6B1, MT-CO2) of complex IV were significantly lower in P-DC compared to A-DC, which was associated with a higher number (6 out of 16) of cytochrome c oxidase subunits that had reduced protein amounts (**Fig. 5.26-5.28**). However, in the adult failing hearts, only 2 out of 16 coding genes (MT-CO1, MT-CO3) and protein subunits (encoded by COX5B, COX6A1) of complex IV were lowered compared to adult controls (**Fig. 5.26-5.28**). Lastly, no statistical differences were noted between adult subgroups at the level of coding genes (18) and proteins (2) for ATP synthase (complex V) (**Fig. 5.26-5.28**). Similarly, no statistical differences were observed between P-DC versus A-DC at the level of proteins for complex V, though 6 out of 18 coding genes were

significantly declined in P-DC (**Fig. 5.26-5.28**). Interestingly, overall higher levels of coding gene and protein expression of ETC complexes were noted in P-DC versus P-NC (**Fig. 5.23-5.28**), indicating our selection of the pediatric control is suboptimal and thus, it was only used for reference purposes.

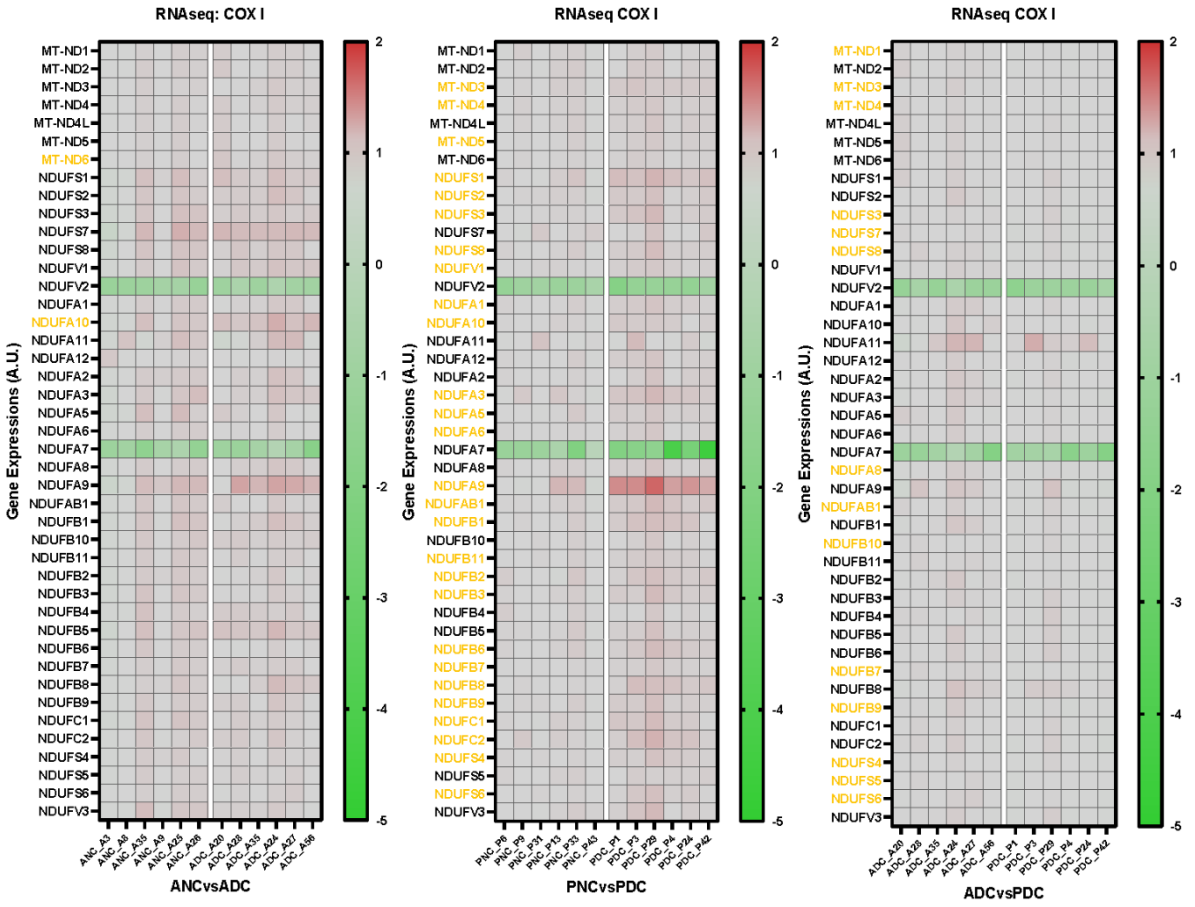

Figure 5.23. Gene expression of complex I subunits between A-DC versus A-NC (A), P-DC versus P-NC (B), A-DC versus P-DC (C) by bulk RNA sequencing. Individual samples included in omics analysis were presented. Red indicated up-regulated, while green indicated down-regulated expression levels across comparisons. Orange referred to those subunits that were significantly altered between comparisons.

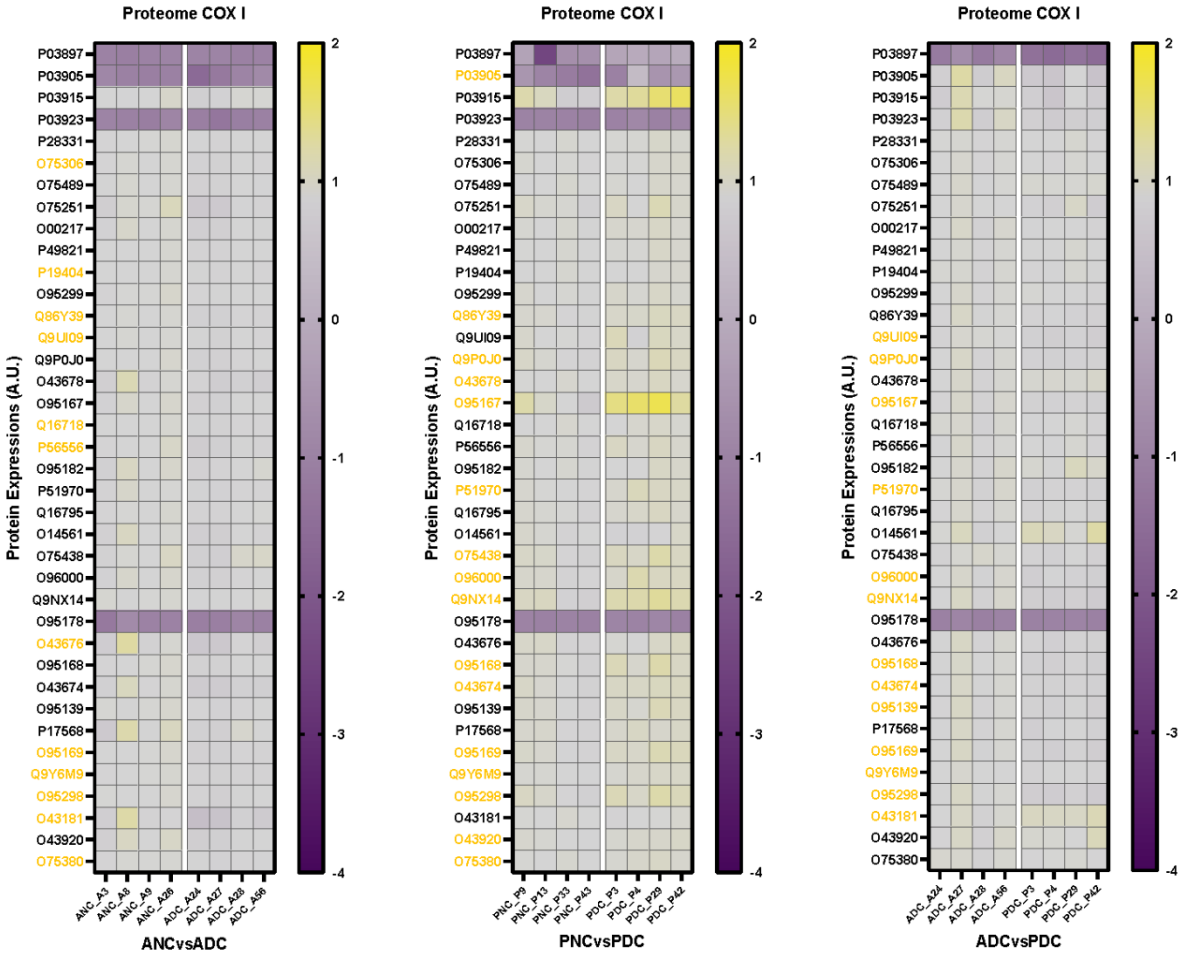

Figure 5.24. Protein expression of complex I subunits between A-DC versus A-NC (A), P-DC versus P-NC (B), A-DC versus P-DC (C) by quantitative precision mass spectrometry. Individual samples included in omics analysis were presented. Yellow indicated up-regulated, while purple indicated down-regulated expression levels across comparisons. Orange referred to those subunits that were significantly altered between comparisons.

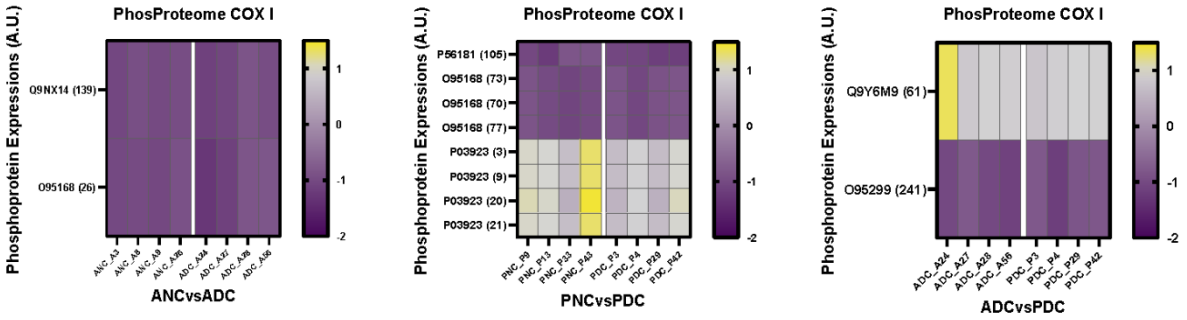

Figure 5.25. Phosphoprotein expression of complex I subunits (that were detectable) between A-DC versus A-NC (A), P-DC versus P-NC (B), A-DC versus P-DC (C) by quantitative precision mass spectrometry. Individual samples included in omics analysis were presented. Yellow indicated up-regulated, while purple indicated down-regulated expression levels across comparisons. Orange referred to those subunits that were significantly altered between comparisons.

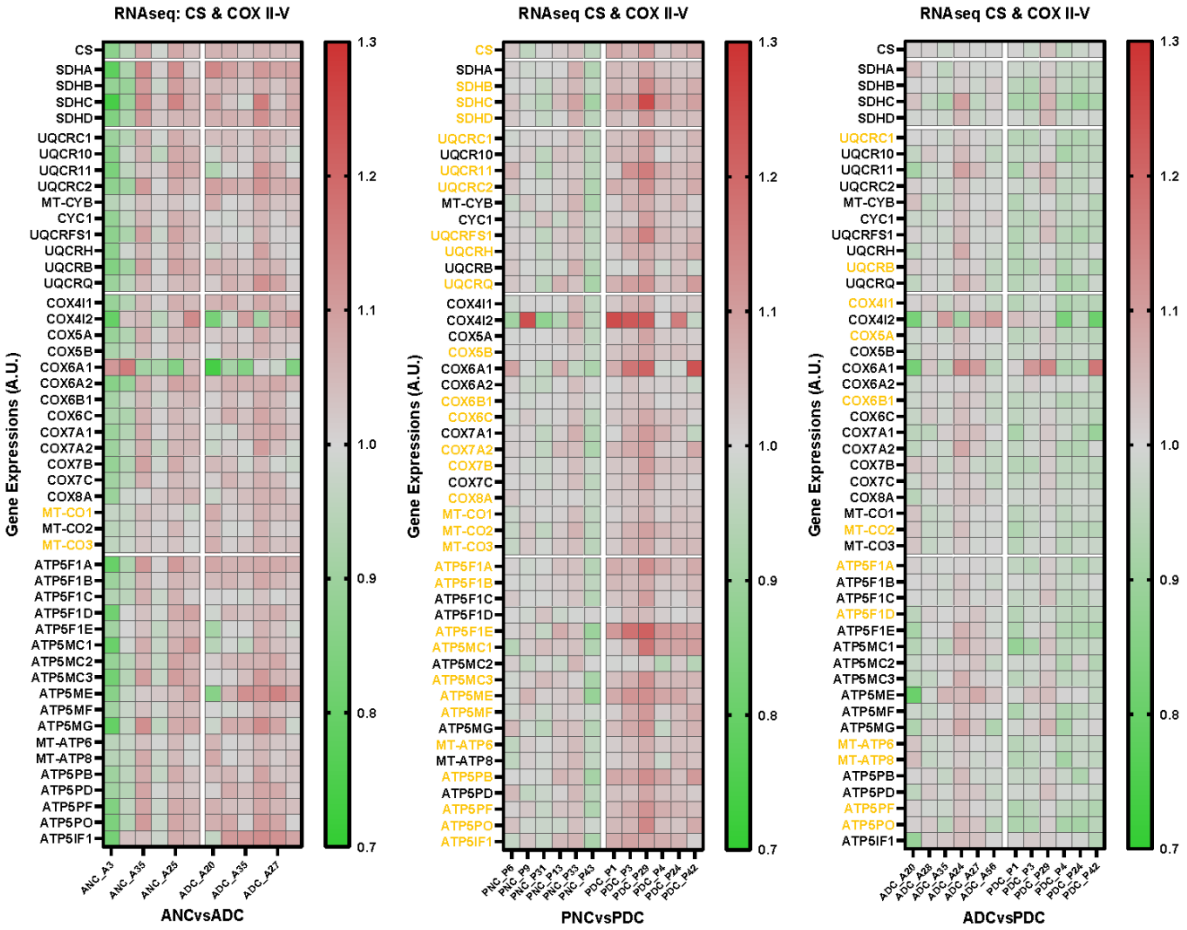

Figure 5.26. Gene expression of complex II-V subunits and citrate synthase between A-DC versus A-NC (A), P-DC versus P-NC (B), A-DC versus P-DC (C) by bulk RNA sequencing. Individual samples included in omics analysis were presented. Red indicated up-regulated, while green indicated down-regulated expression levels across comparisons. Orange referred to those subunits that were significantly altered between comparisons.

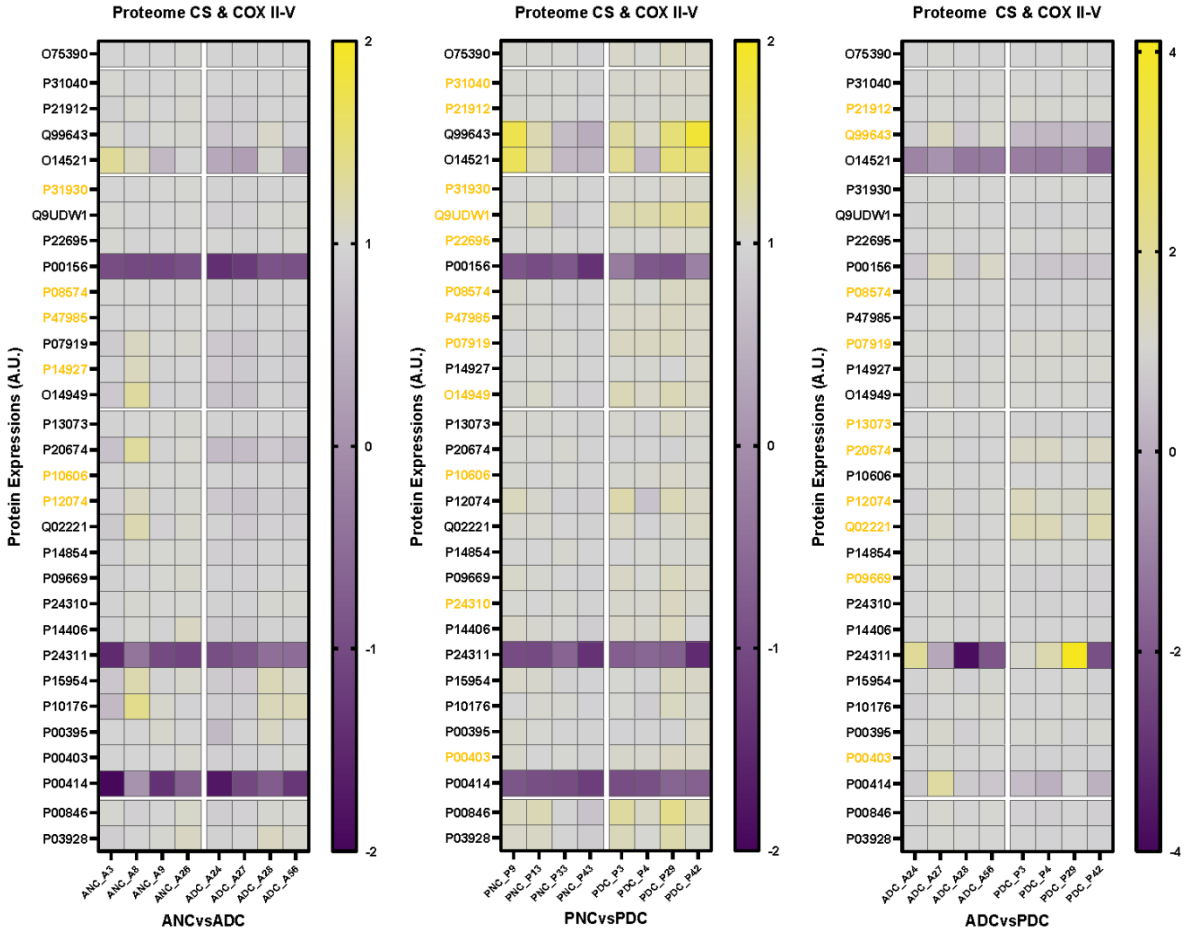

Figure 5.27. Protein expression of complex II-V subunits and citrate synthase between A-DC versus A-NC (A), P-DC versus P-NC (B), A-DC versus P-DC (C) by quantitative precision mass spectrometry. Individual samples included in omics analysis were presented. Yellow indicated up-regulated, while purple indicated down-regulated expression levels across comparisons. Orange referred to those subunits that were significantly altered between comparisons.

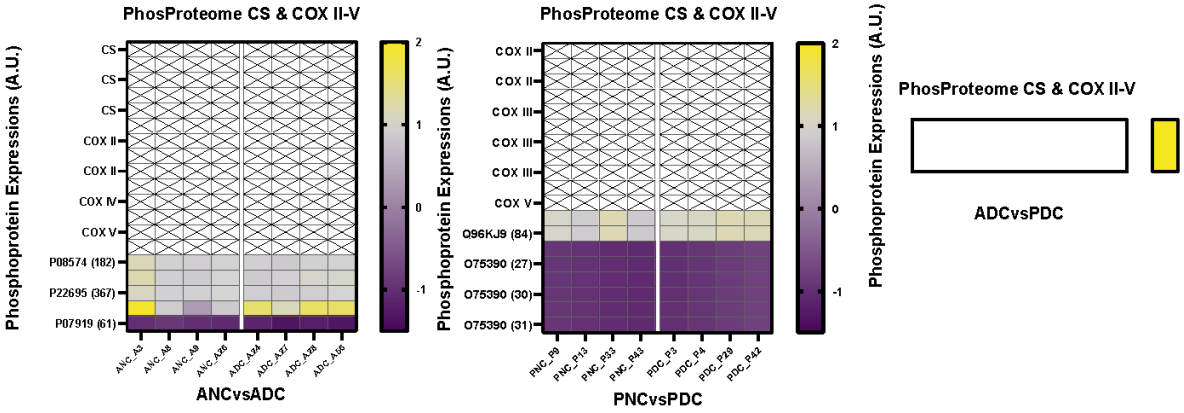

Figure 5.28. Phosphoprotein expression of complex II-V subunits and citrate synthase (that were detectable) between A-DC versus A-NC (A), P-DC versus P-NC (B), A-DC versus P-DC (C) by quantitative precision mass spectrometry. Individual samples included in omics analysis were presented. Yellow indicated up-regulated, while purple indicated down-regulated expression levels across comparisons. Orange referred to those subunits that were significantly altered between comparisons. Undetected hits were represented as blank blocks.

A-DC demonstrated significantly reduced protein expression of pyruvate dehydrogenase (PDH) when compared to both P-DC and adult controls (**Fig. 5.29-5.31**), indicating declined myocardial glycogen mobilization and glucose oxidation in the mitochondria, while possibly coupled with an alternative elevation of glycolysis in the adult failing hearts. Specifically, we found the two subunits of PDH encoded by PDHA1 and PDHB were consistently reduced with statistical significance in A-DC (**Fig. 5.29-5.31**). As a rate-limiting enzyme of glucose oxidation in the heart, PDH is regulated by multiple factors, including pyruvate dehydrogenase kinase (PDK, which inactivates PDH) and pyruvate dehydrogenase phosphatase (PDP, which activates PDH). We further investigated the expressional profiles of those regulators including genes, and we found an overall larger number of phosphorylated PDH (positions: 232; 298, 300; 291, 293; 293, 295) compared to the adult controls, confirming the overly glycolytic metabolic phenotype in the adult failing hearts which was absent in the pediatrics (**Fig. 5.29-5.31**).

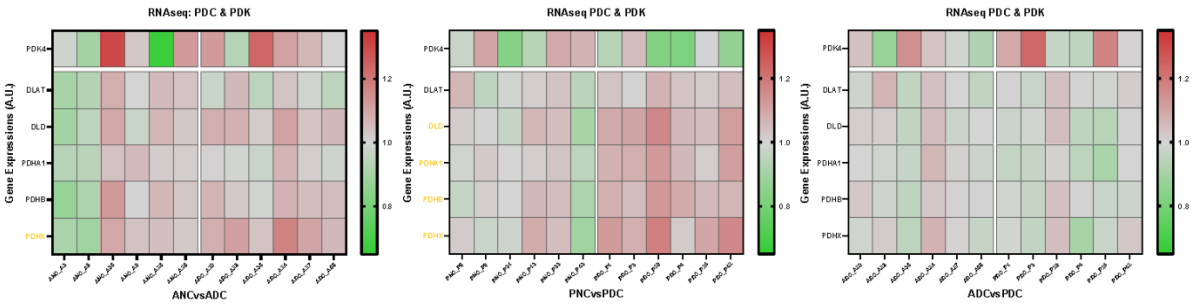

Figure 5.29. Gene expression of pyruvate dehydrogenase (PDH) and pyruvate dehydrogenase kinase (PDK) between A-DC versus A-NC (A), P-DC versus P-NC (B), A-DC versus P-DC (C) by bulk RNA sequencing. Individual samples included in omics analysis were presented. Red indicated up-regulated, while green indicated down-regulated expression levels across comparisons. Orange referred to those subunits that were significantly altered between comparisons.

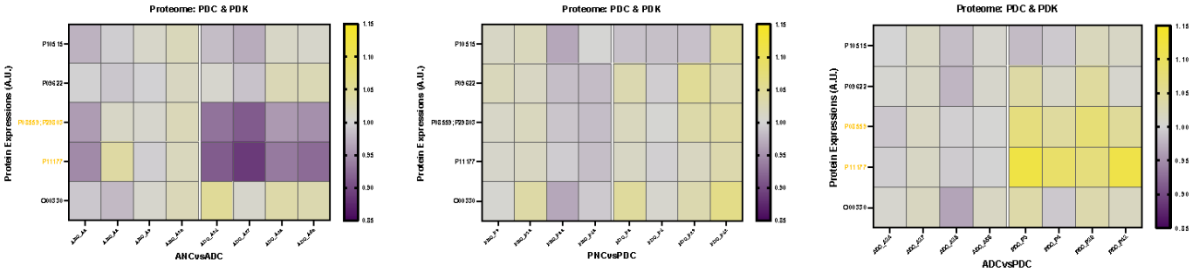

Figure 5.30. Protein expression of pyruvate dehydrogenase (PDH) and pyruvate dehydrogenase kinase (PDK) between A-DC versus A-NC (A), P-DC versus P-NC (B), A-DC versus P-DC (C) by quantitative precision mass spectrometry. Individual samples included in omics analysis were presented. Yellow indicated up-regulated, while purple indicated down-regulated expression levels across comparisons. Orange referred to those subunits that were significantly altered between comparisons.

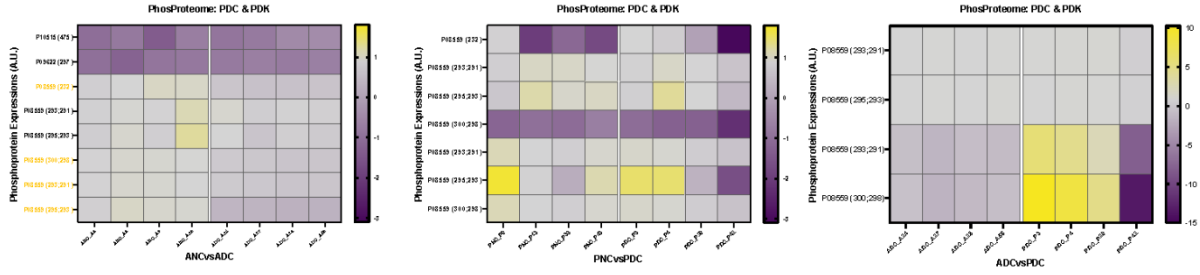

Figure 5.31. Phosphoprotein expression of pyruvate dehydrogenase (PDH) and pyruvate dehydrogenase kinase (PDK) (that were detectable) between A-DC versus A-NC (A), P-DC versus P-NC (B), A-DC versus P-DC (C) by quantitative precision mass spectrometry. Individual samples

included in omics analysis were presented. Yellow indicated up-regulated, while purple indicated down-regulated expression levels across comparisons. Undetected hits were represented as blank blocks. Orange referred to those subunits that were significantly altered between comparisons.

5.5.7. ROS Generation, Regulation and Oxidative Stress in Relation to ETC

Undoubtedly, cardiac mitochondria represent one of the most potent "energy factories" that produce a significant amount of endogenous superoxide as a byproduct of oxidative phosphorylation. In addition to the non-ETC source of ROS such as NADPH oxidase (Nox)-4[429] and alpha-ketoglutarate dehydrogenase (α-KGDH)[430], its generation mainly happens when the final electron receptor – oxygen – is insufficiently reduced due to leak of electrons at complex I and III[157]. In the meantime, superoxide dismutase family (SOD), catalase, glutathione peroxidase and glutathione reductase constitute the ROS-scavenging system. They work coordinately to maintain and prevent the oxidative stress from damaging the heart, given that ROS is also the second messenger of redox-sensitive signaling pathways essential in heart development, angiogenesis, and cellular apoptosis[431-433]. Baseline level of ROS plays a crucial role in the cardiac differentiation from human embryonic stem cells to mature cardiomyocytes[434]. Furthermore, cardiac reparative and regenerative functions are negatively correlated with the overall ROS levels. For instance, the increased ROS production from ETC is associated with restricted regeneration capability of cardiomyocytes, during the metabolic transition from glycolysis to oxidative phosphorylation during the newborn periods[157, 435].

Manganese SOD (MnSOD, SOD2) is a mitochondrial matrix-specific antioxidant responsible for clearing locally produced free radicals by converting them into hydrogen peroxide. Global knockout of *SOD2* in mice led to early death (10 days after birth) due to development of DCM and complications like metabolic acidosis and lipid deposition in liver and skeletal muscles[436], whereas cardiomyocyte-specific knockout mice devoid of *SOD2* led to overwhelmingly higher oxidative stress (by ROS generation) which triggers an overproduction of intramitochondrial 4-hydroxynoneal (4-HNE) as an aldehyde byproduct of lipid peroxidation of cardiolipin on the inner membrane of mitochondria[437, 438]. Pathologically overabundant 4-HNE in heart-specific *SOD2-null* mice specifically targets and alters protein subunits of respiratory ETC complexes and TCA cycle, including NDUFS2 (complex I), SDHA (complex II), ATP5B

(complex V), DLD (dihydrolipoamide dehydrogenase, component of 3 multienzyme complexes, pyruvate dehydrogenase complex, alpha ketoglutarate dehydrogenase complex, and branched-chain alpha ketoacid dehydrogenase complex), thereby damaging the mitochondrial respiration and bioenergetics ultimately leading to DCM and neonatal death due to systolic HF[438].

The expressional profiling of the major antioxidants consistently showed that P-DC had overall reduced gene expressions of all SOD families (SOD1-3) including mitochondria-specific SOD2 when compared to A-DC, though no statistical significance was observed for the protein levels (**Fig. 5.32-5.33**). Similarly, no significant differences at the protein and gene levels were seen for all other major ROS-scavenging proteins, namely, catalase, glutathione peroxidase 1 and glutathione disulfide reductase, between all comparisons across groups. However, we further performed enzymatic activity measurements of individual antioxidant and confirmed functional impairment of SOD2 in both diseased hearts with further reduction in P-DC in comparison to A-DC (**Fig. 5.32-5.33**), which may cause subsequent peroxidation of cardiolipin and mitochondrial membrane damage leading to aggressive ETC deficiency in P-DC.

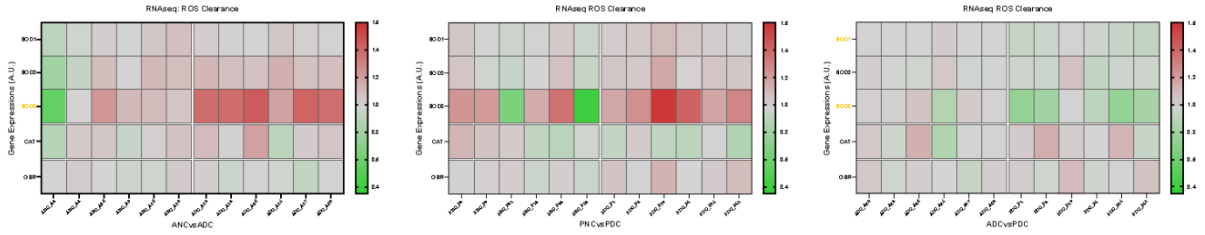

Figure 5.32. Gene expression of antioxidants between A-DC versus A-NC (A), P-DC versus P-NC (B), A-DC versus P-DC (C) by bulk RNA sequencing. Superoxidase dismutase (SOD1-3), catalase, glutathione peroxidase and glutathione reductase were probed. Individual samples included in omics analysis were presented. Red indicated up-regulated, while green indicated down-regulated expression levels across comparisons. Orange referred to those subunits that were significantly altered between comparisons.

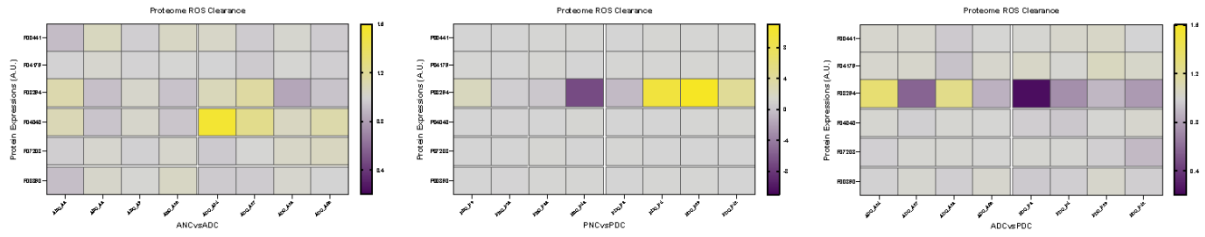

Figure 5.33. Protein expression of antioxidants between A-DC versus A-NC (A), P-DC versus P-NC (B), A-DC versus P-DC (C) by quantitative precision mass spectrometry. Superoxidase dismutase (SOD1-3), catalase, glutathione peroxidase and glutathione reductase were probed. Individual samples included in omics analysis were presented. Yellow indicated up-regulated, while purple indicated down-regulated expression levels across comparisons. Orange referred to those subunits that were significantly altered between comparisons.

5.6. Discussion

DCM can be defined as idiopathic when the case is sporadic and isolated in a single family member without known causes, or familial when two or more related families are affected or in the presence of sudden unexplained death of a first-degree relative at <35 years of age[102, 439, 440]. In most studies, the underlying causes of disease were undifferentiated, and it remains unclear whether the course of disease differs in familial and sporadic forms of DCM. Familial screening at an earlier stage of disease evidently improved the prognosis of pre-symptomatic DCM patients by subsequently intensive use of tailored medical treatments[439], compared to unscreened sporadic cases. The long-term limitation of heart transplantation such as allograft vasculopathy and the shortage of young donors justify the continuing search for pharmacologic therapies[441].

5.6.1. Justification of Control Sample Selections

An age- and sex-matched non-CM group was incorporated as an internal control for both pediatric and adult diseased groups, respectively. Potential confounding determinants, from intrinsic heterogeneities (i.e., development) to extrinsic variables such as specimen handling, were minimized.

Due to the nature of heart donation and explanation, it is close-to-impossible to obtain a truly pristine heart from healthy living individuals. We alternatively adopted non-failing hearts from brain-dead donors as our adult controls (A-NC) who had no major cardiovascular histories. On the other hand, our pediatric controls (P-NC) consisted of congenitally malformed native hearts that were removed from pediatric recipients during transplantation. Unlike adults, the children cohort have an extremely limited number of non-failing heart explants dedicated to research rather

than transplantation[178], because young recipients often have an immature immune system that enables broader listing eligibility for receiving an otherwise incompatible (such as blood type) donor allograft. We acknowledge that neither control represents the truly normal myocardium in humans. There could be potential pathological effects of adrenergic storms on the adult donor hearts following brain death or initial injuries, whereas pediatric controls may have an unidentified cardiomyopathic genetic basis or have scarrings from previous corrective surgeries impacting the myocardium[442, 443]. Nevertheless, neither demonstrated characteristics of reverse remodeling seen in DCM, thereby constituting a reasonable control for an investigation into the cardiomyopathic pathogeneses between children and adults.

Specifically, LV of HLHS, rather than its system ventricle (RV), constituted P-NC. In hearts with biventricular physiology, DCM typically affects the systemic LV; however, we excluded the systemic RV of HLHS in our study to avoid introducing chamber-specific and molecular compositional heterogeneity. Our recent work on healthy adult hearts using state-of-the-art scRNA-Seq and snRNA-Seq techniques has uncovered the divergent cellular landscape between different cardiac chambers[183]. We also ensured specimens were probed from a relatively fixed anatomical position (mid-anterior LV free wall) of different hearts. In addition, RV of HLHS demonstrated characteristics of decompensation (**Table 5.1**) and reverse remodeling (**Fig. 5.34A-E**) as commonly seen in failing hearts. The ultimate failure of systemic RV in hearts with single ventricular physiology remains common listing criterion for transplantation[444-446]. In terms of systemic LV from other congenital hearts such as double outlet right ventricle (DORV) and Tetralogy of Fallot (ToF), we were greatly limited by the scarcity and clinical heterogeneities (e.g., age, gender) of the samples. Indeed, we identified remarkably aggravated remodeling progression in the systemic LV of ToF, characterized as significant cardiac fibrosis and cardiomyocyte atrophy (**Fig. 5.34F-J**), while in direct comparison to the underdeveloped LV of HLHS. Worsened ultrastructural derangements of myofibril and mitochondria were also captured by TEM in LV of ToF, likely caused by the compromised pathology of mixed inter-ventricular circulation imputable to ventricular septal lesions (**Fig. 5.34K**)[447-450].

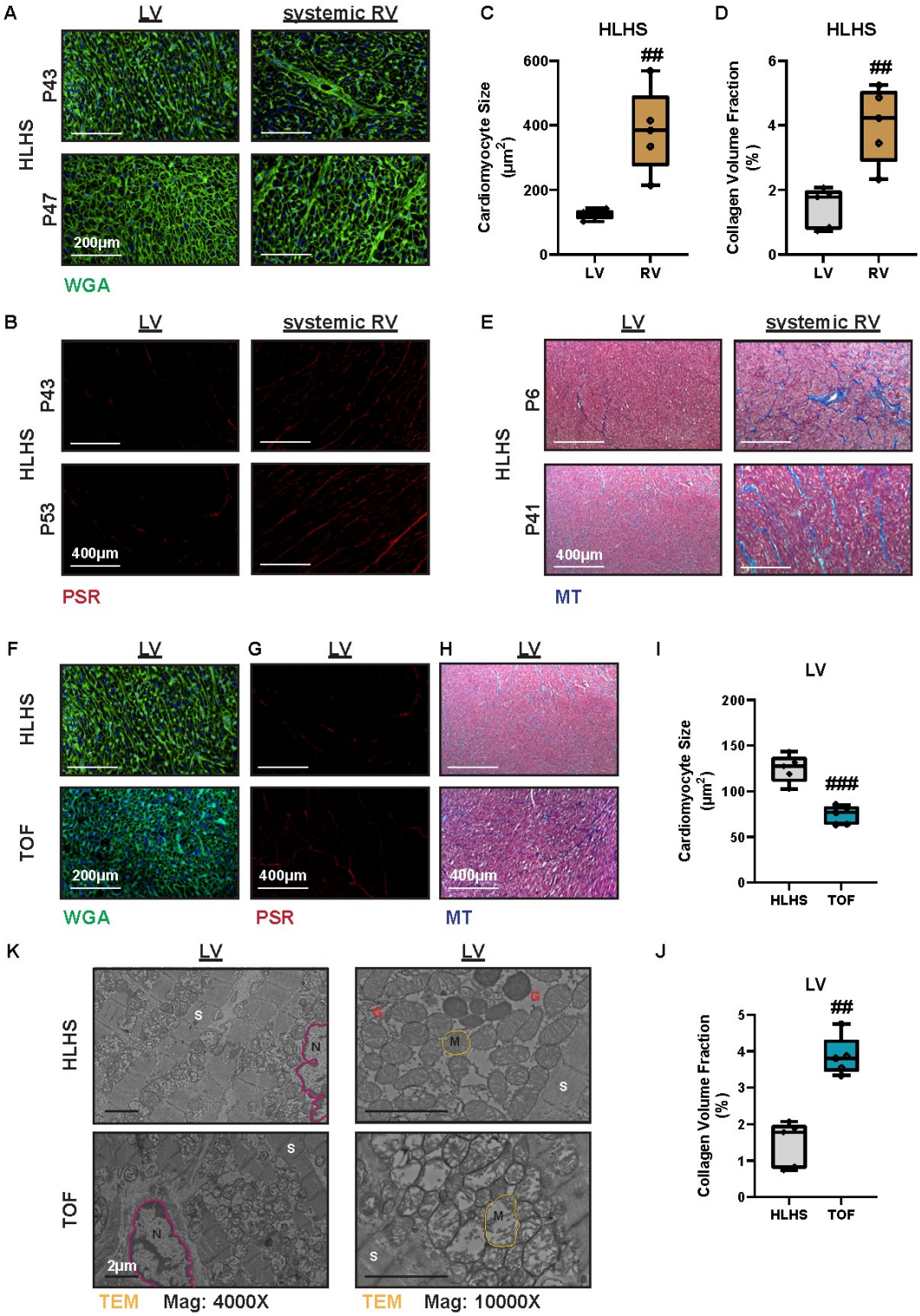

Figure 5.34. Chamber-specific Histological Findings in HLHS, and LV-specific Remodeling Features between HLHS and ToF. A-D. Cross-sectional histological stainings of cardiomyocyte (A, scale bar: 200 μm) and myocardial collagen (B, scale bar: 400 μm) from the middle anterior section of both LV and RV

in HLHS, followed by their corresponding quantifications (C-D), respectively. E. Myocardial collagen content was further confirmed by Mason's trichrome staining (scale bar: 400 μm). F-J. Assessment of cross-sectional cardiomyocyte size (F, scale bar: 200 μm) and tissue collagen volume (G, scale bar: 400 μm) within middle anterior LV free wall between the congenital pathologies of HLHS and ToF, followed by their corresponding quantitative comparisons (I-J). H. Similarly, the myocardial collagen content was further confirmed by Mason's trichrome staining (scale bar: 400 μm). K. Multi-magnitude TEM images capturing overall worsened ultrastructural derangement and mitochondrial lysis in the LV of ToF, while compared with the LV of HLHS (scale bar = 2 μm). G: glucose; M: mitochondrion; N: nucleus; S: sarcomere; purple line outlines nuclear membrane while yellows represent mitochondria. HLHS: hypoplastic left heart syndrome; ToF: Tetralogy of Fallot; LV/RV: left/right ventricle; TEM: transmission electron microscopy. As for histological quantification, n=5 (biological replicates) for WGA and PSR stainings of both chambers (LV vs. RV) in HLHS, with technical replicates of 20-25 images per sample. Similarly, n=5 (biological replicates) for WGA and PSR stainings of the LVs between HLHS and ToF, with technical replicates of 20-25 images per sample. *p<0.05, **p<0.01, ***p<0.001 compared to A-NC; #p<0.05, ##p<0.01, ###p<0.001 compared to P-NC; †p<0.05, ††p<0.01, †††p<0.001 compared to A-DC.

5.6.2. Genetic Background and Pathologic Variants in Analyzed Samples

In our study, the adult patients carried deleterious mutations in *TTN* (2, 15.4%), *MYH7* (1, 7.7%), *LMNA* (2, 15.4%), and *LAMP2* (1, 7.7%), while pediatrics had aberrant expressions of *LMNA* (1, 12.5%), *FLNC* (1, 12.5%), *TPM1* (1, 12.5%). Notably, over half of both cohorts were PV negative (A-DC: 7, 53.8% vs. P-DC: 5, 62.5%) by whole genome sequencing (WGS), which indicates the pathogenic yet unknown roles of transcriptional dysregulation or post-translational alteration in those genotype-negative but phenotype-positive individuals. Indeed, an R14del deletion or R9C mutation in the phospholamban (*PLN*) has previously been described to cause hereditary DCM with variable phenotypes[105, 451-456] that typically manifests after adulthood. Neither diseased group in our study had cardiac *PLN-null* subjects; however, A-DC showed significantly lower phosphorylation levels of PLN than that in both A-NC and P-DC. Our immunoblotting further confirmed greatly disturbed intracellular Ca^{2+} cycling in adult dilated failing hearts, characterized by suppressed expression of SERCA2 and pathologically elevated NCX1 (**Fig. 5.6**) which are absent in the pediatrics. Functional enrichment analyses consistently identified down-represented pathways involved in Ca^{2+}-mediated cardiac contraction in the adult diseased group.

LAMP2 mutation causes profound and accelerated myocardial disease progression that mimics severe HCM with marked LV hypertrophy and early death in young (<25 years) and male patients[457]. Despite the similar phenotypes, it represents a fundamentally distinct pathology results from the genetically dysfunctional lysosome, impaired autophagy, and subsequent glycogen storage disorder. Here, we reported a rare familial case who is a female in her middle age, with cardiac-specific deletion of *LAMP2*, in the absence of other loading conditions such as hypertension. This mutation is X-linked dominant and the nature of inheritance accounts for reported differences in phenotypic severity between genders[154]. Cardiomyopathic symptoms in females tend to be milder and present at a later stage of life than in males. In our study, the patient was morbidly obese and had significant arrhythmogenic problems, whereas her family history of the disease remained unexplored.

Interestingly, we observed a novel *TPM1* mutation in an early-affected infant at the age of 20 months and 9 days. α-tropomyosin is an α-helical, coiled-coil homodimeric thin filament protein participates in Ca^{2+}-regulation of contraction and actomyosin interaction[458]. While *TPM1* mutation is well-known for causing hypertrophic cardiomyopathy (HCM), studies showed contrasting effects of DCM and HCM mutations in *TPM1* and dramatically distinct clinical outcomes of sarcomeric DCM based on the age of presentation[153, 458, 459]. Early presentation in the young often associates with severe or lethal disease progression despite the possibility for substantial recovery, whereas presentation till adulthood is generally benign. Indeed, the infant carrier in our study exhibited severe systolic dysfunction (e.g., LVEF) despite intensive use of inotropes, and we have excluded it as a case of burnt-out HCM by meticulous reviewing of clinical history such as echocardiography. It has important clinical significance because inheritable causes of CMs are frequently overlooked in pediatric-onset HF imputable to the presumptive diagnosis of myocarditis, especially when noticeable improvements are seen[107, 458]. Our study highlights the importance of routine genetic screening in all pediatric DCM cases.

5.6.3. Impaired Contractility in Adult but not Pediatric Failing Hearts

Ca^{2+} plays an integral role in orchestrating cardiac muscle contraction and relaxation via the excitation-contraction (EC) coupling mechanism[171]. Dysregulated calcium signaling has been observed to underlie the adverse remodeling of failing hearts including depressed contractility due

to defective cross-bridge cycling, and fatal arrhythmias[171-173]. Indeed, studies examining the Ca^{2+} cycling profile directly from human explanted hearts have unraveled distinct molecular characteristics between pediatrics HF and their aged counterparts. The differences could include age-related differential β-adrenergic adaptation and downstream signaling pathways, to name a few. After normalized to their age-matched controls, for example, pediatric HF patients had unaltered phosphorylation levels of PLN at both Ser16 and Thr17 sites, but their adult counterparts showed significantly reduced levels of PLN phosphorylation which was consistent with the diminished expression of SERCA2a and elevated NCX1 observed in their failing hearts[460]. The aforementioned alterations were in line with our findings acquired from the adults, and interestingly, such changes are absent in the pediatric failing hearts indicative of distinct pathogeneses driving the early presentation of disease in kids.

5.6.4. Cardiolipin and Mitochondrial Quality Control

Cardiac mitochondria are dynamic organelles that constantly evolve in response to the high energy demands and unique microenvironment. Mitochondrial fitness and dynamism are ensured by the fine interplay between fission and fusion, whereas their imbalance has been shown to correlate with a variety of cardiovascular events[157, 461, 462] exhibiting exacerbated energy metabolism, oxidative stress, calcium mishandling and cell death.

Regulated by dynamin-related protein (Drp)-1, mitochondrial fission factor (Mff) and dynamics proteins (MiD)-49/-51, fission is responsible for mitosis and clearance of injured mitochondria by the mitophagy[157, 463] to preserve a relatively healthier intracellular environment. On the other hand, fusion plays a fundamental role in maintaining the mitochondrial DNA (mtDNA), membrane potential ($\Delta\Psi m$) and Ca^{2+} signaling by forming functionally elongated mitochondria, under the close regulation of mitofusin (Mfn)-1/-2 and optic atrophy (Opa)-1[157, 463]. Importantly, the newborn and adult hearts have varied mitochondrial dynamic profiles, whereby the pediatric cardiomyocytes demonstrate overall higher fission and fusion event rates[157, 464], and distinct cytoplasmic location within myofibers compared to the adults[465]. Mitophagy is a type of autophagy that specifically targets dysfunctional and/or senescent mitochondria for ensuing digestion within autophagosomes[466]. Mechanistically, it is tightly controlled by the mitochondrial PTEN-induced kinase (PINK)-1 and cytosolic ubiquitin ligase Parkin[157] upon loss of the

mitochondrial ΔΨm. Normally, mitophagy plays a cardioprotective role under both baseline and stressed conditions, but it could be detrimental when dysregulated[467, 468]. Interestingly, preclinical studies reported disparate outcomes between the young and aged mouse models following cardiomyocyte-specific ablation of Parkin, which indicates possibly distinct and age-specific autophagic mechanisms including humans[469].

TAFAZZIN encodes a mitochondrial protein named tafazzin that is highly expressed in cardiac and skeletal muscles. Mutation in this gene is best known for causing Barth syndrome; however, it can also result in X-linked infantile DCM[155] with an aggressive nature and fatal outcome. Tafazzin is a phospholipid-lysophospholipid transacylase that catalyzes cardiolipin (CL) remodeling from its immature form to the matured by addition of linoleic acid until it contains a predominance of tetralinoleoyl moieties[470]. Normal functioning of CL requires the characteristic composition of fatty acids by post-synthetic remodeling mediated by taffazzin, and after that, CL can further stabilize the mitochondrial membrane conformation and curvature[471]. Tafazzin activity is important for cardiomyocytes differentiation, during which the typical cristae-rich morphology of cardiac mitochondria evolves[471]. The importance of CL to cristae integrity has been repeatedly demonstrated in various CL-deficient mitochondrial models exhibiting worsened ultrastructure of the inner membrane (IM)[470, 472-478].

CL is a signature polyglycerophospholipid of mitochondria, and remains a key player in the biogenesis, dynamics, supramolecular organization, and structural integrity of the mitochondrial membranes[470-472]. Specifically, it is involved in forming and maintaining the cristae architecture[478], assembly of the ETC complexes[479] and mitochondrial carriers[480], interaction of enzymes to inner mitochondrial membrane[481, 482], and mitochondrial dynamics[483]. CL is reported to significantly improves the efficiency and adaptability of the oxidative phosphorylation (OXPHOS) machinery in several ways. Firstly, it stabilizes the higher order assemblies of respiratory complexes (supercomplexes) and is required for reconstituting the members of major ADP/ATP carriers[472, 484], with the estimate to increase both efficiency of electron flow and ADP/ATP exchange. Secondly, CL functions as a proton trap restricting the flow of protons for OXPHOS, thereby protecting the intramitochondrial compartments from being damaged by extreme pH variations[485]. Perturbed functions of CL could result in a lower electrochemical gradient (ΔΨ) that negatively impacts the biogenesis of proteins being transported to the matrix,

IM via translocases (e.g., TIM22, TIM23)[486] or outer membrane (OM) via TOM and SAM (sorting and assembly machinery)[472, 487]. Mitochondria are dynamic organelles with morphology and quantity constantly changing and under the control of balanced fission and fusion events. CL promotes IM fusion by restricting the short isoforms of the dynamin-regulated GTPases (such as Mgm1p in yeast and OPA1 in mammals) to the CL-enriched membranes with increased activity[483, 488]; on the contrary, its defective binding with the dynamin-related GTPase DRP1 would significantly impede the mitochondrial division with altered shape[489]. The ability to target CL-enriched membranes represents a multitude of pathogeneses that impinge mitochondria, for example, CL provides the anchor and activating platform for caspase 8-mediated apoptosis on the mitochondrial membrane downstream of Fas receptor signaling pathway[472, 490].

5.6.5. Role of Defective ETC in Cardiolipin Peroxidation and Mitochondrial Energetics

Cardiolipin is an essential phospholipid almost exclusively resides in the inner mitochondrial membrane where it is synthesized and intimately involved in multiple important mitochondrial bioenergetic processes[491]. Due to its high content of unsaturated fatty acids, cardiolipin is highly susceptible to reactive oxygen species (ROS) attack consequently leading to cardiolipin peroxidation with alterations in its acyl chain composition and molecular structure. ROS-induced damage to cardiolipin is associated with burnt-out mitochondria in various pathophysiological conditions including aging and HF[491-493]. Peroxidized cardiolipin induced Ca^{2+} accumulation within mitochondria and lowered the threshold of Ca^{2+}-triggered membrane permeability transition pore (mMPT) opening, thereby exacerbating mitochondrial cytochrome c release and subsequent apoptotic or necrotic events associated with cell death[494, 495]. The synergistic effects of cardiolipin peroxidation and Ca^{2+} accumulation on mMPT induction and further mitochondrial dysfunction are characterized as disintegrated ultrastructure, and impaired respiration and oxidative phosphorylation.

Cardiolipin plays an indispensable role in normal electron transferring in complex I[493, 496-499], and that loss of complex I deficiency, presumably caused by ROS-induced oxidation of cardiolipin, was reported to underlie the mitochondrial functional impairment and in turn, to stimulate more ROS generation, which could be entirely restored by addition of tetralinoleoyl cardiolipin[493, 500, 501], or other exogenous agents like melatonin[502, 503], in different models. It holds

great promise in searching potential therapeutic avenues given the fact that cardiolipin acyl chain composition is highly sensitive to dietary supplementation containing linoleic acid and the rich content of melatonin in mitochondria[504].

Chatfield et al.[505] described functional impairments in the mitochondria freshly isolated from explanted human failing hearts including adults and pediatrics with reduced LVEF. The authors further concluded the beneficial effects of elamipretide, a novel mitochondria-targeted compound formerly known as Bendavia[506], MTP-131[507], and SS-31[508], to improve respiratory oxygen flux, and to augment supercomplex-associated enzymes COX I, III, and IV activities of subsarcolemmal mitochondria within failing hearts[505]. COX II is not associated with supercomplex, and its activity was neither perturbed by HF nor was it ameliorated by treatment of elamipretide[505]. CL remodeling was absent despite the therapeutic intervention, as its quantity and quality (i.e., compositions) remained unaltered. Whether CL remodeling is an effector of elamipretide is uncertain, however, due to the acute course (less than a few hours) of intervention and the specific dose of elemipretide applied *ex vivo*. Elamipretide has been proposed to stabilize CL by reducing production of ROS, which inhibits the formation of cytochrome c-cardiolipin peroxidase complex and improves the coupling of the mitochondrial supercomplexes, thereby allowing efficient electron transporting and maximal energy production[421, 505, 509, 510]. Previous studies with elamipretide have also demonstrated its direct effect on improving cardiac energetics in various animal models[511, 512], and it is shown to favorably improve the LV volumes with good tolerability in HF-rEF patients[423, 506], but its long-term safety and efficacy as well as in other HF populations are unexplored[513, 514]. Currently, it is under several major clinical investigations (NCT02788747, NCT02814097, and NCT02914665) in larger HF cohorts[421]. Indeed, this elegant study provided evidence-based benefits of elamipretide on ameliorating mitochondrial energetics within both pediatric and adult failing hearts with several phenotypes, which implies mitochondrial failure may represent a common pathway in end-stage HF and that targeting mitochondrial dysfunction in the children population may offer remarkable efficacy on top of the existing adult-based therapy[421].

5.7. Conclusions & Limitations

Our study aims to evaluate the molecular differences between pediatric and adult advanced HF secondary to primary DCM. The fact P-DC patients responded unfavorably to current HF medications suggested that they are biologically distinct entities from their adult counterparts. Regretfully, the pathogeneses underlying P-DC remained largely uncharted. Given the developmental complexities intrinsic to pediatrics, our opportune application of multi-omics using human heart tissues played an important role in fully recapitulating the unique pathophysiology within P-DC. In our study, we discovered novel and child-specific HF targets, followed by retrospective examinations of previously existing hypotheses derived from adults or preclinical models.

There are a few limitations of our study. Firstly, the study materials were limited by the time of human organ collection and the general heterogeneity of patients, which was intrinsic to working with human specimens[178]. In addition, the experimental findings could possibly be affected by patients' comorbidities, lifestyle, and ongoing medical interventions which complicated the downstream interpretations. However, access to their clinical variables (within three months prior to sample collection) indeed allowed us to assess tissue specimens and perform subgrouping accordingly. Thirdly, we acknowledge that the control hearts were procured from brain-dead donors (for adults) and children with congenitally diseased hearts, HLHS, for pediatrics. Despite the potential pathological effects of adrenergic storm (associated with brain death) on the adult non-failing hearts and the single ventricle physiology of pediatric donor hearts, these hearts did not demonstrate characteristics of reverse remodeling seen in DCM, thereby constituting the reasonable control arms given the extreme difficulty of obtaining truly healthy human hearts as controls[129]. Compared to systemic RV of HLHS, the left chamber, though hypoplastic, evidently demonstrated minimal adverse remodeling (**Fig. 5.34**)[443-446, 450]. Furthermore, working exclusively with clinical allografts might not reflect the full complexity *in vivo*, and would limit the exploration and validation of dynamic biological mechanisms which could be readily tackled by incorporating animal models in the future. Disease duration, for instance, is often inaccessible clinically for patients with chronic HF due to a lack of tracking of the diagnosis date, though emerging evidence has declared its remote association with myocardial remodeling progression in adults[116, 127]. P-DC with less LV dilation at diagnosis independently

predicted functional and structural normalization within 2 years of presentation, however, we did not further separate P-DC based on the age. Therefore, other potential indicators for recovery or remission have not been explored in the current study. In the meantime, we reiterate that both transcriptomic and whole proteomic mappings were implemented at the tissue level, without highlighting the full repertoire of cardiac-resident cell population, cellular heterogeneity, and cell-to-cell interaction by sc/snRNA sequencing[416] in the young and aged DCM hearts, respectively. Molecular validation of cardiac oxidative stress and mitochondrial cardiolipin profile, in complementary to metabolomics[515], is clearly warranted.

Chapter 6

Limitations and Future Directions

6.1. Limitations

As discussed in the **Conclusions and Limitations (Section 4.7 & 5.7)** within each data chapter, the limitations of studies included in this thesis have also been extensively described below.

6.1.1. Use of Clinically Acquired Failing Heart Explants

Although ethically acquired human diseased hearts play an unparallel role in approximating the disease pathogenesis by virtue of their biological affinities to the human cardiovascular illness, there are shortcomings of this approach from different aspects that need to be acknowledged. Firstly, working exclusively with clinically explanted human heart tissues, our studies were conducted in a retrospective manner that could be limited by the time of organ procurement and the general heterogeneities of patients. In addition, the recruited patient cohorts were all at the terminal stage of heart failure (HF) and thus, we only captured a single time point of the entire course of disease secondary to dilated cardiomyopathy (DCM) in either adult or pediatric cohorts. Our studies did not examine other cardiomyopathic etiologies such as hypertrophic and restrictive CMs. The issue of heterogeneity was intrinsic to working with human samples, and consequently, the experimental results could be greatly affected by comorbidities, lifestyles, and pharmaceutical medications. However, access to the associated clinical data allowed us to evaluate specimens and conduct subsequent subgroups and troubleshooting. Another challenge of working with frozen and/or fixed tissues limited the analysis and exploration of dynamic biological mechanisms without the incorporation of primary cardiomyocytes or preclinical animal models.

6.1.2. Use of Non-Failing or Non-Cardiomyopathic Heart Explants as Controls

In general, we acquired the non-failing human hearts (NFC) from brain-dead donors with no prior cardiovascular history or significant comorbidities as a control group in adults. They were declined for transplantation primarily due to blood type (ABO) and/or human leukocyte antigen (HLA) mismatch. Despite their normal antemortem echocardiography, they may not represent truly healthy hearts *in vivo* for reasons including but not limited to their underlying cause of death and the potential pathological effects from the adrenergic storm (associated with brain death) on the heart. Moreover, the heart donors usually spend an average of several days in the hospital before

the declaration of brain death while receiving ongoing supportive therapies, which could have potential effects on the heart as well. Therefore, we must be cautious when interpreting the results and restrain from referring to them as "healthy" or "normal" to avoid ambiguity. On the other hand, we used myocardium tissues from the left ventricle (LV) of pediatric congenital heart diseases (hypoplastic left heart syndrome, HLHS) following successfully staged reconstructions as the non-cardiomyopathic control (NC) group for studying idiopathic DCM in children. As discussed and justified in **Section 5.4.1 & 5.6.1**, those control hearts did not demonstrate cardiomyopathic remodeling features despite their underdeveloped nature of the systemic ventricle, thereby constituting a scientifically reasonable control (since they would not compromise the direct comparison between adult and pediatric DCM), especially given the extreme rarity of non-failing pediatric donor hearts dedicated for research rather than transplantation. Potential interferences from sex or growth hormones were minimized by including only the prepubertal children subjects with matched gender distribution, and we have provided sufficient data in **Section 5.6.1** to justify our use of LV from HLHS as the pediatric controls. Our rational utilization of age- and sex-matched controls assures proper capturing of age-independent disease characteristics at various stages of development. Nevertheless, we must be mindful that the pediatric controls might also have an unidentified cardiomyopathic genetic basis or scarrings from previous corrective surgeries affecting the results obtained from the myocardium. Most importantly, we are currently working to address this issue in future studies by properly and ethically procuring explanted heart tissues from post-mortem pediatric donors several days following their non-cardiac death, based on our research team's preliminary data (not shown) assessing the cardiac RNA degradation over time and outside the rapid autopsy window.

6.1.3. Role of Myocardial Iron Deficiency (MID) in Chronic HF Patients Secondary to Other Cardiomyopathies

In the current study, we explored the pathological role of MID in HF patients with an etiology of non-ischemic DCM or coronary artery disease (CAD). We performed intramyocardial iron measurements from both ventricles in non-ischemic DCM and NFC hearts, and from peri- and non-infarction regions in relation to LAD blockade to fully recapitulate the disease progression. We found that MID is highly prevalent in this cohort with poor association with the systemic iron

or red blood cell status. Approximately every one in four human explanted failing hearts has this hidden disease which is often overlooked in clinical practices. Compared to the iron-sufficient failing hearts, we also found that MID exacerbates the pathological tissue remodeling in iron-deficient HF primarily driven by dysfunctional mitochondria and worsened oxidative stress in the systemic ventricle. With the application of cardiac magnetic resonance (CMR) imaging technique, we demonstrated the feasibility of using CMR as a promising clinical surrogate to detect myocardial iron levels in patients with advanced HF. Our analyses demonstrated that significantly elevated T2 and T2* mapping sequences were featured in iron-deficient failing hearts including both etiologies. While DCM (with and without CAD) represents a significant portion of the chronic HF population with reduced ejection fraction (HF-rEF), we hereby presented the most extensive translation study examining biventricular intramyocardial iron levels directly from human explanted hearts. However, we are not entirely sure if our research findings apply to other cardiomyopathic etiologies in adults such as hypertrophic and restrictive cardiomyopathies during the trajectory of HF, which certainly warrants future investigation.

6.1.4. Lack of Genotype-Stratified Analysis in Pediatric DCM (P-DC) Cohort

Due to a limited sample size, we could not perform genotype-based analysis in our current investigation into idiopathic pediatric DCM patients. P-DC carried deleterious mutations in *LMNA* (1, 12.5%), *FLNC* (1, 12.5%), *TPM1* (1, 12.5%), whereas adult DCM (A-DC) cohort showed aberrant expressions of *TTN* (2, 15.4%), *MYH7* (1, 7.7%), *LMNA* (2, 15.4%), and *LAMP2* (1, 7.7%). More importantly, over half of both cohorts were pathologic variants (PV) negative in both DCM groups (A-DC: 7, 53.8% vs. P-DC: 5, 62.5%) confirmed by whole genome sequencing. Therefore, we were unable to explore whether and how DCM-related genetic mutations affect HF progressions differently or to characterize any common responsive pathways in the young and aged patients. The importance of genetic screening of DCM in younger populations has been highlighted in recent consensus statements in consideration of the familial clustering and hereditary pattern of the disease; therefore, it remains an imperative matter that needs to be addressed in future studies by incorporating more biospecimens with wide mutational coverage. Similarly, we are uncertain whether our research findings could apply to other idiopathic cardiomyopathies in pediatric patients presenting advanced HF at an earlier stage.

6.1.5. Lack of Primary Cell Lines and Preclinical Animal Models for Functional and Patho-Mechanistic Explorations

As presented in **Chapter 5**, our systematic computational analyses were complemented with a plethora of *in vitro* molecular validations retrospectively. Correlative enrichment analyses of differential expression patterns at transcriptional and functional levels captured selective perturbation of key signaling pathways that impact cardiac performance in young failing hearts. Strikingly, the electron transport chain (ETC) pathway, formerly linked to cardiomyopathic pathogeneses[428] but rarely implicated in P-DC before, was a prominently perturbed pathway driving the early presentation of HF. We verified structural and functional alterations of ETC components within the symptomatic myocardium in kids by quantitative precision mass spectrometry (MS) analysis and enzymatic activity assaying. Specifically, our data showed a selective loss of complex I function in P-DC when compared to P-NC and adult cohorts, and we consistently recapitulated unexpected connections between ETC deficiency and oxidative stress-induced cardiolipin peroxidation and remodeling, intracellular Ca^{2+} accumulation, and a series of downstream cell death events such as cytochrome c release, apoptosis and/or necrosis. Loss-of-function of manganese SOD (MnSOD), an intramitochondrial antioxidant, has previously been reported to cause overproduction of 4-hydroxynoneal (4-HNE) on the inner membrane of mitochondria[436, 438], which subsequently targets and alters subunits of respiratory chain complexes and enzymes in Krebs cycle. To the best of our knowledge, this is by far the largest translation study of its kind, and our findings provide fundamental insights into the disparate cardiomyopathic pathogenesis underlying pediatric HF, and shed light on manipulating the MnSOD-mediated 4-HNE signaling axis in future's treatment of pediatric dilated failing hearts. However, those probed biosignatures need further validation in preclinical animal models to determine possible causative effects. For example, overexpression or selective knockout/knockdown of the probed genes using genetic engineering techniques including adenoviral vector, CRISPR-Cas9, and embryonic stem cells would enable manipulation of the isolated primary cells and genetic rodent models, thereby allowing us to examine the genotype-phenotype association and downstream biological implications at different developmental phases.

6.2. Future Directions

The work outlined in this thesis serves as the foundation for future research initiatives. While general research directions relevant to our established HELP platform and tissue biobank were thoroughly discussed in **Sections 3.5−3.7**, specific research initiatives related to my research findings are listed below.

6.2.1. To Further Elucidate the Mechanistic Relation Between Systemic and Cardiac Iron Regulation for Heart-Targeted Iron Delivery

The systemic and myocardial iron homeostasis are under different primary regulations dominated by hepcidin and iron regulatory proteins, respectively, as comprehensively reviewed in **Section 1.1.3−1.1.4**. In addition to the iron regulatory proteins, we indeed investigated into the mRNA expression levels of *hamp* (that encodes hepcidin) using TaqMan real-time polymerase chain reaction (PCR) within the myocardium; however, its expression level is close-to-undetectable with unreliably high cycle thresholds (not shown) when normalized to the technical control (18S). While the heart harbors the second highest expression level of hepcidin[82, 83], its absolute amount in the systemic ventricle is quite low and surprisingly, *hamp* is considerably enriched in more than 50% of all cardiomyocytes within the right atrium rather than other chambers as reported in one of our recent collaborative study published at *Nature*[234] and confirmed by multiplex single-molecule fluorescence in situ hybridization (smFISH). As a master iron regulator at the systemic level, hepcidin promotes proteasomal degradation of ferroportin following internalization into enterocytes and/or other major iron storage cells (e.g., macrophages). Since ferroportin remains the only iron exporter in humans, hepcidin also plays a pathophysiological role in several myocardial conditions related to iron disorders, such as iron-overload cardiomyopathy, ischemia-reperfusion injury, and atherosclerosis[516]. However, this hepatic-produced peptide hormone is a well-established inflammatory marker that can be influenced by multiple systemic factors such as hypoxia, infection, iron level fluctuation and various cardiovascular conditions. As reported in **Chapter 4**, we also included specimens with CAD and investigated the subcellular expressions of ferroportin in peri-infarction and non-infarction regions. Our immunoblotting showed ferroportin consistently increased on sarcolemma with no changes seen in the cytosolic compartments when

compared to iron-sufficient counterparts. But the exact mechanism as to why certain HF patients ended up developing myocardial iron deficiency is still not fully unraveled. Our results showed that restricted iron uptake and increased iron excretion from the cardiomyocytes could underlie the pathogenesis. Therefore, future studies should focus on elucidating the complex interplay between systemic and cardiac iron regulations via hepcidin, which would offer invaluable opportunities to design effective heart-specific iron delivery without the potential risk of developing secondary hemochromatosis as a complication. To fully understand the disease pathogenesis, we could possibly in the future incorporate rodent's ventricular myocytes and induced pluripotent stem cells (iPSC)-derived cardiomyocytes collected from HF patients, and then conduct various experiments to evaluate the pathological remodeling characteristics including expressional gene profiles, molecular assessments (e.g., hydroxyproline assay), mitochondrial functional evaluation (e.g., respiration, myocardial stiffness, contractility) and extracellular matrix (ECM) compositions. Incorporating genetically modified rodents or primary cell lines of cardiomyocytes would be helpful to determine any possible causative effects based on our findings, given that the myocardial iron level and associated tissue phenotypes were only captured at the final stage over the trajectory of the disease. It is also crucial to conduct further investigations of MID in other cardiomyopathies to compare and/or validate our findings.

6.2.2. To Explore the Clinical Application of CMR as Intramyocardial Iron Surrogate in Patients with HF

MID is a relatively new concept in clinical practice, because the diagnosis of iron deficiency (ID) is still relied on circulating hemopoietic biomarkers which represent the systemic iron deficit (SID) status, and screening for SID in HF patients without anemia remains uncommon. However, our current study further confirmed the weak association between cardiac and systemic iron status in HF patients secondary to DCM with or without CAD, indicating that MID can be an independent predictor of inferior clinical prognoses and weakened heart function. Given the invasive nature of the tissue-based measurement of intramyocardial iron levels, there is a lack of reliable clinical surrogates for detecting this hidden yet prevalent disease in HF patients. The use of cardiac magnetic resonance (CMR) imaging to diagnose iron-overload cardiomyopathy is a valid approach in clinics; therefore, CMR was attempted in our study to approximate intramyocardial iron content

in vitro. It was performed on a small piece of explanted heart tissue (length/width/thickness: 10/10/5mm) procured from the mid-septum wall, a more clinically accessible anatomy for biopsy. All specimens, including age- and gender-matched control samples, were processed in the same manner where interferences from susceptibility artifacts were maximally eliminated. In addition, we have highlighted our strategy to minimize the impact of confounders from sample preparation, surrounding environment and technical parameters, and importantly, we applied multi-parametric mapping to evaluate the iron-related signals from the undesirable non-specific noise, since it is the serial magnetic change, using each subject as a reference, that makes the assessment reliable. However, we must acknowledge that our approach to estimating intramyocardial iron content is still quite different from doing that in humans, given the distinct physiology and complex anatomies surrounding the heart. In view of this, it would be important to explore its applicability directly to HF patients of different disease severities at admission and monitor the myocardial iron status following tailored treatments such as intravenous iron supplementation, for the purpose of screening susceptible individuals as well as guiding the iron supplementation therapy to prevent iron-overload cardiomyopathy.

6.2.3. To Validate the Biomarkers Probed by Multi-Omics in Preclinical Animal Models or Primary Cell Lines

Our practical implementation of comparative multi-omics approach illustrated a whole compositional pattern specific to P-DC in an unbiased manner, including thousands of coding RNA, proteins, and phosphoproteins, which altogether indicated that P-DC is a pathologically distinct entity from their adult counterparts. However, those probed biosignatures need to be validated using an array of classic molecular experiments such as immunohistology, immunofluorescent staining, enzymatic assaying, and functional assessment of the explanted heart tissues, and it is critical that we further incorporate preclinical animal models or primary cell lines to confirm any causative rather than associative effects of the findings. Our functional pathway enrichment analyses revealed a strikingly unique metabolic phenotype underlying the pediatric dilated failing hearts, characterized as dysfunctional electron transporting activities primarily driven by Complex I, and significantly upregulated lipid metabolic markers that might be incompatible with the circulating substrates supplied to the hearts given their evolving

developmental physiology. While we verified the expressional and functional alterations of ETC components within the symptomatic myocardium in kids by quantitative precision mass spectrometry analysis and enzymatic activity assaying, our data consistently supported the connections between ETC deficiency and cardiolipin peroxidation and compositional remodeling likely imputable to mitochondria-specific oxidative stress and intracellular Ca^{2+} accumulation. Cardiolipin is a fundamental phospholipid of the inner mitochondrial membrane, and consists of high content of unsaturated (mature form) fatty acids. It is highly susceptible to oxidative stress leading to alterations in its acyl chain composition and molecular structure. To fully recapitulate its compositional remodeling, LC-MS-based lipidomics should be performed to profile its oxidized species in the early symptomatic hearts, in complementation with conventional immunoblotting or immunofluorescent staining of the key regulators such as cardiolipin synthase 1 and taffazin. In addition, colorimetric assaying of the major antioxidants including mitochondria-specific MnSOD and lipid peroxidation aldehyde products such as 4-HNE, malondialdehyde (MDA) and hexanal (HEX) would provide important insights into the disparate pathogenesis of pediatric HF by focusing on the MnSOD-mediated 4-HNE signaling axis. Moreover, our findings indicated disparate metabolic phenotypes between P-DC and A-DC; therefore, it would be important to confirm and characterize the full profile of metabolites within the failing myocardium by cardiac-specific metabolomics.

6.2.4. To Expand Investigations into Other Types of Cardiomyopathies, and in Different HF Patient Populations, using Systems Biology

The systems biology approach, including genome, transcriptome, proteome, and metabolome, has been integrated into my current studies on the explanted human heart tissues. Compared with conventional techniques, it provides non-biased profiling for the identification of novel tissue or disease biomarkers that are implicated in cardiomyopathic diseases. Human Heart Cell Atlas Project, an important international partnership and research initiative, is aiming to build a comprehensive reference map of all cardiac cell types in humans under both healthy and diseased conditions. As a member group of this international collaboration, we were able to learn the state-of-the-art single-cell and single-nucleus RNA sequencing (sc/snRNA-Seq) technique and apply the multi-omics on our invaluable collection of human heart explants as a long-term research

strategy. We have so far constructed the first human heart cell atlas of healthy human hearts, using a combination of multi-modal sc/snRNA-Seq and spatial genomics approaches. In this notable collaborative study accepted by *Nature*[183], we analyzed 487,106 cells and nuclei, and identified 11 major cellular populations and characterized their region-specific heterogeneities within the whole human healthy hearts, which offered fundamental insights into the molecular underpinnings of cardiac physiology. Using a similar approach, we investigated into two major types of cardiomyopathic pathologies (dilated and arrhythmogenic cardiomyopathies) in a total of 61 non-ischemic adult failing hearts, and performed genotype-stratified analyses of the ventricular cell compositions and corresponding transcriptional states. By analyzing 881,081 nuclei from both ventricles of diseased and non-failing controls, we identified 10 major cell types and 71 transcriptional states. This collaborative study has been recently published in *Science*[517], in which we reported a significant loss of cardiomyocytes yet with an increased amount of endothelial and immune cells within both diseased phenotypes. Unexpectedly, the transcriptional state rather than the cellular amount of the fibroblasts was altered in the remarkably fibrotic failing hearts, suggesting activated ECM remodeling and dysregulation, when compared to their controls. Consistently, other cardiomyopathies such as hypertrophic and restrictive CMs should also be investigated in the future for a better and more comprehensive understanding of cardiomyopathic heart diseases. Age and sex are well-known factors that play important roles in the disease pathogeneses of cardiomyopathies; therefore, we should apply the similar multi-modal omics approach to hypertrophic and/or restrictive cardiomyopathic hearts, with the incorporation of age- and sex-matched control hearts. We anticipate identifying the genotype-specific ventricular cell lineages and transcriptional states underlying those cardiomyopathic failing hearts at the tissue level, with validation by smFISH. We are particularly interested in learning how the pathological variants affect the cellular landscape in both ventricles and whether there will be age- or sex-dependent pattern of the shared or distinct cellular composition alterations in those cardiomyopathic diseases.

References

1. Ziaeian B and Fonarow GC. Epidemiology and aetiology of heart failure. *Nature Reviews Cardiology*. 2016;13:368-378.

2. Benjamin EJ, Muntner P, Alonso A, Bittencourt MS, Callaway CW, Carson AP, Chamberlain AM, Chang AR, Cheng S, Das SR, Delling FN, Djousse L, Elkind MSV, Ferguson JF, Fornage M, Jordan LC, Khan SS, Kissela BM, Knutson KL, Kwan TW, Lackland DT, Lewis TT, Lichtman JH, Longenecker CT, Loop MS, Lutsey PL, Martin SS, Matsushita K, Moran AE, Mussolino ME, O'Flaherty M, Pandey A, Perak AM, Rosamond WD, Roth GA, Sampson UKA, Satou GM, Schroeder EB, Shah SH, Spartano NL, Stokes A, Tirschwell DL, Tsao CW, Turakhia MP, VanWagner LB, Wilkins JT, Wong SS and Virani SS. Heart Disease and Stroke Statistics-2019 Update: A Report From the American Heart Association. *Circulation*. 2019;139:e56-e528.

3. Arnold JM, Liu P, Demers C, Dorian P, Giannetti N, Haddad H, Heckman GA, Howlett JG, Ignaszewski A, Johnstone DE, Jong P, McKelvie RS, Moe GW, Parker JD, Rao V, Ross HJ, Sequeira EJ, Svendsen AM, Teo K, Tsuyuki RT and White M. Canadian Cardiovascular Society consensus conference recommendations on heart failure 2006: diagnosis and management. *The Canadian journal of cardiology*. 2006;22:23-45.

4. Ezekowitz JA, O'Meara E, McDonald MA, Abrams H, Chan M, Ducharme A, Giannetti N, Grzeslo A, Hamilton PG, Heckman GA, Howlett JG, Koshman SL, Lepage S, McKelvie RS, Moe GW, Rajda M, Swiggum E, Virani SA, Zieroth S, Al-Hesayen A, Cohen-Solal A, D'Astous M, De S, Estrella-Holder E, Fremes S, Green L, Haddad H, Harkness K, Hernandez AF, Kouz S, LeBlanc MH, Masoudi FA, Ross HJ, Roussin A and Sussex B. 2017 Comprehensive Update of the Canadian Cardiovascular Society Guidelines for the Management of Heart Failure. *The Canadian journal of cardiology*. 2017;33:1342-1433.

5. Yancy C, Jessup M, Bozkurt B, Butler J, Casey Jr D, Drazner M, Fonarow G, Geraci S, Horwich T and Januzzi J. WRITING COMMITTEE MEMBERS; American College of Cardiology Foundation/American Heart Association Task Force on Practice Guidelines. 2013 ACCF/AHA guideline for the management of heart failure: a report of the American College of Cardiology Foundation/American Heart Association Task Force on practice guidelines. *Circulation*. 2013;128:e240-e327.

6. Hunter JJ and Chien KR. Signaling pathways for cardiac hypertrophy and failure. *The New England journal of medicine*. 1999;341:1276-83.

7. Braunwald E and Bristow MR. Congestive heart failure: fifty years of progress. *Circulation*.

2000;102:Iv14-23.

8. Hill JA and Olson EN. Cardiac plasticity. *The New England journal of medicine*. 2008;358:1370-80.

9. Groenewegen A, Rutten FH, Mosterd A and Hoes AW. Epidemiology of heart failure. *European journal of heart failure*. 2020;22:1342-1356.

10. Yancy CW, Jessup M, Bozkurt B, Butler J, Casey DE, Jr., Colvin MM, Drazner MH, Filippatos GS, Fonarow GC, Givertz MM, Hollenberg SM, Lindenfeld J, Masoudi FA, McBride PE, Peterson PN, Stevenson LW and Westlake C. 2017 ACC/AHA/HFSA Focused Update of the 2013 ACCF/AHA Guideline for the Management of Heart Failure: A Report of the American College of Cardiology/American Heart Association Task Force on Clinical Practice Guidelines and the Heart Failure Society of America. *Circulation*. 2017;136:e137-e161.

11. Ponikowski P, Voors AA, Anker SD, Bueno H, Cleland JG, Coats AJ, Falk V, Gonzalez-Juanatey JR, Harjola VP, Jankowska EA, Jessup M, Linde C, Nihoyannopoulos P, Parissis JT, Pieske B, Riley JP, Rosano GM, Ruilope LM, Ruschitzka F, Rutten FH, van der Meer P, Authors/Task Force M and Document R. 2016 ESC Guidelines for the diagnosis and treatment of acute and chronic heart failure: The Task Force for the diagnosis and treatment of acute and chronic heart failure of the European Society of Cardiology (ESC). Developed with the special contribution of the Heart Failure Association (HFA) of the ESC. *Eur J Heart Fail*. 2016;18:891-975.

12. Metra M, Zaca V, Parati G, Agostoni P, Bonadies M, Ciccone M, Dei Cas A, Iacoviello M, Lagioia R and Lombardi C. Cardiovascular and noncardiovascular comorbidities in patients with chronic heart failure. *Journal of Cardiovascular Medicine*. 2011;12:76-84.

13. Theidel U, Vaatainen S, Martikainen J, Soini E, Hardt T and Doehner W. Budget impact of intravenous iron therapy with ferric carboxymaltose in patients with chronic heart failure and iron deficiency in Germany. *ESC Heart Fail*. 2017;4:274-281.

14. Gupta PM, Hamner HC, Suchdev PS, Flores-Ayala R and Mei Z. Iron status of toddlers, nonpregnant females, and pregnant females in the United States. *Am J Clin Nutr*. 2017;106:1640S-1646S.

15. van der Merwe LF and Eussen SR. Iron status of young children in Europe. *Am J Clin Nutr*. 2017;106:1663S-1671S.

16. Andrews NC. Disorders of iron metabolism. *The New England journal of medicine*.

1999;341:1986-95.
17. Oudit GY, Sun H, Trivieri MG, Koch SE, Dawood F, Ackerley C, Yazdanpanah M, Wilson GJ, Schwartz A, Liu PP and Backx PH. L-type Ca2+ channels provide a major pathway for iron entry into cardiomyocytes in iron-overload cardiomyopathy. *Nature medicine*. 2003;9:1187-94.
18. Edwards CQ, Griffen LM, Goldgar D, Drummond C, Skolnick MH and Kushner JP. Prevalence of hemochromatosis among 11,065 presumably healthy blood donors. *The New England journal of medicine*. 1988;318:1355-62.
19. Fibach E and Rachmilewitz EA. Iron overload in hematological disorders. *Presse Med*. 2017;46:e296-e305.
20. Rund D and Rachmilewitz E. Beta-thalassemia. *The New England journal of medicine*. 2005;353:1135-46.
21. Kremastinos DT, Farmakis D, Aessopos A, Hahalis G, Hamodraka E, Tsiapras D and Keren A. Beta-thalassemia cardiomyopathy: history, present considerations, and future perspectives. *Circulation: Heart Failure*. 2010;3:451-8.
22. Piel FB and Weatherall DJ. The alpha-thalassemias. *The New England journal of medicine*. 2014;371:1908-16.
23. Piel FB, Patil AP, Howes RE, Nyangiri OA, Gething PW, Dewi M, Temperley WH, Williams TN, Weatherall DJ and Hay SI. Global epidemiology of sickle haemoglobin in neonates: a contemporary geostatistical model-based map and population estimates. *Lancet*. 2013;381:142-51.
24. Piel FB, Steinberg MH and Rees DC. Sickle Cell Disease. *The New England journal of medicine*. 2017;376:1561-1573.
25. Jankowska EA, Rozentryt P, Witkowska A, Nowak J, Hartmann O, Ponikowska B, Borodulin-Nadzieja L, Banasiak W, Polonski L, Filippatos G, McMurray JJ, Anker SD and Ponikowski P. Iron deficiency: an ominous sign in patients with systolic chronic heart failure. *European heart journal*. 2010;31:1872-80.
26. Das SK, Wang W, Zhabyeyev P, Basu R, McLean B, Fan D, Parajuli N, DesAulniers J, Patel VB, Hajjar RJ, Dyck JR, Kassiri Z and Oudit GY. Iron-overload injury and cardiomyopathy in acquired and genetic models is attenuated by resveratrol therapy. *Scientific reports*. 2015;5:18132.
27. Okonko DO, Mandal AK, Missouris CG and Poole-Wilson PA. Disordered iron homeostasis in chronic heart failure: prevalence, predictors, and relation to anemia, exercise capacity, and survival. *Journal of the American College of Cardiology*. 2011;58:1241-51.

28. Jankowska EA, von Haehling S, Anker SD, Macdougall IC and Ponikowski P. Iron deficiency and heart failure: diagnostic dilemmas and therapeutic perspectives. *European heart journal*. 2013;34:816-29.

29. Vela D. Balance of cardiac and systemic hepcidin and its role in heart physiology and pathology. *Lab Invest*. 2018;98:315-326.

30. Shayeghi M, Latunde-Dada GO, Oakhill JS, Laftah AH, Takeuchi K, Halliday N, Khan Y, Warley A, McCann FE, Hider RC, Frazer DM, Anderson GJ, Vulpe CD, Simpson RJ and McKie AT. Identification of an intestinal heme transporter. *Cell*. 2005;122:789-801.

31. Qiu A, Jansen M, Sakaris A, Min SH, Chattopadhyay S, Tsai E, Sandoval C, Zhao R, Akabas MH and Goldman ID. Identification of an intestinal folate transporter and the molecular basis for hereditary folate malabsorption. *Cell*. 2006;127:917-28.

32. West AR and Oates PS. Mechanisms of heme iron absorption: current questions and controversies. *World J Gastroenterol*. 2008;14:4101-10.

33. Quigley JG, Yang Z, Worthington MT, Phillips JD, Sabo KM, Sabath DE, Berg CL, Sassa S, Wood BL and Abkowitz JL. Identification of a human heme exporter that is essential for erythropoiesis. *Cell*. 2004;118:757-66.

34. Nemeth E, Tuttle MS, Powelson J, Vaughn MB, Donovan A, Ward DM, Ganz T and Kaplan J. Hepcidin regulates cellular iron efflux by binding to ferroportin and inducing its internalization. *Science*. 2004;306:2090-3.

35. Giannetti AM and Bjorkman PJ. HFE and transferrin directly compete for transferrin receptor in solution and at the cell surface. *J Biol Chem*. 2004;279:25866-75.

36. D'Alessio F, Hentze MW and Muckenthaler MU. The hemochromatosis proteins HFE, TfR2, and HJV form a membrane-associated protein complex for hepcidin regulation. *J Hepatol*. 2012;57:1052-60.

37. Lawen A and Lane DJ. Mammalian iron homeostasis in health and disease: uptake, storage, transport, and molecular mechanisms of action. *Antioxid Redox Signal*. 2013;18:2473-507.

38. Zhabyeyev P and Oudit GY. Hemochromatosis Protein (HFE) Knockout Mice As a Novel Model of Hemochromatosis: Implications for Study and Management of Iron-Overload Cardiomyopathy. *The Canadian journal of cardiology*. 2017;33:835-837.

39. Morgan EH. Inhibition of reticulocyte iron uptake by NH4Cl and CH3NH2. *Biochim Biophys Acta*. 1981;642:119-34.

40. Armstrong NJ and Morgan EH. The effect of lysosomotrophic bases and inhibitors of transglutaminase on iron uptake by immature erythroid cells. *Biochim Biophys Acta*. 1983;762:175-86.

41. Ohgami RS, Campagna DR, Greer EL, Antiochos B, McDonald A, Chen J, Sharp JJ, Fujiwara Y, Barker JE and Fleming MD. Identification of a ferrireductase required for efficient transferrin-dependent iron uptake in erythroid cells. *Nat Genet*. 2005;37:1264-9.

42. Garton TP, He Y, Garton HJ, Keep RF, Xi G and Strahle JM. Hemoglobin-induced neuronal degeneration in the hippocampus after neonatal intraventricular hemorrhage. *Brain Res*. 2016;1635:86-94.

43. Chen-Roetling J and Regan RF. Haptoglobin increases the vulnerability of CD163-expressing neurons to hemoglobin. *J Neurochem*. 2016;139:586-595.

44. Kristiansen M, Graversen JH, Jacobsen C, Sonne O, Hoffman HJ, Law SK and Moestrup SK. Identification of the haemoglobin scavenger receptor. *Nature*. 2001;409:198-201.

45. Schaer CA, Vallelian F, Imhof A, Schoedon G and Schaer DJ. CD163-expressing monocytes constitute an endotoxin-sensitive Hb clearance compartment within the vascular system. *J Leukoc Biol*. 2007;82:106-10.

46. Schaer DJ, Vinchi F, Ingoglia G, Tolosano E and Buehler PW. Haptoglobin, hemopexin, and related defense pathways-basic science, clinical perspectives, and drug development. *Front Physiol*. 2014;5:415.

47. Zhabyeyev P and Oudit GY. Unravelling the molecular basis for cardiac iron metabolism and deficiency in heart failure. *European heart journal*. 2017;38:373-375.

48. Cairo G, Bernuzzi F and Recalcati S. A precious metal: Iron, an essential nutrient for all cells. *Genes & nutrition*. 2006;1:25-39.

49. Leidgens S, Bullough KZ, Shi H, Li F, Shakoury-Elizeh M, Yabe T, Subramanian P, Hsu E, Natarajan N, Nandal A, Stemmler TL and Philpott CC. Each member of the poly-r(C)-binding protein 1 (PCBP) family exhibits iron chaperone activity toward ferritin. *J Biol Chem*. 2013;288:17791-802.

50. Hentze MW, Caughman SW, Rouault TA, Barriocanal JG, Dancis A, Harford JB and Klausner RD. Identification of the iron-responsive element for the translational regulation of human ferritin mRNA. *Science*. 1987;238:1570-3.

51. Casey JL, Hentze MW, Koeller DM, Caughman SW, Rouault TA, Klausner RD and Harford

JB. Iron-responsive elements: regulatory RNA sequences that control mRNA levels and translation. *Science*. 1988;240:924-8.

52. Mullner EW and Kuhn LC. A stem-loop in the 3' untranslated region mediates iron-dependent regulation of transferrin receptor mRNA stability in the cytoplasm. *Cell*. 1988;53:815-25.

53. Rouault TA. The role of iron regulatory proteins in mammalian iron homeostasis and disease. *Nat Chem Biol*. 2006;2:406-14.

54. Wilkinson N and Pantopoulos K. The IRP/IRE system in vivo: insights from mouse models. *Front Pharmacol*. 2014;5:176.

55. Guo B, Brown FM, Phillips JD, Yu Y and Leibold EA. Characterization and expression of iron regulatory protein 2 (IRP2). Presence of multiple IRP2 transcripts regulated by intracellular iron levels. *J Biol Chem*. 1995;270:16529-35.

56. Hentze MW, Muckenthaler MU, Galy B and Camaschella C. Two to tango: regulation of Mammalian iron metabolism. *Cell*. 2010;142:24-38.

57. Haddad S, Wang Y, Galy B, Korf-Klingebiel M, Hirsch V, Baru AM, Rostami F, Reboll MR, Heineke J, Flogel U, Groos S, Renner A, Toischer K, Zimmermann F, Engeli S, Jordan J, Bauersachs J, Hentze MW, Wollert KC and Kempf T. Iron-regulatory proteins secure iron availability in cardiomyocytes to prevent heart failure. *European heart journal*. 2017;38:362-372.

58. Wish JB. Assessing iron status: beyond serum ferritin and transferrin saturation. *Clin J Am Soc Nephrol*. 2006;1 Suppl 1:S4-8.

59. Jankowska EA, Kasztura M, Sokolski M, Bronisz M, Nawrocka S, Oleskowska-Florek W, Zymlinski R, Biegus J, Siwolowski P, Banasiak W, Anker SD, Filippatos G, Cleland JG and Ponikowski P. Iron deficiency defined as depleted iron stores accompanied by unmet cellular iron requirements identifies patients at the highest risk of death after an episode of acute heart failure. *European heart journal*. 2014;35:2468-76.

60. Melenovsky V, Petrak J, Mracek T, Benes J, Borlaug BA, Nuskova H, Pluhacek T, Spatenka J, Kovalcikova J, Drahota Z, Kautzner J, Pirk J and Houstek J. Myocardial iron content and mitochondrial function in human heart failure: a direct tissue analysis. *Eur J Heart Fail*. 2017;19:522-530.

61. Jankowska EA, Rozentryt P, Witkowska A, Nowak J, Hartmann O, Ponikowska B, Borodulin-Nadzieja L, von Haehling S, Doehner W, Banasiak W, Polonski L, Filippatos G, Anker SD and Ponikowski P. Iron deficiency predicts impaired exercise capacity in patients with systolic chronic

heart failure. *Journal of cardiac failure*. 2011;17:899-906.

62. Lewis GD, Semigran MJ, Givertz MM, Malhotra R, Anstrom KJ, Hernandez AF, Shah MR and Braunwald E. Oral Iron Therapy for Heart Failure With Reduced Ejection Fraction: Design and Rationale for Oral Iron Repletion Effects on Oxygen Uptake in Heart Failure. *Circulation: Heart Failure*. 2016;9.

63. Lewis GD, Malhotra R, Hernandez AF, McNulty SE, Smith A, Felker GM, Tang WHW, LaRue SJ, Redfield MM, Semigran MJ, Givertz MM, Van Buren P, Whellan D, Anstrom KJ, Shah MR, Desvigne-Nickens P, Butler J, Braunwald E and Network NHFCR. Effect of Oral Iron Repletion on Exercise Capacity in Patients With Heart Failure With Reduced Ejection Fraction and Iron Deficiency: The IRONOUT HF Randomized Clinical Trial. *JAMA*. 2017;317:1958-1966.

64. Organization WH. Haemoglobin concentrations for the diagnosis of anaemia and assessment of severity. 2011. *Download from: http://wwwwhoint/vmnis/indicators/haemoglobinpdf*. 2015.

65. Moreno Chulilla JA, Romero Colas MS and Gutierrez Martin M. Classification of anemia for gastroenterologists. *World J Gastroenterol*. 2009;15:4627-37.

66. Ghali JK, Anand IS, Abraham WT, Fonarow GC, Greenberg B, Krum H, Massie BM, Wasserman SM, Trotman ML, Sun Y, Knusel B and Armstrong P. Randomized double-blind trial of darbepoetin alfa in patients with symptomatic heart failure and anemia. *Circulation*. 2008;117:526-35.

67. van Veldhuisen DJ, Dickstein K, Cohen-Solal A, Lok DJ, Wasserman SM, Baker N, Rosser D, Cleland JG and Ponikowski P. Randomized, double-blind, placebo-controlled study to evaluate the effect of two dosing regimens of darbepoetin alfa in patients with heart failure and anaemia. *European heart journal*. 2007;28:2208-16.

68. Ponikowski P, Anker SD, Szachniewicz J, Okonko D, Ledwidge M, Zymlinski R, Ryan E, Wasserman SM, Baker N, Rosser D, Rosen SD, Poole-Wilson PA, Banasiak W, Coats AJ and McDonald K. Effect of darbepoetin alfa on exercise tolerance in anemic patients with symptomatic chronic heart failure: a randomized, double-blind, placebo-controlled trial. *Journal of the American College of Cardiology*. 2007;49:753-62.

69. Swedberg K, Young JB, Anand IS, Cheng S, Desai AS, Diaz R, Maggioni AP, McMurray JJ, O'Connor C, Pfeffer MA, Solomon SD, Sun Y, Tendera M and van Veldhuisen DJ. Treatment of anemia with darbepoetin alfa in systolic heart failure. *The New England journal of medicine*. 2013;368:1210-9.

70. Anker SD, Comin Colet J, Filippatos G, Willenheimer R, Dickstein K, Drexler H, Luscher TF, Bart B, Banasiak W, Niegowska J, Kirwan BA, Mori C, von Eisenhart Rothe B, Pocock SJ, Poole-Wilson PA, Ponikowski P and Investigators F-HT. Ferric carboxymaltose in patients with heart failure and iron deficiency. *The New England journal of medicine*. 2009;361:2436-48.

71. Ponikowski P, Van Veldhuisen DJ, Comin-Colet J, Ertl G, Komajda M, Mareev V, McDonagh T, Parkhomenko A, Tavazzi L and Levesque V. Beneficial effects of long-term intravenous iron therapy with ferric carboxymaltose in patients with symptomatic heart failure and iron deficiency. *European heart journal*. 2015;36:657-668.

72. Xu W, Barrientos T, Mao L, Rockman HA, Sauve AA and Andrews NC. Lethal Cardiomyopathy in Mice Lacking Transferrin Receptor in the Heart. *Cell Rep*. 2015;13:533-545.

73. Bolger AP, Bartlett FR, Penston HS, O'Leary J, Pollock N, Kaprielian R and Chapman CM. Intravenous iron alone for the treatment of anemia in patients with chronic heart failure. *Journal of the American College of Cardiology*. 2006;48:1225-7.

74. Okonko DO, Grzeslo A, Witkowski T, Mandal AK, Slater RM, Roughton M, Foldes G, Thum T, Majda J, Banasiak W, Missouris CG, Poole-Wilson PA, Anker SD and Ponikowski P. Effect of intravenous iron sucrose on exercise tolerance in anemic and nonanemic patients with symptomatic chronic heart failure and iron deficiency FERRIC-HF: a randomized, controlled, observer-blinded trial. *Journal of the American College of Cardiology*. 2008;51:103-12.

75. Toblli JE, Lombrana A, Duarte P and Di Gennaro F. Intravenous iron reduces NT-pro-brain natriuretic peptide in anemic patients with chronic heart failure and renal insufficiency. *Journal of the American College of Cardiology*. 2007;50:1657-65.

76. Usmanov RI, Zueva EB, Silverberg DS and Shaked M. Intravenous iron without erythropoietin for the treatment of iron deficiency anemia in patients with moderate to severe congestive heart failure and chronic kidney insufficiency. *Journal of nephrology*. 2008;21:236-42.

77. Fishbane S and Kowalski EA. The comparative safety of intravenous iron dextran, iron saccharate, and sodium ferric gluconate. *Seminars in dialysis*. 2000;13:381-4.

78. Moore RA, Gaskell H, Rose P and Allan J. Meta-analysis of efficacy and safety of intravenous ferric carboxymaltose (Ferinject) from clinical trial reports and published trial data. *BMC blood disorders*. 2011;11:4.

79. Drozd M, Jankowska EA, Banasiak W and Ponikowski P. Iron Therapy in Patients with Heart Failure and Iron Deficiency: Review of Iron Preparations for Practitioners. *American journal of*

cardiovascular drugs : drugs, devices, and other interventions. 2017;17:183-201.

80. Maeder MT, Khammy O, dos Remedios C and Kaye DM. Myocardial and systemic iron depletion in heart failure implications for anemia accompanying heart failure. *Journal of the American College of Cardiology*. 2011;58:474-80.

81. McMurray JJ. CONSENSUS to EMPHASIS: the overwhelming evidence which makes blockade of the renin-angiotensin-aldosterone system the cornerstone of therapy for systolic heart failure. *Eur J Heart Fail*. 2011;13:929-36.

82. Krause A, Neitz S, Magert HJ, Schulz A, Forssmann WG, Schulz-Knappe P and Adermann K. LEAP-1, a novel highly disulfide-bonded human peptide, exhibits antimicrobial activity. *FEBS letters*. 2000;480:147-50.

83. Lakhal-Littleton S, Wolna M, Chung YJ, Christian HC, Heather LC, Brescia M, Ball V, Diaz R, Santos A, Biggs D, Clarke K, Davies B and Robbins PA. An essential cell-autonomous role for hepcidin in cardiac iron homeostasis. *Elife*. 2016;5.

84. Island ML, Fatih N, Leroyer P, Brissot P and Loreal O. GATA-4 transcription factor regulates hepatic hepcidin expression. *Biochem J*. 2011;437:477-82.

85. Naito Y, Hosokawa M, Sawada H, Oboshi M, Iwasaku T, Okuhara Y, Morisawa D, Eguchi A, Hirotani S, Ohyanagi M, Tsujino T and Masuyama T. Hepcidin is increased in the hypertrophied heart of Dahl salt-sensitive rats. *Int J Cardiol*. 2014;172:e45-7.

86. Hsieh YP, Huang CH, Lee CY, Lin CY and Chang CC. Silencing of hepcidin enforces the apoptosis in iron-induced human cardiomyocytes. *J Occup Med Toxicol*. 2014;9:11.

87. Kortman GAM, Reijnders D and Swinkels DW. Oral iron supplementation: Potential implications for the gut microbiome and metabolome in patients with CKD. *Hemodialysis international International Symposium on Home Hemodialysis*. 2017;21 Suppl 1:S28-S36.

88. Lee T, Clavel T, Smirnov K, Schmidt A, Lagkouvardos I, Walker A, Lucio M, Michalke B, Schmitt-Kopplin P, Fedorak R and Haller D. Oral versus intravenous iron replacement therapy distinctly alters the gut microbiota and metabolome in patients with IBD. *Gut*. 2017;66:863-871.

89. Tolkien Z, Stecher L, Mander AP, Pereira DI and Powell JJ. Ferrous sulfate supplementation causes significant gastrointestinal side-effects in adults: a systematic review and meta-analysis. *PLoS One*. 2015;10:e0117383.

90. Moretti D, Goede JS, Zeder C, Jiskra M, Chatzinakou V, Tjalsma H, Melse-Boonstra A, Brittenham G, Swinkels DW and Zimmermann MB. Oral iron supplements increase hepcidin and

decrease iron absorption from daily or twice-daily doses in iron-depleted young women. *Blood*. 2015;126:1981-9.

91. Zijp IM, Korver O and Tijburg LB. Effect of tea and other dietary factors on iron absorption. *Critical reviews in food science and nutrition*. 2000;40:371-98.

92. Cook JD, Dassenko SA and Whittaker P. Calcium supplementation: effect on iron absorption. *Am J Clin Nutr*. 1991;53:106-11.

93. Imai R, Higuchi T, Morimoto M, Koyamada R and Okada S. Iron Deficiency Anemia Due to the Long-term Use of a Proton Pump Inhibitor. *Internal medicine (Tokyo, Japan)*. 2018;57:899-901.

94. Sandek A, Bjarnason I, Volk HD, Crane R, Meddings JB, Niebauer J, Kalra PR, Buhner S, Herrmann R, Springer J, Doehner W, von Haehling S, Anker SD and Rauchhaus M. Studies on bacterial endotoxin and intestinal absorption function in patients with chronic heart failure. *Int J Cardiol*. 2012;157:80-5.

95. Jankowska EA, Malyszko J, Ardehali H, Koc-Zorawska E, Banasiak W, von Haehling S, Macdougall IC, Weiss G, McMurray JJ, Anker SD, Gheorghiade M and Ponikowski P. Iron status in patients with chronic heart failure. *European heart journal*. 2013;34:827-34.

96. Ip H, Hyder SM, Haseen F, Rahman M and Zlotkin SH. Improved adherence and anaemia cure rates with flexible administration of micronutrient Sprinkles: a new public health approach to anaemia control. *Eur J Clin Nutr*. 2009;63:165-72.

97. Armstrong GR. The Lucky Iron Fish: a simple solution for iron deficiency. *Blood advances*. 2017;1:330.

98. Macdougall IC. Strategies for iron supplementation: oral versus intravenous. *Kidney international Supplement*. 1999;69:S61-6.

99. Burns DL and Pomposelli JJ. Toxicity of parenteral iron dextran therapy. *Kidney international Supplement*. 1999;69:S119-24.

100. Anker SD, Colet JC, Filippatos G, Willenheimer R, Dickstein K, Drexler H, Luscher TF, Mori C, von Eisenhart Rothe B, Pocock S, Poole-Wilson PA and Ponikowski P. Rationale and design of Ferinject assessment in patients with IRon deficiency and chronic Heart Failure (FAIR-HF) study: a randomized, placebo-controlled study of intravenous iron supplementation in patients with and without anaemia. *Eur J Heart Fail*. 2009;11:1084-91.

101. Jefferies JL and Towbin JA. Dilated cardiomyopathy. *The Lancet*. 2010;375:752-762.

102. Elliott P, Andersson B, Arbustini E, Bilinska Z, Cecchi F, Charron P, Dubourg O, Kühl U, Maisch B and McKenna WJ. Classification of the cardiomyopathies: a position statement from the European Society Of Cardiology Working Group on Myocardial and Pericardial Diseases. *European heart journal*. 2008;29:270-276.
103. Schultheiss H-P, Fairweather D, Caforio AL, Escher F, Hershberger RE, Lipshultz SE, Liu PP, Matsumori A, Mazzanti A and McMurray J. Dilated cardiomyopathy. *Nature reviews Disease primers*. 2019;5:1-19.
104. Weintraub RG, Semsarian C and Macdonald P. Dilated cardiomyopathy. *The Lancet*. 2017;390:400-414.
105. Reichart D, Magnussen C, Zeller T and Blankenberg S. Dilated cardiomyopathy: from epidemiologic to genetic phenotypes: a translational review of current literature. *Journal of internal medicine*. 2019;286:362-372.
106. Lee TM, Hsu DT, Kantor P, Towbin JA, Ware SM, Colan SD, Chung WK, Jefferies JL, Rossano JW and Castleberry CD. Pediatric cardiomyopathies. *Circulation research*. 2017;121:855-873.
107. Towbin JA, Lowe AM, Colan SD, Sleeper LA, Orav EJ, Clunie S, Messere J, Cox GF, Lurie PR and Hsu D. Incidence, causes, and outcomes of dilated cardiomyopathy in children. *Jama*. 2006;296:1867-1876.
108. Zimmerman MS, Smith AGC, Sable CA, Echko MM, Wilner LB, Olsen HE, Atalay HT, Awasthi A, Bhutta ZA, Boucher JL, Castro F, Cortesi PA, Dubey M, Fischer F, Hamidi S, Hay SI, Hoang CL, Hugo-Hamman C, Jenkins KJ, Kar A, Khalil IA, Kumar RK, Kwan GF, Mengistu DT, Mokdad AH, Naghavi M, Negesa L, Negoi I, Negoi RI, Nguyen CT, Nguyen HLT, Nguyen LH, Nguyen SH, Nguyen TH, Nixon MR, Noubiap JJ, Patel S, Peprah EK, Reiner RC, Roth GA, Temsah M-H, Tovani-Palone MR, Towbin JA, Tran BX, Tran TT, Truong NT, Vos T, Vosoughi K, Weintraub RG, Weldegwergs KG, Zaidi Z, Zheleva B, Zuhlke L, Murray CJL, Martin GR and Kassebaum NJ. Global, regional, and national burden of congenital heart disease, 1990-2017: a systematic analysis for the Global Burden of Disease Study 2017. *The Lancet Child & Adolescent Health*. 2020;4:185-200.
109. Lipshultz SE, Sleeper LA, Towbin JA, Lowe AM, Orav EJ, Cox GF, Lurie PR, McCoy KL, McDonald MA, Messere JE and Colan SD. The incidence of pediatric cardiomyopathy in two regions of the United States. *The New England journal of medicine*. 2003;348:1647-55.

110. Andrews RE, Fenton MJ, Ridout DA and Burch M. New-onset heart failure due to heart muscle disease in childhood: a prospective study in the United kingdom and Ireland. *Circulation*. 2008;117:79-84.
111. Nugent AW, Daubeney PE, Chondros P, Carlin JB, Cheung M, Wilkinson LC, Davis AM, Kahler SG, Chow CW, Wilkinson JL and Weintraub RG. The epidemiology of childhood cardiomyopathy in Australia. *The New England journal of medicine*. 2003;348:1639-46.
112. Lipshultz SE. Ventricular dysfunction clinical research in infants, children and adolescents. 2000.
113. Rossano JW, Singh TP, Cherikh WS, Chambers DC, Harhay MO, Hayes D, Hsich E, Khush KK, Meiser B and Potena L. The International Thoracic Organ Transplant Registry of the International Society for Heart and Lung Transplantation: Twenty-second pediatric heart transplantation report–2019; Focus theme: Donor and recipient size match. *The Journal of Heart and Lung Transplantation*. 2019;38:1028-1041.
114. Towbin JA, Lowe AM, Colan SD, Sleeper LA, Orav EJ, Clunie S, Messere J, Cox GF, Lurie PR, Hsu D, Canter C, Wilkinson JD and Lipshultz SE. Incidence, causes, and outcomes of dilated cardiomyopathy in children. *JAMA*. 2006;296:1867-76.
115. Lee TM, Hsu DT, Kantor P, Towbin JA, Ware SM, Colan SD, Chung WK, Jefferies JL, Rossano JW, Castleberry CD, Addonizio LJ, Lal AK, Lamour JM, Miller EM, Thrush PT, Czachor JD, Razoky H, Hill A and Lipshultz SE. Pediatric Cardiomyopathies. *Circulation research*. 2017;121:855-873.
116. Patel MD, Mohan J, Schneider C, Bajpai G, Purevjav E, Canter CE, Towbin J, Bredemeyer A and Lavine KJ. Pediatric and adult dilated cardiomyopathy represent distinct pathological entities. *JCI Insight*. 2017;2.
117. Lopaschuk GD and Jaswal JS. Energy metabolic phenotype of the cardiomyocyte during development, differentiation, and postnatal maturation. *Journal of cardiovascular pharmacology*. 2010;56:130-140.
118. Tatman PD, Woulfe KC, Karimpour-Fard A, Jeffrey DA, Jaggers J, Cleveland JC, Nunley K, Taylor MR, Miyamoto SD and Stauffer BL. Pediatric dilated cardiomyopathy hearts display a unique gene expression profile. *JCI insight*. 2017;2.
119. Stanley WC, Recchia FA and Lopaschuk GD. Myocardial substrate metabolism in the normal and failing heart. *Physiological reviews*. 2005;85:1093-1129.

120. Cubbon RM, Gale CP, Kearney LC, Schechter CB, Brooksby WP, Nolan J, Fox KA, Rajwani A, Baig W and Groves D. Changing characteristics and mode of death associated with chronic heart failure caused by left ventricular systolic dysfunction: a study across therapeutic eras. *Circulation: Heart Failure*. 2011;4:396-403.
121. Kirk R, Dipchand AI, Rosenthal DN, Addonizio L, Burch M, Chrisant M, Dubin A, Everitt M, Gajarski R, Mertens L, Miyamoto S, Morales D, Pahl E, Shaddy R, Towbin J and Weintraub R. The International Society for Heart and Lung Transplantation Guidelines for the management of pediatric heart failure: Executive summary. [Corrected]. *J Heart Lung Transplant*. 2014;33:888-909.
122. Kantor PF, Lougheed J, Dancea A, McGillion M, Barbosa N, Chan C, Dillenburg R, Atallah J, Buchholz H, Chant-Gambacort C, Conway J, Gardin L, George K, Greenway S, Human DG, Jeewa A, Price JF, Ross RD, Roche SL, Ryerson L, Soni R, Wilson J and Wong K. Presentation, diagnosis, and medical management of heart failure in children: Canadian Cardiovascular Society guidelines. *The Canadian journal of cardiology*. 2013;29:1535-52.
123. Shaddy RE, Boucek MM, Hsu DT, Boucek RJ, Canter CE, Mahony L, Ross RD, Pahl E, Blume ED, Dodd DA, Rosenthal DN, Burr J, LaSalle B, Holubkov R, Lukas MA and Tani LY. Carvedilol for children and adolescents with heart failure: a randomized controlled trial. *JAMA*. 2007;298:1171-9.
124. Hsu DT, Zak V, Mahony L, Sleeper LA, Atz AM, Levine JC, Barker PC, Ravishankar C, McCrindle BW, Williams RV, Altmann K, Ghanayem NS, Margossian R, Chung WK, Border WL, Pearson GD, Stylianou MP and Mital S. Enalapril in infants with single ventricle: results of a multicenter randomized trial. *Circulation*. 2010;122:333-40.
125. Wilkinson JD, Landy DC, Colan SD, Towbin JA, Sleeper LA, Orav EJ, Cox GF, Canter CE, Hsu DT and Webber SA. The pediatric cardiomyopathy registry and heart failure: key results from the first 15 years. *Heart failure clinics*. 2010;6:401-413.
126. Miyamoto SD, Stauffer BL, Nakano S, Sobus R, Nunley K, Nelson P and Sucharov CC. Beta-adrenergic adaptation in paediatric idiopathic dilated cardiomyopathy. *European heart journal*. 2014;35:33-41.
127. Woulfe KC, Siomos AK, Nguyen H, SooHoo M, Galambos C, Stauffer BL, Sucharov C and Miyamoto S. Fibrosis and fibrotic gene expression in pediatric and adult patients with idiopathic dilated cardiomyopathy. *Journal of cardiac failure*. 2017;23:314-324.

128.Nakano SJ, Walker JS, Walker LA, Li X, Du Y, Miyamoto SD, Sucharov CC, Garcia AM, Mitchell MB and Ambardekar AV. Increased myocyte calcium sensitivity in end-stage pediatric dilated cardiomyopathy. *American Journal of Physiology-Heart and Circulatory Physiology*. 2019;317:H1221-H1230.
129.Jana S, Zhang H, Lopaschuk GD, Freed DH, Sergi C, Kantor PF, Oudit GY and Kassiri Z. Disparate Remodeling of the Extracellular Matrix and Proteoglycans in Failing Pediatric Versus Adult Hearts. *J Am Heart Assoc*. 2018;7:e010427.
130.Pinto YM, Elliott PM, Arbustini E, Adler Y, Anastasakis A, Böhm M, Duboc D, Gimeno J, De Groote P and Imazio M. Proposal for a revised definition of dilated cardiomyopathy, hypokinetic non-dilated cardiomyopathy, and its implications for clinical practice: a position statement of the ESC working group on myocardial and pericardial diseases. *European heart journal*. 2016;37:1850-1858.
131.Taylor MR, Fain PR, Sinagra G, Robinson ML, Robertson AD, Carniel E, Di Lenarda A, Bohlmeyer TJ, Ferguson DA and Brodsky GL. Natural history of dilated cardiomyopathy due to lamin A/C gene mutations. *Journal of the American College of Cardiology*. 2003;41:771-780.
132.McNally EM, Golbus JR and Puckelwartz MJ. Genetic mutations and mechanisms in dilated cardiomyopathy. *The Journal of clinical investigation*. 2013;123:19-26.
133.Olson TM, Michels VV, Thibodeau SN, Tai Y-S and Keating MT. Actin mutations in dilated cardiomyopathy, a heritable form of heart failure. *Science*. 1998;280:750-752.
134.Kamisago M, Sharma SD, DePalma SR, Solomon S, Sharma P, McDonough B, Smoot L, Mullen MP, Woolf PK and Wigle ED. Mutations in sarcomere protein genes as a cause of dilated cardiomyopathy. *New England Journal of Medicine*. 2000;343:1688-1696.
135.Gerull B, Gramlich M, Atherton J, McNabb M, Trombitás K, Sasse-Klaassen S, Seidman J, Seidman C, Granzier H and Labeit S. Mutations of TTN, encoding the giant muscle filament titin, cause familial dilated cardiomyopathy. *Nature genetics*. 2002;30:201-204.
136.Fatkin D, MacRae C, Sasaki T, Wolff MR, Porcu M, Frenneaux M, Atherton J, Vidaillet Jr HJ, Spudich S and De Girolami U. Missense mutations in the rod domain of the lamin A/C gene as causes of dilated cardiomyopathy and conduction-system disease. *New England Journal of Medicine*. 1999;341:1715-1724.
137.Muchir A, Bonne G, van der Kooi AJ, van Meegen M, Baas F, Bolhuis PA, de Visser M and Schwartz K. Identification of mutations in the gene encoding lamins A/C in autosomal dominant

limb girdle muscular dystrophy with atrioventricular conduction disturbances (LGMD1B). *Human molecular genetics*. 2000;9:1453-1459.

138. Brodsky GL, Muntoni F, Miocic S, Sinagra G, Sewry C and Mestroni L. Lamin A/C gene mutation associated with dilated cardiomyopathy with variable skeletal muscle involvement. *Circulation*. 2000;101:473-476.

139. Sinagra G, Dal Ferro M and Merlo M. Lamin A/C cardiomyopathy: cutting edge to personalized medicine. 2017;10:e002004.

140. LeWinter MM and Granzier HL. Cardiac titin and heart disease. *Journal of cardiovascular pharmacology*. 2014;63:207.

141. Herman DS, Lam L, Taylor MR, Wang L, Teekakirikul P, Christodoulou D, Conner L, DePalma SR, McDonough B and Sparks E. Truncations of titin causing dilated cardiomyopathy. *New England Journal of Medicine*. 2012;366:619-628.

142. Hasselberg NE, Haland TF, Saberniak J, Brekke PH, Berge KE, Leren TP, Edvardsen T and Haugaa KH. Lamin A/C cardiomyopathy: young onset, high penetrance, and frequent need for heart transplantation. *European heart journal*. 2018;39:853-860.

143. Hershberger RE and Morales A. LMNA-related dilated cardiomyopathy. 2016.

144. Priori SG, Blomström-Lundqvist C, Mazzanti A, Blom N, Borggrefe M, Camm J, Elliott PM, Fitzsimons D, Hatala R and Hindricks G. ESC Scientific Document Group. 2015 ESC Guidelines for the management of patients with ventricular arrhythmias and the prevention of sudden cardiac death: The Task Force for the Management of Patients with Ventricular Arrhythmias and the Prevention of Sudden Cardiac Death of the European Society of Cardiology (ESC). Endorsed by: Association for European Paediatric and Congenital Cardiology (AEPC). *European heart journal*. 2015;36:2793-2867.

145. Li D, Morales A, Gonzalez-Quintana J, Norton N, Siegfried JD, Hofmeyer M and Hershberger RE. Identification of novel mutations in RBM20 in patients with dilated cardiomyopathy. *Clinical and translational science*. 2010;3:90-97.

146. Brauch KM, Karst ML, Herron KJ, de Andrade M, Pellikka PA, Rodeheffer RJ, Michels VV and Olson TM. Mutations in ribonucleic acid binding protein gene cause familial dilated cardiomyopathy. *Journal of the American College of Cardiology*. 2009;54:930-941.

147. Hoogenhof MMGvd, Beqqali A, Amin AS, Made Ivd, Aufiero S, Khan MAF, Schumacher CA, Jansweijer JA, Spaendonck-Zwarts KYv, Remme CA, Backs J, Verkerk AO, Baartscheer A,

Pinto YM and Creemers EE. RBM20 Mutations Induce an Arrhythmogenic Dilated Cardiomyopathy Related to Disturbed Calcium Handling. *Circulation*. 2018;138:1330-1342.
148.Muntoni F, Cau M, Ganau A, Congiu R, Arvedi G, Mateddu A, Marrosu MG, Cianchetti C, Realdi G and Cao A. Deletion of the dystrophin muscle-promoter region associated with X-linked dilated cardiomyopathy. *New England Journal of Medicine*. 1993;329:921-925.
149.Towbin JA, Hejtmancik JF, Brink P, Gelb B, Zhu XM, Chamberlain JS, McCabe E and Swift M. X-linked dilated cardiomyopathy. Molecular genetic evidence of linkage to the Duchenne muscular dystrophy (dystrophin) gene at the Xp21 locus. *Circulation*. 1993;87:1854-1865.
150.Tsubata S, Bowles KR, Vatta M, Zintz C, Titus J, Muhonen L, Bowles NE and Towbin JA. Mutations in the human δ-sarcoglycan gene in familial and sporadic dilated cardiomyopathy. *The Journal of clinical investigation*. 2000;106:655-662.
151.Li D, Tapscoft T, Gonzalez O, Burch PE, Quiñones MA, Zoghbi WA, Hill R, Bachinski LL, Mann DL and Roberts R. Desmin mutation responsible for idiopathic dilated cardiomyopathy. *Circulation*. 1999;100:461-464.
152.Begay RL, Tharp CA, Martin A, Graw SL, Sinagra G, Miani D, Sweet ME, Slavov DB, Stafford N and Zeller MJ. FLNC gene splice mutations cause dilated cardiomyopathy. *JACC: Basic to Translational Science*. 2016;1:344-359.
153.Olson TM, Kishimoto NY, Whitby FG and Michels VV. Mutations that alter the surface charge of alpha-tropomyosin are associated with dilated cardiomyopathy. *Journal of molecular and cellular cardiology*. 2001;33:723-732.
154.Gourzi P, Pantou MP, Gkouziouta A, Kaklamanis L, Tsiapras D, Zygouri C, Constantoulakis P, Adamopoulos S and Degiannis D. A new phenotype of severe dilated cardiomyopathy associated with a mutation in the LAMP2 gene previously known to cause hypertrophic cardiomyopathy in the context of Danon disease. *European Journal of Medical Genetics*. 2019;62:77-80.
155.D'Adamo P, Fassone L, Gedeon A, Janssen EA, Bione S, Bolhuis PA, Barth PG, Wilson M, Haan E and Örstavik KH. The X-linked gene G4. 5 is responsible for different infantile dilated cardiomyopathies. *The American Journal of Human Genetics*. 1997;61:862-867.
156.Lopaschuk GD and Jaswal JS. Energy metabolic phenotype of the cardiomyocyte during development, differentiation, and postnatal maturation. *Journal of cardiovascular pharmacology*. 2010;56:130-40.
157.Ramaccini D, Montoya-Uribe V, Aan FJ, Modesti L, Potes Y, Wieckowski MR, Krga I,

Glibetić M, Pinton P, Giorgi C and Matter ML. Mitochondrial Function and Dysfunction in Dilated Cardiomyopathy. *Front Cell Dev Biol*. 2020;8:624216.
158. Gilde AJ, van der Lee KA, Willemsen PH, Chinetti G, van der Leij FR, van der Vusse GJ, Staels B and van Bilsen M. Peroxisome proliferator-activated receptor (PPAR) alpha and PPARbeta/delta, but not PPARgamma, modulate the expression of genes involved in cardiac lipid metabolism. *Circulation research*. 2003;92:518-24.
159. Burkart EM, Sambandam N, Han X, Gross RW, Courtois M, Gierasch CM, Shoghi K, Welch MJ and Kelly DP. Nuclear receptors PPARbeta/delta and PPARalpha direct distinct metabolic regulatory programs in the mouse heart. *J Clin Invest*. 2007;117:3930-9.
160. Lopaschuk GD, Karwi QG, Tian R, Wende AR and Abel ED. Cardiac Energy Metabolism in Heart Failure. *Circulation research*. 2021;128:1487-1513.
161. Stanley WC, Recchia FA and Lopaschuk GD. Myocardial substrate metabolism in the normal and failing heart. *Physiological reviews*. 2005;85:1093-129.
162. Vander Heiden MG, Cantley LC and Thompson CB. Understanding the Warburg effect: the metabolic requirements of cell proliferation. *Science*. 2009;324:1029-33.
163. Yatscoff MA, Jaswal JS, Grant MR, Greenwood R, Lukat T, Beker DL, Rebeyka IM and Lopaschuk GD. Myocardial hypertrophy and the maturation of fatty acid oxidation in the newborn human heart. *Pediatric research*. 2008;64:643-7.
164. Lopaschuk GD and Spafford MA. Energy substrate utilization by isolated working hearts from newborn rabbits. *The American journal of physiology*. 1990;258:H1274-80.
165. Lopaschuk GD, Collins-Nakai RL and Itoi T. Developmental changes in energy substrate use by the heart. *Cardiovascular research*. 1992;26:1172-80.
166. Fisher DJ, Heymann MA and Rudolph AM. Regional myocardial blood flow and oxygen delivery in fetal, newborn, and adult sheep. *The American journal of physiology*. 1982;243:H729-31.
167. Lopaschuk GD, Witters LA, Itoi T, Barr R and Barr A. Acetyl-CoA carboxylase involvement in the rapid maturation of fatty acid oxidation in the newborn rabbit heart. *J Biol Chem*. 1994;269:25871-8.
168. Makinde AO, Gamble J and Lopaschuk GD. Upregulation of 5'-AMP-activated protein kinase is responsible for the increase in myocardial fatty acid oxidation rates following birth in the newborn rabbit. *Circulation research*. 1997;80:482-9.

169.Gamble J and Lopaschuk GD. Insulin inhibition of 5' adenosine monophosphate-activated protein kinase in the heart results in activation of acetyl coenzyme A carboxylase and inhibition of fatty acid oxidation. *Metabolism: clinical and experimental*. 1997;46:1270-4.
170.Lee GY, Kim NH, Zhao ZS, Cha BS and Kim YS. Peroxisomal-proliferator-activated receptor alpha activates transcription of the rat hepatic malonyl-CoA decarboxylase gene: a key regulation of malonyl-CoA level. *Biochem J*. 2004;378:983-90.
171.Lehnart SE, Maier LS and Hasenfuss G. Abnormalities of calcium metabolism and myocardial contractility depression in the failing heart. *Heart failure reviews*. 2009;14:213-24.
172.Priori SG, Napolitano C, Tiso N, Memmi M, Vignati G, Bloise R, Sorrentino V and Danieli GA. Mutations in the cardiac ryanodine receptor gene (hRyR2) underlie catecholaminergic polymorphic ventricular tachycardia. *Circulation*. 2001;103:196-200.
173.Laitinen PJ, Brown KM, Piippo K, Swan H, Devaney JM, Brahmbhatt B, Donarum EA, Marino M, Tiso N, Viitasalo M, Toivonen L, Stephan DA and Kontula K. Mutations of the cardiac ryanodine receptor (RyR2) gene in familial polymorphic ventricular tachycardia. *Circulation*. 2001;103:485-90.
174.Williams GS, Boyman L and Lederer WJ. Mitochondrial calcium and the regulation of metabolism in the heart. *Journal of molecular and cellular cardiology*. 2015;78:35-45.
175.Lopaschuk GD, Ussher JR, Folmes CD, Jaswal JS and Stanley WC. Myocardial fatty acid metabolism in health and disease. *Physiological reviews*. 2010;90:207-58.
176.Schönekess BO, Brindley PG and Lopaschuk GD. Calcium regulation of glycolysis, glucose oxidation, and fatty acid oxidation in the aerobic and ischemic heart. *Canadian journal of physiology and pharmacology*. 1995;73:1632-40.
177.Territo PR, Mootha VK, French SA and Balaban RS. Ca2+ activation of heart mitochondrial oxidative phosphorylation: role of the F0/F1-ATPase. *American Journal of Physiology-Cell Physiology*. 2000;278:C423-C435.
178.Zhang H, Viveiros A, Nikhanj A, Nguyen Q, Wang K, Wang W, Freed DH, Mullen JC, MacArthur R and Kim DH. The Human Explanted Heart Program: A Translational Bridge for Cardiovascular Medicine. *Biochim Biophys Acta Mol Basis Dis*. 2020:165995.
179.Jana S, Zhang H, Lopaschuk GD, Freed DH, Sergi C, Kantor PF, Oudit GY and Kassiri Z. Disparate Remodeling of the Extracellular Matrix and Proteoglycans in Failing Pediatric Versus Adult Hearts. *J Am Heart Assoc*. 2018;7:e010427. :DOI: 10.1161/JAHA.118.010427.

180.Chen X, Zhabyeyev P, Azad AK, Wang W, Minerath RA, DesAulniers J, Grueter CE, Murray AG, Kassiri Z, Vanhaesebroeck B and Oudit GY. Endothelial and cardiomyocyte PI3Kβ divergently regulate cardiac remodelling in response to ischaemic injury. *Cardiovascular research*. 2019;115:1343-1356.
181.Chen X, Zhabyeyev P, Azad AK, Vanhaesebroeck B, Grueter CE, Murray AG, Kassiri Z and Oudit GY. Pharmacological and cell-specific genetic PI3Kα inhibition worsens cardiac remodeling after myocardial infarction. *Journal of molecular and cellular cardiology*. 2021;157:17-30.
182.Zhang H, Viveiros A, Nikhanj A, Nguyen Q, Wang K, Wang W, Freed DH, Mullen JC, MacArthur R, Kim DH, Tymchak W, Sergi CM, Kassiri Z, Wang S and Oudit GY. The Human Explanted Heart Program: A translational bridge for cardiovascular medicine. *Biochimica et Biophysica Acta (BBA) - Molecular Basis of Disease*. 2021;1867:165995-166009.
183.Litvinukova M, Talavera-Lopez C, Maatz H, Reichart D, Worth CL, Lindberg EL, Kanda M, Polanski K, Heinig M, Lee M, Nadelmann ER, Roberts K, Tuck L, Fasouli ES, DeLaughter DM, McDonough B, Wakimoto H, Gorham JM, Samari S, Mahbubani KT, Saeb-Parsy K, Patone G, Boyle JJ, Zhang H, Zhang H, Viveiros A, Oudit GY, Bayraktar OA, Seidman JG, Seidman CE, Noseda M, Hubner N and Teichmann SA. Cells of the adult human heart. *Nature*. 2020;588:466-472.
184.Li H and Durbin R. Fast and accurate short read alignment with Burrows–Wheeler transform. *bioinformatics*. 2009;25:1754-1760.
185.McKenna A, Hanna M, Banks E, Sivachenko A, Cibulskis K, Kernytsky A, Garimella K, Altshuler D, Gabriel S and Daly M. The Genome Analysis Toolkit: a MapReduce framework for analyzing next-generation DNA sequencing data. *Genome research*. 2010;20:1297-1303.
186.Liu X, Jian X and Boerwinkle E. dbNSFP v2. 0: a database of human non-synonymous SNVs and their functional predictions and annotations. *Human mutation*. 2013;34:E2393-E2402.
187.Karczewski KJ, Francioli LC, Tiao G, Cummings BB, Alföldi J, Wang Q, Collins RL, Laricchia KM, Ganna A and Birnbaum DP. The mutational constraint spectrum quantified from variation in 141,456 humans. *Nature*. 2020;581:434-443.
188.Oudit GY, Trivieri MG, Khaper N, Husain T, Wilson GJ, Liu P, Sole MJ and Backx PH. Taurine supplementation reduces oxidative stress and improves cardiovascular function in an iron-overload murine model. *Circulation*. 2004;109:1877-85.
189.Jamieson KL, Keshavarz-Bahaghighat H, Darwesh AM, Sosnowski DK and Seubert JM. Age

and Sex Differences in Hearts of Soluble Epoxide Hydrolase Null Mice. *Front Physiol*. 2020;11:48.
190. Patel VB, Wang Z, Fan D, Zhabyeyev P, Basu R, Das SK, Wang W, Desaulniers J, Holland SM, Kassiri Z and Oudit GY. Loss of p47phox subunit enhances susceptibility to biomechanical stress and heart failure because of dysregulation of cortactin and actin filaments. *Circulation research*. 2013;112:1542-56.
191. Patel VB, Zhabyeyev P, Chen X, Wang F, Paul M, Fan D, McLean BA, Basu R, Zhang P, Shah S, Dawson JF, Pyle WG, Hazra M, Kassiri Z, Hazra S, Vanhaesebroeck B, McCulloch CA and Oudit GY. PI3Kalpha-regulated gelsolin activity is a critical determinant of cardiac cytoskeletal remodeling and heart disease. *Nat Commun*. 2018;9:5390.
192. Viveiros A, Gheblawi M, Aujla PK, Sosnowski DK, Seubert JM, Kassiri Z and Oudit GY. Sex-and age-specific regulation of ACE2: Insights into severe COVID-19 susceptibility. *Journal of molecular and cellular cardiology*. 2022;164:13-16.
193. Mortazavi A, Williams BA, McCue K, Schaeffer L and Wold B. Mapping and quantifying mammalian transcriptomes by RNA-Seq. *Nature methods*. 2008;5:621-628.
194. Reimand J, Isserlin R, Voisin V, Kucera M, Tannus-Lopes C, Rostamianfar A, Wadi L, Meyer M, Wong J and Xu C. Pathway enrichment analysis and visualization of omics data using g: Profiler, GSEA, Cytoscape and EnrichmentMap. *Nature protocols*. 2019;14:482-517.
195. Kuzmanov U, Wang EY, Vanderlaan R, Kim DH, Lee S-H, Hadipour-Lakmehsari S, Guo H, Zhao Y, McFadden M and Sharma P. Mapping signalling perturbations in myocardial fibrosis via the integrative phosphoproteomic profiling of tissue from diverse sources. *Nature biomedical engineering*. 2020;4:889-900.
196. Kuzmanov U, Guo H, Buchsbaum D, Cosme J, Abbasi C, Isserlin R, Sharma P, Gramolini AO and Emili A. Global phosphoproteomic profiling reveals perturbed signaling in a mouse model of dilated cardiomyopathy. *Proceedings of the National Academy of Sciences*. 2016;113:12592-12597.
197. Tyanova S, Temu T, Sinitcyn P, Carlson A, Hein MY, Geiger T, Mann M and Cox J. The Perseus computational platform for comprehensive analysis of (prote) omics data. *Nature methods*. 2016;13:731-740.
198. Subramanian A, Tamayo P, Mootha VK, Mukherjee S, Ebert BL, Gillette MA, Paulovich A, Pomeroy SL, Golub TR and Lander ES. Gene set enrichment analysis: a knowledge-based approach for interpreting genome-wide expression profiles. *Proceedings of the National Academy*

of Sciences. 2005;102:15545-15550.
199.Reimand J, Isserlin R, Voisin V, Kucera M, Tannus-Lopes C, Rostamianfar A, Wadi L, Meyer M, Wong J, Xu C, Merico D and Bader GD. Pathway enrichment analysis and visualization of omics data using g:Profiler, GSEA, Cytoscape and EnrichmentMap. *Nature protocols*. 2019;14:482-517.
200.Raudvere U, Kolberg L, Kuzmin I, Arak T, Adler P, Peterson H and Vilo J. g: Profiler: a web server for functional enrichment analysis and conversions of gene lists (2019 update). *Nucleic acids research*. 2019;47:W191-W198.
201.Merico D, Isserlin R, Stueker O, Emili A and Bader GD. Enrichment map: a network-based method for gene-set enrichment visualization and interpretation. *PLoS One*. 2010;5:e13984.
202.Johnson EK, Matkovich SJ and Nerbonne JM. Regional differences in mRNA and lncRNA expression profiles in non-failing human atria and ventricles. *Scientific reports*. 2018;8:1-13.
203.Kucera M, Isserlin R, Arkhangorodsky A and Bader GD. AutoAnnotate: A Cytoscape app for summarizing networks with semantic annotations. *F1000Research*. 2016;5:1717.
204.Roth GA, Abate D, Abate KH, Abay SM, Abbafati C, Abbasi N, Abbastabar H, Abd-Allah F, Abdela J, Abdelalim A, Abdollahpour I, Abdulkader RS, Abebe HT, Abebe M, Abebe Z, Abejie AN, Abera SF, Abil OZ, Abraha HN, Abrham AR, Abu-Raddad LJ, Accrombessi MMK, Acharya D, Adamu AA, Adebayo OM, Adedoyin RA, Adekanmbi V, Adetokunboh OO, Adhena BM, Adib MG, Admasie A, Afshin A, Agarwal G, Agesa KM, Agrawal A, Agrawal S, Ahmadi A, Ahmadi M, Ahmed MB, Ahmed S, Aichour AN, Aichour I, Aichour MTE, Akbari ME, Akinyemi RO, Akseer N, Al-Aly Z, Al-Eyadhy A, Al-Raddadi RM, Alahdab F, Alam K, Alam T, Alebel A, Alene KA, Alijanzadeh M, Alizadeh-Navaei R, Aljunid SM, Alkerwi Aa, Alla F, Allebeck P, Alonso J, Altirkawi K, Alvis-Guzman N, Amare AT, Aminde LN, Amini E, Ammar W, Amoako YA, Anber NH, Andrei CL, Androudi S, Animut MD, Anjomshoa M, Ansari H, Ansha MG, Antonio CAT, Anwari P, Aremu O, Ärnlöv J, Arora A, Arora M, Artaman A, Aryal KK, Asayesh H, Asfaw ET, Ataro Z, Atique S, Atre SR, Ausloos M, Avokpaho EFGA, Awasthi A, Quintanilla BPA, Ayele Y, Ayer R, Azzopardi PS, Babazadeh A, Bacha U, Badali H, Badawi A, Bali AG, Ballesteros KE, Banach M, Banerjee K, Bannick MS, Banoub JAM, Barboza MA, Barker-Collo SL, Bärnighausen TW, Barquera S, Barrero LH, Bassat Q, Basu S, Baune BT, Baynes HW, Bazargan-Hejazi S, Bedi N, Beghi E, Behzadifar M, Behzadifar M, Béjot Y, Bekele BB, Belachew AB, Belay E, Belay YA, Bell ML, Bello AK, Bennett DA, Bensenor IM, Berman AE, Bernabe E, Bernstein RS, Bertolacci

GJ, Beuran M, Beyranvand T, Bhalla A, Bhattarai S, Bhaumik S, Bhutta ZA, Biadgo B, Biehl MH, Bijani A, Bikbov B, Bilano V, Bililign N, Bin Sayeed MS, Bisanzio D, Biswas T, Blacker BF, Basara BB, Borschmann R, Bosetti C, Bozorgmehr K, Brady OJ, Brant LC, Brayne C, Brazinova A, Breitborde NJK, Brenner H, Briant PS, Britton G, Brugha T, Busse R, Butt ZA, Callender CSKH, Campos-Nonato IR, Campuzano Rincon JC, Cano J, Car M, Cárdenas R, Carreras G, Carrero JJ, Carter A, Carvalho F, Castañeda-Orjuela CA, Castillo Rivas J, Castle CD, Castro C, Castro F, Catalá-López F, Cerin E, Chaiah Y, Chang J-C, Charlson FJ, Chaturvedi P, Chiang PP-C, Chimed-Ochir O, Chisumpa VH, Chitheer A, Chowdhury R, Christensen H, Christopher DJ, Chung S-C, Cicuttini FM, Ciobanu LG, Cirillo M, Cohen AJ, Cooper LT, Cortesi PA, Cortinovis M, Cousin E, Cowie BC, Criqui MH, Cromwell EA, Crowe CS, Crump JA, Cunningham M, Daba AK, Dadi AF, Dandona L, Dandona R, Dang AK, Dargan PI, Daryani A, Das SK, Gupta RD, Neves JD, Dasa TT, Dash AP, Davis AC, Davis Weaver N, Davitoiu DV, Davletov K, De La Hoz FP, De Neve J-W, Degefa MG, Degenhardt L, Degfie TT, Deiparine S, Demoz GT, Demtsu BB, Denova-Gutiérrez E, Deribe K, Dervenis N, Des Jarlais DC, Dessie GA, Dey S, Dharmaratne SD, Dicker D, Dinberu MT, Ding EL, Dirac MA, Djalalinia S, Dokova K, Doku DT, Donnelly CA, Dorsey ER, Doshi PP, Douwes-Schultz D, Doyle KE, Driscoll TR, Dubey M, Dubljanin E, Duken EE, Duncan BB, Duraes AR, Ebrahimi H, Ebrahimpour S, Edessa D, Edvardsson D, Eggen AE, El Bcheraoui C, El Sayed Zaki M, El-Khatib Z, Elkout H, Ellingsen CL, Endres M, Endries AY, Er B, Erskine HE, Eshrati B, Eskandarieh S, Esmaeili R, Esteghamati A, Fakhar M, Fakhim H, Faramarzi M, Fareed M, Farhadi F, Farinha CSEs, Faro A, Farvid MS, Farzadfar F, Farzaei MH, Feigin VL, Feigl AB, Fentahun N, Fereshtehnejad S-M, Fernandes E, Fernandes JC, Ferrari AJ, Feyissa GT, Filip I, Finegold S, Fischer F, Fitzmaurice C, Foigt NA, Foreman KJ, Fornari C, Frank TD, Fukumoto T, Fuller JE, Fullman N, Fürst T, Furtado JM, Futran ND, Gallus S, Garcia-Basteiro AL, Garcia-Gordillo MA, Gardner WM, Gebre AK, Gebrehiwot TT, Gebremedhin AT, Gebremichael B, Gebremichael TG, Gelano TF, Geleijnse JM, Genova-Maleras R, Geramo YCD, Gething PW, Gezae KE, Ghadami MR, Ghadimi R, Ghasemi Falavarjani K, Ghasemi-Kasman M, Ghimire M, Gibney KB, Gill PS, Gill TK, Gillum RF, Ginawi IA, Giroud M, Giussani G, Goenka S, Goldberg EM, Goli S, Gómez-Dantés H, Gona PN, Gopalani SV, Gorman TM, Goto A, Goulart AC, Gnedovskaya EV, Grada A, Grosso G, Gugnani HC, Guimaraes ALS, Guo Y, Gupta PC, Gupta R, Gupta R, Gupta T, Gutiérrez RA, Gyawali B, Haagsma JA, Hafezi-Nejad N, Hagos TB, Hailegiyorgis TT, Hailu GB, Haj-Mirzaian A, Haj-Mirzaian A, Hamadeh RR, Hamidi S, Handal

AJ, Hankey GJ, Harb HL, Harikrishnan S, Haro JM, Hasan M, Hassankhani H, Hassen HY, Havmoeller R, Hay RJ, Hay SI, He Y, Hedayatizadeh-Omran A, Hegazy MI, Heibati B, Heidari M, Hendrie D, Henok A, Henry NJ, Herteliu C, Heydarpour F, Heydarpour P, Heydarpour S, Hibstu DT, Hoek HW, Hole MK, Homaie Rad E, Hoogar P, Hosgood HD, Hosseini SM, Hosseinzadeh M, Hostiuc M, Hostiuc S, Hotez PJ, Hoy DG, Hsiao T, Hu G, Huang JJ, Husseini A, Hussen MM, Hutfless S, Idrisov B, Ilesanmi OS, Iqbal U, Irvani SSN, Irvine CMS, Islam N, Islam SMS, Islami F, Jacobsen KH, Jahangiry L, Jahanmehr N, Jain SK, Jakovljevic M, Jalu MT, James SL, Javanbakht M, Jayatilleke AU, Jeemon P, Jenkins KJ, Jha RP, Jha V, Johnson CO, Johnson SC, Jonas JB, Joshi A, Jozwiak JJ, Jungari SB, Jürisson M, Kabir Z, Kadel R, Kahsay A, Kalani R, Karami M, Karami Matin B, Karch A, Karema C, Karimi-Sari H, Kasaeian A, Kassa DH, Kassa GM, Kassa TD, Kassebaum NJ, Katikireddi SV, Kaul A, Kazemi Z, Karyani AK, Kazi DS, Kefale AT, Keiyoro PN, Kemp GR, Kengne AP, Keren A, Kesavachandran CN, Khader YS, Khafaei B, Khafaie MA, Khajavi A, Khalid N, Khalil IA, Khan EA, Khan MS, Khan MA, Khang Y-H, Khater MM, Khoja AT, Khosravi A, Khosravi MH, Khubchandani J, Kiadaliri AA, Kibret GD, Kidanemariam ZT, Kiirithio DN, Kim D, Kim Y-E, Kim YJ, Kimokoti RW, Kinfu Y, Kisa A, Kissimova-Skarbek K, Kivimäki M, Knudsen AKS, Kocarnik JM, Kochhar S, Kokubo Y, Kolola T, Kopec JA, Koul PA, Koyanagi A, Kravchenko MA, Krishan K, Kuate Defo B, Kucuk Bicer B, Kumar GA, Kumar M, Kumar P, Kutz MJ, Kuzin I, Kyu HH, Lad DP, Lad SD, Lafranconi A, Lal DK, Lalloo R, Lallukka T, Lam JO, Lami FH, Lansingh VC, Lansky S, Larson HJ, Latifi A, Lau KM-M, Lazarus JV, Lebedev G, Lee PH, Leigh J, Leili M, Leshargie CT, Li S, Li Y, Liang J, Lim L-L, Lim SS, Limenih MA, Linn S, Liu S, Liu Y, Lodha R, Lonsdale C, Lopez AD, Lorkowski S, Lotufo PA, Lozano R, Lunevicius R, Ma S, Macarayan ERK, Mackay MT, MacLachlan JH, Maddison ER, Madotto F, Magdy Abd El Razek H, Magdy Abd El Razek M, Maghavani DP, Majdan M, Majdzadeh R, Majeed A, Malekzadeh R, Malta DC, Manda A-L, Mandarano-Filho LG, Manguerra H, Mansournia MA, Mapoma CC, Marami D, Maravilla JC, Marcenes W, Marczak L, Marks A, Marks GB, Martinez G, Martins-Melo FR, Martopullo I, März W, Marzan MB, Masci JR, Massenburg BB, Mathur MR, Mathur P, Matzopoulos R, Maulik PK, Mazidi M, McAlinden C, McGrath JJ, McKee M, McMahon BJ, Mehata S, Mehndiratta MM, Mehrotra R, Mehta KM, Mehta V, Mekonnen TC, Melese A, Melku M, Memiah PTN, Memish ZA, Mendoza W, Mengistu DT, Mengistu G, Mensah GA, Mereta ST, Meretoja A, Meretoja TJ, Mestrovic T, Mezgebe HB, Miazgowski B, Miazgowski T, Millear AI, Miller TR, Miller-Petrie MK, Mini GK, Mirabi P,

Mirarefin M, Mirica A, Mirrakhimov EM, Misganaw AT, Mitiku H, Moazen B, Mohammad KA, Mohammadi M, Mohammadifard N, Mohammed MA, Mohammed S, Mohan V, Mokdad AH, Molokhia M, Monasta L, Moradi G, Moradi-Lakeh M, Moradinazar M, Moraga P, Morawska L, Moreno Velásquez I, Morgado-Da-Costa J, Morrison SD, Moschos MM, Mouodi S, Mousavi SM, Muchie KF, Mueller UO, Mukhopadhyay S, Muller K, Mumford JE, Musa J, Musa KI, Mustafa G, Muthupandian S, Nachega JB, Nagel G, Naheed A, Nahvijou A, Naik G, Nair S, Najafi F, Naldi L, Nam HS, Nangia V, Nansseu JR, Nascimento BR, Natarajan G, Neamati N, Negoi I, Negoi RI, Neupane S, Newton CRJ, Ngalesoni FN, Ngunjiri JW, Nguyen AQ, Nguyen G, Nguyen HT, Nguyen HT, Nguyen LH, Nguyen M, Nguyen TH, Nichols E, Ningrum DNA, Nirayo YL, Nixon MR, Nolutshungu N, Nomura S, Norheim OF, Noroozi M, Norrving B, Noubiap JJ, Nouri HR, Nourollahpour Shiadeh M, Nowroozi MR, Nyasulu PS, Odell CM, Ofori-Asenso R, Ogbo FA, Oh I-H, Oladimeji O, Olagunju AT, Olivares PR, Olsen HE, Olusanya BO, Olusanya JO, Ong KL, Ong SKS, Oren E, Orpana HM, Ortiz A, Ortiz JR, Otstavnov SS, Øverland S, Owolabi MO, Özdemir R, P A M, Pacella R, Pakhale S, Pakhare AP, Pakpour AH, Pana A, Panda-Jonas S, Pandian JD, Parisi A, Park E-K, Parry CDH, Parsian H, Patel S, Pati S, Patton GC, Paturi VR, Paulson KR, Pereira A, Pereira DM, Perico N, Pesudovs K, Petzold M, Phillips MR, Piel FB, Pigott DM, Pillay JD, Pirsaheb M, Pishgar F, Polinder S, Postma MJ, Pourshams A, Poustchi H, Pujar A, Prakash S, Prasad N, Purcell CA, Qorbani M, Quintana H, Quistberg DA, Rade KW, Radfar A, Rafay A, Rafiei A, Rahim F, Rahimi K, Rahimi-Movaghar A, Rahman M, Rahman MHU, Rahman MA, Rai RK, Rajsic S, Ram U, Ranabhat CL, Ranjan P, Rao PC, Rawaf DL, Rawaf S, Razo-García C, Reddy KS, Reiner RC, Reitsma MB, Remuzzi G, Renzaho AMN, Resnikoff S, Rezaei S, Rezaeian S, Rezai MS, Riahi SM, Ribeiro ALP, Rios-Blancas MJ, Roba KT, Roberts NLS, Robinson SR, Roever L, Ronfani L, Roshandel G, Rostami A, Rothenbacher D, Roy A, Rubagotti E, Sachdev PS, Saddik B, Sadeghi E, Safari H, Safdarian M, Safi S, Safiri S, Sagar R, Sahebkar A, Sahraian MA, Salam N, Salama JS, Salamati P, Saldanha RDF, Saleem Z, Salimi Y, Salvi SS, Salz I, Sambala EZ, Samy AM, Sanabria J, Sanchez-Niño MD, Santomauro DF, Santos IS, Santos JV, Milicevic MMS, Sao Jose BP, Sarker AR, Sarmiento-Suárez R, Sarrafzadegan N, Sartorius B, Sarvi S, Sathian B, Satpathy M, Sawant AR, Sawhney M, Saxena S, Sayyah M, Schaeffner E, Schmidt MI, Schneider IJC, Schöttker B, Schutte AE, Schwebel DC, Schwendicke F, Scott JG, Sekerija M, Sepanlou SG, Serván-Mori E, Seyedmousavi S, Shabaninejad H, Shackelford KA, Shafieesabet A, Shahbazi M, Shaheen AA, Shaikh MA, Shams-Beyranvand M,

Shamsi M, Shamsizadeh M, Sharafi K, Sharif M, Sharif-Alhoseini M, Sharma R, She J, Sheikh A, Shi P, Shiferaw MS, Shigematsu M, Shiri R, Shirkoohi R, Shiue I, Shokraneh F, Shrime MG, Si S, Siabani S, Siddiqi TJ, Sigfusdottir ID, Sigurvinsdottir R, Silberberg DH, Silva DAS, Silva JP, Silva NTD, Silveira DGA, Singh JA, Singh NP, Singh PK, Singh V, Sinha DN, Sliwa K, Smith M, Sobaih BH, Sobhani S, Sobngwi E, Soneji SS, Soofi M, Sorensen RJD, Soriano JB, Soyiri IN, Sposato LA, Sreeramareddy CT, Srinivasan V, Stanaway JD, Starodubov VI, Stathopoulou V, Stein DJ, Steiner C, Stewart LG, Stokes MA, Subart ML, Sudaryanto A, Sufiyan MaB, Sur PJ, Sutradhar I, Sykes BL, Sylaja PN, Sylte DO, Szoeke CEI, Tabarés-Seisdedos R, Tabuchi T, Tadakamadla SK, Takahashi K, Tandon N, Tassew SG, Taveira N, Tehrani-Banihashemi A, Tekalign TG, Tekle MG, Temsah M-H, Temsah O, Terkawi AS, Teshale MY, Tessema B, Tessema GA, Thankappan KR, Thirunavukkarasu S, Thomas N, Thrift AG, Thurston GD, Tilahun B, To QG, Tobe-Gai R, Tonelli M, Topor-Madry R, Torre AE, Tortajada-Girbés M, Touvier M, Tovani-Palone MR, Tran BX, Tran KB, Tripathi S, Troeger CE, Truelsen TC, Truong NT, Tsadik AG, Tsoi D, Tudor Car L, Tuzcu EM, Tyrovolas S, Ukwaja KN, Ullah I, Undurraga EA, Updike RL, Usman MS, Uthman OA, Uzun SB, Vaduganathan M, Vaezi A, Vaidya G, Valdez PR, Varavikova E, Vasankari TJ, Venketasubramanian N, Villafaina S, Violante FS, Vladimirov SK, Vlassov V, Vollset SE, Vos T, Wagner GR, Wagnew FS, Waheed Y, Wallin MT, Walson JL, Wang Y, Wang Y-P, Wassie MM, Weiderpass E, Weintraub RG, Weldegebreal F, Weldegwergs KG, Werdecker A, Werkneh AA, West TE, Westerman R, Whiteford HA, Widecka J, Wilner LB, Wilson S, Winkler AS, Wiysonge CS, Wolfe CDA, Wu S, Wu Y-C, Wyper GMA, Xavier D, Xu G, Yadgir S, Yadollahpour A, Yahyazadeh Jabbari SH, Yakob B, Yan LL, Yano Y, Yaseri M, Yasin YJ, Yentür GK, Yeshaneh A, Yimer EM, Yip P, Yirsaw BD, Yisma E, Yonemoto N, Yonga G, Yoon S-J, Yotebieng M, Younis MZ, Yousefifard M, Yu C, Zadnik V, Zaidi Z, Zaman SB, Zamani M, Zare Z, Zeleke AJ, Zenebe ZM, Zhang AL, Zhang K, Zhou M, Zodpey S, Zuhlke LJ, Naghavi M and Murray CJL. Global, regional, and national age-sex-specific mortality for 282 causes of death in 195 countries and territories, 1980-2017: a systematic analysis for the Global Burden of Disease Study 2017. *Lancet*. 2018;392:1736-1788.

205.Ziaeian B and Fonarow GC. Epidemiology and aetiology of heart failure. *Nature reviews Cardiology*. 2016;13:368-78.

206.Coronel R, Wilders R, Verkerk AO, Wiegerinck RF, Benoist D and Bernus O. Electrophysiological changes in heart failure and their implications for arrhythmogenesis. *Biochim Biophys Acta*. 2013;1832:2432-2441.

207. Oudit GY, Kassiri Z, Sah R, Ramirez RJ, Zobel C and Backx PH. The molecular physiology of the cardiac transient outward potassium current (Ito) in normal and diseased myocardium. *Journal of molecular and cellular cardiology*. 2001;33:851-872.
208. Zhang H, Zhabyeyev P, Wang S and Oudit GY. Role of iron metabolism in heart failure: From iron deficiency to iron overload. *Biochim Biophys Acta*. 2019;1865:1925-1937.
209. Oudit GY, Sun H, Trivieri MG, Koch SE, Dawood F, Ackerley C, Yazdanpanah M, Wilson GJ, Schwartz A and Liu PP. L-type Ca 2+ channels provide a major pathway for iron entry into cardiomyocytes in iron-overload cardiomyopathy. *Nature medicine*. 2003;9:1187-1194.
210. Lopaschuk GD, Ussher JR, Folmes CDL, Jaswal JS and Stanley WC. Myocardial fatty acid metabolism in health and disease. *Physiological reviews*. 2010;90:207-258.
211. Rossignol P, Hernandez AF, Solomon SD and Zannad F. Heart failure drug treatment. *Lancet*. 2019;393:1034-1044.
212. Kaye DM and Krum H. Drug discovery for heart failure: a new era or the end of the pipeline? *Nature reviews Drug discovery*. 2007;6:127-39.
213. Slaughter MS, Rogers JG, Milano CA, Russell SD, Conte JV, Feldman D, Sun B, Tatooles AJ, Delgado RM, 3rd, Long JW, Wozniak TC, Ghumman W, Farrar DJ and Frazier OH. Advanced heart failure treated with continuous-flow left ventricular assist device. *The New England journal of medicine*. 2009;361:2241-51.
214. Drazner MH. A New Left Ventricular Assist Device — Better, but Still Not Ideal. *The New England journal of medicine*. 2018;378:1442-1443.
215. Abouna GM. Organ shortage crisis: problems and possible solutions. *Transplantation proceedings*. 2008;40:34-8.
216. Zaroff JG, Rosengard BR, Armstrong WF, Babcock WD, D'Alessandro A, Dec GW, Edwards NM, Higgins RS, Jeevanandum V, Kauffman M, Kirklin JK, Large SR, Marelli D, Peterson TS, Ring WS, Robbins RC, Russell SD, Taylor DO, Van Bakel A, Wallwork J and Young JB. Maximizing use of organs recovered from the cadaver donor: cardiac recommendations. *J Heart Lung Transplant*. 2002;21:1153-1160.
217. Isaac D, Chan M, Haddad H, Cheung A, West L, Rao V and Dipchand AI. Cardiac transplantation: Eligibility and listing criteria in Canada 2012. 2011.
218. Rajab TK and Singh SK. Donation after cardiac death heart transplantation in America is clinically necessary and ethically justified. *Circulation: Heart Failure*. 2018;11:e004884.

219.Kirk R, Dipchand AI, Davies RR, Miera O, Chapman G, Conway J, Denfield S, Gossett JG, Johnson J, McCulloch M, Schweiger M, Zimpfer D, Ablonczy L, Adachi I, Albert D, Alexander P, Amdani S, Amodeo A, Azeka E, Ballweg J, Beasley G, Böhmer J, Butler A, Camino M, Castro J, Chen S, Chrisant M, Christen U, Danziger-Isakov L, Das B, Everitt M, Feingold B, Fenton M, Garcia-Guereta L, Godown J, Gupta D, Irving C, Joong A, Kemna M, Khulbey SK, Kindel S, Knecht K, Lal AK, Lin K, Lord K, Möller T, Nandi D, Niesse O, Peng DM, Pérez-Blanco A, Punnoose A, Reinhardt Z, Rosenthal D, Scales A, Scheel J, Shih R, Smith J, Smits J, Thul J, Weintraub R, Zangwill S and Zuckerman WA. ISHLT consensus statement on donor organ acceptability and management in pediatric heart transplantation. *J Heart Lung Transplant*. 2020;39:331-341.

220.Nguyen Q, Lim KRQ and Yokota T. Genome Editing for the Understanding and Treatment of Inherited Cardiomyopathies. *International journal of molecular sciences*. 2020;21:733.

221.Strong A and Musunuru K. Genome editing in cardiovascular diseases. *Nature reviews Cardiology*. 2017;14:11-20.

222.Perel P, Roberts I, Sena E, Wheble P, Briscoe C, Sandercock P, Macleod M, Mignini LE, Jayaram P and Khan KS. Comparison of treatment effects between animal experiments and clinical trials: systematic review. *BMJ (Clinical research ed)*. 2007;334:197.

223.van der Worp HB, Howells DW, Sena ES, Porritt MJ, Rewell S, O'Collins V and Macleod MR. Can animal models of disease reliably inform human studies? *PLoS medicine*. 2010;7:e1000245.

224.Hewitt R and Watson P. Defining biobank. *Biopreservation and biobanking*. 2013;11:309-15.

225.Bartels P and Kotze A. Wildlife biomaterial banking in Africa for now and the future. *Journal of environmental monitoring : JEM*. 2006;8:779-81.

226.Paskal W, Paskal AM, Debski T, Gryziak M and Jaworowski J. Aspects of Modern Biobank Activity - Comprehensive Review. *Pathology oncology research : POR*. 2018;24:771-785.

227.Patel VB, Mori J, McLean BA, Basu R, Das SK, Ramprasath T, Parajuli N, Penninger JM, Grant MB and Lopaschuk GD. ACE2 deficiency worsens epicardial adipose tissue inflammation and cardiac dysfunction in response to diet-induced obesity. *Diabetes*. 2016;65:85-95.

228.Spitler KM, Ponce JM, Oudit GY, Hall DD and Grueter CE. Cardiac Med1 deletion promotes early lethality, cardiac remodeling, and transcriptional reprogramming. *Am J Physiol Heart Circ Physiol*. 2017;312:H768-H780.

229.Hall DD, Ponce JM, Chen B, Spitler KM, Alexia A, Oudit GY, Song L-S and Grueter CE.

Ectopic expression of Cdk8 induces eccentric hypertrophy and heart failure. *JCI insight*. 2017;2:e92476.

230.Chen X, Zhabyeyev P, Azad AK, Wang W, Minerath RA, DesAulniers J, Grueter CE, Murray AG, Kassiri Z and Vanhaesebroeck B. Endothelial and cardiomyocyte PI3Kβ divergently regulate cardiac remodelling in response to ischaemic injury. *Cardiovascular research*. 2019;115:1343-1356.

231.Ponce Jessica M, Coen G, Spitler Kathryn M, Dragisic N, Martins I, Hinton A, Mungai M, Tadinada Satya M, Zhang H, Oudit Gavin Y, Song LS, Li N, Sicinski P, Strack S, Abel ED, Mitchell C, Hall Duane D and Grueter Chad E. Stress-Induced Cyclin C Translocation Regulates Cardiac Mitochondrial Dynamics. *J Am Heart Assoc*. 2020;9:e014366.

232.Masoud AG, Lin J, Azad AK, Farhan MA, Fischer C, Zhu LF, Zhang H, Sis B, Kassiri Z and Moore RB. Apelin directs endothelial cell differentiation and vascular repair following immune-mediated injury. *J Clin Invest*. 2019;130:94-107.

233.Sakamuri SS, Takawale A, Basu R, Fedak PW, Freed D, Sergi C, Oudit GY and Kassiri Z. Differential impact of mechanical unloading on structural and nonstructural components of the extracellular matrix in advanced human heart failure. *Transl Res*. 2016;172:30-44.

234.Litviňuková M, Talavera-López C, Maatz H, Reichart D, Worth CL, Lindberg EL, Kanda M, Polanski K, Heinig M, Lee M, Nadelmann ER, Roberts K, Tuck L, Fasouli ES, DeLaughter DM, McDonough B, Wakimoto H, Gorham JM, Samari S, Mahbubani KT, Saeb-Parsy K, Patone G, Boyle JJ, Zhang H, Zhang H, Viveiros A, Oudit GY, Bayraktar O, Seidman JG, Seidman CE, Noseda M, Hubner N and Teichmann SA. Cells of the adult human heart. *Nature*. 2020.

235.Haddad H, Isaac D, Legare JF, Pflugfelder P, Hendry P, Chan M, Cantin B, Giannetti N, Zieroth S, White M, Warnica W, Doucette K, Rao V, Dipchand A, Cantarovich M, Kostuk W, Cecere R, Charbonneau E, Ross H and Poirier N. Canadian Cardiovascular Society Consensus Conference update on cardiac transplantation 2008: Executive Summary. *The Canadian journal of cardiology*. 2009;25:197-205.

236.Canadian Organ Replacement Register. Organ replacement in Canada: CORR annual statistics. 2019.

237.Canadian Organ Replacement Register. e-Statistics On Organ Transplants, Waiting Lists And Donors. 2019.

238.Canadian Society of Transplantation. Transplant Programs & OPOS. 2020.

239.Conway J and Dipchand AI. Heart Transplantation in Children. *Pediatr Clin North Am*. 2010;57:353-373.
240.Mehra MR, Canter CE, Hannan MM, Semigran MJ, Uber PA, Baran DA, Danziger-Isakov L, Kirklin JK, Kirk R, Kushwaha SS, Lund LH, Potena L, Ross HJ, Taylor DO, Verschuuren EAM and Zuckermann A. The 2016 International Society for Heart Lung Transplantation listing criteria for heart transplantation: A 10-year update. *J Heart Lung Transplant*. 2016;35:1-23.
241.Hu XJ, Dong NG, Liu JP, Li F, Sun YF and Wang Y. Status on Heart Transplantation in China. *Chinese medical journal*. 2015;128:3238-42.
242.Abouna GM. The use of marginal-suboptimal donor organs: a practical solution for organ shortage. *Annals of transplantation*. 2004;9:62-6.
243.Zaroff JG, Rosengard BR, Armstrong WF, Babcock WD, D'Alessandro A, Dec GW, Edwards NM, Higgins RS, Jeevanandum V, Kauffman M, Kirklin JK, Large SR, Marelli D, Peterson TS, Ring WS, Robbins RC, Russell SD, Taylor DO, Van Bakel A, Wallwork J and Young JB. Consensus conference report: maximizing use of organs recovered from the cadaver donor: cardiac recommendations, March 28-29, 2001, Crystal City, Va. *Circulation*. 2002;106:836-41.
244.Costanzo MR, Dipchand A, Starling R, Anderson A, Chan M, Desai S, Fedson S, Fisher P, Gonzales-Stawinski G, Martinelli L and Crespo-Leiro M. The International Society of Heart and Lung Transplantation Guidelines for the care of heart transplant recipients. *J Heart Lung Transplant*. 2010;29:914-56.
245.Kilic A, Emani S, Sai-Sudhakar CB, Higgins RS and Whitson BA. Donor selection in heart transplantation. *Journal of thoracic disease*. 2014;6:1097-104.
246.Wittwer T and Wahlers T. Marginal donor grafts in heart transplantation: lessons learned from 25 years of experience. *Transplant international : official journal of the European Society for Organ Transplantation*. 2008;21:113-25.
247.Rose EA, Gelijns AC, Moskowitz AJ, Heitjan DF, Stevenson LW, Dembitsky W, Long JW, Ascheim DD, Tierney AR, Levitan RG, Watson JT, Meier P, Ronan NS, Shapiro PA, Lazar RM, Miller LW, Gupta L, Frazier OH, Desvigne-Nickens P, Oz MC and Poirier VL. Long-term use of a left ventricular assist device for end-stage heart failure. *The New England journal of medicine*. 2001;345:1435-43.
248.VanderPluym CJ, Rebeyka IM, Ross DB and Buchholz H. The use of ventricular assist devices in pediatric patients with univentricular hearts. *The Journal of thoracic and cardiovascular surgery*.

2011;141:588-90.
249.Feldman D, Pamboukian SV, Teuteberg JJ, Birks E, Lietz K, Moore SA, Morgan JA, Arabia F, Bauman ME and Buchholz HW. The 2013 International Society for Heart and Lung Transplantation Guidelines for mechanical circulatory support: executive summary. *J Heart Lung Transplant*. 2013;32:157-187.
250.Zhong J, Basu R, Guo D, Chow FL, Byrns S, Schuster M, Loibner H, Wang XH, Penninger JM, Kassiri Z and Oudit GY. Angiotensin-converting enzyme 2 suppresses pathological hypertrophy, myocardial fibrosis, and cardiac dysfunction. *Circulation*. 2010;122:717-28, 18 p following 728.
251.Shen M, Morton J, Davidge ST and Kassiri Z. Loss of smooth muscle cell disintegrin and metalloproteinase 17 transiently suppresses angiotensin II-induced hypertension and end-organ damage. *Journal of molecular and cellular cardiology*. 2017;103:11-21.
252.Shen M, Hu M, Fedak PWM, Oudit GY and Kassiri Z. Cell-Specific Functions of ADAM17 Regulate the Progression of Thoracic Aortic Aneurysm. *Circulation research*. 2018;123:372-388.
253.Wang W, Shen M, Fischer C, Basu R, Hazra S, Couvineau P, Paul M, Wang F, Toth S, Mix DS, Poglitsch M, Gerard NP, Bouvier M, Vederas JC, Penninger JM, Kassiri Z and Oudit GY. Apelin protects against abdominal aortic aneurysm and the therapeutic role of neutral endopeptidase resistant apelin analogs. *Proceedings of the National Academy of Sciences of the United States of America*. 2019;116:13006-13015.
254.Dipla K, Mattiello JA, Jeevanandam V, Houser SR and Margulies KB. Myocyte recovery after mechanical circulatory support in humans with end-stage heart failure. *Circulation*. 1998;97:2316-22.
255.Williams ML, Hata JA, Schroder J, Rampersaud E, Petrofski J, Jakoi A, Milano CA and Koch WJ. Targeted beta-adrenergic receptor kinase (betaARK1) inhibition by gene transfer in failing human hearts. *Circulation*. 2004;109:1590-3.
256.Perrino C, Schroder JN, Lima B, Villamizar N, Nienaber JJ, Milano CA and Naga Prasad SV. Dynamic regulation of phosphoinositide 3-kinase-gamma activity and beta-adrenergic receptor trafficking in end-stage human heart failure. *Circulation*. 2007;116:2571-9.
257.Nuss HB and Houser SR. Voltage dependence of contraction and calcium current in severely hypertrophied feline ventricular myocytes. *Journal of molecular and cellular cardiology*. 1991;23:717-26.

258.Bird SD, Doevendans PA, van Rooijen MA, Brutel de la Riviere A, Hassink RJ, Passier R and Mummery CL. The human adult cardiomyocyte phenotype. *Cardiovascular research*. 2003;58:423-34.
259.del Monte F, Harding SE, Schmidt U, Matsui T, Kang ZB, Dec GW, Gwathmey JK, Rosenzweig A and Hajjar RJ. Restoration of contractile function in isolated cardiomyocytes from failing human hearts by gene transfer of SERCA2a. *Circulation*. 1999;100:2308-11.
260.O'Connell TD, Rodrigo MC and Simpson PC. Isolation and culture of adult mouse cardiac myocytes. *Methods in molecular biology (Clifton, NJ)*. 2007;357:271-96.
261.Guo GR, Chen L, Rao M, Chen K, Song JP and Hu SS. A modified method for isolation of human cardiomyocytes to model cardiac diseases. *Journal of translational medicine*. 2018;16:288.
262.Neuss M, Regitz-Zagrosek V, Hildebrandt A and Fleck E. Isolation and characterisation of human cardiac fibroblasts from explanted adult hearts. *Cell and tissue research*. 1996;286:145-53.
263.Doppler SA, Carvalho C, Lahm H, Deutsch MA, Dreßen M, Puluca N, Lange R and Krane M. Cardiac fibroblasts: more than mechanical support. *Journal of thoracic disease*. 2017;9:S36-s51.
264.Lee CS, Bishop ES, Zhang R, Yu X, Farina EM, Yan S, Zhao C, Zheng Z, Shu Y, Wu X, Lei J, Li Y, Zhang W, Yang C, Wu K, Wu Y, Ho S, Athiviraham A, Lee MJ, Wolf JM, Reid RR and He TC. Adenovirus-Mediated Gene Delivery: Potential Applications for Gene and Cell-Based Therapies in the New Era of Personalized Medicine. *Genes & diseases*. 2017;4:43-63.
265.Ardehali H, Qasim A, Cappola T, Howard D, Hruban R, Hare JM, Baughman KL and Kasper EK. Endomyocardial biopsy plays a role in diagnosing patients with unexplained cardiomyopathy. *American heart journal*. 2004;147:919-23.
266.Luk A, Metawee M, Ahn E, Gustafsson F, Ross H and Butany J. Do clinical diagnoses correlate with pathological diagnoses in cardiac transplant patients? The importance of endomyocardial biopsy. *The Canadian journal of cardiology*. 2009;25:e48-54.
267.Mazur P. Freezing of living cells: mechanisms and implications. *The American journal of physiology*. 1984;247:C125-42.
268.Michel SG, LaMuraglia Ii GM, Madariaga MLL and Anderson LM. Innovative cold storage of donor organs using the Paragonix Sherpa Pak ™ devices. *Heart, Lung and Vessels*. 2015;7:246-255.
269.Jewell SD, Srinivasan M, McCart LM, Williams N, Grizzle WH, LiVolsi V, MacLennan G

and Sedmak DD. Analysis of the molecular quality of human tissues: an experience from the Cooperative Human Tissue Network. *American journal of clinical pathology*. 2002;118:733-41.
270. Spruessel A, Steimann G, Jung M, Lee SA, Carr T, Fentz AK, Spangenberg J, Zornig C, Juhl HH and David KA. Tissue ischemia time affects gene and protein expression patterns within minutes following surgical tumor excision. *BioTechniques*. 2004;36:1030-7.
271. Grizzle WE, Bell WC and Sexton KC. Issues in collecting, processing and storing human tissues and associated information to support biomedical research. *Cancer biomarkers : section A of Disease markers*. 2010;9:531-49.
272. Huang J, Qi R, Quackenbush J, Dauway E, Lazaridis E and Yeatman T. Effects of ischemia on gene expression. *The Journal of surgical research*. 2001;99:222-7.
273. Leon-Mimila P, Wang J and Huertas-Vazquez A. Relevance of Multi-Omics Studies in Cardiovascular Diseases. *Frontiers in cardiovascular medicine*. 2019;6:91.
274. Andersson C, Lin H, Liu C, Levy D, Mitchell GF, Larson MG and Vasan RS. Integrated Multiomics Approach to Identify Genetic Underpinnings of Heart Failure and Its Echocardiographic Precursors: Framingham Heart Study. *Circulation Genomic and precision medicine*. 2019;12:e002489.
275. Rau CD, Lusis AJ and Wang Y. Systems Genetics for Mechanistic Discovery in Heart Diseases. *Circulation research*. 2020;126:1795-1815.
276. O'Donnell CJ and Nabel EG. Genomics of cardiovascular disease. *The New England journal of medicine*. 2011;365:2098-109.
277. Lee DS, Pencina MJ, Benjamin EJ, Wang TJ, Levy D, O'Donnell CJ, Nam BH, Larson MG, D'Agostino RB and Vasan RS. Association of parental heart failure with risk of heart failure in offspring. *The New England journal of medicine*. 2006;355:138-47.
278. Ganesh SK, Arnett DK, Assimes TL, Basson CT, Chakravarti A, Ellinor PT, Engler MB, Goldmuntz E, Herrington DM, Hershberger RE, Hong Y, Johnson JA, Kittner SJ, McDermott DA, Meschia JF, Mestroni L, O'Donnell CJ, Psaty BM, Vasan RS, Ruel M, Shen WK, Terzic A and Waldman SA. Genetics and genomics for the prevention and treatment of cardiovascular disease: update: a scientific statement from the American Heart Association. *Circulation*. 2013;128:2813-51.
279. Lopes LR and Elliott PM. Genetics of heart failure. *Biochim Biophys Acta*. 2013;1832:2451-2461.

280.Dainis AM and Ashley EA. Cardiovascular Precision Medicine in the Genomics Era. *JACC Basic to translational science*. 2018;3:313-326.
281.Pedrotty DM, Morley MP and Cappola TP. Transcriptomic biomarkers of cardiovascular disease. *Progress in cardiovascular diseases*. 2012;55:64-9.
282.Napoli C, Lerman LO, Sica V, Lerman A, Tajana G and de Nigris F. Microarray analysis: a novel research tool for cardiovascular scientists and physicians. *Heart (British Cardiac Society)*. 2003;89:597-604.
283.Russo G, Zegar C and Giordano A. Advantages and limitations of microarray technology in human cancer. *Oncogene*. 2003;22:6497-507.
284.Pawlak M, Niescierowicz K and Winata CL. Decoding the Heart through Next Generation Sequencing Approaches. *Genes (Basel)*. 2018;9:289.
285.Yang KC, Yamada KA, Patel AY, Topkara VK, George I, Cheema FH, Ewald GA, Mann DL and Nerbonne JM. Deep RNA sequencing reveals dynamic regulation of myocardial noncoding RNAs in failing human heart and remodeling with mechanical circulatory support. *Circulation*. 2014;129:1009-21.
286.Wang L, Yu P, Zhou B, Song J, Li Z, Zhang M, Guo G, Wang Y, Chen X, Han L and Hu S. Single-cell reconstruction of the adult human heart during heart failure and recovery reveals the cellular landscape underlying cardiac function. *Nature cell biology*. 2020;22:108-119.
287.Jo BS, Koh IU, Bae JB, Yu HY, Jeon ES, Lee HY, Kim JJ, Choi M and Choi SS. Data of methylome and transcriptome derived from human dilated cardiomyopathy. *Data in brief*. 2016;9:382-387.
288.Hall CL, Gurha P, Sabater-Molina M, Asimaki A, Futema M, Lovering RC, Suárez MP, Aguilera B, Molina P, Zorio E, Coarfa C, Robertson MJ, Cheedipudi SM, Ng K-E, Delaney P, Hernández JP, Pastor F, Gimeno JR, McKenna WJ, Marian AJ and Syrris P. RNA sequencing-based transcriptome profiling of cardiac tissue implicates novel putative disease mechanisms in FLNC-associated arrhythmogenic cardiomyopathy. *Int J Cardiol*. 2020;302:124-130.
289.Haywood ME, Cocciolo A, Porter KF, Dobrinskikh E, Slavov D, Graw SL, Reece TB, Ambardekar AV, Bristow MR, Mestroni L and Taylor MRG. Transcriptome signature of ventricular arrhythmia in dilated cardiomyopathy reveals increased fibrosis and activated TP53. *Journal of molecular and cellular cardiology*. 2020;139:124-134.
290.Sweet ME, Cocciolo A, Slavov D, Jones KL, Sweet JR, Graw SL, Reece TB, Ambardekar AV,

Bristow MR, Mestroni L and Taylor MRG. Transcriptome analysis of human heart failure reveals dysregulated cell adhesion in dilated cardiomyopathy and activated immune pathways in ischemic heart failure. *BMC Genomics*. 2018;19:812-812.

291.Jo BS, Koh IU, Bae JB, Yu HY, Jeon ES, Lee HY, Kim JJ, Choi M and Choi SS. Methylome analysis reveals alterations in DNA methylation in the regulatory regions of left ventricle development genes in human dilated cardiomyopathy. *Genomics*. 2016;108:84-92.

292.Sharma P, Cosme J and Gramolini AO. Recent advances in cardiovascular proteomics. *J Proteomics*. 2013;81:3-14.

293.Lindsey ML, Mayr M, Gomes AV, Delles C, Arrell DK, Murphy AM, Lange RA, Costello CE, Jin YF, Laskowitz DT, Sam F, Terzic A, Van Eyk J and Srinivas PR. Transformative Impact of Proteomics on Cardiovascular Health and Disease: A Scientific Statement From the American Heart Association. *Circulation*. 2015;132:852-72.

294.Gramolini AO, Kislinger T, Alikhani-Koopaei R, Fong V, Thompson NJ, Isserlin R, Sharma P, Oudit GY, Trivieri MG, Fagan A, Kannan A, Higgins DG, Huedig H, Hess G, Arab S, Seidman JG, Seidman CE, Frey B, Perry M, Backx PH, Liu PP, MacLennan DH and Emili A. Comparative proteomics profiling of a phospholamban mutant mouse model of dilated cardiomyopathy reveals progressive intracellular stress responses. *Molecular & cellular proteomics : MCP*. 2008;7:519-33.

295.Van Eyk JE. Overview: the maturing of proteomics in cardiovascular research. *Circulation research*. 2011;108:490-8.

296.Lam MP, Ping P and Murphy E. Proteomics Research in Cardiovascular Medicine and Biomarker Discovery. *Journal of the American College of Cardiology*. 2016;68:2819-2830.

297.Zhabyeyev P, Gandhi M, Mori J, Basu R, Kassiri Z, Clanachan A, Lopaschuk GD and Oudit GY. Pressure-overload-induced heart failure induces a selective reduction in glucose oxidation at physiological afterload. *Cardiovascular research*. 2013;97:676-85.

298.Zhang Y and Ren J. Epigenetics and obesity cardiomyopathy: From pathophysiology to prevention and management. *Pharmacology & therapeutics*. 2016;161:52-66.

299.Neubauer S. The failing heart--an engine out of fuel. *The New England journal of medicine*. 2007;356:1140-1151.

300.Lopaschuk GD. Metabolic abnormalities in the diabetic heart. *Heart failure reviews*. 2002;7:149-159.

301. Uddin GM, Zhang L, Shah S, Fukushima A, Wagg CS, Gopal K, Al Batran R, Pherwani S, Ho KL, Boisvenue J, Karwi QG, Altamimi T, Wishart DS, Dyck JRB, Ussher JR, Oudit GY and Lopaschuk GD. Impaired branched chain amino acid oxidation contributes to cardiac insulin resistance in heart failure. *Cardiovascular diabetology*. 2019;18:86.
302. Li YY, Feng Y, McTiernan CF, Pei W, Moravec CS, Wang P, Rosenblum W, Kormos RL and Feldman AM. Downregulation of matrix metalloproteinases and reduction in collagen damage in the failing human heart after support with left ventricular assist devices. *Circulation*. 2001;104:1147-1152.
303. McCarthy PM, Nakatani S, Vargo R, Kottke-Marchant K, Harasaki H, James KB, Savage RM and Thomas JD. Structural and left ventricular histologic changes after implantable LVAD insertion. *Ann Thorac Surg*. 1995;59:609-613.
304. Nakatani S, McCarthy PM, Kottke-Marchant K, Harasaki H, James KB, Savage RM and Thomas JD. Left ventricular echocardiographic and histologic changes: impact of chronic unloading by an implantable ventricular assist device. *Journal of the American College of Cardiology*. 1996;27:894-901.
305. Heerdt PM, Holmes JW, Cai B, Barbone A, Madigan JD, Reiken S, Lee DL, Oz MC, Marks AR and Burkhoff D. Chronic unloading by left ventricular assist device reverses contractile dysfunction and alters gene expression in end-stage heart failure. *Circulation*. 2000;102:2713-2719.
306. Drakos SG, Terrovitis JV, Anastasiou-Nana MI and Nanas JN. Reverse remodeling during long-term mechanical unloading of the left ventricle. *Journal of molecular and cellular cardiology*. 2007;43:231-42.
307. Argiriou M, Kolokotron SM, Sakellaridis T, Argiriou O, Charitos C, Zarogoulidis P, Katsikogiannis N, Kougioumtzi I, Machairiotis N, Tsiouda T, Tsakiridis K and Zarogoulidis K. Right heart failure post left ventricular assist device implantation. *Journal of thoracic disease*. 2014;6:S52-9.
308. Zaman MA, Oparil S and Calhoun DA. Drugs targeting the renin-angiotensin-aldosterone system. *Nature reviews Drug discovery*. 2002;1:621-36.
309. Wang W, Bodiga S, Das SK, Lo J, Patel V and Oudit GY. Role of ACE2 in diastolic and systolic heart failure. *Heart failure reviews*. 2012;17:683-91.
310. Wang K, Gheblawi M and Oudit GY. Angiotensin Converting Enzyme 2: A Double-Edged

Sword. *Circulation*. 2020.
311. Crackower MA, Oudit GY, Kozieradzki I, Sarao R, Sun H, Sasaki T, Hirsch E, Suzuki A, Shioi T, Irie-Sasaki J, Sah R, Cheng HY, Rybin VO, Lembo G, Fratta L, Oliveira-dos-Santos AJ, Benovic JL, Kahn CR, Izumo S, Steinberg SF, Wymann MP, Backx PH and Penninger JM. Regulation of myocardial contractility and cell size by distinct PI3K-PTEN signaling pathways. *Cell*. 2002;110:737-49.
312. Oudit GY, Crackower MA, Backx PH and Penninger JM. The role of ACE2 in cardiovascular physiology. *Trends in cardiovascular medicine*. 2003;13:93-101.
313. Patel VB, Zhong JC, Grant MB and Oudit GY. Role of the ACE2/Angiotensin 1-7 Axis of the Renin-Angiotensin System in Heart Failure. *Circulation research*. 2016;118:1313-26.
314. Bodiga S, Zhong JC, Wang W, Basu R, Lo J, Liu GC, Guo D, Holland SM, Scholey JW, Penninger JM, Kassiri Z and Oudit GY. Enhanced susceptibility to biomechanical stress in ACE2 null mice is prevented by loss of the p47(phox) NADPH oxidase subunit. *Cardiovascular research*. 2011;91:151-61.
315. Oudit GY, Kassiri Z, Jiang C, Liu PP, Poutanen SM, Penninger JM and Butany J. SARS-coronavirus modulation of myocardial ACE2 expression and inflammation in patients with SARS. *European journal of clinical investigation*. 2009;39:618-25.
316. Gheblawi M, Wang K, Viveiros A, Nguyen Q, Zhong JC, Turner AJ, Raizada MK, Grant MB and Oudit GY. Angiotensin-Converting Enzyme 2: SARS-CoV-2 Receptor and Regulator of the Renin-Angiotensin System: Celebrating the 20th Anniversary of the Discovery of ACE2. *Circulation research*. 2020;126:1456-1474.
317. Lo J, Patel VB, Wang Z, Levasseur J, Kaufman S, Penninger JM and Oudit GY. Angiotensin-converting enzyme 2 antagonizes angiotensin II-induced pressor response and NADPH oxidase activation in Wistar–Kyoto rats and spontaneously hypertensive rats. *Experimental physiology*. 2013;98:109-122.
318. Oudit GY, Kassiri Z, Patel MP, Chappell M, Butany J, Backx PH, Tsushima RG, Scholey JW, Khokha R and Penninger JM. Angiotensin II-mediated oxidative stress and inflammation mediate the age-dependent cardiomyopathy in ACE2 null mice. *Cardiovascular research*. 2007;75:29-39.
319. Patel VB, Bodiga S, Fan D, Das SK, Wang Z, Wang W, Basu R, Zhong J, Kassiri Z and Oudit GY. Cardioprotective Effects Mediated by Angiotensin II Type 1 Receptor Blockade and Enhancing Angiotensin 1-7 in Experimental Heart Failure in Angiotensin-Converting Enzyme 2–

Null Mice. *Hypertension*. 2012;59:1195-1203.
320.Oudit GY and Penninger JM. Recombinant human angiotensin-converting enzyme 2 as a new renin-angiotensin system peptidase for heart failure therapy. *Current heart failure reports*. 2011;8:176-183.
321.Patel VB, Takawale A, Ramprasath T, Das SK, Basu R, Grant MB, Hall DA, Kassiri Z and Oudit GY. Antagonism of angiotensin 1-7 prevents the therapeutic effects of recombinant human ACE2. *Journal of molecular medicine (Berlin, Germany)*. 2015;93:1003-13.
322.Urata H, Healy B, Stewart RW, Bumpus FM and Husain A. Angiotensin II-forming pathways in normal and failing human hearts. *Circulation research*. 1990;66:883-90.
323.Juillerat L, Nussberger J, Menard J, Mooser V, Christen Y, Waeber B, Graf P and Brunner HR. Determinants of angiotensin II generation during converting enzyme inhibition. *Hypertension*. 1990;16:564-72.
324.van de Wal RM, Plokker HW, Lok DJ, Boomsma F, van der Horst FA, van Veldhuisen DJ, van Gilst WH and Voors AA. Determinants of increased angiotensin II levels in severe chronic heart failure patients despite ACE inhibition. *Int J Cardiol*. 2006;106:367-72.
325.Roig E, Perez-Villa F, Morales M, Jimenez W, Orus J, Heras M and Sanz G. Clinical implications of increased plasma angiotensin II despite ACE inhibitor therapy in patients with congestive heart failure. *European heart journal*. 2000;21:53-7.
326.Basu R, Poglitsch M, Yogasundaram H, Thomas J, Rowe BH and Oudit GY. Roles of Angiotensin Peptides and Recombinant Human ACE2 in Heart Failure. *Journal of the American College of Cardiology*. 2017;69:805-819.
327.Zhong JC, Zhang ZZ, Wang W, McKinnie SMK, Vederas JC and Oudit GY. Targeting the apelin pathway as a novel therapeutic approach for cardiovascular diseases. *Biochim Biophys Acta*. 2017;1863:1942-1950.
328.Kazemi-Bajestani SM, Patel VB, Wang W and Oudit GY. Targeting the ACE2 and Apelin Pathways Are Novel Therapies for Heart Failure: Opportunities and Challenges. *Cardiology research and practice*. 2012;2012:823193.
329.Pitkin SL, Maguire JJ, Bonner TI and Davenport AP. International Union of Basic and Clinical Pharmacology. LXXIV. Apelin receptor nomenclature, distribution, pharmacology, and function. *Pharmacological reviews*. 2010;62:331-42.
330.Japp AG, Cruden NL, Barnes G, van Gemeren N, Mathews J, Adamson J, Johnston NR,

Denvir MA, Megson IL, Flapan AD and Newby DE. Acute cardiovascular effects of apelin in humans: potential role in patients with chronic heart failure. *Circulation*. 2010;121:1818-27.
331. Zhang ZZ, Wang W, Jin HY, Chen X, Cheng YW, Xu YL, Song B, Penninger JM, Oudit GY and Zhong JC. Apelin Is a Negative Regulator of Angiotensin II-Mediated Adverse Myocardial Remodeling and Dysfunction. *Hypertension*. 2017;70:1165-1175.
332. Liang D, Han D, Fan W, Zhang R, Qiao H, Fan M, Su T, Ma S, Li X, Chen J, Wang Y, Ren J and Cao F. Therapeutic efficacy of apelin on transplanted mesenchymal stem cells in hindlimb ischemic mice via regulation of autophagy. *Scientific reports*. 2016;6:21914.
333. Wang W, McKinnie SM, Patel VB, Haddad G, Wang Z, Zhabyeyev P, Das SK, Basu R, McLean B, Kandalam V, Penninger JM, Kassiri Z, Vederas JC, Murray AG and Oudit GY. Loss of Apelin exacerbates myocardial infarction adverse remodeling and ischemia-reperfusion injury: therapeutic potential of synthetic Apelin analogues. *J Am Heart Assoc*. 2013;2:e000249.
334. McKinnie SM, Fischer C, Tran KM, Wang W, Mosquera F, Oudit GY and Vederas JC. The Metalloprotease Neprilysin Degrades and Inactivates Apelin Peptides. *Chembiochem : a European journal of chemical biology*. 2016;17:1495-8.
335. Ceylan-Isik AF, Kandadi MR, Xu X, Hua Y, Chicco AJ, Ren J and Nair S. Apelin administration ameliorates high fat diet-induced cardiac hypertrophy and contractile dysfunction. *Journal of molecular and cellular cardiology*. 2013;63:4-13.
336. Baker AH, Edwards DR and Murphy G. Metalloproteinase inhibitors: biological actions and therapeutic opportunities. *Journal of cell science*. 2002;115:3719-27.
337. Moore L, Fan D, Basu R, Kandalam V and Kassiri Z. Tissue inhibitor of metalloproteinases (TIMPs) in heart failure. *Heart failure reviews*. 2012;17:693-706.
338. Kandalam V, Basu R, Moore L, Fan D, Wang X, Jaworski DM, Oudit GY and Kassiri Z. Lack of tissue inhibitor of metalloproteinases 2 leads to exacerbated left ventricular dysfunction and adverse extracellular matrix remodeling in response to biomechanical stress. *Circulation*. 2011;124:2094-105.
339. Basu R, Lee J, Morton JS, Takawale A, Fan D, Kandalam V, Wang X, Davidge ST and Kassiri Z. TIMP3 is the primary TIMP to regulate agonist-induced vascular remodelling and hypertension. *Cardiovascular research*. 2013;98:360-71.
340. Sakamuri S, Watts R, Takawale A, Wang X, Hernandez-Anzaldo S, Bahitham W, Fernandez-Patron C, Lehner R and Kassiri Z. Absence of Tissue Inhibitor of Metalloproteinase-4 (TIMP4)

ameliorates high fat diet-induced obesity in mice due to defective lipid absorption. *Scientific reports*. 2017;7:6210.
341. Spinale FG. Myocardial matrix remodeling and the matrix metalloproteinases: influence on cardiac form and function. *Physiological reviews*. 2007;87:1285-342.
342. Zannad F, Rossignol P and Iraqi W. Extracellular matrix fibrotic markers in heart failure. *Heart failure reviews*. 2010;15:319-29.
343. Pouleur A-C, Barkoudah E, Uno H, Skali H, Finn PV, Zelenkofske SL, Belenkov YN, Mareev V, Velazquez EJ, Rouleau JL, Maggioni AP, Køber L, Califf RM, McMurray JJV, Pfeffer MA, Solomon SD and Investigators V. Pathogenesis of sudden unexpected death in a clinical trial of patients with myocardial infarction and left ventricular dysfunction, heart failure, or both. *Circulation*. 2010;122:597-602.
344. Jugdutt BI. Preventing adverse remodeling and rupture during healing after myocardial infarction in mice and humans. *Circulation*. 2010;122:103-105.
345. Jugdutt BI and Dhalla NS. *Cardiac remodeling: molecular mechanisms*: Springer Science & Business Media; 2013.
346. Li YY, Feldman AM, Sun Y and McTiernan CF. Differential expression of tissue inhibitors of metalloproteinases in the failing human heart. *Circulation*. 1998;98:1728-1734.
347. Tummalapalli CM, Heath BJ and Tyagi SC. Tissue inhibitor of metalloproteinase-4 instigates apoptosis in transformed cardiac fibroblasts. *Journal of cellular biochemistry*. 2001;80:512-521.
348. Thomas CV, Coker ML, Zellner JL, Handy JR, Crumbley AJ, 3rd and Spinale FG. Increased matrix metalloproteinase activity and selective upregulation in LV myocardium from patients with end-stage dilated cardiomyopathy. *Circulation*. 1998;97:1708-1715.
349. Shaddy RE, Boucek MM, Hsu DT, Boucek RJ, Canter CE, Mahony L, Ross RD, Pahl E, Blume ED and Dodd DA. Carvedilol for children and adolescents with heart failure: a randomized controlled trial. *Jama*. 2007;298:1171-1179.
350. Shah S, Yogasundaram H, Basu R, Wang F, Paterson DI, Alastalo TP and Oudit GY. Novel Dominant-Negative Mutation in Cardiac Troponin I Causes Severe Restrictive Cardiomyopathy. *Circulation: Heart Failure*. 2017;10:e003820.
351. Miskew Nichols B, Nikhanj A, Wang F, Freed DH and Oudit GY. Advanced Dilated Cardiomyopathy in a Patient With Hutterite Limb-Girdle Muscular Dystrophy: Use of a Left Ventricular Assist Device. *Circulation: Heart Failure*. 2018;11:e004960.

352. Yogasundaram H, Paterson ID, Graham M, Sergi C and Oudit GY. Glycogen Storage Disease Because of a PRKAG2 Mutation Causing Severe Biventricular Hypertrophy and High-Grade Atrio-Ventricular Block. *Circulation: Heart Failure*. 2016;9:e003367.
353. Yogasundaram H, Putko BN, Tien J, Paterson DI, Cujec B, Ringrose J and Oudit GY. Hydroxychloroquine-induced cardiomyopathy: case report, pathophysiology, diagnosis, and treatment. *The Canadian journal of cardiology*. 2014;30:1706-15.
354. Yogasundaram H, Kim D, Oudit O, Thompson RB, Weidemann F and Oudit GY. Clinical Features, Diagnosis, and Management of Patients With Anderson-Fabry Cardiomyopathy. *The Canadian journal of cardiology*. 2017;33:883-897.
355. Yogasundaram H, Nikhanj A, Putko BN, Boutin M, Jain-Ghai S, Khan A, Auray-Blais C, West ML and Oudit GY. Elevated Inflammatory Plasma Biomarkers in Patients With Fabry Disease: A Critical Link to Heart Failure With Preserved Ejection Fraction. *J Am Heart Assoc*. 2018;7:e009098.
356. Nikhanj A, Yogasundaram H, Miskew Nichols B, Richman-Eisenstat J, Phan C, Bakal JA, Siddiqi ZA and Oudit GY. Cardiac Intervention Improves Heart Disease and Clinical Outcomes in Patients With Muscular Dystrophy in a Multidisciplinary Care Setting. *J Am Heart Assoc*. 2020;9:e014004.
357. Nikhanj A, Sivakumaran S, Yogasundaram H, Becher H, Kimber S, Siddiqi ZA and Oudit GY. Comparison of Usefulness of Cardiac Resynchronization Therapy in Patients With Type 1 Myotonic Dystrophy With Versus Without Left Bundle Branch Block. *The American journal of cardiology*. 2019;124:1770-1774.
358. Nikhanj A, Sivakumaran S, Miskew-Nichols B, Siddiqi ZA and Oudit GY. Ventricular tachycardia in patients with type 1 myotonic dystrophy: a case series. *European heart journal Case reports*. 2019;3:ytz095.
359. Iacobellis G and Willens HJ. Echocardiographic epicardial fat: a review of research and clinical applications. *Journal of the American Society of Echocardiography : official publication of the American Society of Echocardiography*. 2009;22:1311-9; quiz 1417-8.
360. Talman AH, Psaltis PJ, Cameron JD, Meredith IT, Seneviratne SK and Wong DT. Epicardial adipose tissue: far more than a fat depot. *Cardiovascular diagnosis and therapy*. 2014;4:416-29.
361. Iacobellis G. Epicardial and pericardial fat: close, but very different. *Obesity (Silver Spring, Md)*. 2009;17:625; author reply 626-7.

362.Rafeh R, Viveiros A, Oudit GY and El-Yazbi AF. Targeting perivascular and epicardial adipose tissue inflammation: therapeutic opportunities for cardiovascular disease. *Clinical science (London, England : 1979)*. 2020;134:827-851.

363.Corradi D, Maestri R, Callegari S, Pastori P, Goldoni M, Luong TV and Bordi C. The ventricular epicardial fat is related to the myocardial mass in normal, ischemic and hypertrophic hearts. *Cardiovascular pathology : the official journal of the Society for Cardiovascular Pathology*. 2004;13:313-6.

364.Iacobellis G and Bianco AC. Epicardial adipose tissue: emerging physiological, pathophysiological and clinical features. *Trends in endocrinology and metabolism: TEM*. 2011;22:450-7.

365.Patel VB, Shah S, Verma S and Oudit GY. Epicardial adipose tissue as a metabolic transducer: role in heart failure and coronary artery disease. *Heart failure reviews*. 2017;22:889-902.

366.Mazurek T, Zhang L, Zalewski A, Mannion JD, Diehl JT, Arafat H, Sarov-Blat L, O'Brien S, Keiper EA, Johnson AG, Martin J, Goldstein BJ and Shi Y. Human epicardial adipose tissue is a source of inflammatory mediators. *Circulation*. 2003;108:2460-6.

367.Yamaguchi Y, Cavallero S, Patterson M, Shen H, Xu J, Kumar SR and Sucov HM. Adipogenesis and epicardial adipose tissue: a novel fate of the epicardium induced by mesenchymal transformation and PPARgamma activation. *Proceedings of the National Academy of Sciences of the United States of America*. 2015;112:2070-5.

368.Al-Khatib SM, Stevenson WG, Ackerman MJ, Bryant WJ, Callans DJ, Curtis AB, Deal BJ, Dickfeld T, Field ME, Fonarow GC, Gillis AM, Granger CB, Hammill SC, Hlatky MA, Joglar JA, Kay GN, Matlock DD, Myerburg RJ and Page RL. 2017 AHA/ACC/HRS Guideline for Management of Patients With Ventricular Arrhythmias and the Prevention of Sudden Cardiac Death: A Report of the American College of Cardiology/American Heart Association Task Force on Clinical Practice Guidelines and the Heart Rhythm Society. *Journal of the American College of Cardiology*. 2018;72:e91-e220.

369.Witkowski FX, Leon LJ, Penkoske PA, Giles WR, Spano ML, Ditto WL and Winfree AT. Spatiotemporal evolution of ventricular fibrillation. *Nature*. 1998;392:78-82.

370.Zhabyeyev P, McLean B, Chen X, Vanhaesebroeck B and Oudit GY. Inhibition of PI3Kinase-α is pro-arrhythmic and associated with enhanced late Na(+) current, contractility, and Ca(2+) release in murine hearts. *Journal of molecular and cellular cardiology*. 2019;132:98-109.

371.Mihic A, Chauhan VS, Gao X, Oudit GY and Tsushima RG. Trafficking defect and proteasomal degradation contribute to the phenotype of a novel KCNH2 long QT syndrome mutation. *PLoS One*. 2011;6:e18273-e18273.
372.Virani SS, Alonso A, Benjamin EJ, Bittencourt MS, Callaway CW, Carson AP, Chamberlain AM, Chang AR, Cheng S, Delling FN, Djousse L, Elkind MSV, Ferguson JF, Fornage M, Khan SS, Kissela BM, Knutson KL, Kwan TW, Lackland DT, Lewis TT, Lichtman JH, Longenecker CT, Loop MS, Lutsey PL, Martin SS, Matsushita K, Moran AE, Mussolino ME, Perak AM, Rosamond WD, Roth GA, Sampson UKA, Satou GM, Schroeder EB, Shah SH, Shay CM, Spartano NL, Stokes A, Tirschwell DL, VanWagner LB, Tsao CW, American Heart Association Council on E, Prevention Statistics C and Stroke Statistics S. Heart Disease and Stroke Statistics-2020 Update: A Report From the American Heart Association. *Circulation*. 2020;141:e139-e596.
373.Anand IS and Gupta P. Anemia and Iron Deficiency in Heart Failure: Current Concepts and Emerging Therapies. *Circulation*. 2018;138:80-98.
374.Ponikowski P, Voors AA, Anker SD, Bueno H, Cleland JG, Coats AJ, Falk V, Gonzalez-Juanatey JR, Harjola VP, Jankowska EA, Jessup M, Linde C, Nihoyannopoulos P, Parissis JT, Pieske B, Riley JP, Rosano GM, Ruilope LM, Ruschitzka F, Rutten FH, van der Meer P and Authors/Task Force M. 2016 ESC Guidelines for the diagnosis and treatment of acute and chronic heart failure: The Task Force for the diagnosis and treatment of acute and chronic heart failure of the European Society of Cardiology (ESC)Developed with the special contribution of the Heart Failure Association (HFA) of the ESC. *Eur Heart J*. 2016;37:2129-200.
375.Klip IT, Comin-Colet J, Voors AA, Ponikowski P, Enjuanes C, Banasiak W, Lok DJ, Rosentryt P, Torrens A and Polonski L. Iron deficiency in chronic heart failure: an international pooled analysis. *American heart journal*. 2013;165:575-582. e3.
376.Tkaczyszyn M, Comin-Colet J, Voors AA, van Veldhuisen DJ, Enjuanes C, Moliner-Borja P, Rozentryt P, Polonski L, Banasiak W, Ponikowski P, van der Meer P and Jankowska EA. Iron deficiency and red cell indices in patients with heart failure. *Eur J Heart Fail*. 2018;20:114-122.
377.Anker SD, Comin Colet J, Filippatos G, Willenheimer R, Dickstein K, Drexler H, Lüscher TF, Bart B, Banasiak W, Niegowska J, Kirwan B-A, Mori C, von Eisenhart Rothe B, Pocock SJ, Poole-Wilson PA and Ponikowski P. Ferric Carboxymaltose in Patients with Heart Failure and Iron Deficiency. *New England Journal of Medicine*. 2009;361:2436-2448.
378.Leszek P, Sochanowicz B, Szperl M, Kolsut P, Brzoska K, Piotrowski W, Rywik TM, Danko

B, Polkowska-Motrenko H, Rozanski JM and Kruszewski M. Myocardial iron homeostasis in advanced chronic heart failure patients. *Int J Cardiol*. 2012;159:47-52.
379.Neubauer S. The Failing Heart — An Engine Out of Fuel. *New England Journal of Medicine*. 2007;356:1140-1151.
380.Hoes MF, Grote Beverborg N, Kijlstra JD, Kuipers J, Swinkels DW, Giepmans BNG, Rodenburg RJ, van Veldhuisen DJ, de Boer RA and van der Meer P. Iron deficiency impairs contractility of human cardiomyocytes through decreased mitochondrial function. *Eur J Heart Fail*. 2018;20:910-919.
381.van der Meer P, van der Wal HH and Melenovsky V. Mitochondrial Function, Skeletal Muscle Metabolism, and Iron Deficiency in Heart Failure. *Circulation*. 2019;139:2399-2402.
382.Zhang H, Zhabyeyev P, Wang S and Oudit GY. Role of iron metabolism in heart failure: From iron deficiency to iron overload. *Biochim Biophys Acta Mol Basis Dis*. 2019;1865:1925-1937.
383.Galy B, Ferring-Appel D, Sauer SW, Kaden S, Lyoumi S, Puy H, Kolker S, Grone HJ and Hentze MW. Iron regulatory proteins secure mitochondrial iron sufficiency and function. *Cell Metab*. 2010;12:194-201.
384.Spinazzi M, Casarin A, Pertegato V, Salviati L and Angelini C. Assessment of mitochondrial respiratory chain enzymatic activities on tissues and cultured cells. *Nature protocols*. 2012;7:1235-46.
385.Das SK, Patel VB, Basu R, Wang W, DesAulniers J, Kassiri Z and Oudit GY. Females Are Protected From Iron-Overload Cardiomyopathy Independent of Iron Metabolism: Key Role of Oxidative Stress. *J Am Heart Assoc*. 2017;6.
386.Weydert CJ and Cullen JJ. Measurement of superoxide dismutase, catalase and glutathione peroxidase in cultured cells and tissue. *Nature protocols*. 2010;5:51-66.
387.Zhang Y, El-Sikhry H, Chaudhary KR, Batchu SN, Shayeganpour A, Jukar TO, Bradbury JA, Graves JP, DeGraff LM, Myers P, Rouse DC, Foley J, Nyska A, Zeldin DC and Seubert JM. Overexpression of CYP2J2 provides protection against doxorubicin-induced cardiotoxicity. *Am J Physiol Heart Circ Physiol*. 2009;297:H37-46.
388.Dieterich S, Bieligk U, Beulich K, Hasenfuss G and Prestle J. Gene expression of antioxidative enzymes in the human heart: increased expression of catalase in the end-stage failing heart. *Circulation*. 2000;101:33-9.
389.Rahman I, Kode A and Biswas SK. Assay for quantitative determination of glutathione and

glutathione disulfide levels using enzymatic recycling method. *Nature protocols*. 2006;1:3159-65.
390.Patel VB, Bodiga S, Basu R, Das SK, Wang W, Wang Z, Lo J, Grant MB, Zhong J, Kassiri Z and Oudit GY. Loss of angiotensin-converting enzyme-2 exacerbates diabetic cardiovascular complications and leads to systolic and vascular dysfunction: a critical role of the angiotensin II/AT1 receptor axis. *Circulation research*. 2012;110:1322-35.
391.Zhong J, Basu R, Guo D, Chow FL, Byrns S, Schuster M, Loibner H, Wang X-h, Penninger JM and Kassiri Z. Angiotensin-converting enzyme 2 suppresses pathological hypertrophy, myocardial fibrosis, and cardiac dysfunction. *Circulation*. 2010;122:717-28, 18 p following 728.
392.Messroghli DR, Moon JC, Ferreira VM, Grosse-Wortmann L, He T, Kellman P, Mascherbauer J, Nezafat R, Salerno M, Schelbert EB, Taylor AJ, Thompson R, Ugander M, van Heeswijk RB and Friedrich MG. Clinical recommendations for cardiovascular magnetic resonance mapping of T1, T2, T2* and extracellular volume: A consensus statement by the Society for Cardiovascular Magnetic Resonance (SCMR) endorsed by the European Association for Cardiovascular Imaging (EACVI). *J Cardiovasc Magn Reson*. 2017;19:75.
393.Burchfield JS, Xie M and Hill JA. Pathological ventricular remodeling: mechanisms: part 1 of 2. *Circulation*. 2013;128:388-400.
394.Kim GH, Uriel N and Burkhoff D. Reverse remodelling and myocardial recovery in heart failure. *Nature Reviews Cardiology*. 2018;15:83.
395.van Deursen VM, Urso R, Laroche C, Damman K, Dahlstrom U, Tavazzi L, Maggioni AP and Voors AA. Co-morbidities in patients with heart failure: an analysis of the European Heart Failure Pilot Survey. *Eur J Heart Fail*. 2014;16:103-11.
396.Filippatos G, Farmakis D, Colet JC, Dickstein K, Luscher TF, Willenheimer R, Parissis J, Gaudesius G, Mori C, von Eisenhart Rothe B, Greenlaw N, Ford I, Ponikowski P and Anker SD. Intravenous ferric carboxymaltose in iron-deficient chronic heart failure patients with and without anaemia: a subanalysis of the FAIR-HF trial. *Eur J Heart Fail*. 2013;15:1267-76.
397.Reddy S and Bernstein D. Molecular mechanisms of right ventricular failure. *Circulation*. 2015;132:1734-1742.
398.Kobak KA, Radwanska M, Dziegala M, Kasztura M, Josiak K, Banasiak W, Ponikowski P and Jankowska EA. Structural and functional abnormalities in iron-depleted heart. *Heart failure reviews*. 2019;24:269-277.
399.Lakhal-Littleton S, Wolna M, Carr CA, Miller JJ, Christian HC, Ball V, Santos A, Diaz R,

Biggs D, Stillion R, Holdship P, Larner F, Tyler DJ, Clarke K, Davies B and Robbins PA. Cardiac ferroportin regulates cellular iron homeostasis and is important for cardiac function. *Proceedings of the National Academy of Sciences of the United States of America*. 2015;112:3164-9.

400. Moliner P, Enjuanes C, Tajes M, Cainzos-Achirica M, Lupon J, Garay A, Jimenez-Marrero S, Yun S, Farre N, Cladellas M, Diez C, Gonzalez-Costello J and Comin-Colet J. Association Between Norepinephrine Levels and Abnormal Iron Status in Patients With Chronic Heart Failure: Is Iron Deficiency More Than a Comorbidity? *J Am Heart Assoc*. 2019;8:e010887.

401. Grote Beverborg N, van der Wal HH, Klip IT, Anker SD, Cleland J, Dickstein K, van Veldhuisen DJ, Voors AA and van der Meer P. Differences in Clinical Profile and Outcomes of Low Iron Storage vs Defective Iron Utilization in Patients With Heart Failure: Results From the DEFINE-HF and BIOSTAT-CHF Studies. *JAMA Cardiol*. 2019;4:696-701.

402. Charles-Edwards G, Amaral N, Sleigh A, Ayis S, Catibog N, McDonagh T, Monaghan M, Amin-Youssef G, Kemp GJ, Shah AM and Okonko DO. Effect of Iron Isomaltoside on Skeletal Muscle Energetics in Patients With Chronic Heart Failure and Iron Deficiency. *Circulation*. 2019;139:2386-2398.

403. Carpenter JP, He T, Kirk P, Roughton M, Anderson LJ, de Noronha SV, Sheppard MN, Porter JB, Walker JM, Wood JC, Galanello R, Forni G, Catani G, Matta G, Fucharoen S, Fleming A, House MJ, Black G, Firmin DN, St Pierre TG and Pennell DJ. On T2* magnetic resonance and cardiac iron. *Circulation*. 2011;123:1519-28.

404. Lota AS, Gatehouse PD and Mohiaddin RH. T2 mapping and T2* imaging in heart failure. *Heart failure reviews*. 2017;22:431-440.

405. Nunez J, Minana G, Cardells I, Palau P, Llacer P, Facila L, Almenar L, Lopez-Lereu MP, Monmeneu JV, Amiguet M, Gonzalez J, Serrano A, Montagud V, Lopez-Vilella R, Valero E, Garcia-Blas S, Bodi V, de la Espriella-Juan R, Lupon J, Navarro J, Gorriz JL, Sanchis J, Chorro FJ, Comin-Colet J, Bayes-Genis A and Myocardial IId. Noninvasive Imaging Estimation of Myocardial Iron Repletion Following Administration of Intravenous Iron: The Myocardial-IRON Trial. *J Am Heart Assoc*. 2020;9:e014254.

406. Ponikowski P, Voors AA, Anker SD, Bueno H, Cleland JGF, Coats AJS, Falk V, González-Juanatey JR, Harjola VP, Jankowska EA, Jessup M, Linde C, Nihoyannopoulos P, Parissis JT, Pieske B, Riley JP, Rosano GMC, Ruilope LM, Ruschitzka F, Rutten FH and van der Meer P. 2016 ESC Guidelines for the diagnosis and treatment of acute and chronic heart failure: The Task Force

for the diagnosis and treatment of acute and chronic heart failure of the European Society of Cardiology (ESC) Developed with the special contribution of the Heart Failure Association (HFA) of the ESC. *European heart journal*. 2016;37:2129-2200.

407. Hsu DT and Pearson GD. Heart failure in children: part I: history, etiology, and pathophysiology. *Circulation: Heart Failure*. 2009;2:63-70.

408. Thakur V, Fouron J-C, Mertens L and Jaeggi ET. Diagnosis and management of fetal heart failure. *Canadian Journal of Cardiology*. 2013;29:759-767.

409. Puggia I, Merlo M, Barbati G, Rowland TJ, Stolfo D, Gigli M, Ramani F, Di Lenarda A, Mestroni L and Sinagra G. Natural history of dilated cardiomyopathy in children. *Journal of the American Heart Association*. 2016;5:e003450.

410. Everitt MD, Sleeper LA, Lu M, Canter CE, Pahl E, Wilkinson JD, Addonizio LJ, Towbin JA, Rossano J and Singh RK. Recovery of echocardiographic function in children with idiopathic dilated cardiomyopathy: results from the pediatric cardiomyopathy registry. *Journal of the American College of Cardiology*. 2014;63:1405-1413.

411. Bayes-Genis A, Liu PP, Lanfear DE, de Boer RA, González A, Thum T, Emdin M and Januzzi JL. Omics phenotyping in heart failure: the next frontier. *European heart journal*. 2020.

412. Cox B, Kotlyar M, Evangelou AI, Ignatchenko V, Ignatchenko A, Whiteley K, Jurisica I, Adamson SL, Rossant J and Kislinger T. Comparative systems biology of human and mouse as a tool to guide the modeling of human placental pathology. *Mol Syst Biol*. 2009;5:279.

413. Huertas-Vazquez A, Leon-Mimila P and Wang J. Relevance of multi-omics studies in cardiovascular diseases. *Front Cardiovasc Med*. 2019;6:91.

414. Andersson C, Lin H, Liu C, Levy D, Mitchell GF, Larson MG and Vasan RS. Integrated Multiomics Approach to Identify Genetic Underpinnings of Heart Failure and Its Echocardiographic Precursors: Framingham Heart Study. *Circulation: Genomic and Precision Medicine*. 2019;12:e002489.

415. Zhang H, Jamieson KL, Grenier J, Nikhanj A, Tang Z, Wang F, Wang S, Seidman JG, Seidman CE and Thompson R. Myocardial Iron Deficiency and Mitochondrial Dysfunction in Advanced Heart Failure in Humans. *Journal of the American Heart Association*. 2021:e022853.

416. Litviňuková M, Talavera-López C, Maatz H, Reichart D, Worth CL, Lindberg EL, Kanda M, Polanski K, Heinig M and Lee M. Cells of the adult human heart. *Nature*. 2020:1-10.

417. Jamieson KL, Keshavarz-Bahaghighat H, Darwesh AM, Sosnowski DK and Seubert JM. Age

and sex differences in hearts of soluble epoxide hydrolase null mice. *Frontiers in Physiology*. 2020;11:48.

418.Collins HE, Kane MS, Litovsky SH, Darley-Usmar VM, Young ME, Chatham JC and Zhang J. Mitochondrial morphology and mitophagy in heart diseases: qualitative and quantitative analyses using transmission electron microscopy. *Frontiers in Aging*. 2021;2:670267.

419.Treskatsch S, Shakibaei M, Feldheiser A, Shaqura M, Dehe L, Roepke T, Spies C, Schäfer M and Mousa S. Ultrastructural changes associated with myocardial apoptosis, in failing rat hearts induced by volume overload. *International journal of cardiology*. 2015;197:327-332.

420.Wang Y. Mitogen-activated protein kinases in heart development and diseases. *Circulation*. 2007;116:1413-1423.

421.Khan MS and Butler J. Targeting Mitochondrial Function in Heart Failure: Makes Sense But Will it Work? 2019;4:158-160.

422.Törnroth-Horsefield S and Neutze R. Opening and closing the metabolite gate. *Proceedings of the National Academy of Sciences*. 2008;105:19565-19566.

423.Mann DL. Targeting myocardial energetics in the failing heart: are we there yet? *Circulation: Heart Failure*. 2017;10:e004658.

424.Doenst T, Nguyen TD and Abel ED. Cardiac metabolism in heart failure: implications beyond ATP production. *Circulation research*. 2013;113:709-724.

425.Brown DA, Perry JB, Allen ME, Sabbah HN, Stauffer BL, Shaikh SR, Cleland JG, Colucci WS, Butler J and Voors AA. Mitochondrial function as a therapeutic target in heart failure. *Nature Reviews Cardiology*. 2017;14:238-250.

426.Eirin A, Ebrahimi B, Zhang X, Zhu X-Y, Woollard JR, He Q, Textor SC, Lerman A and Lerman LO. Mitochondrial protection restores renal function in swine atherosclerotic renovascular disease. *Cardiovascular research*. 2014;103:461-472.

427.Anderson EJ, Lustig ME, Boyle KE, Woodlief TL, Kane DA, Lin C-T, Price JW, Kang L, Rabinovitch PS and Szeto HH. Mitochondrial H 2 O 2 emission and cellular redox state link excess fat intake to insulin resistance in both rodents and humans. *The Journal of clinical investigation*. 2009;119:573-581.

428.Casademont J and Miró Ò. Electron transport chain defects in heart failure. *Heart failure reviews*. 2002;7:131-139.

429.Kuroda J, Ago T, Matsushima S, Zhai P, Schneider MD and Sadoshima J. NADPH oxidase 4

(Nox4) is a major source of oxidative stress in the failing heart. *Proceedings of the National Academy of Sciences of the United States of America*. 2010;107:15565-70.

430.Tretter L and Adam-Vizi V. Alpha-ketoglutarate dehydrogenase: a target and generator of oxidative stress. *Philos Trans R Soc Lond B Biol Sci*. 2005;360:2335-45.

431.Cave AC, Brewer AC, Narayanapanicker A, Ray R, Grieve DJ, Walker S and Shah AM. NADPH oxidases in cardiovascular health and disease. *Antioxid Redox Signal*. 2006;8:691-728.

432.Tretter L and Adam-Vizi V. Generation of reactive oxygen species in the reaction catalyzed by alpha-ketoglutarate dehydrogenase. *The Journal of neuroscience : the official journal of the Society for Neuroscience*. 2004;24:7771-8.

433.Zhang M, Brewer AC, Schröder K, Santos CX, Grieve DJ, Wang M, Anilkumar N, Yu B, Dong X, Walker SJ, Brandes RP and Shah AM. NADPH oxidase-4 mediates protection against chronic load-induced stress in mouse hearts by enhancing angiogenesis. *Proceedings of the National Academy of Sciences of the United States of America*. 2010;107:18121-6.

434.Ji AR, Ku SY, Cho MS, Kim YY, Kim YJ, Oh SK, Kim SH, Moon SY and Choi YM. Reactive oxygen species enhance differentiation of human embryonic stem cells into mesendodermal lineage. *Experimental & molecular medicine*. 2010;42:175-86.

435.Puente BN, Kimura W, Muralidhar SA, Moon J, Amatruda JF, Phelps KL, Grinsfelder D, Rothermel BA, Chen R, Garcia JA, Santos CX, Thet S, Mori E, Kinter MT, Rindler PM, Zacchigna S, Mukherjee S, Chen DJ, Mahmoud AI, Giacca M, Rabinovitch PS, Aroumougame A, Shah AM, Szweda LI and Sadek HA. The oxygen-rich postnatal environment induces cardiomyocyte cell-cycle arrest through DNA damage response. *Cell*. 2014;157:565-79.

436.Li Y, Huang T-T, Carlson EJ, Melov S, Ursell PC, Olson JL, Noble LJ, Yoshimura MP, Berger C and Chan PH. Dilated cardiomyopathy and neonatal lethality in mutant mice lacking manganese superoxide dismutase. *Nature genetics*. 1995;11:376-381.

437.Liu W, Porter NA, Schneider C, Brash AR and Yin H. Formation of 4-hydroxynonenal from cardiolipin oxidation: Intramolecular peroxyl radical addition and decomposition. *Free Radical Biology and Medicine*. 2011;50:166-178.

438.Sharma S, Bhattarai S, Ara H, Sun G, St Clair DK, Bhuiyan MS, Kevil C, Watts MN, Dominic P, Shimizu T, McCarthy KJ, Sun H, Panchatcharam M and Miriyala S. SOD2 deficiency in cardiomyocytes defines defective mitochondrial bioenergetics as a cause of lethal dilated cardiomyopathy. *Redox Biology*. 2020;37:101740.

439.Moretti M, Merlo M, Barbati G, Di Lenarda A, Brun F, Pinamonti B, Gregori D, Mestroni L and Sinagra G. Prognostic impact of familial screening in dilated cardiomyopathy. *European journal of heart failure*. 2010;12:922-927.
440.Mestroni L, Maisch B, McKenna W, Schwartz K, Charron P, Rocco C, Tesson F, Richter R, Wilke A and Komajda M. Guidelines for the study of familial dilated cardiomyopathies. *European heart journal*. 1999;20:93-102.
441.Daubeney PE, Nugent AW, Chondros P, Carlin JB, Colan SD, Cheung M, Davis AM, Chow C and Weintraub RG. Clinical features and outcomes of childhood dilated cardiomyopathy: results from a national population-based study. *Circulation*. 2006;114:2671-2678.
442.Zhang H, Viveiros A, Nikhanj A, Nguyen Q, Wang K, Wang W, Freed DH, Mullen JC, MacArthur R, Kim DH, Tymchak W, Sergi CM, Kassiri Z, Wang S and Oudit GY. The Human Explanted Heart Program: A translational bridge for cardiovascular medicine. *Biochim Biophys Acta Mol Basis Dis*. 2021;1867:165995.
443.Ruotsalainen HK, Pihkala J, Salminen J, Hornberger LK, Sairanen H and Ojala T. Initial shunt type at the Norwood operation impacts myocardial function in hypoplastic left heart syndrome. *European Journal of Cardio-Thoracic Surgery*. 2017;52:234-240.
444.Brooks PA, Khoo NS, Mackie AS and Hornberger LK. Right ventricular function in fetal hypoplastic left heart syndrome. *Journal of the American Society of Echocardiography*. 2012;25:1068-1074.
445.Saraf A, Book WM, Nelson TJ and Xu C. Hypoplastic left heart syndrome: From bedside to bench and back. *Journal of molecular and cellular cardiology*. 2019;135:109-118.
446.Crucean A, Alqahtani A, Barron D, Brawn W, Richardson R, O'Sullivan J, Anderson R, Henderson D and Chaudhry B. Re-evaluation of hypoplastic left heart syndrome from a developmental and morphological perspective. *Orphanet Journal of Rare Diseases*. 2017;12:1-10.
447.Cuypers JA, Menting ME, Konings EE, Opić P, Utens EM, Helbing WA, Witsenburg M, van den Bosch AE, Ouhlous M and van Domburg RT. Unnatural history of tetralogy of Fallot: prospective follow-up of 40 years after surgical correction. *Circulation*. 2014;130:1944-1953.
448.Davlouros PA, Kilner PJ, Hornung TS, Li W, Francis JM, Moon JC, Smith GC, Tat T, Pennell DJ and Gatzoulis MA. Right ventricular function in adults with repaired tetralogy of Fallot assessed with cardiovascular magnetic resonance imaging: detrimental role of right ventricular outflow aneurysms or akinesia and adverse right-to-left ventricular interaction. *Journal of the*

American College of Cardiology. 2002;40:2044-2052.

449. Andrade AC, Jerosch-Herold M, Wegner P, Gabbert DD, Voges I, Pham M, Shah R, Hedderich J, Kramer HH and Rickers C. Determinants of left ventricular dysfunction and remodeling in patients with corrected tetralogy of Fallot. *Journal of the American Heart Association*. 2019;8:e009618.

450. Eckersley L and Hornberger LK. Cardiac function and dysfunction in the fetus. *Echocardiography*. 2017;34:1776-1787.

451. Haghighi K, Kolokathis F, Pater L, Lynch RA, Asahi M, Gramolini AO, Fan G-C, Tsiapras D, Hahn HS and Adamopoulos S. Human phospholamban null results in lethal dilated cardiomyopathy revealing a critical difference between mouse and human. *The Journal of clinical investigation*. 2003;111:869-876.

452. Schmitt JP, Kamisago M, Asahi M, Li GH, Ahmad F, Mende U, Kranias EG, MacLennan DH, Seidman J and Seidman CE. Dilated cardiomyopathy and heart failure caused by a mutation in phospholamban. *Science*. 2003;299:1410-1413.

453. Liu G-S, Morales A, Vafiadaki E, Lam CK, Cai W-F, Haghighi K, Adly G, Hershberger RE and Kranias EG. A novel human R25C-phospholamban mutation is associated with super-inhibition of calcium cycling and ventricular arrhythmia. *Cardiovascular research*. 2015;107:164-174.

454. Van Der Zwaag PA, Van Rijsingen IA, Asimaki A, Jongbloed JD, Van Veldhuisen DJ, Wiesfeld AC, Cox MG, Van Lochem LT, De Boer RA and Hofstra RM. Phospholamban R14del mutation in patients diagnosed with dilated cardiomyopathy or arrhythmogenic right ventricular cardiomyopathy: evidence supporting the concept of arrhythmogenic cardiomyopathy. *European journal of heart failure*. 2012;14:1199-1207.

455. DeWitt MM, MacLeod HM, Soliven B and McNally EM. Phospholamban R14 deletion results in late-onset, mild, hereditary dilated cardiomyopathy. *Journal of the American College of Cardiology*. 2006;48:1396-1398.

456. Haghighi K, Kolokathis F, Gramolini AO, Waggoner JR, Pater L, Lynch RA, Fan G-C, Tsiapras D, Parekh RR and Dorn GW. A mutation in the human phospholamban gene, deleting arginine 14, results in lethal, hereditary cardiomyopathy. *Proceedings of the National Academy of Sciences*. 2006;103:1388-1393.

457. Maron BJ, Roberts WC, Arad M, Haas TS, Spirito P, Wright GB, Almquist AK, Baffa JM,

Saul JP and Ho CY. Clinical outcome and phenotypic expression in LAMP2 cardiomyopathy. *Jama*. 2009;301:1253-1259.

458.Lakdawala NK, Dellefave L, Sparks E, Cirino A, Depalma S, Funke B, Colan SD, Watkins H, Robinson P and Redwood CS. Familial Dilated Cardiomyopathy Caused by an Alpha-Tropomyosin Mutation: The Distinctive Natural History of Sarcomeric DCM. *Journal of cardiac failure*. 2009;15:S3.

459.Man Y, Yi C, Fan M, Yang T, Liu P, Liu S and Wang G. Identification of a novel missense mutation in the TPM1 gene via exome sequencing in a Chinese family with dilated cardiomyopathy: A case report and literature review. *Medicine*. 2022;101.

460.Miyamoto SD, Stauffer BL, Nakano S, Sobus R, Nunley K, Nelson P and Sucharov CC. Beta-adrenergic adaptation in paediatric idiopathic dilated cardiomyopathy. *European heart journal*. 2014;35:33-41.

461.Marín-García J and Akhmedov AT. Mitochondrial dynamics and cell death in heart failure. *Heart failure reviews*. 2016;21:123-36.

462.Hu L, Ding M, Tang D, Gao E, Li C, Wang K, Qi B, Qiu J, Zhao H, Chang P, Fu F and Li Y. Targeting mitochondrial dynamics by regulating Mfn2 for therapeutic intervention in diabetic cardiomyopathy. *Theranostics*. 2019;9:3687-3706.

463.Ong SB, Kalkhoran SB, Hernández-Reséndiz S, Samangouei P, Ong SG and Hausenloy DJ. Mitochondrial-Shaping Proteins in Cardiac Health and Disease - the Long and the Short of It! *Cardiovascular drugs and therapy*. 2017;31:87-107.

464.Forte M, Schirone L, Ameri P, Basso C, Catalucci D, Modica J, Chimenti C, Crotti L, Frati G, Rubattu S, Schiattarella GG, Torella D, Perrino C, Indolfi C and Sciarretta S. The role of mitochondrial dynamics in cardiovascular diseases. *Br J Pharmacol*. 2021;178:2060-2076.

465.Vásquez-Trincado C, García-Carvajal I, Pennanen C, Parra V, Hill JA, Rothermel BA and Lavandero S. Mitochondrial dynamics, mitophagy and cardiovascular disease. *J Physiol*. 2016;594:509-25.

466.Shires SE and Gustafsson Å B. Mitophagy and heart failure. *Journal of molecular medicine (Berlin, Germany)*. 2015;93:253-62.

467.Saito T and Sadoshima J. Molecular mechanisms of mitochondrial autophagy/mitophagy in the heart. *Circulation research*. 2015;116:1477-90.

468.Morciano G, Patergnani S, Bonora M, Pedriali G, Tarocco A, Bouhamida E, Marchi S, Ancora

G, Anania G, Wieckowski MR, Giorgi C and Pinton P. Mitophagy in Cardiovascular Diseases. *Journal of clinical medicine*. 2020;9.

469.Gong G, Song M, Csordas G, Kelly DP, Matkovich SJ and Dorn GW, 2nd. Parkin-mediated mitophagy directs perinatal cardiac metabolic maturation in mice. *Science*. 2015;350:aad2459.

470.Acehan D, Vaz F, Houtkooper RH, James J, Moore V, Tokunaga C, Kulik W, Wansapura J, Toth MJ and Strauss A. Cardiac and skeletal muscle defects in a mouse model of human Barth syndrome. *Journal of biological chemistry*. 2011;286:899-908.

471.Schlame M. Cardiolipin remodeling and the function of tafazzin. *Biochimica et Biophysica Acta (BBA)-Molecular and Cell Biology of Lipids*. 2013;1831:582-588.

472.Claypool SM and Koehler CM. The complexity of cardiolipin in health and disease. *Trends in biochemical sciences*. 2012;37:32-41.

473.Claypool SM, Boontheung P, McCaffery JM, Loo JA and Koehler CM. The cardiolipin transacylase, tafazzin, associates with two distinct respiratory components providing insight into Barth syndrome. *Molecular biology of the cell*. 2008;19:5143-5155.

474.Mileykovskaya E and Dowhan W. Cardiolipin membrane domains in prokaryotes and eukaryotes. *Biochimica et Biophysica Acta (BBA)-Biomembranes*. 2009;1788:2084-2091.

475.Soustek MS, Falk DJ, Mah CS, Toth MJ, Schlame M, Lewin AS and Byrne BJ. Characterization of a transgenic short hairpin RNA-induced murine model of Tafazzin deficiency. *Human gene therapy*. 2011;22:865-871.

476.Acehan D, Xu Y, Stokes DL and Schlame M. Comparison of lymphoblast mitochondria from normal subjects and patients with Barth syndrome using electron microscopic tomography. *Laboratory investigation*. 2007;87:40-48.

477.Acehan D, Malhotra A, Xu Y, Ren M, Stokes DL and Schlame M. Cardiolipin affects the supramolecular organization of ATP synthase in mitochondria. *Biophysical journal*. 2011;100:2184-2192.

478.Acehan D, Khuchua Z, Houtkooper RH, Malhotra A, Kaufman J, Vaz FM, Ren M, Rockman HA, Stokes DL and Schlame M. Distinct effects of tafazzin deletion in differentiated and undifferentiated mitochondria. *Mitochondrion*. 2009;9:86-95.

479.Kiebish MA, Han X, Cheng H, Chuang JH and Seyfried TN. Cardiolipin and electron transport chain abnormalities in mouse brain tumor mitochondria: lipidomic evidence supporting the Warburg theory of cancer. *Journal of lipid research*. 2008;49:2545-2556.

480.Klingenberg M. Cardiolipin and mitochondrial carriers. *Biochimica et Biophysica Acta (BBA)-Biomembranes*. 2009;1788:2048-2058.
481.Lacombe M-L, Tokarska-Schlattner M, Epand RF, Boissan M, Epand RM and Schlattner U. Interaction of NDPK-D with cardiolipin-containing membranes: Structural basis and implications for mitochondrial physiology. *Biochimie*. 2009;91:779-783.
482.Schlattner U, Tokarska-Schlattner M, Ramirez S, Brückner A, Kay L, Polge C, Epand RF, Lee RM, Lacombe M-L and Epand RM. Mitochondrial kinases and their molecular interaction with cardiolipin. *Biochimica et Biophysica Acta (BBA)-Biomembranes*. 2009;1788:2032-2047.
483.Ban T, Heymann JA, Song Z, Hinshaw JE and Chan DC. OPA1 disease alleles causing dominant optic atrophy have defects in cardiolipin-stimulated GTP hydrolysis and membrane tubulation. *Human molecular genetics*. 2010;19:2113-2122.
484.Claypool SM. Cardiolipin, a critical determinant of mitochondrial carrier protein assembly and function. *Biochimica et Biophysica Acta (BBA)-Biomembranes*. 2009;1788:2059-2068.
485.Haines TH and Dencher NA. Cardiolipin: a proton trap for oxidative phosphorylation. *FEBS letters*. 2002;528:35-39.
486.Joshi AS, Zhou J, Gohil VM, Chen S and Greenberg ML. Cellular functions of cardiolipin in yeast. *Biochimica et Biophysica Acta (BBA)-Molecular Cell Research*. 2009;1793:212-218.
487.Gebert N, Joshi AS, Kutik S, Becker T, McKenzie M, Guan XL, Mooga VP, Stroud DA, Kulkarni G and Wenk MR. Mitochondrial cardiolipin involved in outer-membrane protein biogenesis: implications for Barth syndrome. *Current biology*. 2009;19:2133-2139.
488.DeVay RM, Dominguez-Ramirez L, Lackner LL, Hoppins S, Stahlberg H and Nunnari J. Coassembly of Mgm1 isoforms requires cardiolipin and mediates mitochondrial inner membrane fusion. *Journal of Cell Biology*. 2009;186:793-803.
489.Montessuit S, Somasekharan SP, Terrones O, Lucken-Ardjomande S, Herzig S, Schwarzenbacher R, Manstein DJ, Bossy-Wetzel E, Basañez G and Meda P. Membrane remodeling induced by the dynamin-related protein Drp1 stimulates Bax oligomerization. *Cell*. 2010;142:889-901.
490.Gonzalvez F, Schug ZT, Houtkooper RH, MacKenzie ED, Brooks DG, Wanders RJ, Petit PX, Vaz FM and Gottlieb E. Cardiolipin provides an essential activating platform for caspase-8 on mitochondria. *The Journal of cell biology*. 2008;183:681-696.
491.Paradies G, Petrosillo G, Paradies V and Ruggiero FM. Role of cardiolipin peroxidation and

Ca2+ in mitochondrial dysfunction and disease. *Cell calcium*. 2009;45:643-50.
492.Paradies G, Petrosillo G, Paradies V and Ruggiero FM. Oxidative stress, mitochondrial bioenergetics, and cardiolipin in aging. *Free radical biology & medicine*. 2010;48:1286-95.
493.Petrosillo G, Matera M, Moro N, Ruggiero FM and Paradies G. Mitochondrial complex I dysfunction in rat heart with aging: critical role of reactive oxygen species and cardiolipin. *Free radical biology & medicine*. 2009;46:88-94.
494.Petrosillo G, Casanova G, Matera M, Ruggiero FM and Paradies G. Interaction of peroxidized cardiolipin with rat-heart mitochondrial membranes: induction of permeability transition and cytochrome c release. *FEBS letters*. 2006;580:6311-6.
495.Petrosillo G, Casanova G, Matera M, Ruggiero FM and Paradies G. Synergistic effect of Ca2+ and peroxidized cardiolipin in the induction of permeability transition and cytochrome c release in rat heart mitochondria. *The Italian journal of biochemistry*. 2007;56:307-9.
496.Fry M and Green DE. Cardiolipin requirement for electron transfer in complex I and III of the mitochondrial respiratory chain. *Journal of Biological Chemistry*. 1981;256:1874-1880.
497.Ohtsuka T, Nishijima M, Suzuki K and Akamatsu Y. Mitochondrial dysfunction of a cultured Chinese hamster ovary cell mutant deficient in cardiolipin. *Journal of Biological Chemistry*. 1993;268:22914-22919.
498.Dröse S, Zwicker K and Brandt U. Full recovery of the NADH: ubiquinone activity of complex I (NADH: ubiquinone oxidoreductase) from Yarrowia lipolytica by the addition of phospholipids. *Biochimica et Biophysica Acta (BBA)-Bioenergetics*. 2002;1556:65-72.
499.Sharpley MS, Shannon RJ, Draghi F and Hirst J. Interactions between phospholipids and NADH: ubiquinone oxidoreductase (complex I) from bovine mitochondria. *Biochemistry*. 2006;45:241-248.
500.Petrosillo G, Matera M, Casanova G, Ruggiero FM and Paradies G. Mitochondrial dysfunction in rat brain with aging Involvement of complex I, reactive oxygen species and cardiolipin. *Neurochemistry international*. 2008;53:126-31.
501.Oemer G, Edenhofer ML, Wohlfarter Y, Lackner K, Leman G, Koch J, Cardoso LHD, Lindner HH, Gnaiger E, Dubrac S, Zschocke J and Keller MA. Fatty acyl availability modulates cardiolipin composition and alters mitochondrial function in HeLa cells. *J Lipid Res*. 2021;62:100111.
502.Petrosillo G, Moro N, Ruggiero FM and Paradies G. Melatonin inhibits cardiolipin peroxidation in mitochondria and prevents the mitochondrial permeability transition and

cytochrome c release. *Free radical biology & medicine*. 2009;47:969-74.
503.Petrosillo G, Moro N, Paradies V, Ruggiero FM and Paradies G. Increased susceptibility to Ca(2+)-induced permeability transition and to cytochrome c release in rat heart mitochondria with aging: effect of melatonin. *Journal of pineal research*. 2010;48:340-6.
504.He Q and Han X. Cardiolipin remodeling in diabetic heart. *Chemistry and physics of lipids*. 2014;179:75-81.
505.Chatfield KC, Sparagna GC, Chau S, Phillips EK, Ambardekar AV, Aftab M, Mitchell MB, Sucharov CC, Miyamoto SD and Stauffer BL. Elamipretide improves mitochondrial function in the failing human heart. *JACC: Basic to Translational Science*. 2019;4:147-157.
506.Daubert MA, Yow E, Dunn G, Marchev S, Barnhart H, Douglas PS, O'Connor C, Goldstein S, Udelson JE and Sabbah HN. Novel mitochondria-targeting peptide in heart failure treatment: a randomized, placebo-controlled trial of elamipretide. *Circulation: Heart Failure*. 2017;10:e004389.
507.Szeto HH. First-in-class cardiolipin-protective compound as a therapeutic agent to restore mitochondrial bioenergetics. *British journal of pharmacology*. 2014;171:2029-2050.
508.Ajith TA and Jayakumar TG. Mitochondria-targeted agents: Future perspectives of mitochondrial pharmaceutics in cardiovascular diseases. *World journal of cardiology*. 2014;6:1091.
509.Dai D-F, Hsieh EJ, Chen T, Menendez LG, Basisty NB, Tsai L, Beyer RP, Crispin DA, Shulman NJ and Szeto HH. Global proteomics and pathway analysis of pressure-overload–induced heart failure and its attenuation by mitochondrial-targeted peptides. *Circulation: Heart Failure*. 2013;6:1067-1076.
510.Birk A, Chao W, Bracken C, Warren J and Szeto H. Targeting mitochondrial cardiolipin and the cytochrome c/cardiolipin complex to promote electron transport and optimize mitochondrial ATP synthesis. *British journal of pharmacology*. 2014;171:2017-2028.
511.Sabbah HN, Gupta RC, Kohli S, Wang M, Hachem S and Zhang K. Chronic therapy with elamipretide (MTP-131), a novel mitochondria-targeting peptide, improves left ventricular and mitochondrial function in dogs with advanced heart failure. *Circulation: Heart Failure*. 2016;9:e002206.
512.Shi J, Dai W, Hale SL, Brown DA, Wang M, Han X and Kloner RA. Bendavia restores mitochondrial energy metabolism gene expression and suppresses cardiac fibrosis in the border zone of the infarcted heart. *Life sciences*. 2015;141:170-178.

513.Butler J, Khan MS, Anker SD, Fonarow GC, Kim RJ, Nodari S, O'Connor CM, Pieske B, Pieske-Kraigher E and Sabbah HN. Effects of elamipretide on left ventricular function in patients with heart failure with reduced ejection fraction: the PROGRESS-HF phase 2 trial. *Journal of cardiac failure*. 2020;26:429-437.

514.Obi C, Smith AT, Hughes GJ and Adeboye AA. Targeting mitochondrial dysfunction with elamipretide. *Heart failure reviews*. 2022.

515.Taegtmeyer H, Young ME, Lopaschuk GD, Abel ED, Brunengraber H, Darley-Usmar V, Des Rosiers C, Gerszten R, Glatz JF and Griffin JL. Assessing cardiac metabolism: a scientific statement from the American Heart Association. *Circulation research*. 2016;118:1659-1701.

516.Merle U, Fein E, Gehrke SG, Stremmel W and Kulaksiz H. The iron regulatory peptide hepcidin is expressed in the heart and regulated by hypoxia and inflammation. *Endocrinology*. 2007;148:2663-2668.

517.Reichart D, Lindberg EL, Maatz H, Miranda AM, Viveiros A, Shvetsov N, Gärtner A, Nadelmann ER, Lee M and Kanemaru K. Pathogenic variants damage cell composition and single cell transcription in cardiomyopathies. *Science*. 2022;377:eabo1984.